

Department of Chemistry

Application of Barium Zirconate Ceramics to the Synthesis of Ammonia

Joshua Fellowes

Magdalen College

Supervisor:

Professor Edman Tsang

A thesis submitted in partial fulfilment of the requirements for the degree of Doctor of Philosophy

Michaelmas Term 2019

Declaration

I confirm that this is my own work, and that assistance from others and external source materials have been fully acknowledged and referenced when appropriate.

Application of Barium Zirconate Ceramics to the Synthesis of Ammonia

A Thesis submitted for the degree of Doctor of Philosophy

Joshua Fellowes, Magdalen College, Michaelmas Term 2019

This thesis describes investigations into the synthesis of ammonia using the ceramic proton conductor, barium zirconate. Described are the results of the fabrication and testing of barium zirconate cells for the electrochemical synthesis of ammonia, and investigations on the use of proton conducting ceramics as supports in heterogeneous catalysis. While ammonia synthesis is perhaps the most studied and optimised chemical reaction, new challenges are facing the century old Haber-Bosch process in the 21st century. As part of the need to move towards a carbon-free economy, new catalysts, and processes for the synthesis of ammonia are currently being developed.

Electrochemical ammonia synthesis is a promising avenue of research, attracting much interest in recent years. However, the goal of selectively and efficiently reducing the highly stable dinitrogen bond is not easy to realise. Previous literature investigations of this process in high temperature proton conducting cells have focussed on optimisation of electrolytes, leaving electrode catalysts relatively unexplored. This thesis aims to investigate how modification of electrode catalysts may alter rates of electrochemical ammonia synthesis. It is found that modification of the anode and cathode materials can dramatically alter the rates of electrochemical processes, but that the elucidation of electrochemical ammonia is more complex.

Barium zirconate was explored as support material for ruthenium catalysts. Due to the ability of the barium zirconate lattice to trap and store protons, it was proposed this could influence the ammonia synthesis reaction over ruthenium particles. A systematic study of how barium zirconate materials may promote ammonia synthesis was undertaken.

It was found that use of doped barium zirconate supports can provide a significant promotion effect for the synthesis of ammonia over ruthenium nanocatalysts. This promoting effect which, can be quantified using kinetic parameters, is ascribed to differences in the proton conductivities of the ceramic materials. The mechanism of this promotion is explored using neutron diffraction and in-situ x-ray photoelectron spectroscopy techniques.

Acknowledgments

My thanks go to Professor Edman Tsang, for the opportunity to undertake this research, the engaging discussions, and supervision. I am also extremely grateful to my college supervisor Professor Andrew Weller, for helping me to navigate the oftentimes mystifying world of Oxford. Siemens PLC are gratefully acknowledged for funding this research, which has allowed me to see and do many amazing things.

Within the wider chemistry department, there are many people who have made contributions towards this work, small and large. Dr Robert Jacobs and Dr Ashley Shepherd from the Surface Analysis Facility both contributed to the collection of microscopy and surface analysis data. My thanks to Mr Peter Fair from the student workshop for helping on several projects, without him there would have been many more failures. Also, to Mr Nenad Vranješ and Mr Alex Garzón from the electronics workshops, and Ms Terri Adams from the glassblowing workshop for helping to repair my repeatedly broken equipment.

I am grateful to all Tsang group members, past and present, who have contributed to this thesis. A special mention is deserved for Dr Tugce Ayvali, Dr Jianwei Zheng, Dr Pu Zhao, Dr Elizabeth Raine, Dr Haohong Duan, Dr Bozhidar Stefanov, Dr Ben Lo, Mr Simson Wu, Mr Chris Foo, Ms Tatchamapan Yoskamtorn, and Mr Ping-Luen (Baron) Ho for their assistance with experiments and fruitful discussions. Above all my sincere thanks go to Dr Ian McPherson and Mr Tim Sudmeier, the many discussions, crazy ideas (some successful and some less so), and lab assistance were instrumental to my finishing this thesis. My caffeine addiction is not the same without you guys.

To all the friends that have listened to my complaints and provided support & advice over the past four years, thanks for everything. To the (ex)residents of number 22, James Eaton, Lukas Lange, Adam Kenny, and Hamish Lemmey, it was great. Congratulations on your soon-to-be Dr statuses.

To mum, dad, and Thomas, thank you for all the support, both practical and emotional. Finally, to my wife, Magda. This could not have happened without you, and I will always remember your love, patience, and morning cappuccinos throughout this process.

Where relevant, significant individual contributions are acknowledged on a per-chapter basis.

Nomenclature

AC	Alternating current
BC	Barium cerate
BCZY	$BaCe_{0.2}Zr_{0.7}Y_{0.1}O_{3-\delta}$
BET	Brunauer–Emmett–Teller
BSEs	Back-scattered electrons
CA	Citric acid
CD	Current density
CPE	Constant phase element
CV	Cyclic voltammetry
DC	direct current
ΔH	Enthalpy of reaction
ΔS	Entropy of reaction
DFT	Density functional theory
DOE	Department of energy (U.S.)
E_a	Activation energy
EC NH3	Electrochemical ammonia
EDTA	Ethylenediaminetetraacetic acid
EIS	Electrochemical impedance spectroscopy
FWHM	Full-width half maximum
HER	Hydrogen evolution reaction
ICP-AES	Inductively coupled plasma atomic emission spectroscopy
IPA	Isopropanol
ISE	Ion selective electrode
IUPAC	International Union of Pure and Applied Chemistry
I-V curves	Current - potential curves
KAAP	Kellogg Advanced Ammonia Process
LDS	Laser diffraction spectroscopy
LSV	Linear sweep voltammetry
NAP-XPS	Near-ambient pressure XPS
NEMCA	Non-Faradaic modification of catalytic activity
NIST	National Institute of Standards and Technology
NMR	Nuclear magnetic resonance (spectroscopy)
ppm	parts per million
PTFE	Polytetrafluoroethylene
Ru NPs	Ruthenium nanoparticles
RuBZLn	Lanthanide-doped barium zirconate

SEM	Scanning electron microscopy
SOFC	Solid oxide fuel cell
STEM-HAADF	Scanning transmission electron microscope annular dark-field imaging
TCD	Thermal conductivity detector
TEM	Transmission electron microscope
TGA	Thermogravimetric analysis
THF	Tetrahydrofuran
TPR	Temperature programmed reduction
XPS	X-ray photoelectron spectroscopy
XRD	X-ray diffraction

Contents

Chapter 1 Introduction xi

1. 1 Ammonia & its Synthesis 1

1. 1. 1 The Challenge of Synthesis 2

1. 2 Development of the Haber-Bosch Process 8

1. 2. 1 Catalysts 9

1. 2. 2 Iron Based Catalysts 14

1. 2. 3 Ruthenium Based Catalysts 19

1. 3 Proton Conducting Ceramics 25

1. 3. 1 Proton Conductivity in Barium Cerates & Zirconates 32

1. 4 Electrochemical Ammonia Synthesis 38

1. 4. 1 Cell & Electrode Design 39

1. 5 Project Aims 43

1. 6 Research Contributions 44

1. 7 Acknowledgements 44

1. 8 References 45

Chapter 2 Experimental Methods & Characterisation 56

2. 1 Synthetic Techniques 56

2. 1. 1 Ceramic Oxide Synthesis 56

2. 1. 2 Sintering of Ceramic Powders 58

2. 1. 3 Ball Milling of Ceramic Powders for Size Reduction 59

2. 1. 4 Wet-Impregnation Synthesis of Ruthenium Nanoparticles 60

2. 2 Electrochemical Characterisation Techniques 62

2. 2. 1 Electrochemical Impedance Spectroscopy 62

2. 2. 2 Voltammetry 63

2. 3 Material Characterisation 65

2. 3. 1 Crystal Structure Determination via Diffraction Techniques 65

2. 3. 2 Electron Microscopy 69

2. 3. 3 Thermo-Gravimetric Analysis 72

2. 3. 4 Temperature Programmed Reduction 73

2. 3. 5 Laser Diffraction Particle Size Analysis 74

2. 3. 6 Quantification of Dissolved Ammonia 74

2. 3. 7 X-Ray Photoelectron Spectroscopy 76

2. 3. 8 Gas Adsorption Techniques 78

2. 4 References 79

Chapter 3 Synthesis of Barium Zirconate Powders & Preparation of Ammonia Synthesis Cells 82

3. 1 Background 82

3. 2 Objectives 83

3. 3 Sol-Gel Synthesis of Barium Zirconate Powders & Processing into Dense Pellets 84

3. 3. 1 Sol-Gel Synthesis 84

3. 3. 2 Milling of Powders 88

3. 3. 3 Sintering of Powders 91

3. 4 Electrochemical Testing 95

3. 4. 1 Conductivity in Cells Prepared from Unmilled Powders 95

3. 4. 2 Conductivity in Cells Prepared from Milled Powders 97

3. 4. 3 Electrochemical Ammonia Synthesis 99

3. 5 Conclusions 101

3. 6 References 102

Chapter 4 Electrochemical Ammonia Synthesis in Barium-Cerate-Zirconate Cells 104

4. 1 Background 104

4. 1. 1 Objectives 106

4. 2 Experimental 107

4. 2. 1 Cell & Electrode Preparations 107

4. 2. 2 Testing of Electrochemical Cells 109

4. 3 Characterisation 112

4. 4 Electrochemical Ammonia Synthesis 116

4. 5 Impedance & Voltammetry Characterisation 121

4. 6 Two-Chamber Cell 127

4. 7 Conclusion 129

4. 8 Acknowledgements 131

4. 9 References 131

Chapter 5 Barium Zirconate Supported Ruthenium Nano-Catalysts for Heterogeneous Ammonia Production 133

5. 1 Background 133

5. 2 Objectives 135

5. 3 Experimental 137

5. 3. 1 Preparation of Barium Zirconate Powders 137

5. 3. 2 Synthesis of Supported Ruthenium Nanocatalysts 138

5. 3. 3 Addition of Caesium Promoter 139

5. 3. 4 Catalytic Testing 139

5. 4 Characterisation 141

5. 4. 1 Ruthenium Nanocatalysts Derived from $Ru(acac)_3$ on Lanthanide-Doped Barium Zirconate Supports 141

5. 4. 2 Ruthenium Nanocatalysts Derived from $Ru_3(CO)_{12}$ on Yttrium-Doped Barium Zirconate supports 146

5. 5 Catalytic Testing 154

5. 5. 1 Catalysts Derived from Lanthanide-Doped Supports 154

5. 5. 2 Catalysts Derived from Yttrium-Doped Supports 156

5. 5. 3 Caesium Promoted Catalysts: Rates and Conversions 158

5. 6 Investigation of Hydrogen Spillover 161

5. 6. 1 Neutron diffraction 161

5. 6. 2 In-situ XPS 164

5. 7 Discussion 172

5. 7. 1 Catalyst Development 172

5. 7. 2 Relationship Between Support Conductivity and Activity 175

5. 7. 3 Spillover of Hydrogen 177

5. 8 Conclusions 178

5. 9 Acknowledgements 178

5. 10 References 179

Chapter 6 Conclusions, Future Work, & Outlook 182

6. 1 Conclusions 182

6. 2 Future Work 184

6. 3 Outlook 185

6. 4 References 189

Chapter 7 Appendices 191

7. 1 List of Publications & Conference Presentations 191

7. 2 Python Code 192

7. 3 XPS Calibration Spectra 194

List of Figures

Figure 1-1: Equilibrium conversion of ammonia vs temperature 4

Figure 1-2: NH3 conversion vs temperature for various catalysts at atmospheric pressure 5

Figure 1-3: Equilibrium partial pressures of atomic N and H 6

Figure 1-4: Energy profiles of dinitrogen reduction to ammonia. 6

Figure 1-5: Results per year when searching the Scopus database 9

Figure 1-6: Dissociative energy pathway profile. 12

Figure 1-7: Experimentally determined vs calculated exit NH3 mole fraction 12

Figure 1-8: Volcano plots 13

Figure 1-9: Rates of ammonia synthesis over the surfaces 16

Figure 1-10: Schematic representation of the iron surfaces 17

Figure 1-11: Difference in NH3 conversion vs temperature 20

Figure 1-12: Change in concentration of edge atoms, and concentration of B5 active sites 22

Figure 1-13: Arrhenius plot of conductivities in proton conducting ceramics 26

Figure 1-14: Calculated values of enthalpy and entropy change of reaction 34

Figure 1-15: Mechanism of proton hopping within perovskite 35

Figure 1-16: Concentration change of dopant ions, oxygen vacancies, and protons 36

Figure 1-17: Results per year when searching the Scopus database. 38

Figure 1-18: Graphical representation of rates and current efficiencies from literature 39

Figure 1-19: Cells reported for electrochemical NH3 synthesis 40

Figure 2-1: a) Grinding bowls b) movement of grinding balls 60

Figure 2-2: Crystal lattice unit cells, description, and crystal planes 65

Figure 2-3: (a) Scattering of waves (b) Interference. (c) typical diffraction pattern 66

Figure 2-4: Intensity of X-ray radiation as a function of wavelength 68

Figure 2-5: Electron scattering interactions. 70

Figure 2-6: Bright and dark field modes of TEM imaging. 71

Figure 2-7: Typical raw TGA curve 73

Figure 2-8: A typical ammonium ISE 75

Figure 2-9: Equation 2.17 expressed graphically 77
Figure 3-1: Schematic overview of whole pellet preparation process 84
Figure 3-2: Typical TGA plot of $ZrO(NO_3)_2\ xH_2O$ 85
Figure 3-3: XRD patterns of BZY20 ash calcined under different conditions. 86
Figure 3-4: XRD patterns recorded during milling experiments 89
Figure 3-5: Particle sizes as measured by laser diffraction spectroscopy 90
Figure 3-6: Photos of sintering process 92
Figure 3-7: SEM analysis of cell from unmilled powder 93
Figure 3-8: SEM analysis of cell from milled powder 94
Figure 3-9: I-V curves obtained under humidified N2 and 5% H2 / N2 at varying temperatures. 96
Figure 3-10: Conductivities of cell under humidified 5% H_2 / N_2 at various temperatures 97
Figure 3-11: Nyquist and Bode plots. 98
Figure 3-12: Equivalent circuit model used for AC impedance spectroscopy analysis 99
Figure 3-13: Rates, current densities and current efficiencies vs applied potential 100
Figure 4-1: Possible reactions pathways for N_2 and H_2 105
Figure 4-2: Photos of cells during electrode preparations 109
Figure 4-3: a & b) Cell testing apparatus c) Electrochemical cell design 111
Figure 4-4: SEM images of Ag | BCZY | Ni/BCZY cell 113
Figure 4-5: SEM images of Pt | BCZY | Ni/BCZY cell 114
Figure 4-6: Ni/BCZY cermet before (a) and after (b-d) impregnation and reduction of $Ru(acac)_3$ 115
Figure 4-7: Ammonia synthesis rates & current densities 117
Figure 4-8: Rates and CDs of ammonia synthesis from Ag | BCZY | Ni/BCZY cell 118
Figure 4-9: Rates & CDs in Pt | BCZY | Ni/BCZY cells. 119
Figure 4-10: Rates & CDs of Ag | BCZY | Ru/Ni/BCZY cell 120
Figure 4-11: Diagram of ideal reference electrode 121
Figure 4-12: Voltammetry of Ag | BCZY | Ru/Ni/BCZY cell 122
Figure 4-13: Equivalent circuit model utilised for modelling. 123
Figure 4-14: EIS data from Ag | BCZY | Ni/BCZY cell 123

Figure 4-15: EIS data from Pt | BCZY | Ni/BCZY cell 124
Figure 4-16: EIS data from Ag | BCZY | Ru/Ni/BCZY cell 125
Figure 4-17: Arrhenius plots showing activation energies of intra- and inter-grain conduction 126
Figure 4-18: Design and construction of two-chamber cell for ammonia synthesis 127
Figure 4-19: (a) Mass trace of He and N_2 (b) Current densities and rates for two chamber cell 128
Figure 5-1: XRD patterns of lanthanide-doped supports 142
Figure 5-2: RuBZEr20 (left) and RuBZY20 (right) TEM data 143
Figure 5-3: TEM images and Ru particle size histograms 144
Figure 5-4: TPR plots of BZY20 and BZYb20 supports before and after synthesis of Ru NPs. 145
Figure 5-5: a) TGA plot and b) TPR plot of RuBZY20 catalyst 147
Figure 5-6: Pulse titration analysis of Ru barium zirconate catalysts 149
Figure 5-7: TEM images of RuBZ catalyst post catalytic testing 151
Figure 5-8: TEM images of Ru barium zirconate catalysts before and after catalytic testing 152
Figure 5-9: STEM-HAADF images of RuBZY10 catalyst 153
Figure 5-10: Rates over Ru/BZLn catalysts 154
Figure 5-11: Rates over Ru/BZY catalysts 156
Figure 5-12: Long term catalytic testing 157
Figure 5-13: Reaction rates for Cs-Ru catalysts on Y-doped barium zirconate supports 158
Figure 5-14: Conversion of reactant gases to ammonia for indicated catalysts vs temperature 159
Figure 5-15: Effect of changing partial pressure on rate, at indicated temperatures 160
Figure 5-16: Proposed mechanism for reversible hydrogen spillover process 161
Figure 5-17: Neutron diffraction data of BZY20 and RuBZY20 samples 162
Figure 5-18: Deuterium position in BZY20 lattice 162
Figure 5-19: Proton dynamics in BZY20 structure 164
Figure 5-20: Variation of transmitted X-ray flux with changes in Ar pressure 165
Figure 5-21: BZY conductivity (a) temperature dependance (b) dopant-level dependance 176

List of Tables

Table 1-1: Yields of industrial Ru and Fe catalysts 20

Table 1-2: Reported conductivities and activation energies of barium cerate proton conductors 28

Table 1-3: Reported conductivities and activation energies of barium zirconate proton conductors ... 30

Table 3-1: XRD peaks of BZY20 calcined at 1100 ºC for 5 hrs 86

Table 3-2: XRD peaks of BZY20 calcined at 1300 ºC for 4 hrs 87

Table 3-3: XRD peaks of BZY20 calcined at 1300 ºC for 3 hrs 87

Table 3-4: BET surface areas of milled samples 88

Table 3-5: BET surface areas of pelletised samples 91

Table 3-6: Recorded conductivity values from I-V curve gradients 97

Table 3-7: Fitted values for equivalent circuit components 98

Table 3-8: Tabulated values from Figure 3-13 100

Table 4-1: All tested cells, and the anode & cathode formulations for each. 108

Table 4-2: EIS fitting parameters for all cells, at all temperatures. 126

Table 5-1: Formulas of investigated lanthanide and yttrium doped ceramics. 138

Table 5-2: Weight percent values as determined from ICP-AES analysis. 146

Table 5-3: Total volume and moles of CO adsorbed to each catalyst during pulse-titration analysis. 150

Table 5-4: Neutron diffraction fitted parameters for all samples 163

Table 5-5: Test conditions and ammonia synthesis rates of literature, and investigated catalysts 174

Table 6-1: Cost of raw minerals needed to produce BZY or carbon supports 188

Chapter 1 Introduction

Ammonia is one of the most important materials to human society. Our reliance on the carbon-intensive Haber-Bosch process will not be sustainable in decades to come. A new, efficient, and scalable alternative must be found. To this end, this thesis investigated ammonia synthesis methods suitable for carbon-free operation.

Barium zirconate perovskites can react with and trap protons, up to stoichiometric equivalence with dopant ions in the structure. Once trapped in the lattice, protons conduct through under an applied potential. The proton trapping and conducting properties of barium zirconate are applied to the thermal and electro catalysis of ammonia synthesis.

1. 1 Ammonia & its Synthesis

Ammonia is ubiquitous in modern life, with the human diet relying on fertilisers produced from ammonia. According to R. Schlögl in the 'Handbook of Heterogeneous Catalysis', around 40% of nitrogen in the global food chain is reliant on the Haber-Bosch process. In 2018, 88% of the 144 million tons of ammonia produced globally went towards production of fertilisers.[1] It is also essential to the chemical industry, as the choice of chemical whenever an activated nitrogen building block is required. The remaining 12% of the 2018 stock was used for plastics, pharmaceuticals, and explosives, among many other industrial products.

Fixation of nitrogen to ammonia (Scheme 1) is the most important industrial chemical process for humanity. Ammonia is currently produced through the Haber-Bosch process, one of the best established industrial chemical processes. The development of this process has been attributed as being the trigger for the human population explosion after the early 20th century, due to increases in food availability thanks to nitrogen based fertilisers.[2] The process requires extremely forcing conditions, to push the reaction to industrially acceptable yields.

$$N_{2\,(g)} + 3H_{2\,(g)} \rightleftharpoons 2NH_{3\,(g)}$$

Scheme 1: Reduction of dinitrogen to ammonia

At atmospheric pressure ammonia boils at 240 K, but is produced industrially in the compressed, anhydrous form. This anhydrous ammonia can then be used directly as a fertiliser or used to produce ammonium salts or urea. Ammonia is required for further applications in its pure form, which has limited the applicability of biosynthesis processes, which yield a dilute solution.[3]

Currently around 1% of all global energy goes towards making ammonia.[4] This is associated with high CO_2 emissions, made worse by the fact that the hydrogen for the process comes from steam reformation of methane. Such an important but energy intensive process would obviously benefit from any reduction in energy requirements. It is reported that each ton of ammonia produced results in the release of 2 – 3

tons CO_2.[5] Given the urgent need to decarbonise our economies, a carbon-free ammonia synthesis process must be implemented on a large scale as soon as possible.

So called agile ammonia synthesis reactors powered by renewable energy have been proposed as a solution to this problem.[6] Current industrial ammonia synthesis plants are huge in scale, although this is primarily due to the apparatus for hydrogen production via methane steam reformation.[7] Due to isolated nature of renewable energy plants and the intermittent power generation, reactors need to be small, have low capital expense, and be capable of agile operation (i.e. easy to start and stop).

Small scale plants powered by renewables which produce hydrogen through water electrolysis could allow carbon-free ammonia to become a reality. However high costs associated with water electrolysis, and the low cost of methane make this process 1.5 – 3 times more expensive than conventional synthesis.[8]

New ruthenium-based catalysts capable of operating at lower temperatures and pressures than the current iron-based ones are an important avenue of development for this technology. The large compressors required to achieve the high pressures of the Haber-Bosch process could be replaced by much smaller ones with lower capital costs.

An alternative to agile heterogeneous catalysis reactors is to use direct electrochemical reduction of dinitrogen to ammonia. In the ideal scenario, the hydrogen for the reduction would be provided directly from water, eliminating the need for a separate water electrolysis process. However, it remains to be seen if this electrochemical process can compete with agile heterogeneous reactors.

Ammonia also shows much promise as an energy storage material. Ammonia contains 17.6 wt. % hydrogen and has an energy density of 13.6 GJ m^{-3} (pressurized tank at 10 bar).[9] Pure hydrogen has an energy density of 3.6 GJ m^{-3} (pressurized tank at 14 Bar, metal hydride storage system).[9] This is lower than liquid hydrocarbons which have an energy density of 34.4 GJ m^{-3} (C_8H_{18} liquid tank),[9] however ammonia has the advantage of carbon free combustion. For this reason it has been proposed as a potential primary energy vector when transitioning to a carbon-free economy.[10]

1. 1. 1 The Challenge of Synthesis

The reaction of dinitrogen and dihydrogen to ammonia is exothermic (ΔH^0 = -92 kJ mol^{-1}), with a Gibbs free energy (ΔG^0) of -33 kJ mol^{-1}, making it spontaneous at room temperature.[3] The endothermic reverse reaction (ΔG^0 = 16 kJ mol^{-1}, ΔH^0 = 46 kJ mol^{-1})[3] will, however, easily occur under the elevated temperatures used for synthesis. Ammonia, nitrogen, and hydrogen are all gasses under standard conditions, and synthesis takes place in the gas phase.

The position of equilibrium, or equilibrium constant K, for the reaction is given by Equation 1.1, where a_i is activity coefficient for each component. This is equivalent to the partial pressure of each component, modified by a fugacity coefficient, φ_i: a function of the temperature, pressure, and composition of the system, and is derived from an equation of state, such as Equation 1.4.[11] Fugacity is computed due to the inter-molecular interactions deviating from ideal behaviour, at the high pressures utilised in the Haber-

Bosch process. At low pressures, the relationship between pressure (p), temperature (T), volume (V), and number of moles (n), is described by the ideal gas law (Equation 1.3). This assumes molecules are non-interacting points (have no volume), however at high pressures this relationship can no longer describe the system accurately. By substituting the number of moles in the ideal gas law with a compressibility factor, Z, an equation of state applicable at higher pressures can be formulated (Equation 1.4).

$$K = \frac{a_{NH_3}}{{a_{N_2}}^{1/2}{a_{H_2}}^{3/2}} \qquad \textit{Equation 1.1}$$

$$a_i = y_i \varphi_i p \qquad \textit{Equation 1.2}$$

$$pV = nRT \qquad \textit{Equation 1.3}$$

$$pV = ZRT \qquad \textit{Equation 1.4}$$

$$K = \frac{y_{NH_3} p}{\left(y_{N_2} p\right)^{\frac{1}{2}}\left(y_{H_2} p\right)^{\frac{3}{2}}} \frac{\varphi_{NH_3}}{{\varphi_{N_2}}^{\frac{1}{2}}{\varphi_{H_2}}^{\frac{3}{2}}} = K_p K_\varphi \qquad \textit{Equation 1.5}$$

The equilibrium composition can then be calculated from the composition of the ideal gas (K_p), after correction with the non-ideal contribution, K_φ (Equation 1.5). Christiansen, in 'Ammonia Catalysis and Manufacture', calculated the equilibrium compositions across a wide temperature range, at different pressure values, Figure 1-1. This is a convenient way to show the maximum conversion of ammonia that can be achieved under a given set of conditions. A more detailed description of how equations of state can be used to calculate fugacity can be found in Chapter 1 of 'Ammonia Catalysis and Manufacture' (L. J. Christiansen).[11] Figure 1-1 also shows how pressure can be used to overcome the unfavourable thermodynamics. Due to the reaction creating 2 moles of gas for every 4 reactant moles, pressure can be used to drive the reaction to completion. Le Chatelier's principle states that a system will act to oppose any changes on it, so increasing the pressure will push the equilibrium to the right. For the same temperature, the equilibrium conversion will increase at higher pressures.

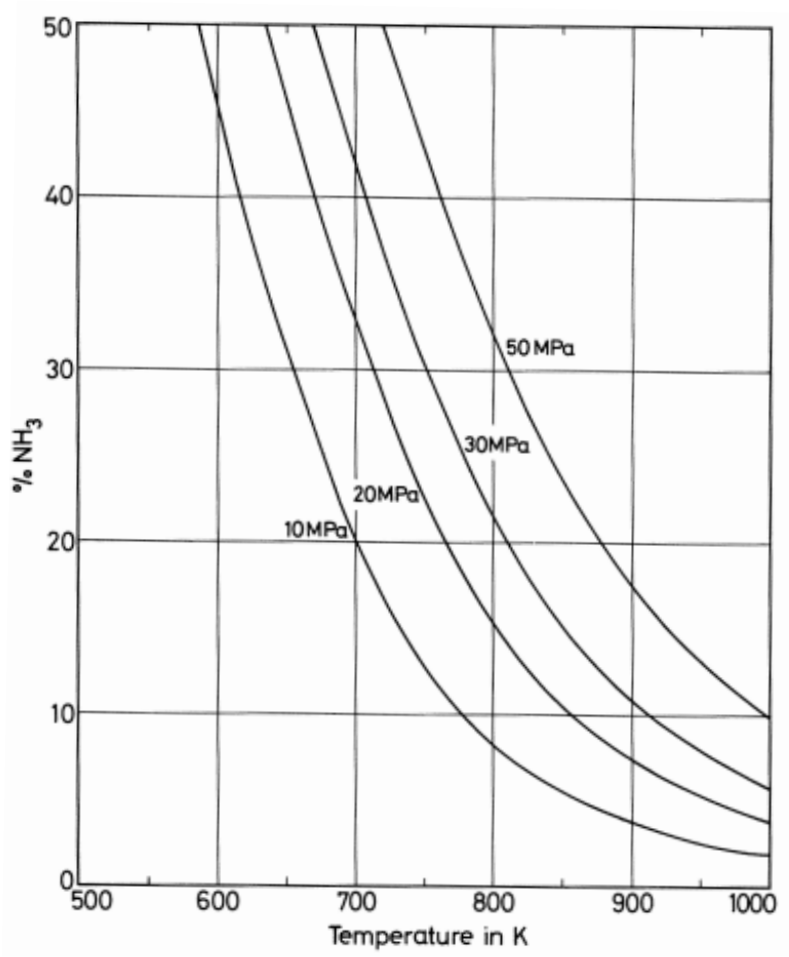


Figure 1-1: Equilibrium conversion of ammonia vs temperature, at indicated pressure. Reproduced from 'Thermodynamic Properties in Ammonia Synthesis', L. J. Christensen.[11]

While the reaction is thermodynamically favoured at low temperatures, it is too kinetically sluggish to be of any practical interest. According to the Arrhenius equation (Equation 1.6) the rate constant of a reaction (k) increases at higher temperatures.

$$k = Ae^{-E_a/RT} \qquad \textit{Equation 1.6}$$

It is desirable to maximise production of ammonia by increasing the rate constant for the formation of ammonia, however at higher temperatures the yield of ammonia is severely limited by equilibrium. This need to balance synthesis rate vs decomposition rate can be visualised as in Figure 1-2. A range of catalysts were evaluated by Rosowski et al. in the conversion-temperature plane.[12] The increasing rate of reaction with temperature causes conversion to increase. As the conversion approaches the equilibrium line however, it becomes limited by decomposition of ammonia.

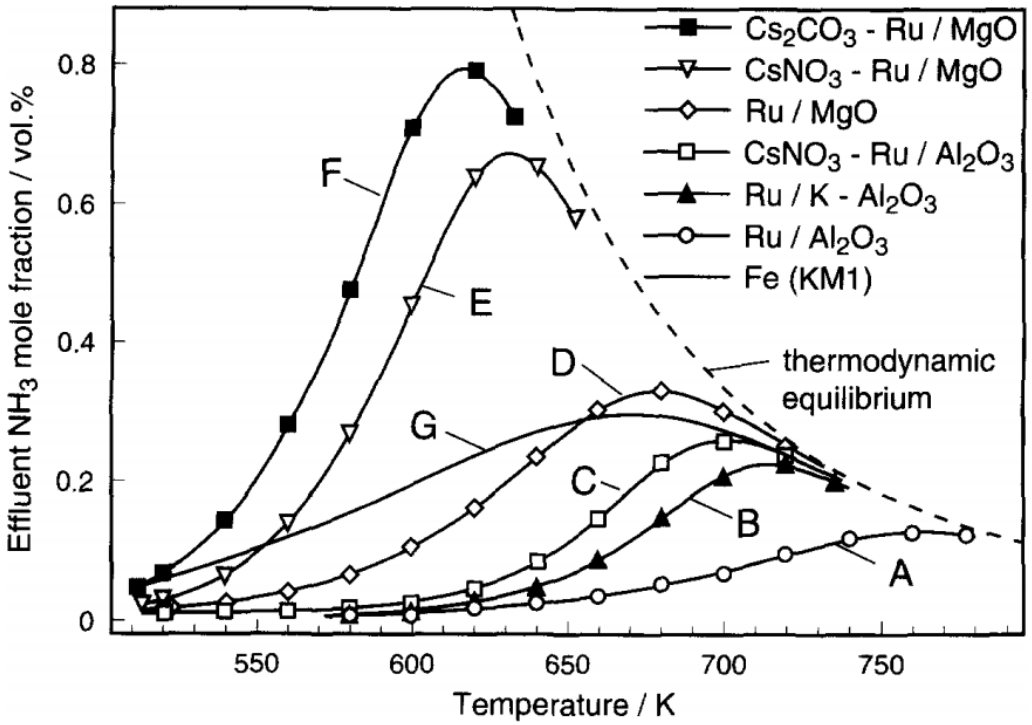


Figure 1-2: NH_3 conversion vs temperature for various catalysts at atmospheric pressure (3:1 H_2:N_2). Reproduced from Rosowski et al.[12]

Activation of dinitrogen presents a challenging problem. The nitrogen-nitrogen triple bond is one of the strongest known bonds with a bond dissociation energy of 945 kJ mol^{-1} (9.79 eV), second only to CO (1077 kJ mol^{-1}, 11.16 eV). This results in an extremely small equilibrium dissociation constant for dinitrogen into nitrogen atoms. Figure 1-3 shows the equilibrium pressures of atomic hydrogen and nitrogen relative to the diatomic forms as a function of temperature. The tiny fraction of dissociated nitrogen atoms at 500 K shows how urgently a catalyst is needed to provide a source of activated nitrogen which can be hydrogenated to ammonia. The comparatively much easier activation of dihydrogen does not present a challenge under the conditions used for ammonia synthesis.

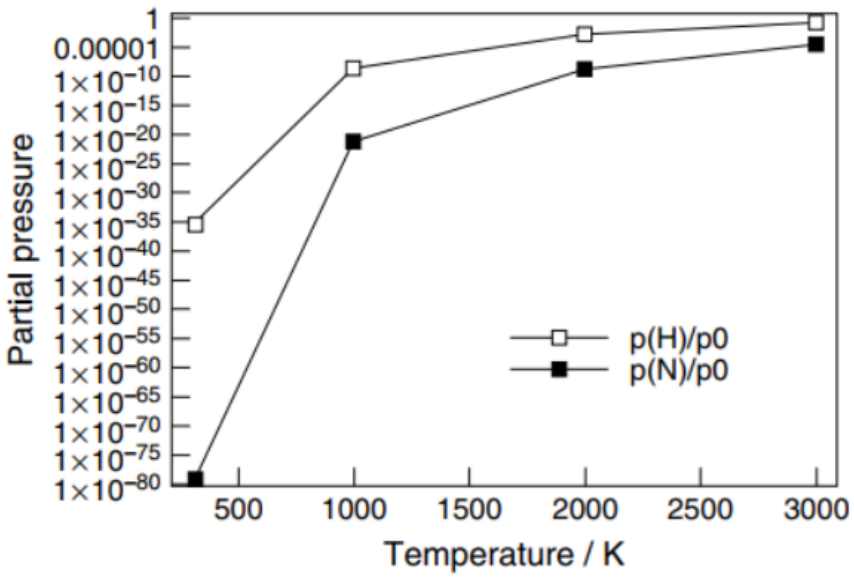


Figure 1-3: Equilibrium partial pressures of atomic N and H relative to the diatomic species as a function of temperature. Reproduced from 'Ammonia Synthesis' by R. Schlögl.[3]

Over an iron surface, this reaction may proceed at near-ambient pressures at temperatures as low as 580 K.[13] The catalyst works both by constraining reactant molecules on the surface, reducing their range of translational motion such that the chance of a reaction event increases, and by activating the dinitrogen bond so it may more easily be reduced by hydrogen. The energy profiles of the reaction with and without a catalyst are seen in Figure 1-4.

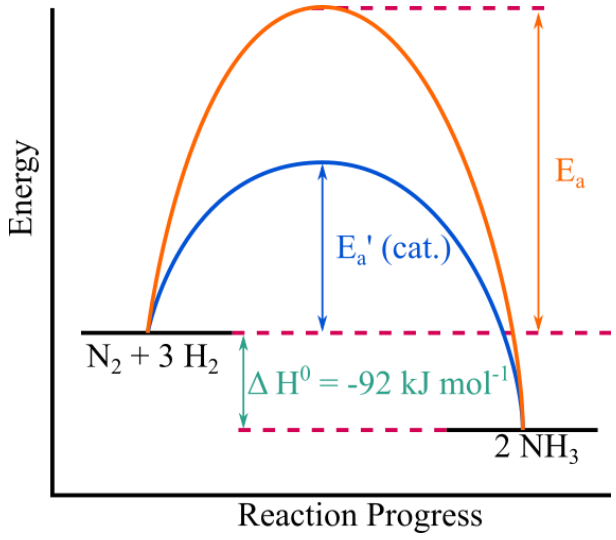


Figure 1-4: Energy profiles of dinitrogen reduction to ammonia with (blue) and without (orange) a catalyst. Reaction is exothermic, with $\Delta H^0 = -92$ kJ mol^{-1}.

The ammonia synthesis reaction is challenging due to the difficulty of activating the dinitrogen bond, which requires high temperatures to occur at a meaningful rate. However, the exothermic and reversible nature of the reaction means that at high temperatures, ammonia decomposition limits the conversion. Higher pressures increase the maximum possible conversion at the same temperature, however to reach the high pressures (150 bar) utilised with the industrial iron catalyst, significant infrastructure investments are required.[6] The use of a catalyst provides a lower energy pathway for the reaction to proceed, increasing the rate of reaction. Research into new catalysts for ammonia synthesis is ongoing. A review of the development of iron and ruthenium catalysts is found below (section 1. 2. 2 & 1. 2. 3) and a some more recent advances are presented in Chapter 5. More active catalysts may reduce the energy and infrastructure costs while maintaining the same ammonia output; operating temperature may be reduced thanks to the higher activity, meaning the pressure can be reduced without conversion being limited by equilibrium.

1. 2 Development of the Haber-Bosch Process

The opening of the first commercial ammonia synthesis plant in September 1913, in Ludwigshafen, Germany, was the start of a new era for chemistry, and for humanity at large. Prior to the invention of the Haber-Bosch process, fertilisers were reliant on nitrogen from ammonium sulphate, a by-product of coal coking, or from mined Chilean saltpetre (sodium nitrate). The primary Chilean source was reported at the time to be exhausting it's richest deposits, so commercialisation of synthetic ammonia production was most timely.[14]

Prof. Fritz Haber's work in the early 20th century at Karlsruhe Institute of Technology on the "Synthesis of ammonia from its elements" laid the groundwork for commercialisation by developing the chemical process. From his investigations he proposed three key changes to the chemical process, permitting ammonia to be produced at a competitive price point. Firstly, he recognised that extreme pressures were required to drive the reversible reaction to the right-hand side (Scheme 1). Secondly, he developed the concept of a gas recycling system, in which the ammonia product was condensed out, and unreacted nitrogen and hydrogen were fed back into the reactor, mitigating the very low per-pass conversion (up to 12% conversion at 550 ºC, 200 atmospheres).[14] Finally, in collaboration with Robert Le Rossignol, catalysts based on finely powdered osmium, and uranium carbide were developed. These were capable of producing one kilogram of ammonia per litre of reactor space, at 500 – 600 ºC.[14]

After the procedure was purchased by BASF, they set to work on developing a new catalyst for the process, as the proposed uranium and osmium catalysts were not cost-effective. Alwin Mittasch was assigned to this task, and between 1909 and 1922, over 5000 materials were tested.[15] The fortuitous discovery of a cheap, highly active iron-based catalyst was made by fusing magnetite (Fe_3O_4) with irreducible oxides of potassium and aluminium, in an oxide melt.

Before the catalyst could be put to work, it required a reactor in which to work. This task fell to Carl Bosch. He designed ammonia plants such that they were able to operate at production scale, under high pressure. This required a redesign of the reactor chambers, as during testing the main pressure chamber ruptured under the extreme conditions. Bosch found that hot, high pressure hydrogen was reacting with carbon in the steel reactor walls, softening and weakening them. To counter this, Bosch proposed two changes to the vessel: a thin layer of soft, low-carbon iron on the inner surface of the vessel to provide a protective layer; and drilling small holes into the inner wall, to allow hydrogen dissolved in the iron lattice to escape.

With the chemical process, catalyst, and reactor in place, the production of ammonia could begin, signalling a new era in chemistry. The development of the process did not, however, end here, as demonstrated by the increasing number of annual publications on the topic found in the Scopus database (Figure 1-5).

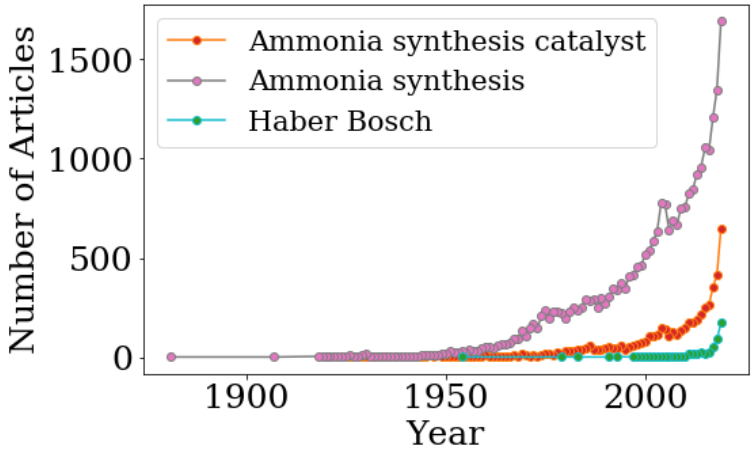


Figure 1-5: Results per year when searching the Scopus database for the indicated keywords. Results shown up to 2019.

It is possibly the most studied chemical reaction, with the huge body of work including three Nobel prizes. Fritz Haber was awarded the 1918 Nobel prize in chemistry for the discovery of the conversion of gaseous nitrogen and hydrogen to ammonia. Carl Bosch and Friedrich Bergius were awarded the prize in 1931 for their contributions to the invention and development of chemical high-pressure methods, which allowed the large scale and continuous flow operation of the process. Finally, the 2007 prize was awarded to Gerhard Ertl for his contributions to surface science, and its use in his elucidation of the mechanism of dinitrogen reduction to ammonia over iron surfaces.

Thanks to the continuous development of the process, industrial synthesis of ammonia can now be achieved with up to 70% efficiency, including the steam reformation of methane. Indeed, of the energy losses, only around 8% occur during the reduction of dinitrogen to ammonia, with the largest losses stemming from the steam reformation process (I. Dybkjaer in 'Ammonia Catalysis and Manufacture').[16] From this, it can be said that the process most in need of improvement is the generation of pure hydrogen. Any process that could use direct reaction of water and nitrogen to produce ammonia would be highly desirable.

1. 2. 1 Catalysts

The most important characteristic for a catalyst is its activity; ostensibly the rate at which it converts reactants into products. The activity is determined both by the ability of the catalyst to activate the reactant molecules (surface reactions) and subsequently desorb the product, but also by many other factors including transport phenomena (macroscopically within the reactor, and microscopically on the catalyst surface), adsorption and desorption processes, and other surface reactions.[17] Activity is, however, a poorly defined concept, not accounting for the number of active centres at which the reaction may occur. Michel Boudart proposed the adoption of a standard measure of activity, the turnover frequency (TOF): the number molecules reacting per second per surface metal atom, as determined by selective chemisorption titration techniques.[18] While this concept has been adopted in the catalysis science field, it is not without its

problems; namely that the number of active centres is very difficult to determine. It cannot be said that every surface metal atom participates in the reaction mechanism as an active centre, nor is the number of these surface metal atoms straightforward to measure. While measurement of TOF is imperfect, it does allow an approximation of the catalyst activity.

To examine the mode of operation of a catalyst, and hopefully optimise the activity, great efforts are made to determine the reaction pathway, or mechanism. By examining the energetic changes of each step, the 'rate determining step' (RDS, the reaction with the highest activation energy) can be ascertained. In a well optimised industrial catalyst, it should be difficult to determine the RDS, as to have one, clear limiting step, would warrant refinement of the catalyst or process.[19] In order to identify the energetics of each step, what are known as 'single-crystal studies' are carried out. These low-pressure experiments can show in detail the interactions of reactant, intermediate, and product molecules with the catalyst surface, and with each other. By determining reaction parameters, such as the activation energies and sticking coefficients, these can be fitted into a microkinetic model, allowing extrapolation and calculation of reaction parameters at different temperatures and pressures, where direct measurement would simply not be possible. These models are not perfect, however a detailed discussion of these is beyond the scope of this discussion, and the reader is referred to a 2015 article by Prof. Robert Schlögl.[17]

Reduction of dinitrogen to ammonia on a surface can proceed by two main mechanisms: associative or dissociative. In an associative mechanism, the nitrogen atoms of dinitrogen remain bound to each other during most of the reaction, and the triple bond is hydrogenated in a stepwise manner to diamine or hydrazine, before the N-N bond is broken, yielding two surface NH_x species. A dissociative mechanism is characterised by the dissociative adsorption of the dinitrogen, yielding two adsorbed nitrogen atoms on the surface, which are then hydrogenated. It is generally now accepted in literature that the reaction on metal surfaces proceeds by a dissociative mechanism. This was demonstrated by Gerhard Ertl, with the help of many others, in a series of publications between 1977 and 1983. Using photoelectron spectroscopy, the presence of atomic nitrogen on clean iron surfaces (Fe 100, 111, 110) was found under Ultra-High Vacuum (UHV, ~10^{-10} Torr) conditions at elevated temperatures.[20,21] This exceeded the presence of molecular nitrogen in all cases except at much lower temperatures (140 K). It was also noted that the adsorption to Fe(111) surfaces proceeds with a lower activation barrier and higher sticking probability.

The kinetics of the dinitrogen adsorption were probed, and it was found that the activation energy for the dissociative adsorption of the nitrogen molecule is low, but that the overall rate of formation of atomic nitrogen on the surface is limited by a low sticking coefficient of dinitrogen.[22] The activation energy is also dependant on the degree of surface coverage. Additionally, under the experimental conditions (120 K, UHV), the rate of desorption of molecular nitrogen is two orders of magnitude greater than the dissociation of the molecular nitrogen to atomic nitrogen. Using Low-Energy Electron Diffraction experiments, a structural model for the 'surface nitride' formation was suggested.[23]

To connect these UHV experiments to the high-pressure industrial process, X-ray photoelectron and Auger electron spectroscopy were used to characterise the surface species present on industrial catalysts before and after reduction.[24] A catalyst sample exposed to 600 – 700 Torr of dinitrogen and dihydrogen (N_2:H_2 = 1:2 – 1:3) between 350 – 400 ºC showed a three-fold increase in surface metallic iron species. Other metallic oxide species were found to be irreducible under the conditions. After the reduction, the presence of NH_3 and NH/NH_2 species was detected on the catalyst surface. By examining how the surface coverage of atomic nitrogen (N_{ad}) varies with H_2 pressure in the reaction chamber, it could be shown that increasing H_2 pressure leads to a decrease in N_{ad} coverage. If an associative mechanism were operative, it would be expected that N_{ad} coverage would reach a saturation point, as there would be no mechanism for its removal except for recombination to dinitrogen and desorption. As the N_{ad} species had been previously shown to be strongly chemisorbed to iron surfaces (Ertl et al., 1982)[22], it could be stated that the loss of N_{ad} with increasing H_2 pressure, was due to reduction to $NH/NH_2/NH_3$ species, and that a dissociative mechanism was operative.

Separate investigations by Spencer et al. showed that the reduction of dinitrogen to ammonia over iron surfaces proceeds with rates in the order Fe(111) > Fe(100) > Fe(110).[25] Ertl wrote that if these values were converted into a sticking coefficient, a value of 10^{-7} would be obtained.[26] The previous results on model systems showed values of 10^{-6} – 10^{-8}, and followed the same order of reactivity (Fe(111) > Fe(100) > Fe(110)).[20,21]

Finally, to obtain details on the intermediate and final steps of the mechanism, Ertl started with NH_3 and worked backwards. Exposing a clean iron surface to ammonia gas under room temperature, adsorbed ammonia could be characterised using spectroscopic methods and mass spectrometry. The appearance of N_{ad} and NH_{ad} species was further evidence of a dissociative mechanism. NH_2 species did not occur in large enough concentrations to be detected directly, but by co-adsorbing NH_3 and D_2 to an iron surface, the presence of NH_2D was detected in thermal desorption spectra, showing Scheme 2(e) must be operative. The mechanism for ammonia synthesis could then be all but confirmed as that described in Scheme 2.

$$H_{2,g} \rightleftharpoons 2H_{ad} \quad \text{(a)}$$

$$N_{2,g} \rightleftharpoons N_{2,ad} \rightleftharpoons 2N_{ad} \quad \text{(b)}$$

$$N_{ad} + H_{ad} \rightleftharpoons NH_{ad} \quad \text{(c)}$$

$$NH_{ad} + H_{ad} \rightleftharpoons NH_{2,ad} \quad \text{(d)}$$

$$NH_{2,ad} + H_{ad} \rightleftharpoons NH_{3,ad} \quad \text{(e)}$$

$$NH_{3,ad} \rightleftharpoons NH_{3,g} \quad \text{(f)}$$

Scheme 2: Dissociative mechanism of ammonia synthesis

By combining the data from these many experiments, an approximate energy pathway for the dissociative reduction of dinitrogen to ammonia could be formulated for the first time.[26]

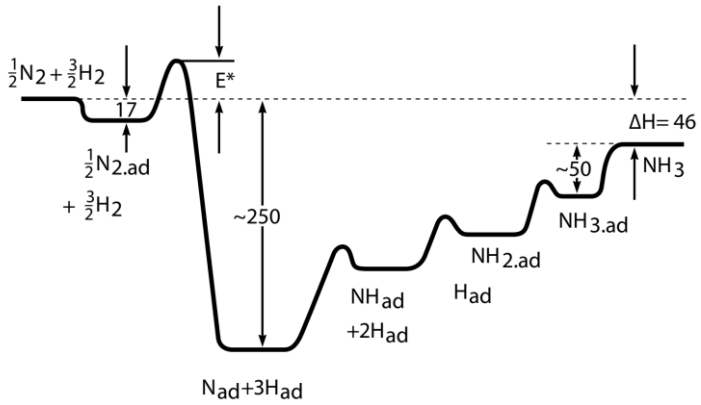


Figure 1-6: Dissociative energy pathway profile of reaction of nitrogen and hydrogen to ammonia on iron surfaces. Reproduced from [27]. Energies in kJ mol^{-1}.

If this mechanism determined at UHV pressures translates to the industrial process was not immediately clear. The agreement with the investigations of nitrogen reactivity over iron facets discussed *vide supra* hints at the correctness of the mechanism. However, the clearest picture of the applicability can be seen in a figure presented by R. Schlögl in the Handbook of Heterogeneous catalysis. Presented are the measured exit fractions of ammonia over an iron catalyst, against the exit fractions predicted from a microkinetic model, derived using only parameters directly observed from experiments or from fundamental constants. The almost perfect agreement between the values at a range of pressures shows how the model determined at UHV conditions is a good predictor of the activity at higher pressures.

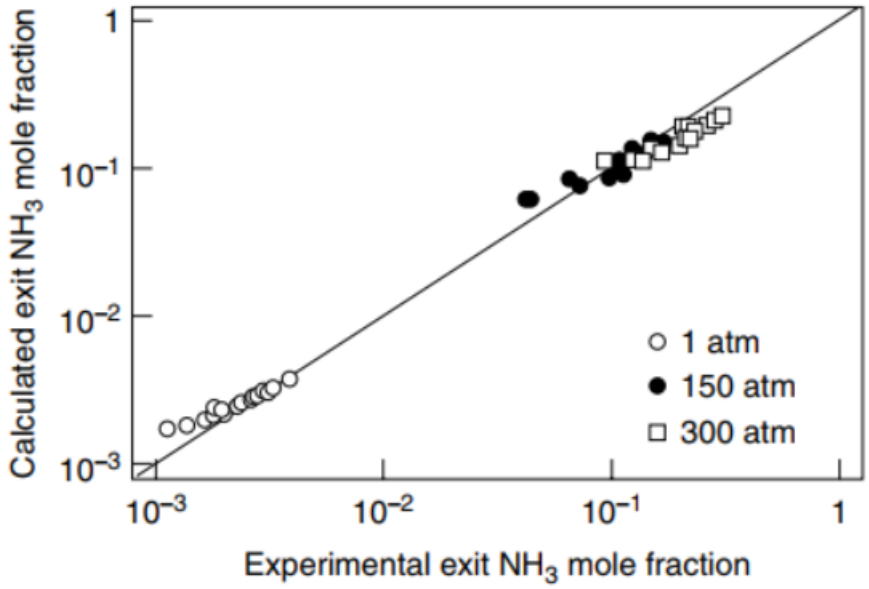


Figure 1-7: Experimentally determined vs calculated exit NH_3 mole fraction, at a range of pressures. Reproduced from 'Ammonia Synthesis' by R. Schlögl.[3]

By understanding the reaction mechanism, we can make some predictions about what will make a good catalyst. Firstly, it must be able to activate the extremely strong triple bond of dinitrogen. According to Figure 1-6, ΔH for the step $N_2 \rightarrow 2N_{ad}$ is about 250 kJ mol^{-1}, and the only exothermic step in the mechanism. However once ammonia has been formed on the catalyst surface, it must be able to desorb before it undergoes the reverse reaction to surface NH_x species. Therefore, the bond formed between nitrogen and the catalyst surface must not be too strong. This is the Sabatier principle, and can be represented by a 'volcano plot', whereby the turnover frequency of a catalyst is plotted against some descriptor of bond strength, Figure 1-8a.

Medford et al. visualised this for ammonia synthesis catalysts by presenting a volcano plot of turn over frequency of ammonia against the nitrogen adsorption energy, Figure 1-8b. By using density functional theory to calculate the adsorption energy of a nitrogen atom, it was shown this is a good descriptor of the bond strength, giving a highly correlated volcano plot with experimentally determined rates.[28] In this paper they highlighted a theorised cobalt-molybdenum alloy, with a predicted turn over frequency higher than even ruthenium catalysts.

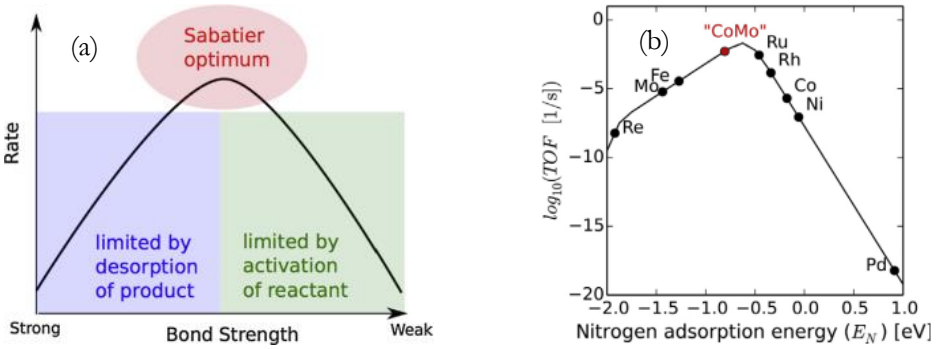


Figure 1-8: (a) Volcano plot showing Sabatier principle (b) Volcano plot showing how experimentally reported rates of transition metal catalysts correlate strongly with computed N-atom adsorption energies. Theorised rate of a CoMo alloy catalyst is highlighted. Both graphs reproduced from Medford et al.[28]

Iron based catalysts are still by far the most utilised catalyst for the industrial process, and accordingly the most studied catalyst in the literature. A ruthenium-based catalyst was developed by British Petroleum in the 1970s, and a new process developed utilising a higher N_2/H_2 ratio, named the Kellogg Advanced Ammonia Process (KAAP). The ruthenium catalyst and accompanying process have not, however, been widely adopted, with only a reported 7 plants worldwide producing ~14,000 tonnes daily, less than 4% of global production.[29] The most likely explanation of this is the cost of retrofitting a plant to work with a new catalyst system, and the high cost of ruthenium metal. Other catalyst systems have been reported in the literature, but to the authors knowledge these are not utilised in any commercial setting.

Apart from the popular ruthenium and iron systems, an extensive list of catalysts has been trialled for the ammonia synthesis process. Most, however, do not yet show promise for use the industrial process. One notable example discussed previously in Figure 1-8 is a cobalt-molybdenum alloy. This catalyst emerged from DFT calculations, reported by Jacobsen et al., as it is known that Mo binds too weakly to

dinitrogen, and cobalt too strongly.[30] A number of papers have reported the use of Co_3Mo_3N catalysts for ammonia synthesis, operating via a Mars van Krevelin mechanism.[31–33]

1. 2. 2 Iron Based Catalysts

Iron based ammonia synthesis catalysts have a complicated active phase, of which the exact structure under working conditions is still the subject of debate. The active catalyst is commonly termed in literature as 'ammonia iron'. The Mittasch iron catalyst consists of an Fe_3O_4 based pre-catalyst, which is slowly reduced to give an α-Fe catalyst promoted by the irreducible oxides K_2O, Al_2O_3 and CaO.[34] It has been shown that the reaction is surface-structure sensitive, and proceeds most rapidly on the Fe(111) crystal face.[35] The activity of this face was attributed to highly coordinated (C7) sites. Structural calcium and aluminium promoters prevent the sintering of iron surfaces, increasing the Brunauer-Emmett-Teller (BET) surface area relative to catalysts without these promoters.[36] The role of the potassium is somewhat more complex, and still the matter of some debate. However, it is well accepted that potassium is not merely a structural promoter, as the presence of it has been shown to change the work function, and kinetics of nitrogen adsorption of iron catalysts.[37] The structure and mode of operation of the active catalyst is still the subject of debate, even after more than 100 years of study. It is then of no surprise that ammonia iron displays a complex and unusual structure.

The bulk structure of the industrial iron catalyst under conditions close to the operating conditions of the industrial process was examined by Kandemir et al. in 2013, using in-situ neutron diffraction studies.[34] In these investigations, bulk iron nitride could not be detected, and indeed the catalyst was observed to be pure α-Fe phase. When comparing the diffraction pattern captured from the catalyst to a pure α-Fe reference pattern, some peak broadening, and differences in relative intensities of the peaks was observed. However, this was attributed to 'structural anisotropy' caused by defects, and strain and size effects caused during the reduction process needed to generate the 'ammonia iron' catalyst phase. This structural anisotropy did not diminish after a time-on-steam (TOS) of more than 88 hours. As diffraction studies examine the bulk structure of materials, this study does not disprove reports of surface nitride species.

Over several papers in 1975, H. Topsøe, M. Boudart, and colleagues examined the size dependence, and in-situ reconstruction of iron particles supported on MgO. Iron particles with sizes ranging from 1.5 to 30 nm were prepared and characterised.[38] The catalyst with the largest particles (30 nm) was found to be the most active showing that the idea of small particles with high exposed metal surface giving the highest rates, is not always true. Compared to a doubly promoted commercial iron catalyst, the 30 nm iron particles were found to have similar turnover numbers and efficiencies (the measured conversion over the thermodynamic equilibrium conversion under the same conditions), indicating promoters are not essential to obtain a highly active iron catalyst.[39] In the same study, catalysts were treated with ammonia, to saturate the surface with nitrogen atoms via ammonia decomposition. This was demonstrated to cause an increase in the content of metallic iron in all Fe/MgO catalysts, as well as a surface reconstruction. These reconstructed catalysts showed higher activity for ammonia synthesis when the gas flow was returned to a hydrogen/nitrogen mix.

This increased activity slowly decreased with time over the smaller iron particles (1.5 and 4.0 nm). The increase in activity over the larger 30 nm particles was much less notable. Using CO chemisorption and Mossbauer spectroscopy, it could be demonstrated that after ammonia treatment, a significant surface reconstruction had occurred.[40] These changes could not be reproduced by hydrogen treatment alone, so it was concluded that these reconstructions could not be attributed to a greater degree of reduction of the iron. Brill et al. had previously showed, using field emission microscopy, how an iron tip of (110) and (100) facets would reconstruct to (111) facets in the presence of nitrogen.[41] Nitrogen adsorbed to the tip caused this reconstruction after heating to 400 ºC, attributing this to the reduction in surface energy of the (111) face after adsorption of nitrogen. From the evidence of Brill et al., Dumesic et al. concluded it was most likely the rearrangement had created Fe(111) faces with a high concentration of C7 sites, reported to be the most active site for dissociative dinitrogen adsorption.

Surface structure had been known to play a significant role in the rates of dissociative dinitrogen adsorption, from the previously discussed work of Spencer et al., in which it was shown the rate of ammonia synthesis was highest over a preferentially (111) orientated iron surface.[25] Strongin et al. (1987) expanded on this work by examining the source of this high activity, concluding that the presence of high-coordination (C7) sites is the most important factor. The rates of ammonia synthesis at high pressures (20 atm.) (under kinetic control) over various facets of iron was recorded, confirming that Fe(111) was indeed the most active of those tested (Figure 1-9).

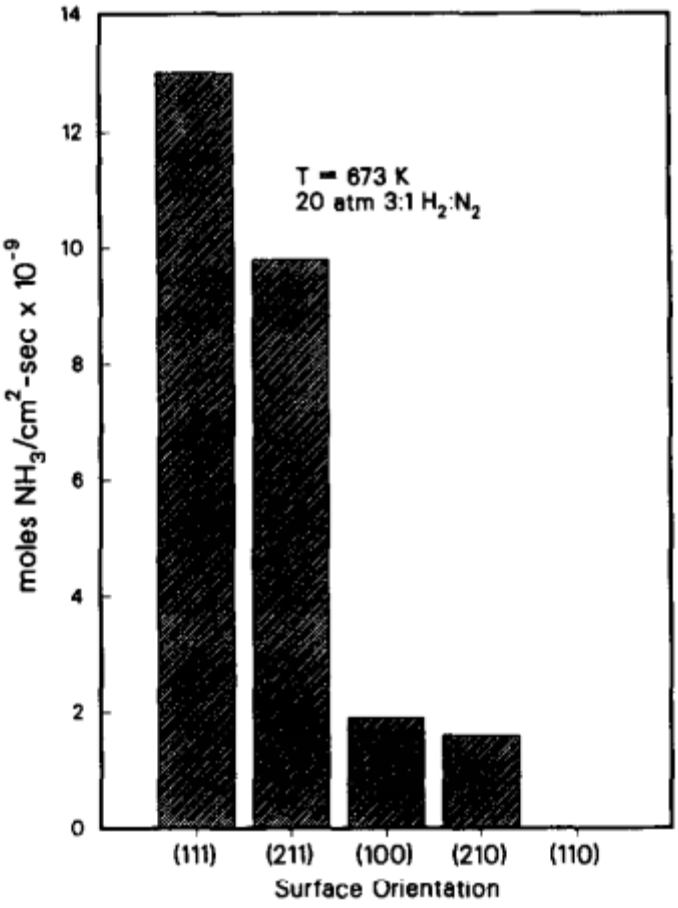


Figure 1-9: Rates of ammonia synthesis over the surfaces. Reproduced from Strongin et al.[35]

Two theories had been previously proposed as to the origin of high activity of Fe(111) surfaces: the presence of highly coordinated (C7) sites, and greater surface roughness. Rough surfaces have high surface free energy, and therefore could form more stable bonds with nitrogen atoms. Surface roughness, and surface free energy, is related to the work function of a material. Work function measurements were not available for all facets of iron investigated, so a comparison was made to the analogous material (also BCC) structure tungsten. The roughness of iron surfaces was also considered qualitatively, i.e. how many atoms from the 2nd and 3rd layers of the material are exposed to the surface.

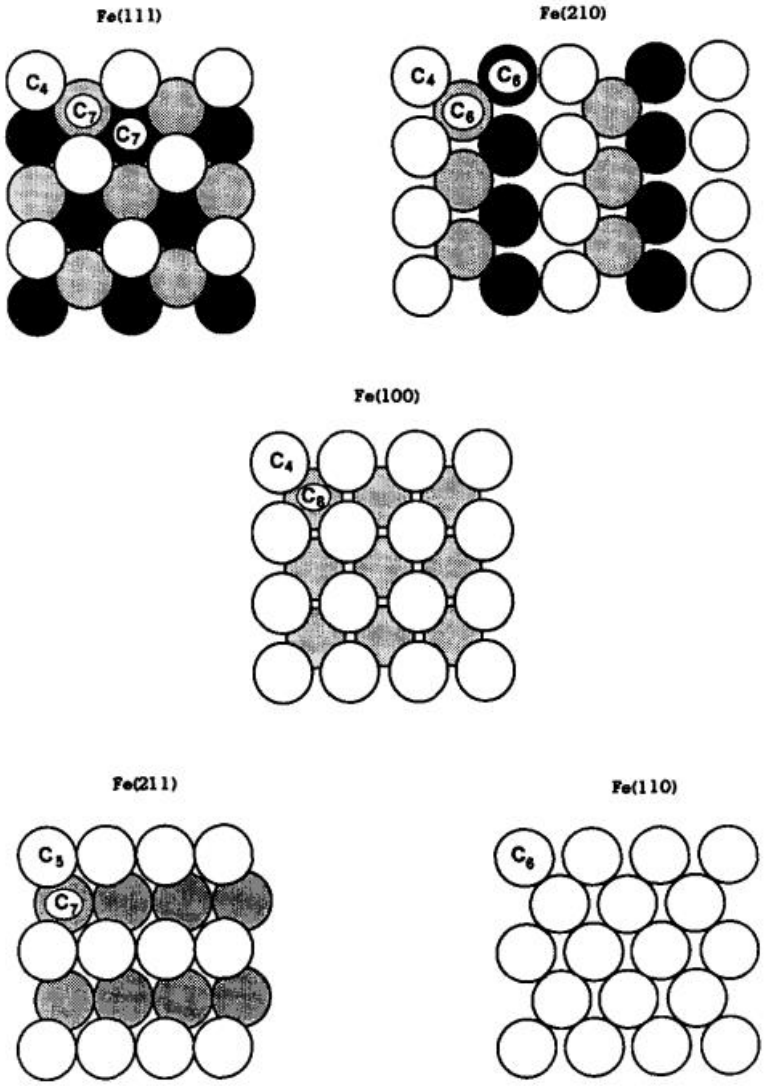


Figure 1-10: Schematic representation of the iron surfaces studied by Strongin et al. Coordination number for the different types of atom in each surface is indicated. White represents the top layer, grey the second, and black the third. Reproduced from Strongin et al.[35]

As seen from Figure 1-10, the highly active Fe(111) surface displays both high roughness and sites with high coordination numbers. The next most active surface, Fe(211), has highly coordinated sites but does not display the same degree of roughness. Fe(210) displays a high degree of surface roughness, but not the presence of highly coordinated C7 sites. From these observations, it was concluded that the presence of C7 sites is the key factor in determining the activity over Fe(111) surfaces.

Falicov and Somorjai published a joint theoretical and experimental study showing how the presence of high-coordination number transition metal atoms surrounded by larger numbers of metallic non-magnetic or weakly magnetic atoms, leads to sites with low-energy electronic fluctuations.[42] The presence of these sites was linked to the catalytic activity of a surface. The fluctuations can have several different origins but can essentially be summarised as the electrons in the iron 3d band being described by multiple quantum states. For example, configuration fluctuations between $3d^{10}$, $3d^{9}4s^{1}$, and $3d^{8}4s^{2}$ electronic configurations will lead to multiple energetic states. Spin fluctuations in which an electron may be described by a spin

quantum state of +1/2 or -1/2 will also lead to different energetic states when considered as part of a metallic band structure of many atoms. The authors linked the high density of states found in transition metals with unfilled 3d orbitals to their catalytic activity for ammonia synthesis. It was shown how the chosen descriptors for energy fluctuations could be calculated and correlated with experimentally determined catalytic activities.

The effect of promoters for ammonia synthesis are described as structural, modifying the catalyst morphology, or electronic, modifying the binding of surface species to the catalyst. It is now accepted that most promoters of industrial catalysts are structural promoters.[36,43] However, the situation is less clear with potassium promoters. It is known potassium increases the concentration of adsorbed nitrogen species on the iron surface, and the most obvious explanation for this is the electropositive potassium atoms increase the electron density of the iron.[44] However, reports have documented that potassium exists on the iron surface as an oxide,[36,37] casting doubt on how much electronic transfer can occur between the metals.

Ertl et al. used spectroscopic and microscopic techniques to investigate the surface composition and structure of an industrial iron catalyst under UHV conditions.[36] The catalyst was a magnetite iron-based catalyst promoted with Al_2O_3, K_2O, and CaO. The unreduced catalyst was found to be smooth and free of large pores according to SEM, and Auger electron spectroscopy showed inhomogeneous distribution of different metal oxides (Fe, Ca, K, Al). XPS showed that surface composition is drastically different to bulk composition, with significant potassium enrichment identified at the surface. After complete reduction of the catalyst, SEM showed the appearance of pore structures. Auger maps showed the surface consisted mainly of Fe, covered with a thin (1 atomic layer) of potassium. The presence of Al_2O_3 was found to increase BET surface area linearly until a plateau around 2.5% in unreduced magnetite. In the unreduced state Al_2O_3 was found to be mainly dissolved into the magnetite lattice, and partially existing as large crystallites. After reduction, the Al_2O_3 does not remain dissolved in the α-iron lattice, and instead segregates at the surface of the iron particles. It was suggested this forms a rigid framework, preventing sintering of the iron particles. The increased surface area and suggested role of the Al_2O_3 after reduction indicate it is working as a structural promoter. The XPS data suggested the formation of a potassium oxide monolayer atop the iron substrate. This Fe-O-K monolayer had been previously reported by Paál et al.[37] CaO was found to segregate from the catalytically active Fe particles and it's role was attributed again as a structural promoter.

Adsorption of dinitrogen to iron surfaces with and without potassium promoters was described by Ertl et al.[44] Under the UHV conditions employed, the potassium was observed to induce changes in the iron surface, and in the interactions of nitrogen with the iron surface. Heat of adsorption of molecular nitrogen to iron is increased in the vicinity of potassium atoms. Effective activation energy is reduced, which significantly increases the sticking coefficient for dissociative dinitrogen adsorption. Increasing potassium surface concentration decreased the work function of the iron surfaces. Surfaces with adsorbed nitrogen atoms showed a higher absolute work function than clean surfaces. From this data it was concluded that

potassium transfers electrons to the iron surfaces, and in the presence of nitrogen, these electrons transfer to the adsorbed nitrogen atoms. The increase of heat of adsorption and reduction in activation energy were then described by a back-bonding model. The iron surface donates electrons into dinitrogen anti-bonding orbitals, weakening the nitrogen-nitrogen bond and reducing the activation energy. Formation of Fe-N bonds stabilises the surface. However, it was acknowledged in the paper that this model can not necessarily be easily applied to the high-pressure case.

Literature reports of wüstite pre-catalysts should also be briefly discussed. In the 1980s, it was reported by researchers at Zheijang University of Technology that replacing the magnetite (Fe_3O_4) iron source with wüstite (FeO) led to dramatic increases in the activity for ammonia synthesis.[45] Despite some debate in the literature,[46] the high activities of the catalyst formed from this oxide precursor were again reported by Pernicone et al.[47] However, since it is now known the main phase of the catalyst is pure reduced α-Fe,[34] it seems likely the difference in activities is due to the details of the reduction of the pre-catalyst. Indeed, as discussed by R. Schlögl in the "Handbook of Heterogeneous Catalysis", magnetite precursors are deliberately reduced to wüstite during the reduction process.[3] For a more detailed discussion of the reduction processes for industrial iron catalysts the reader is referred to the aforementioned book.

Iron catalysts for the Haber-Bosch process are some of the only catalysts for which a complete picture of their mode of action has been established, including the elucidation of the structure under operating conditions, development of a mechanism via use of single crystal and theoretical studies, and the linking of the mechanism measured under UHV conditions to the high pressure process. The sheer volume of work necessitates that many interesting aspects are not covered in this summary. The most notable absence is discussion of the theoretical studies by Norskov and co-workers, which was instrumental in the understanding of the energetics of the process.[48–50] It is attempted here to highlight the most relevant and interesting works involved in the development of these materials from an inorganic chemistry perspective, and to cover the key aspects in their function. It is, however, clear that iron-based catalysts have been extensively optimised, and any further improvements to their activities are likely to be marginal.

1. 2. 3 Ruthenium Based Catalysts

Ruthenium metal shows the highest activity towards reduction of dinitrogen to ammonia, of any transition metal. This higher activity means the reaction temperature may be lowered while maintaining the same rate of ammonia synthesis. At a lower temperature, the pressure may then be reduced without the conversion being limited by equilibrium. As discussed previously (Section 1. 1), reduction of synthesis pressure is a key requirement for development of an agile Haber-Bosch process.

Ruthenium catalysts for ammonia synthesis are almost always in the form of nanoparticles. This allows for efficient use of the expensive metal by maximising the ratio of surface to bulk atoms. There is an ideal size for these nanoparticles, determined by the concentration of specific surface sites where dinitrogen adsorption occurs. Nanoparticles are usually dispersed on a support material which facilitates handling and

prevents aggregation. Additionally, supports may influence the rate of reaction over the nanoparticles via electronic or ionic interactions.

A comparison of industrial ruthenium and iron catalysts reported by Brown et al. is reproduced in Table 1-1.[29] The ruthenium catalyst dramatically outperforms the iron one, but this difference is even more pronounced under mild conditions.

Table 1-1: Yields of industrial Ru and Fe catalysts as reported by Brown et al (arbitrary units).[29]

Conditions	Magnetite Catalyst (3:1 H_2/N_2)	Promoted Ru/C Catalyst (1.5:1 H_2/N_2)
86 bar, 653 K	1	26
138 bar, 673 K	3	55

Ruthenium has another advantage over iron for use as an agile Haber Bosch catalyst: iron catalysts requires a long reduction and activation period before they reach peak activity. Figure 1-11 shows the difference in ammonia output for an industrial iron catalyst reduced for 24 and 50 hours, with the longer activation leading to an almost doubling of conversion at a lower temperature. In contrast, no such activation process is reported for ruthenium catalysts, and many literature reports use short reduction programs (often only a few hours).[51–53] As discussed in section 1. 2. 1, despite the development of the KAAP process, ruthenium catalysts are not in wide use. New catalyst systems with higher activities are required to compete with the well-established iron materials.

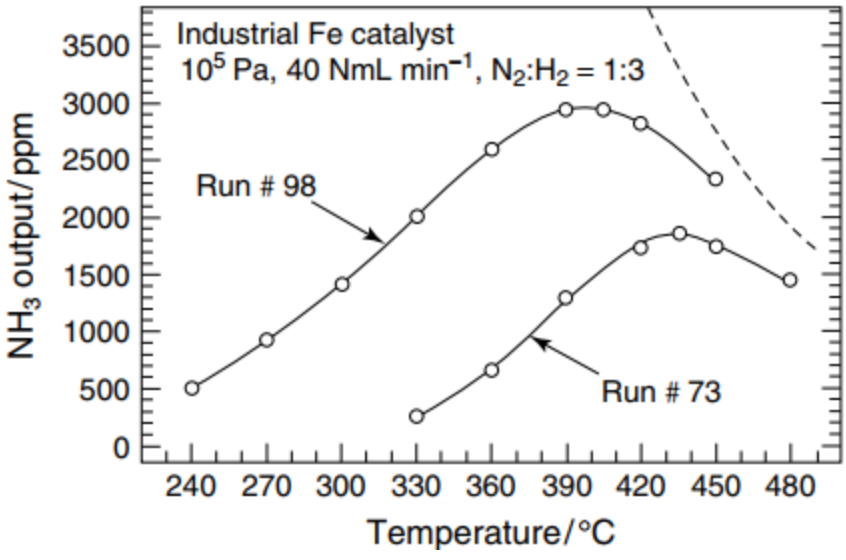


Figure 1-11: Difference in NH_3 conversion vs temperature for an industrial iron catalyst reduced under two differing conditions: Run #73 was reduced for 24 hours, run #98 for 50 hours. Reproduced from 'Ammonia Synthesis' by R. Schlögl.[3]

The catalyst used in the KAAP process consists of doubly promoted carbon-supported ruthenium nanoparticles. Details of the catalyst were summarised by the inventors in 2014.[29] The carbon support is key to its success and is prepared by a three stage process: firstly it is heated to 1770 – 2270 K under inert

atmosphere, then treated with oxygen (or air) at 570 – 670 K, before finally heating again to 1770 – 2270 K under inert atmosphere. The first high temperature treatment modifies the porosity of the carbon and causes a slight graphitisation of the carbon. The low temperature treatment further modifies the porosity, but also disrupts the graphitisation. The final high temperature treatment restores the graphitisation and further modifies the porosity. This results in a mesoporous material with an average pore diameter of 5 nm and a surface area (as determined from BET) of 600 $m^2\ g^{-1}$. The surface is hydrophobic and composed of graphite-like basal planes with very little oxygen. The support can stabilise ruthenium particles at relatively high loadings (up to 8%), while maintaining dispersion of the nanometre size particles. Graphitisation provides a conductive surface, facilitating electronic promotion.

In contrast to the case of iron catalysts, the effects of alkali metal promotion for Ru catalysts is relatively well understood. Mortensen et al conducted DFT studies on the effects of alkali promoters on the dissociation of dinitrogen on Ru(0001) surfaces. It was found that promoters lower the barrier for dissociative dinitrogen adsorption through a direct electrostatic attraction between the adsorbed alkali metal atoms and the dinitrogen molecule. Aika et al. tested the efficacy of Ru/C catalysts promoted by alkali and alkali-earth metals.[54] Rb was found to be the most effective of the tested alkali metal promoters (better than Cs or K). Alkali-earth metals were found to be effective promoters in the order (Ba>Sr>Ca>Mg). Activity of Ba-Ru/C was found to be comparable to Rb-Ru/C and better than Cs-Ru/C.

Work by Raróg-Pilecka et al. looked at the state of the caesium during reduction and synthesis of ammonia over Cs-Ru/C catalysts.[55] Following the reduction of $CsNO_3$ via in-situ XRD and TPR-MS showed the reduction proceeded via a CsOH intermediate before formation of an amorphous sub-stoichiometric caesium oxide (Cs_xO_y). The presence of ruthenium particles was found to significantly reduce the reduction temperature of $CsNO_3$. Ruthenium particle morphologies were examined as a function of support characteristics, and metal loading. High surface area supports led to a significant decrease in particle diameter. Increases in metal loading led to increases in ruthenium particle diameter, although had less of an impact than surface area (7-fold increase in loading gave an approximate doubling in particle diameter). TOF was also measured as a function of caesium loading and found to increase up to a maximum of around 2.5 mmol Cs/g_{C+Ru}.

As in the case of iron catalysts, the reduction of dinitrogen to ammonia over ruthenium surfaces is known to be extremely structure sensitive. Adsorption of nitrogen to the ruthenium surface is understood to occur at 5-coordinate sites which fulfil specific requirements. They must expose a three-fold hollow site and a bridge site in close proximity and (2) some of the atoms must be low-coordinated surface atoms such as edge atoms on small crystals.[56] This ensures that the two atomic nitrogen species are bound to different ruthenium atoms.[57] While the possibility of adsorption at other sites is not ruled out, the dissociative adsorption was reported to be 90 – 129 kJ mol^{-1} more energetically favourable at step sites over terrace sites.[56] These sites were termed B5 sites by Van Hardeveld & Van Montfoort (shown in Figure 1-12 inset), and the concentration has been shown to be heavily dependent on the size and structure of the ruthenium

particles.[58,59] Figure 1-12, reproduced from Jacobson et al., shows how the concentration of edge atoms and B5 sites varies with ruthenium crystal size. The concentration of B5-sites peaks when the Ru crystal is around 2nm in diameter; below this size it is rare for the surface atoms to come together in the required shape, whereas above this size a (0001) surface dominates, meaning edge sites are fewer (Figure 1-12).[58,59]

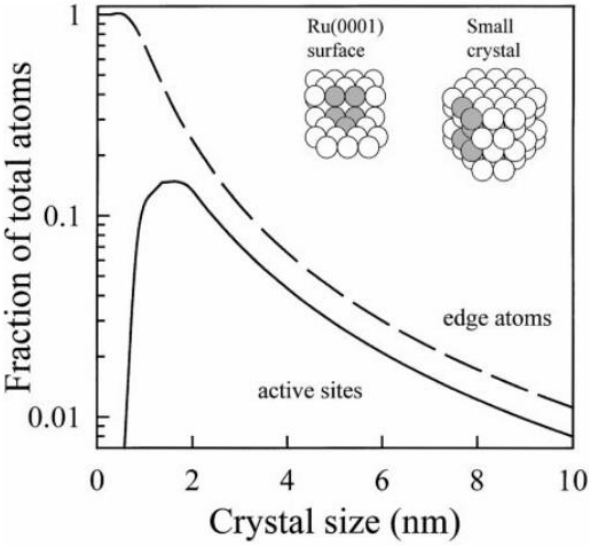


Figure 1-12: Change in concentration of edge atoms, and concentration of B5 active sites with increasing Ru particle size. Inset diagrams shows arrangement of surface atoms at B5 active sites. Reproduced from Jacobsen et al.[58]

The active site of nitrogen adsorption was directly identified by Zambelli et al via scanning tunnelling microscopy (STM). They studied the dissociation of NO over ruthenium (0001) single crystals, and by locating the positions of the N atoms after dissociation of the NO, they could identify 'active sites'.[60] Differences in how N and O atoms are imaged by STM allowed differentiation between the two species. The N atoms are less mobile than the O atoms, therefore the finding that N atoms cluster at the steps, and O atoms away from the steps on the terraces was taken as evidence for the dissociation occurring at steps. NO species are extremely mobile, and not detectable via STM. N atoms could diffuse away from the steps overtime, but were not found to diffuse over steps onto the adjacent terrace. The terrace sites can therefore act as reservoirs for the N atoms. Two different step structures were identified on the surface, differing in how many immediate neighbours a Ru atom on the top step had in the lower layer (1 vs 2). The step type in which the Ru atoms were more coordinated showed a higher activity for NO dissociation.

Reduction of dinitrogen to ammonia over ruthenium surfaces proceeds via the same dissociative mechanism as in iron systems. Detailed studies of surface reactions by Hinrichsen et al. confirmed this.[61] Hydrogenation of pre-adsorbed atomic nitrogen was followed using temperature programmed reactions, with varying starting conditions. The surface of a Ru/MgO catalyst was saturated with N_2 prior to reaction. Heating the catalyst at different rates up to 600 K yielded differing effluent NH_3 concentration profiles, from which activation energies could be determined via an Arrhenius plot. No desorption of dinitrogen was observed during this process, so the possibility of molecular adsorption and an associative mechanism

could be ruled out. Reaction profiles reproduced by a microkinetic model, with a Langmuir-Hinshelwood mechanism, showed good agreement with the experimental data.

Kinetic models have been used with great success to compare between ruthenium-based catalysts. Hinrichsen et al. reported a kinetic model of dinitrogen adsorption and ammonia synthesis over Ru/Al_2O_3, Ru/MgO, and Cs-Ru/MgO catalysts.[62] Equilibrium nitrogen desorption constants (k_{des}) were obtained from nitrogen TPD studies with different heating rates. Nitrogen adsorption equilibrium constants (k_{ads}) were obtained by fitting results from isotopic studies, and previously obtained k_{des} into a microkinetic model. Using calculated parameters to model the isotopic exchange reaction gave good agreement with measured experimental data. Cs promoters were found to enhance both rates of adsorption and desorption. A Langmuir–Hinshelwood Hougen–Watson mechanism could be used to make good predictions of experimental results. Microkinetic modelling suggested that the number of active sites is dependent on temperature. Extrapolating k_{ads} to room temperature yielded a result in agreement with sticking coefficients obtained from single crystal studies.[63]

Rosowski et al. derived power-law rate equations at ambient pressure and 20 bar, for ruthenium nanocrystals supported on MgO or Al_2O_3 supports.[12] Caesium promoters were used, and it was found that the Cs source affected the activity of the catalysts. Strong inhibition of the catalysts by hydrogen was confirmed. Aqueous impregnation of Ru/MgO catalysts with $CsNO_3$ was found to significantly increase Ru particle size. The same effect was not observed on Al_2O_3 supports. A less significant change in Ru particle morphology was observed with non-aqueous (ethanol) impregnations. Cs promotion had a more significant effect on MgO supported catalysts over Al_2O_3 supports, which was attributed to the acidity of the alumina. All hydrogen reaction orders were negative, and addition of Cs promoter was found to reduce the order even further. Inhibition by hydrogen was worse at 20 bar than at atmospheric pressure. Ammonia reaction order was negative in catalysts without Cs promoters, but zero in promoted catalysts.

In a series of papers, Aika et al. investigated rates of ammonia synthesis over supported and powdered ruthenium catalysts, with and without promoters. A comparison of MgO, CaO, and Al_2O_3 as supports for ruthenium particles showed the alkali-earth oxide supports gave significantly more active catalysts than the alumina support, attributed to the higher basicity of the MgO and CaO supports.[64] The rates and kinetics of ammonia synthesis over powdered ruthenium and supported ruthenium catalysts, with and without promoters were presented.[65] It was reported that synthesis over powdered ruthenium is strongly retarded by the preferential adsorption of hydrogen over nitrogen. This presents one of the most significant challenge for ammonia synthesis over ruthenium catalysts. Adding a caesium promoter increased the reaction rate but increased the poisoning of the ruthenium by hydrogen. While high rates could be obtained over powdered catalysts, due to low dispersion of the ruthenium, the rates per ruthenium atom were several orders of magnitude lower than supported catalysts.[64] For a metal as expensive as ruthenium, reaching high dispersion value in the synthesis of supported nanoparticles is critical for a catalyst to be economically viable.

Hydrogen poisoning has been shown to be a significant problem for ruthenium catalysts. As stated above, kinetic investigations have shown hydrogen has a negative order of reaction, indicating that ammonia production is retarded significantly by hydrogen in the gas stream, or on the catalyst surface. Rates of both dinitrogen dissociative adsorption, and the subsequent hydrogenation are much faster over ruthenium surfaces than on iron ones, however the poisoning effect is so strong, the rates of ammonia synthesis are comparable. Rambeau and Amariglio reported that the rate of dissociative dinitrogen adsorption over Ru powder is at least 500 times that of the rate over an Fe powder. However, due to the strong inhibition from adsorbed hydrogen, both metals show comparable rates of ammonia synthesis.[66] Aika in 'Ammonia Catalysis and Manufacture' reported that at temperatures above 431 K hydrogenation of adsorbed nitrogen is controlled by the availability of hydrogen in the gas stream, and equilibrium ammonia pressure.[67] The hydrogenation rate can only be measured independently at low temperatures (below 300 K). Isotopic equilibration studies confirmed hydrogen retards the dissociative adsorption of dinitrogen. Urabe et al. looked at the rates of isotopic equilibration of $^{28}N_2$ and $^{30}N_2$ over various ruthenium catalysts.[68] In all studied ruthenium catalysts, the rate of production of $^{29}N_2$ dropped with increasing H_2 partial pressure.

Several recent studies from the Tokyo Institute of technology report a reduction in hydrogen poisoning of ruthenium catalysts due to properties of the support.[69–72] Kitano et al. showed in 2015 how supports based on a calcium-aluminium oxide structure were capable of absorbing appreciable quantities of hydrogen. A ruthenium-based catalyst support on an electride was found to have the highest activity of those tested and showed the greatest incorporation of hydrogen as measured by TGA. Kinetic analysis showed that the order of reaction with respect to hydrogen (a measured of the extent of hydrogen poisoning) was lower on supports showing the greatest degree of hydrogen incorporation. Preparation of this electride is challenging, however. Five independent steps, including four high temperature treatments, vacuum heat-treatments, and handling of pure calcium metal in a glovebox are required. This reduces the attractiveness of this material for industrial application.

Some of the key developments for ruthenium ammonia synthesis catalysts have been discussed. Ruthenium is a highly active metal for the dissociative adsorption of dinitrogen; however, the overall rate of ammonia synthesis is significantly impeded by hydrogen poisoning.

1. 3 Proton Conducting Ceramics

Oxide materials displaying appreciable protonic conductivity have historically been of interest for fuel cell applications.[73] However, these materials may also provide opportunities for reactions involving hydrogenation or dehydrogenation processes. As one of the most studied chemical reactions, it is only natural that ammonia synthesis would be near the top of the list for investigation. They have also attracted interest for application as hydrogen separation/purification membranes.[74]

Protonic conduction in ceramics at elevated temperatures was first confirmed by Iwahara et al. in 1981, when they found that an ytterbium or magnesium-doped $SrCeO_3$ perovskite pellet with platinum electrodes would generate an electromotive force when the (hermetically separated) electrodes were exposed to water-containing gas on one side, and oxygen containing gas on the other.[75] The phenomenon has been reported in crystals with various structures, including perovskite, brownmillerite, fluorite, apatite, and mayenite among others.[76]

Conductivity in these materials arises due to the presence of oxygen vacancies, deliberately introduced into the lattice by doping of aliovalent cations, or through structural disordering to create reduced coordination polyhedra. Some structures display intrinsic oxygen vacancies in high enough concentrations to not require deliberate structural modification.[77] It is also the case that oxides may display mixed conductivity; purely protonic, mixed oxide and protonic, or mixed n- & p-type electronic/protonic conductivity.[76] Materials can be deliberately designed to achieve mixed conductivity,[78] or display different conductivities under differing temperature regimes and gas atmospheres.[79]

Bohn and Schober classified the total conductivity (σ) in a $BaZr_{0.9}Y_{0.1}O_{3-\delta}$ electrolyte as consisting of contributions from oxygen ion ($\sigma_{V\ddot{o}}$), electron hole ($\sigma_{h\cdot}$), electron ($\sigma_{e'}$), and proton ($\sigma_{H\cdot}$) conduction (Equation 1.7).[80]

$$\sigma = \sigma_{V_{\ddot{o}}} + \sigma_{h\cdot} + \sigma_{e'} + \sigma_{H\cdot}$$

$$= \frac{F}{V_m}\left(2[V_{\ddot{o}}]\mu_{V_{\ddot{o}}} + [V_{h\cdot}]\mu_{h\cdot} + [V_{e'}]\mu_{e'} + [V_{H\cdot}]\mu_{H\cdot}\right) \qquad \textit{Equation 1.7}$$

F is the Faradays constant, and V_m the molar volume of $BaZr_{0.9}Y_{0.1}O_{3-\delta}$ (44.757 cm^3). $\mu_{V\ddot{o}}$, $\mu_{h\cdot}$, $\mu_{e'}$, and $\mu_{H\cdot}$ represent the mobilities of oxygen ions, electron holes, electrons and protons, respectively. $[V_{V\ddot{o}}]$, $[V_{h\cdot}]$, $[V_{e'}]$, and $[V_{H\cdot}]$ represent the concentrations of oxygen ions, electron holes, electrons, and protons, respectively. Proton conduction dominates when the concentration of protons in the lattice (in the form of hydroxyl groups) is much higher than the concentration of other conductive species. This occurs at lower temperatures, and in hydrogen-rich atmospheres (containing gaseous water or hydrogen).[80,81]

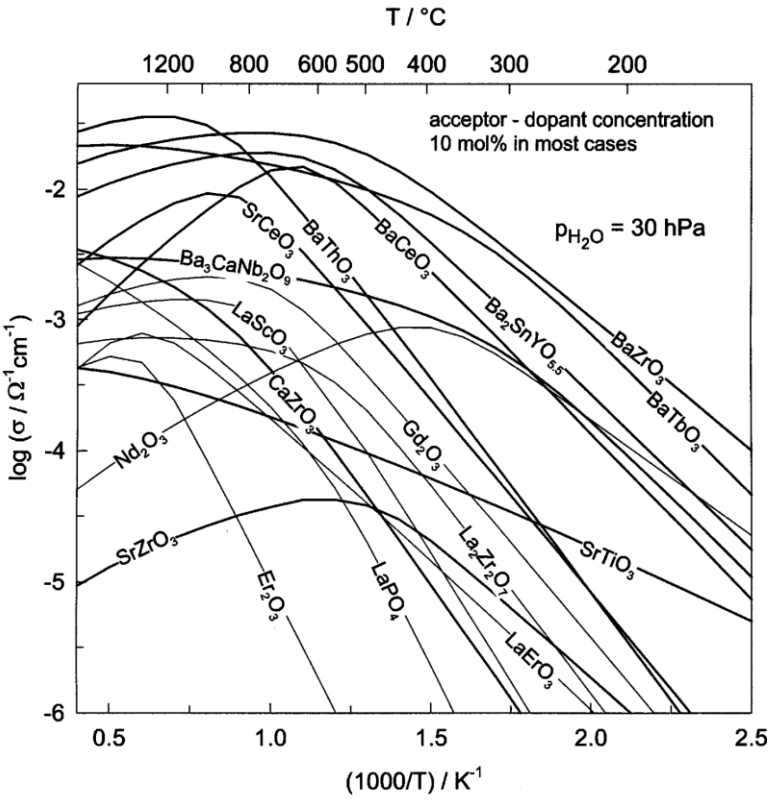


Figure 1-13: Arrhenius plot of conductivities in proton conducting ceramics, reproduced from Kreuer et al.[82]

Many different protonic conductors have been synthesised and characterised, succinctly summarised by Kreuer in 2003, Figure 1-13. It is apparent that barium-based perovskite structures display the highest overall conductivities, particularly at lower temperatures. The two most studied barium-based perovskites are barium zirconate and barium cerate. Table 1-2 and Table 1-3 give the proton conductivities and activation energies of proton transport in a range of reported barium cerates and zirconates.

Examining the values in Table 1-2 and Table 1-3, some notable differences emerge between the barium cerate and zirconate based materials. Barium zirconate requires high sintering temperatures and long sintering times to achieve dense materials (Laidoudi, Abu Talib, & Omar 2002; Gorelov et al. 2010).[83,84] However, dense barium cerate can be synthesised at lower temperatures and with shorter sintering times than barium zirconate (Amsif et al. 2011; Zhang et al. 2011).[85,86] Sintering aids such as NiO can be used to reduce sintering times and temperatures of barium zirconate materials (Yoo et al. 2015).[87] Work by Cevera et al. showed how an electrolyte sintered at 1250 ºC had conductivity values 3 orders of magnitude higher than a pellet sintered at 800 ºC.[88]

Doping of the lattice with aliovalent cations increase the maximum possible concentration of hydroxyl groups in the lattice, leading to higher proton conductivity according to Equation 1.7. In both barium cerates and zirconates, 10 – 20% doped structures lead to significantly higher conductivities than higher or lower doping levels (Islam et al. 2013; Zhang et al. 2011; Kuz'min et al. 2009).[86,89,90] Amsif et al. showed how in barium cerates, Y and Gd dopants lead to higher conductivity values compared to other lanthanide dopants.[85] Laidoudi, Abu Talib, & Omar reported that a Yb doped barium zirconate material had the

highest overall value of proton conductivity amongst a range of lanthanide doped barium zirconates.[83] However, Gorelov et al. reported that for barium zirconate, Y actually gave the highest conductivity from a range of lanthanide dopants.[84] In general, there are many more reports of Y-doped barium zirconates, and the highest reported conductivities are achieved when using 10-20% yttrium doped materials (e.g. Yamazaki et al., Babilo et al.).[91,92] A study by Fabbri et al. found conductivity decreased at doping levels greater than 20%.[93]

Table 1-2: Reported conductivities and activation energies of barium cerate proton conductors. All gasses are humidified, except when marked as dry. Hydrogen is diluted with inert gasses in all cases. Data from references [85,86,89,94,95]

Material			Synthesis				Testing		Conductivity ($\mu S\ cm^{-1}$, total or bulk)	Activation Energy (eV)			Reference	
Parent oxide	Dopant	x	Preparation	Sintering temp. (ºC)	Sintering time (h)	Density (%)	Gas	T test (ºC)		Total	Grain Boundary	Bulk	Year	Author
$Ba_{0.8}Ce$	-	-	Glycine Nitrate Synthesis (GNS)	1550	6	-	Dry Air	850	115 (B)	-	-	-	2013	Islam, Nag, & Basu
$Ba_{0.8}Ce_{1-x}$	Tb	0.05							71 (B)					
$Ba_{0.8}Ce_{1-x}$	Tb	0.1							603 (B)					
$Ba_{0.8}Ce_{1-x}$	Tb	0.15							976 (B)					
BaCe	-	-	Solid State Reaction Method (SSRM)	1500	24	-	Dry H_2	200	5 (B)	1.042	0.931	0.433	2009	Pasierb et al.
								300	33 (B)					
								350	57 (B)					
								570	278 (B)					
$BaCe_{1-x}$	Y	0.1	SSRM	1700	10	-	H_2	600	11000 (T)	0.35	-	-	2000	Katahira et al.
$BaCe_{1-x}$	Gd	0.1	Freeze Drying (FD)	1400	4	98	Air	200	289 (B)	-	0.72	0.49	2011	Amsif et al.
	La					95			33 (B)		0.82	0.53		
	Nd					96			36 (B)		0.75	0.53		
	Sm					100			151 (B)		0.76	0.49		

$BaCe_{1-x}$	Y Yb	0.1	FD	1400	4	95 98	Air	200	212 (B) 148 (B)	-	0.77 0.77	0.48 0.47	2011	Amsif et al.
	Sm	0.01 0.01 0.01 0.01 0.03 0.1 0.2	Citrate Nitrate Synthesis (CNS)	1500	5	~95	H_2	300 400 500 600 300 300 300	122 (B) 292 (B) 515 (B) 685 (B) 317 (B) 679 (B) 872 (B)	-	-	-	2011	Zhang et al.

Table 1-3: Reported conductivities and activation energies of barium zirconate proton conductors. All gasses are humidified. Hydrogen is diluted with inert gasses in all cases. Data from references [83,84,87,88,90–92,96–100]

Material			Synthesis				Testing		Conductivity ($\mu S\ cm^{-1}$, total or bulk)	Activation Energy (eV)			Reference	
Parent oxide	Dopant	x	Preparation	Sintering temp. (°C)	Sintering time (h)	Density %	Gas	T test (°C)		Total	Grain Boundary	Bulk	Year	Author
$BaZr_{1-x}$	Er	0.05	SSRM	1500	40	-	N_2	600	5 (B)	0.46	-	-	2002	Laidoudi, Abu Talib, & Omar
	Ho								4 (B)	0.47				
	Y								1.8 (B)	0.45				
	Yb								10 (B)	0.46				
	Tm								4 (B)	0.51				
$BaZr_{1-x}$	In	0.05	SSRM	1650	10	-	H_2	600	200 (T)	-	-	-	1993	Iwahara et al.
$BaZr_{1-x}$	In	0.1	SSRM	1350	40	-	N_2	700	90 (T)	1.12	-	-	1993	Manthiram et al.
		0.2							300 (T)	0.83				
$BaZr_{1-x}$	Y	0.2	Sol Gel (SG)	1400	10	78.3	N_2	600	8600 (B)	0.66	-	-	2012	Sawant et al.
$BaZr_{1-x}$	Y	0.02	SSRM	1600	15	95	Air	700	500 (T)	1.21	-	-	2009	Kuz'min et al.
		0.05				90			900 (T)	0.99				
		0.1				95			2100 (T)	0.91				
		0.15				95			4000 (T)	0.84				

$BaZr_{1-x}$	Y	0.2	SSRM	1600	15	95	Air	700	5300 (T)	0.96	-	-	2009	Kuz'min et al.
$BaZr_{1-x}$	Y	0.02 0.15	SSRM	1800	1	~95	Air	700	500 (T) 600 (T)	-	-	-	2010	Gorelov et al.
$BaZr_{1-x}$	Y	0.07	SSRM	1650	10	57.7	Air N_2	600 600	4200 (T) 3800 (T)	-	-	-	2005	Wang & Virkar
$BaZr_{1-x}$	Y	0.01	SG	1700	24	95	N_2	376	50 (B)	-	1.17	0.4	2011	H. J. Park
$BaZr_{1-x}$	Y	0.2	SSRS (NiO sintering aid)	1450	5	95	Ar	600	3200 (T)	0.45	-	-	2015	Yoo et al.
$BaZr_{1-x}$	Y	0.2	GN	1600	24	99	N_2	600	8000 (T)	-	0.45	0.71	2007	Babilo et al.
$BaZr_{1-x}$	Y	0.2	SG	1600	24	>90	N_2	600	8100 (T)	-	0.66	0.46	2009	Yamazaki et al.
$BaZr_{1-x}$	Y	0.2	SG SG	800 1250	-	90.3 98.1	Ar	500	8.7 (T) 2000 (T)	0.79 0.59	-	-	2008	Cervera et al
$BaZr_{1-x}$	Y	0.2 0.3 0.4 0.5	SG	1600	12	90 - - -	H_2 H_2 H_2 H_2	625 625 625 625	900 (B) 400 (B) 200 (B) 70 (B)	0.62 0.62 0.63 0.62	0.69 0.73 0.75 0.78	0.44 0.44 0.46 0.49	2010	Fabbri et al.

1. 3. 1 Proton Conductivity in Barium Cerates & Zirconates

Large band gap perovskites such as barium cerates and zirconates will display almost purely proton conducting behaviour under low temperatures before the thermal population of the conduction band creates electron-hole pairs, and in hydrogen rich environments where the concentration of lattice protons is not limited by water or hydrogen availability in the surrounding atmosphere. In these conditions, the formation and migration of other charge carrier species (i.e. holes, oxide ions, and electrons) is supressed.[101]

Under such conditions, positively charged lattice hydroxyl groups ($OH_{\dot{o}}$) form by dissociative absorption of water via reaction with oxygen vacancies ($V_{\ddot{o}}$). Hydroxyl groups may also form by the reaction of dihydrogen with lattice oxide species. Scheme 3a & b show the formation of lattice OH groups in Kroger-Vink notation, from both water and hydrogen.

$$H_2O_{(g)} + V_{\ddot{o}} + O_o^x \rightarrow 2OH_{\dot{o}} \quad \text{(a)}$$

$$H_{2(g)} + 2O_o^x \rightarrow 2OH_{\dot{o}} + 2e' \quad \text{(b)}$$

Scheme 3: (a) Formation of OH groups by reaction of water with oxygen vacancy and lattice oxygen (b) dissolution of protons into crystal lattice by reaction of hydrogen and lattice oxide. Electro-neutrality maintained by loss of electrons

Oxygen vacancies can be formed intrinsically by varying the ratios of the main metals, such as the $Ba_{0.8}CeO_3$ material reported by Islam, Nag, & Basu and detailed in Table 1-2,[89] or extrinsically to compensate for doping of the cerium or zirconium sublattice. A higher concentration of oxygen vacancies will permit a higher maximum concentration of lattice hydroxyl groups, leading to a higher proton conductivity according to Equation 1.7.

Kreuer showed how under appropriate conditions, the maximum concentration of lattice hydroxyl groups is determined by the dopant concentration.[102] TGA curves were generated for range of simple (ABO_3) and complex perovskite oxides under gas flow with a constant humidity. $BaCe_{0.9}Y_{0.1}O_{3-\delta}$ and $BaZr_{0.9}Y_{0.1}O_{3-\delta}$ samples were both found to have hydration levels of 10%, the maximum permitted by the levels of yttrium doping. However, it should be noted that this holds only for cubic perovskites, where all oxygen sites are equivalent. Perovskites with less symmetric lattices do not show the same behaviour.

The actual concentration is determined by the Gibbs free energy of the hydration reaction (Equation 1.8), where K is the equilibrium constant of Scheme 3a (Equation 1.9).[101] The equilibrium constant is equivalent to the level of hydration of the lattice, as determined from the TGA curves. The hydration reaction shows Arrhenius type behaviour (the thermodynamic parameters are independent of temperature). Therefore, rearranging Equation 1.8 to Equation 1.10 allows the entropy (ΔS_{hyd}) and enthalpy (ΔH_{hyd}) of hydration to be calculated by plotting the natural logarithm of the equilibrium constant against the inverse of temperature, as shown in Figure 1-14.

$$\Delta G_{hyd} = -kT \ln K$$
$$= \Delta H_{hyd} - T\Delta S_{hyd} \qquad \textit{Equation 1.8}$$

$$K = \frac{[OH_{\ddot{o}}]^2}{[V_{\ddot{o}}][O_O^x]P_{H2O}} \qquad \textit{Equation 1.9}$$

$$ln\, K = \frac{\Delta S_{hyd}}{k} - \frac{\Delta H_{hyd}}{kT} \qquad \textit{Equation 1.10}$$

Kreuer et al suggested in 1996 that ΔH_{hyd} was dependant on the basicity of the lattice oxygen. As seen in Figure 1-14, the enthalpy of hydration becomes more exothermic with changing B-site cation in the order titanate < niobate < zirconate < stannate < cerate (original data reported by Kreuer in 1999).[102] This was attributed to decreasing basicity of the B-site cation, which in turn affects the oxygen basicity. Norby et al. reported in 2004 that the ΔH_{hyd} values of various ABO_3 perovskites correlated with the difference of electronegativity between the B and A site cations ($\Delta X_{B\text{-}A}$).

The values of ΔS_{hyd} are negative, meaning the reaction is entropically disfavoured. Kreuer reported that ΔS_{hyd} becomes more negative as the enthalpy change of hydration becomes more exothermic (determined from equilibrium constant measurements, of multiple perovskite oxides).[101] However, Norby et al reported that for a range of perovskite oxides, ΔS_{hyd} could not be correlated with other material parameters.[103] Measured values of ΔS_{hyd} were in the range of -120 ± 40 J mol^{-1} K^{-1}, in agreement with the empirical energy change from the loss of 1 gas molecule per unit reaction.[103]

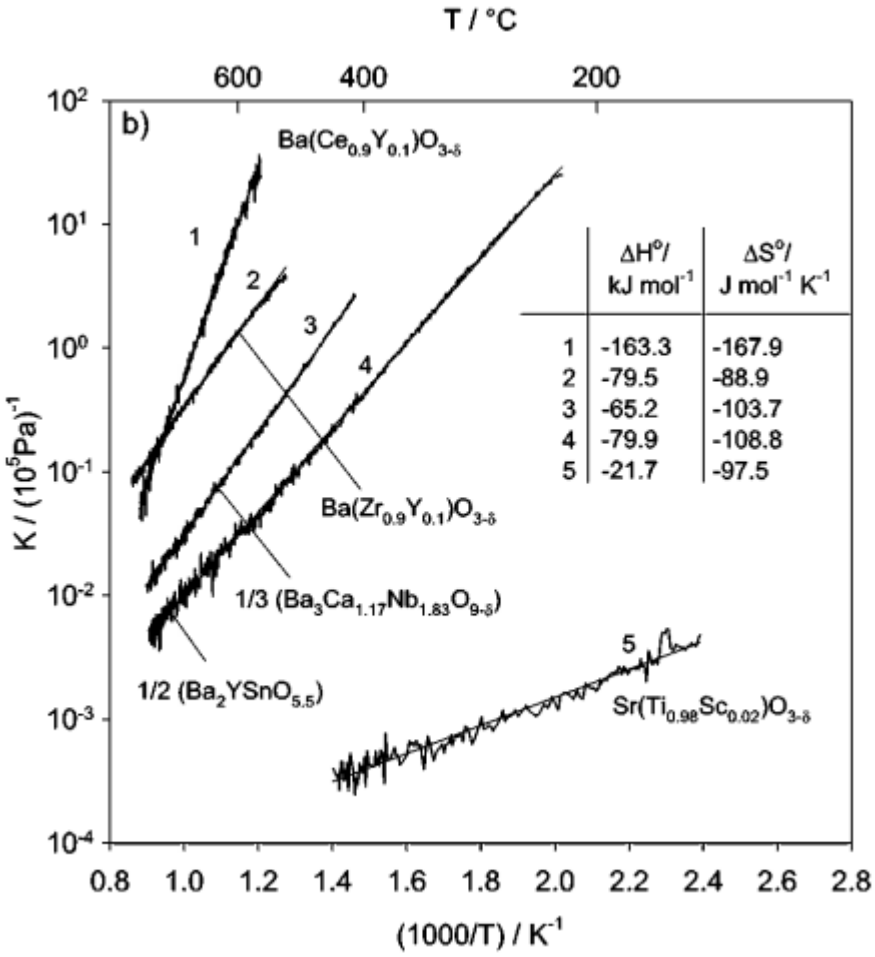


Figure 1-14: Calculated values of enthalpy and entropy change of reaction, as determined from plot. Reproduced from Kreuer.[101]

Once protons are present in the lattice in the form of lattice hydroxyl groups, they can move between adjacent lattice sites. The protons can 'hop' between adjacent oxide sites via the Grotthuss mechanism (Figure 1-15a).[104,105] This proton conduction can be observed at low temperature (below 100 ºC),[106] however for the proton flux to increase to useful levels, high temperatures between 300 – 600 ºC are required.

The mobility of the protons in the lattice has two components; the rotational diffusion of the protons around the oxide ions, and proton transfer to a neighbouring oxide, Figure 1-15b. The rotational diffusion has been shown to be a rapid process with a low energy barrier, indicating the rate limiting process is the proton transfer.[107] Yamazaki et al. examined the energies of the proton motion using an in-situ NMR experiment, reporting energies of 13 – 16 kJ mol^{-1} for proton rotational reorientation, and an energy of 29 kJ mol^{-1} to form a new hydrogen bond between YO_6 and ZrO_6 octahedra. The interaction between the proton and the oxide ion is strong, but the oxide ion maintains a stronger interaction with the parent lattice, so it is only the proton and not the OH group that transfers through the lattice.[76]

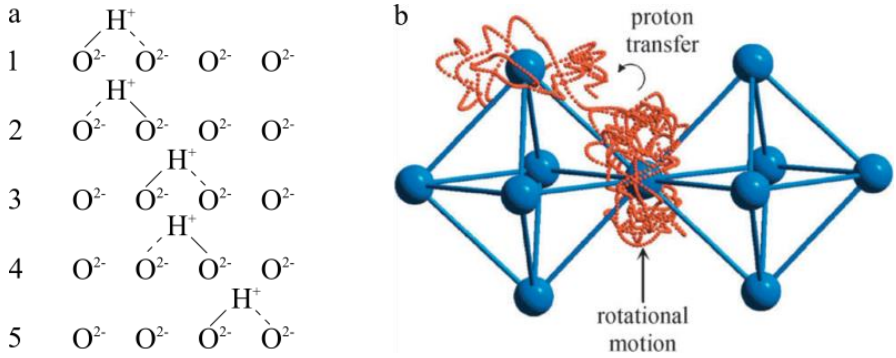


Figure 1-15: (a) Grotthuss mechanism of proton hopping through perovskite lattice. Redrawn from [96] (b) Proton motion within perovskite lattice. Reproduced from Malavasi et al.[108]

Kreuer wrote in 2000 that the exact mechanism of the transfer reaction is somewhat complex; while the reorientation process is rapid, strong hydrogen bond interactions have been measured between protons and oxide ion species.[109] To avoid breaking these strong bonds, a temporary structural reorientation of the lattice may occur, allowing a new hydrogen bond to be formed as the old one is broken. Therefore, vibrations of the oxide ions within the lattice can play an important role in the proton transfer.[76] Lattices with short distances between adjacent oxide ions will be more able to transfer protons in this manner. [101]

Proton conduction can be measured and reported as a raw value of proton conductance, expressed in units of Siemens. Usually this is scaled by cell dimensions by multiplying by the separation between the two electrolytes (electrolyte pellet thickness) and dividing by the surface area of the electrolyte pellet face, giving final units of Siemens per centimetre. To more easily compare between conductivities measured at different temperatures, the activation energy of proton conduction may be used. In conditions which the expression for total material conductivity (Equation 1.7) reduces to include only the term for proton conduction (Equation 1.11), proton mobility ($\mu_{H^\cdot}$) is related to the activation energy of proton transport by Equation 1.12.

$$\sigma = \frac{F}{V_m}[V_{H^\cdot}]\mu_{H^\cdot} \qquad \textit{Equation 1.11}$$

$$\mu_{H^\cdot} = \frac{\mu^0_{H^\cdot}}{T} exp\left(-\frac{E_{H^\cdot}}{kT}\right) \qquad \textit{Equation 1.12}$$

Protons proceed through the lattice in this manner until reaching a grain boundary. At this point, there is a different barrier to conduction. Therefore, proton conductivity is made up of two components: the grain interior (intra-grain) and grain boundary (inter-grain) conduction, each with a different activation energy. While material grains of a well sintered ceramic do not show an obvious physical separation, as observed in TEM images, the area between grains does not permit protonic conduction in the same manner as grain interiors. The difference between intra- and inter-grain conductivity can be several orders of magnitude.[106] Barium zirconate materials especially suffer from poor grain boundary conductivities.

Kreuer et al. wrote that the structural distortions from the bulk structure at grain boundaries, and the loss of cubic perovskite symmetry leads to the significant decrease in proton mobility.[101] Iguchi et al. modelled the conductivity at grain boundaries as a Mott-Schottky type space-charge layer. They found that proton concentration decreases when moving from the bulk to grain-boundary, as calculated from the Mott-Schottky model. The dopant concentration was observed, by STEM-EDS, to increase close to the grain boundary. Secondary phase formation was not observed at grain boundaries; therefore, it was proposed that the dopant cation (Y or Gd) replaces the Zr cation, without forming an oxygen vacancy. This leads to a build-up of negative charge and loss of oxygen vacancies. During sintering, a positively charged grain boundary core, an oxygen vacancy depletion layer and a negatively charged dopant accumulation layer are generated, Figure 1-16. This space-charge layer presents a significant barrier to proton conduction.

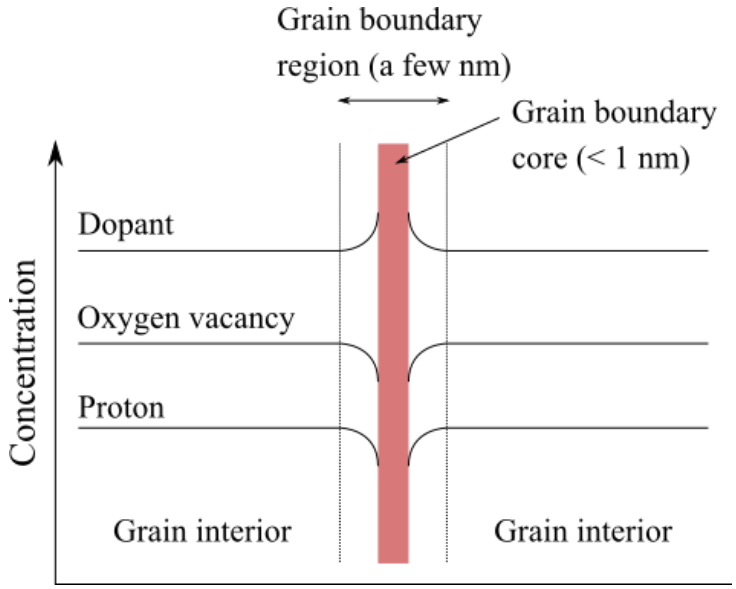


Figure 1-16: Concentration change of dopant ions, oxygen vacancies, and protons at the grain boundary region of barium zirconate ceramics. Redrawn from Iguchi et al.[110]

Doping strategies for barium zirconates and cerates centre around substitution of a minority of the B-site cation with an aliovalent cation. For a cation to be successfully doped into the lattice, it should create an oxygen vacancy without excessive disruption of the local crystal structure and electronic environment. This usually involves changing the 4+ Zr or Ce with a 3+ ion to generate an oxygen vacancy. The resulting structure will have the formula $BaM_{1-x}C_xO_{3-\delta}$, with M being either Zr or Ce, and δ representing the number of oxygen vacancies.

Kreuer et al. compared different barium zirconate dopants (Y, Gd, In, Sc), reporting that yttrium dopants performed best. It was observed that enthalpy of hydration and activation energy of proton transport are unchanged by presence of Y-dopant ions. Therefore, they concluded that the superior performance of these materials is due to the Y-dopant leaving the chemical environment almost unchanged.

Münch et al. compared the proton concentrations and mobilities of 10% Y doped $SrCeO_3$ and $BaCeO_3$. $SrCe_{0.9}Y_{0.1}O_{3-\delta}$ showed significant deviation away from ideal cubic perovskite structure, with much lower proton concentration and mobilities than $BaCe_{0.9}Y_{0.1}O_{3-\delta}$. The symmetry reduction leads to two distinct oxygen sites in the lattice, inhibiting the rotational orientation of the proton prior to transfer. In the aforementioned study by Kreuer, it was actually reported that Y-doped barium zirconate adopts a tetragonal crystal structure at doping levels between 10-20 %.[111] However the larger lattice constants (10% Y-BZ; a = 4.2151, c = 4.2047 and 10% In-BZ; a = 4.1989, c = 4.2022) of the Y-doped sample compared to others means the arrangement can occur while maintaining a close to cubic structure, and without reducing the proton solubility. The high lattice constant of barium zirconate, and covalency of the Zr-O bond also reduce repulsive Zr/H interactions.[111] Subsequent studies have, however, found using both electron and x-ray diffraction that pure cubic barium zirconate exists, even at 20% doping.[88]

Looking at Table 1-2 and Table 1-3: among reports which study the effect of doping level on conductivity (Islam, Nag, & Basu; Zhang et al.; Kuz'min et al.; Gorelov et al.; Fabbri et al.), in all cases it was concluded that doping levels of 10 – 20 % yield the highest conductivities.

When choosing between barium cerates and zirconates for study, the major consideration was the chemical stability. It is well known that barium cerates will react with gases such as CO_2 and H_2O to form multiple-phase materials, greatly reducing or completely nullifying the proton conductivity.[112,113] For this thesis it was decided to work only with perovskite structured barium zirconate materials or cerate/zirconate mixtures, due to their high intrinsic conductivity and stability.[73,106]

Barium zirconate does have a significant disadvantage compared to other proton conducting ceramics: as mentioned previously it has low inter-grain boundary conductivity. This value worsens in samples with more significant spatial gaps between adjacent grains.[106] It is generally accepted that this problem is largely due to the extreme conditions required to sinter barium zirconate into dense membranes, summarised in Table 1-3 and discussed further in Chapter 3. One proposed solution is to use mixed solid solutions of barium zirconate and cerate, creating a material with the benefits of both. Indeed, ultra-thin BCZY membranes are now commercially available.[114]

1. 4 Electrochemical Ammonia Synthesis

An alternative process to the energy intensive Haber-Bosch process has been proposed, where applied voltage provides the driving force for the reaction. This process has attracted increased interest in recent years, with the number of articles containing the phrase 'electrochemical ammonia synthesis' per year when searching the Scopus database rapidly accelerating, Figure 1-17. It will be shown how the hydrogen for ammonia can be directly provided from water, effectively integrating electrochemical hydrogen generation and dinitrogen reduction into a single process.

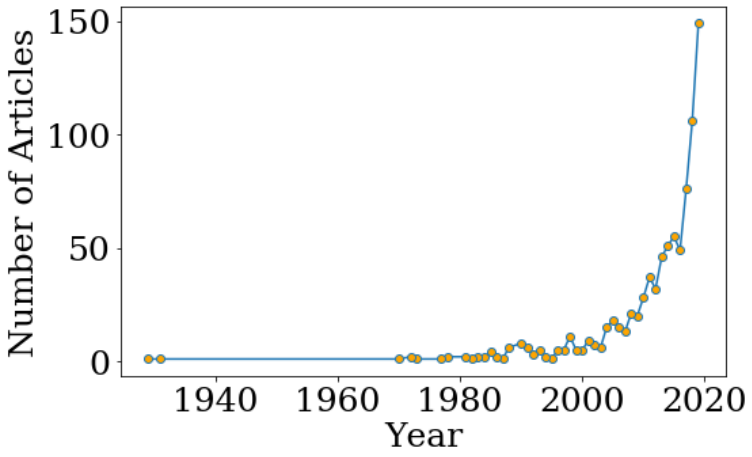


Figure 1-17: Results per year when searching the Scopus database for the phrase 'electrochemical ammonia synthesis'. Results shown up to 2019.

The recent explosion of published work, as well as previous articles has recently been comprehensively reviewed by a number of authors, including ourselves.[115–120] In our review all rates were compared to a target set by the U.S. Department of Energy (DOE) in a recent round of funding for their ARPA-E REFUEL program (current density >300 mA cm^{-2} and current efficiency >90%, which is an effective rate of 9.3×10^{-7} mol cm^{-2} $s^{-1)}$. Figure 1-18 shows graphically the rates, current density equivalents (at 100% efficiency), and current efficiencies of many literature reports for electrochemical ammonia synthesis. The data can be roughly grouped into systems operating at low (< 100 ºC), medium (100 – 400 ºC) and high (> 400 ºC) temperatures. Specific examples of these cells are discussed below.

Despite a large degree of scatter in the data, some trends emerge. Firstly, reported rates do not seem to increase with temperature although the reports with the highest current efficiency all come at temperatures of 400 ºC or greater. Secondly, despite significant effort, most reports fall below rates of 10^{-8} mols s^{-1} cm^{-2}. This corresponds to a current density of 3 mA cm^{-2} at 100% efficiency, far below the DOE target. Finally, very few articles report current efficiencies above 10%. This is attributed to the challenge of reducing the highly inert dinitrogen molecule in the presence of more easily reduced species, such as water or protons.

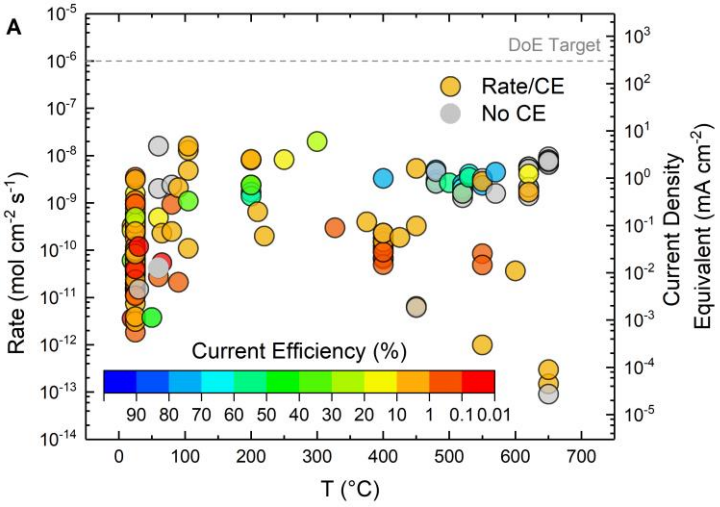


Figure 1-18: Graphical representation of rates and current efficiencies from literature reports of electrochemical ammonia synthesis. Full details of figure and references can be found in the review article.[120]

1. 4. 1 Cell & Electrode Design

To maximise the productivity of electrochemical cells, three elements must be considered; the anode & cathode which must be able to efficiently carry out the two electrochemical half-cell reactions, and the electrolyte, which must display the highest possible conductivity.

An interesting aspect of synthesis in electrochemical cells is the Non-Faradaic Electrochemical Modification of Catalytic Activity, or NEMCA, effect. Applying an electrical potential between a catalytic film and a counter electrode both in contact with an electrolyte has been shown to enhance catalytic rates by many orders of magnitude.[121] This is well beyond the rate enhancement expected due to directly supplying ionic species involved in the reaction. It is now accepted that this effect is due to spillover of ionic species from the electrolyte to the catalyst/electrolyte surface. A weak NEMCA effect has been documented for the electrochemical synthesis of ammonia using solid state electrolytes.[122]

1. 4. 1. A Cell Design

Electrochemical cells for ammonia synthesis tend to employ one of four reaction schemes (Figure 1-19). By far the most common geometry is direct reduction of N_2 at a cathode in the presence of H^+ (Figure 1-19a). The H is supplied by the electrolyte, either solid or liquid, and is generated at the anode by H_2O or H_2 oxidation. Significantly, the theoretical standard potential (where $P_{N2} = P_{NH3} = P_{O2} = 1$) of the N_2/NH_3 couple is slightly more positive than that of H^+/ H_2, providing a small window in which N_2 reduction is favoured over H_2 evolution (this window then increasing for P_{NH3} and $P_{O2} < 1$). The second type of cell involves non-proton coupled N_2 reduction at a cathode, forming the nitride ion, N^{3-}, with subsequent reaction of H_2O or H_2 occurring either at the anode or in the electrolyte (Figure 1-19b). Interestingly, the reaction between N_2 and H_2 (as opposed to H_2O) is spontaneous at room temperature, and only becomes slightly unfavourable at higher temperatures, providing very small theoretical potentials.[123] The third type of cell proposed involves reduction of Li at the cathode, which

itself is sufficiently reducing to reduce N_2 to Li_3N. This can subsequently react with a H^+ source, away from the cathode, to generate NH_3 (Figure 1-19c). While this approach has been suggested as a way to solve the competitive reduction of H_2O to H_2, there is a significant energy penalty for producing a more reduced species as an intermediate.[124] Finally, an alternative approach attempts to combine alkaline water electrolysis with N_2 sparging and a thermal NH_3 catalyst in one pot (Figure 1-19d). While the results are promising, the mechanism remains unclear.[125]

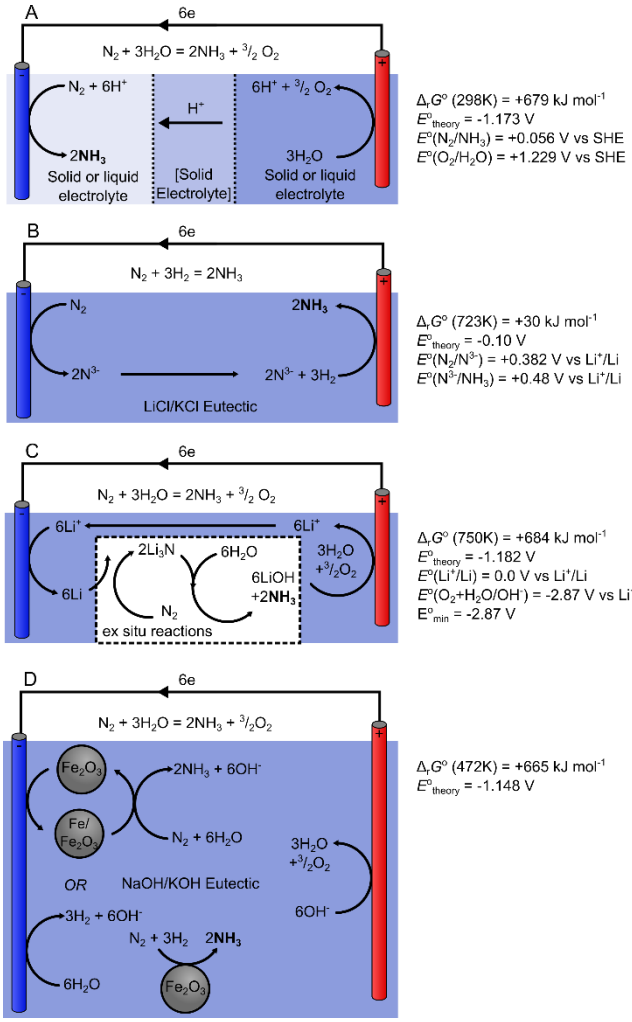


Figure 1-19: Cells reported for electrochemical NH_3 synthesis. Gibbs energies of reaction are calculated using FactSage,[126] except for B which uses literature values.[123] $E^o_{theory} = -\Delta_r G/nF$, where n is the number of electrons and F is the Faraday constant. $E^o(O_2/OH^-)$ is from a separate study.[127]

Our group has recently published work looking at the synthesis of ammonia in molten salts, as these present some of the most promising rates and current efficiencies in the literature.[128] However, this thesis focuses on the use of high-temperature proton conducting ceramic cells.

The cell design for high temperature proton conducting cells is relatively simple, although greatly complicated by the preparation of electrolyte materials, discussed in section 1. 3. 1 and Chapter 3. Cell designs can be roughly broken down into one of two designs: single or double chamber. In a single chamber cell, the anode and cathodes are subject to the same gas atmosphere. This has the advantage

of being easy to construct, but the major disadvantage of not being able to separate the anode and cathode gas streams. This results in the thermal production of ammonia, which may not be easy to deconvolute from the electrochemical production. It also means that both electrodes must be capable of operating under the same gas conditions. In contrast, double chamber cells present a real challenge to prepare; a gas tight seal must be made around the electrolyte, which must also have been well sintered to a gas-tight standard. However, if they can be prepared successfully, double chamber cells will very obviously highlight any electrochemical products, and additionally a difference in gas atmosphere between the two electrodes can be used to provide a chemical driving force for the electrode reactions and ion transport processes.

1. 4. 1. B Electrode Design

Catalysis at electrodes presents a particular challenge. In the case of electrochemical ammonia synthesis, three separate reactants (dinitrogen, protons, and electrons) must come together at a point in space, known as the triple phase boundary. The dinitrogen must be in a reduced state to stand any chance of reacting further, and the hydrogenation of reduced nitrogen will be much more facile if it can react directly with protons. It is also the case that protons on a cathode surface in the presence of electrons will be reduced to dihydrogen, resulting in a loss of efficiency.

Electrode catalysts for low temperature liquid cells have received the most attention thus far in literature. Several classes of catalyst have shown activity in these cells: those based on noble metals, those using transition metals, and those based on nitrogen-doped carbons. The recent surge in reports of catalysts for aqueous ammonia synthesis started with Au nanoparticle systems,[129,130] with the best Au nanoparticle catalyst based on a nanoporous graphitic carbon support.[131] A range of other Au nanomaterials have been tested and show moderate N_2 reduction rates, and in some cases higher current efficiencies.[129–133] Other noble metals such as Pt, Ru, Pd and Rh also show some activity for N_2 reduction, but often have very low current efficiency due to the competing HER.[134–138]

Metal nitrides have also attracted interest for electrochemical ammonia synthesis due to the possibility of a Mars-van Krevelen mechanism in which N from the lattice first reacts with H^+ to form NH_3, followed by regeneration of the resulting vacancy via dissociation of N_2.[33,139] Thermal ammonia synthesis via such a mechanism has been demonstrated with the ternary nitride Co_3Mo_3N,[32] and calculations suggest that the binary rock salt nitrides VN and ZrN should permit such a mechanism to be competitive with HER under aqueous conditions.[139]

Pure carbon materials represent a highly attractive class of catalyst, and metal-free N-doped carbons show high interest for several reactions in electrocatalysis, with N_2 reduction being no exception.[140] Materials formed from pyrolysis of the readily prepared zinc-based zeolitic imidazolate framework 8 (ZIF-8) provide a highly disordered but porous and nitrogen-doped carbon framework, and have been applied successfully to low-temperature electrochemical ammonia synthesis.[141]

For cells operating at higher temperatures, there has thus far been far less investigation into catalytic materials for use at the electrodes. Most reports using molten salt electrolytes have focussed on nickel foam electrodes, although as mentioned before the use of an iron oxide catalyst suspended in the melt has also been demonstrated. For ceramic electrolyte-based cells, many reported cells use metal pastes such as Ag-Pd. The use of noble metals is not essential, however, and catalysts based on Ni/ceramic composites (cermets e.g. Ni-$BaCe_{0.2}Zr_{0.7}Y_{0.1}O_{2.9}$, Ni-BCZY)[142–144], and even pure ceramics, such as $Ba_{0.5}Sr_{0.5}Co_{0.8}Fe_{0.2}O_{3-\delta}$ (BSCF),[145] have been reported to show similar rates.

It is important to note that these reported rates are normalized to a geometric surface area. For planar electrodes this is trivial, however for many technical electrodes such as nanoparticle composites, foams, and felts this area is somewhat arbitrary and may account for significant variations in their intrinsic rates.

1. 5 Project Aims

Reinvention of the current ammonia synthesis process is crucial to ensure a continued food supply for humanity, but at a much lower carbon footprint. The previously discussed agile ammonia synthesis setups would allow decarbonisation of the process, but given the intermittency of the energy supply could be difficult to run using iron catalysts, as discussed in Section 1. 2. 1. Ruthenium catalysts operating at lower pressures hold promise for this application. Current ruthenium catalysts are limited at the low temperatures required for agile synthesis by hydrogen poisoning. An alternative to the high-pressure heterogeneous reaction is the electrochemical reduction of dinitrogen to ammonia. This process could permit the integration of hydrogen generation and nitrogen reduction into the same system. From the electrochemical ammonia synthesis cells discussed *vide supra*, those based on a solid electrolyte operating at high temperatures show the most similarities to the Haber-Bosch process. Therefore, knowledge and insight about heterogeneous catalysts might be applied to develop these cells.

Barium zirconate ceramics can trap and conduct high concentrations of protons at elevated temperatures. This thesis first sets out to examine how applied potential can be used to modify proton concentrations and therefore electrochemical ammonia synthesis rates in barium zirconate cells.

Chapter 3 uses barium zirconate cells prepared in the lab and examines how processing conditions affect the sensitivity of the synthesis reaction towards applied potential. The outcome of processing conditions on cell morphology, conductivities, and electrochemical ammonia synthesis rates is presented. Similar investigations are carried out in Chapter 4, instead using a commercial barium zirconate material. Several electrocatalysts are applied and compared.

Emphasis then switches to looking at how proton-conducting supports may be used to alleviate hydrogen poisoning of ruthenium catalysts. As discussed in section 1. 2. 3, it has been previously shown how electride supports can reduce the hydrogen poisoning due to their ability to absorb hydrogen. The high proton conductivities of barium zirconate materials may facilitate a similar reduction in poisoning. Furthermore, barium zirconate powders are facile to prepare, making them suitable for use in an industrial process. Chapter 5 investigates how barium zirconates may be used as supports for ruthenium particles.

1. 6 Research Contributions

The key contributions of this thesis can be summarised as the following:

1. Demonstration of a silver catalyst which shows equivalent hydrogen-evolution reaction performance to a silver-platinum catalyst (Chapter 4).

2. Identification of weaknesses within the experimental methods commonly reported in literature for electrochemical ammonia synthesis. Specifically, the failure to report conversions or account for the conversion limit imposed by thermal equilibrium, and additionally the lack of reporting of leak rates in two-chamber cells (Chapter 4).

3. Preparation of Cs-promoted Ru catalysts on Y-doped barium zirconate supports showing synthesis rates among the highest in literature (Chapter 5).

4. Demonstration that Y-doped barium zirconate supports can reduce hydrogen poisoning of Ru catalysts (Chapter 5).

5. Identification of a hydrogen-spillover mechanism from ruthenium particles to Y-doped barium zirconate supports (Chapter 5).

The work in this thesis has been presented at two conferences: the 2016 UK Catalysis Conference, and the Materials Research Society winter meeting 2017.

The author has contributed to three papers during the thesis: a review on materials for electrochemical ammonia synthesis, a study on reduction of dinitrogen to ammonia in molten salt reactors, and an investigation of the ammonia synthesis reaction over lithium promoted ruthenium nanoparticles.[120,128,146]

1. 7 Acknowledgements

Sections of this introduction are based on a review article written jointly by Dr Ian McPherson, Dr Tim Sudmeier, and the author.

1. 8 References

(1) Apodaca, L. E. *Mineral Commodity Summaries*; Nitrogen (Fixed)- Ammonia; United States Geological Survey; 2018; pp 116–117.

(2) Smil, V. Detonator of the Population Explosion. *Nature* **1999**, *400* (6743), 415–415. https://doi.org/10.1038/22672.

(3) Schlögl, R. Ammonia Synthesis. In *Handbook of Heterogeneous Catalysis*; Ertl, G., Knözinger, H., Schüth, F., Weitkamp, J., Eds.; WILEY-VCH: Weinheim, Germany, 2008; Vol. 1, pp 2501–2575.

(4) Erisman, J. W.; Sutton, M. A.; Galloway, J.; Klimont, Z.; Winiwarter, W. How a Century of Ammonia Synthesis Changed the World. *Nat. Geosci.* **2008**, *1*, 636.

(5) Brown, T. Ammonia Production Causes 1% of Total Global GHG Emissions. *AMMONIA INDUSTRY*, 2016.

(6) Morgan, E.; Manwell, J.; McGowan, J. Wind-Powered Ammonia Fuel Production for Remote Islands: A Case Study. *Renew. Energy* **2014**, *72*, 51–61. https://doi.org/10.1016/j.renene.2014.06.034.

(7) Schlögl, R. Catalytic Synthesis of Ammonia—A "Never-Ending Story"? *Angew. Chem. Int. Ed.* **2003**, *42* (18), 2004–2008. https://doi.org/10.1002/anie.200301553.

(8) Bañares-Alcántara, R.; Dericks III, G.; Grünewald, P.; Masa Lopez, J.; Tsang, E.; Yang, A.; Ye, L.; Zhao, S. *Analysis of Islanded Ammonia-Based Energy Storage Systems*; University of Oxford: Oxford, 2015.

(9) Zamfirescu, C.; Dincer, I. Using Ammonia as a Sustainable Fuel. *J. Power Sources* **2008**, *185* (1), 459–465. https://doi.org/10.1016/j.jpowsour.2008.02.097.

(10) Elishav, O.; Lewin, D. R.; Shter, G. E.; Grader, G. S. The Nitrogen Economy: Economic Feasibility Analysis of Nitrogen-Based Fuels as Energy Carriers. *Appl. Energy* **2017**, *185*, 183–188. https://doi.org/10.1016/j.apenergy.2016.10.088.

(11) Christensen, L. J. Thermodynamic Properties in Ammonia Synthesis. In *Ammonia: Catalysis and Manufacture*; Nielsen, A., Ed.; Springer-Verlag: Berlin Heidelberg, 1995; pp 1–16.

(12) Rosowski, F.; Hornung, A.; Hinrichsen, O.; Herein, D.; Muhler, M.; Ertl, G. Ruthenium Catalysts for Ammonia Synthesis at High Pressures: Preparation, Characterization, and Power-Law Kinetics. *Appl. Catal. Gen.* **1997**, *151* (2), 443–460. https://doi.org/10.1016/S0926-860X(96)00304-3.

(13) Ertl, G.; Huber, M.; Lee, S. B.; Paál, Z.; Weiss, M. Interactions of Nitrogen and Hydrogen on Iron Surfaces. *Appl. Surf. Sci.* **1981**, *8* (4), 373–386. https://doi.org/10.1016/0378-5963(81)90092-1.

(14) Haber, F. The Hurter Memorial Lecture. "Modern Chemical Industry." *J. Soc. Chem. Ind.* **1914**, *33* (2), 49–54. https://doi.org/10.1002/jctb.5000330201.

(15) Liu, H. Ammonia Synthesis Catalyst 100 Years: Practice, Enlightenment and Challenge. *Chin. J. Catal.* **2014**, *35* (10), 1619–1640. https://doi.org/10.1016/S1872-2067(14)60118-2.

(16) Dybkjaer, I. Ammonia Production Processes. In *Ammonia: Catalysis and Manufacture*; Nielsen, A., Ed.; Springer-Verlag: Berlin Heidelberg, 1995; pp 199–328.

(17) Schlögl, R. Heterogeneous Catalysis. *Angew. Chem. Int. Ed.* **2015**, *54* (11), 3465–3520. https://doi.org/10.1002/anie.201410738.

(18) Boudart, M. Heterogeneous Catalysis by Metals. *J. Mol. Catal.* **1985**, *30* (1), 27–38. https://doi.org/10.1016/0304-5102(85)80014-6.

(19) Spencer, M. S. On the Rate-Determining Step and the Role of Potassium in the Catalytic Synthesis of Ammonia. *Catal. Lett.* **1992**, *13* (1), 45–53. https://doi.org/10.1007/BF00770946.

(20) Bozso, F.; Ertl, G.; Grunze, M.; Weiss, M. Interaction of Nitrogen with Iron Surfaces. *J. Catal.* **1977**, *49* (1), 18–41. https://doi.org/10.1016/0021-9517(77)90237-8.

(21) Bozso, F.; Ertl, G.; Weiss, M. Interaction of Nitrogen with Iron Surfaces: II. Fe(110). *J. Catal.* **1977**, *50* (3), 519–529. https://doi.org/10.1016/0021-9517(77)90063-X.

(22) Ertl, G.; Lee, S. B.; Weiss, M. Kinetics of Nitrogen Adsorption on Fe(111). *Surf. Sci.* **1982**, *114* (2), 515–526. https://doi.org/10.1016/0039-6028(82)90702-6.

(23) Imbihl, R.; Behm, R. J.; Ertl, G.; Moritz, W. The Structure of Atomic Nitrogen Adsorbed on Fe(100). *Surf. Sci.* **1982**, *123* (1), 129–140. https://doi.org/10.1016/0039-6028(82)90135-2.

(24) Ertl, G.; Thiele, N. XPS Studies with Ammonia Synthesis Catalysts. *Appl. Surf. Sci.* **1979**, *3* (1), 99–112. https://doi.org/10.1016/0378-5963(79)90064-3.

(25) Spencer, N. Iron Single Crystals as Ammonia Synthesis Catalysts: Effect of Surface Structure on Catalyst Activity. *J. Catal.* **1982**, *74* (1), 129–135. https://doi.org/10.1016/0021-9517(82)90016-1.

(26) Primary Steps in Catalytic Synthesis of Ammonia. *J. Vac. Sci. Technol. Vac. Surf. Films* **1983**, *1* (2), 1247–1253. https://doi.org/10.1116/1.572299.

(27)The Nobel Prize in Chemistry 2007
https://www.nobelprize.org/prizes/chemistry/2007/summary/ (accessed Oct 13, 2019).

(28) Medford, A. J.; Vojvodic, A.; Hummelshøj, J. S.; Voss, J.; Abild-Pedersen, F.; Studt, F.; Bligaard, T.; Nilsson, A.; Nørskov, J. K. From the Sabatier Principle to a Predictive Theory of Transition-Metal Heterogeneous Catalysis. *J. Catal.* **2015**, *328*, 36–42. https://doi.org/10.1016/j.jcat.2014.12.033.

(29) Brown, D. E.; Edmonds, T.; Joyner, R. W.; McCarroll, J. J.; Tennison, S. R. The Genesis and Development of the Commercial BP Doubly Promoted Catalyst for Ammonia Synthesis. *Catal. Lett.* **2014**, *144* (4), 545–552. https://doi.org/10.1007/s10562-014-1226-4.

(30) Jacobsen, C. J. H.; Dahl, S.; Clausen, B. S.; Bahn, S.; Logadottir, A.; Nørskov, J. K. Catalyst Design by Interpolation in the Periodic Table: Bimetallic Ammonia Synthesis Catalysts. *J. Am. Chem. Soc.* **2001**, *123* (34), 8404–8405. https://doi.org/10.1021/ja010963d.

(31) Kojima, R.; Aika, K. Cobalt Molybdenum Bimetallic Nitride Catalysts for Ammonia Synthesis. *Chem. Lett.* **2000**, *29* (5), 514–515. https://doi.org/10.1246/cl.2000.514.

(32) Hunter, S. M.; Mckay, D.; Smith, R. I.; Hargreaves, J. S. J.; Gregory, D. H. Topotactic Nitrogen Transfer: Structural Transformation in Cobalt Molybdenum Nitrides. *Chem. Mater.* **2010**, *22* (9), 2898–2907. https://doi.org/10.1021/cm100208a.

(33) Zeinalipour-Yazdi, C. D.; Hargreaves, J. S. J.; Catlow, C. R. A. Nitrogen Activation in a Mars–van Krevelen Mechanism for Ammonia Synthesis on Co3Mo3N. *J. Phys. Chem. C* **2015**. https://doi.org/10.1021/acs.jpcc.5b06811.

(34) Kandemir, T.; Schuster, M. E.; Senyshyn, A.; Behrens, M.; Schlögl, R. The Haber-Bosch Process Revisited: On the Real Structure and Stability of "Ammonia Iron" under Working Conditions. *Angew. Chem. Int. Ed.* **2013**, *52* (48), 12723–12726. https://doi.org/10.1002/anie.201305812.

(35) Strongin, D. The Importance of C7 Sites and Surface Roughness in the Ammonia Synthesis Reaction over Iron. *J. Catal.* **1987**, *103* (1), 213–215. https://doi.org/10.1016/0021-9517(87)90109-6.

(36) Ertl, G.; Prigge, D.; Schloegl, R.; Weiss, M. Surface Characterization of Ammonia Synthesis Catalysts. *J. Catal.* **1983**, *79* (2), 359–377. https://doi.org/10.1016/0021-9517(83)90330-5.

(37) Paál, Z.; Ertl, G.; Lee, S. B. Interactions of Potassium, Oxygen and Nitrogen with Polycrystalline Iron Surfaces. *Appl. Surf. Sci.* **1981**, *8* (3), 231–249. https://doi.org/10.1016/0378-5963(81)90119-7.

(38) Boudart, M.; Delbouille, A.; Dumesic, J. A.; Khammouma, S.; Topsøe, H. Surface, Catalytic and Magnetic Properties of Small Iron Particles: I. Preparation and Characterization of Samples. *J. Catal.* **1975**, *37* (3), 486–502. https://doi.org/10.1016/0021-9517(75)90184-0.

(39) Dumesic, J. A.; Topsøe, H.; Khammouma, S.; Boudart, M. Surface, Catalytic and Magnetic Properties of Small Iron Particles: II. Structure Sensitivity of Ammonia Synthesis. *J. Catal.* **1975**, *37* (3), 503–512. https://doi.org/10.1016/0021-9517(75)90185-2.

(40) Dumesic, J. A.; Topsøe, H.; Boudart, M. Surface, Catalytic and Magnetic Properties of Small Iron Particles: III. Nitrogen Induced Surface Reconstruction. *J. Catal.* **1975**, *37* (3), 513–522. https://doi.org/10.1016/0021-9517(75)90186-4.

(41) Brill, R.; Richter, E.-L.; Ruch, E. Adsorption of Nitrogen on Iron. *Angew. Chem. Int. Ed. Engl.* **1967**, *6* (10), 882–883. https://doi.org/10.1002/anie.196708822.

(42) Falicov, L. M.; Somorjai, G. A. Correlation between Catalytic Activity and Bonding and Coordination Number of Atoms and Molecules on Transition Metal Surfaces: Theory and Experimental Evidence. *Proc. Natl. Acad. Sci.* **1985**, *82* (8), 2207–2211. https://doi.org/10.1073/pnas.82.8.2207.

(43) Kuznetsov, B. N.; Perov, V. M.; Alekseev, A. M.; Yakerson, V. I. XPS Study of the Surface Composition of a Catalytic System: Iron Promoted by Potassium and Aluminum Oxides. *Kinet. Catal.* **2001**, *42* (1), 92–96. https://doi.org/10.1023/A:1004809014917.

(44) Ertl, G.; Lee, S. B.; Weiss, M. Adsorption of Nitrogen on Potassium Promoted Fe(111) and (100) Surfaces. *Surf. Sci.* **1982**, *114* (2), 527–545. https://doi.org/10.1016/0039-6028(82)90703-8.

(45) Liu, H.-Z.; Li, X.-N.; Hu, Z.-N. Development of Novel Low Temperature and Low Pressure Ammonia Synthesis Catalyst. *Appl. Catal. Gen.* **1996**, *142* (2), 209–222. https://doi.org/10.1016/0926-860X(96)00047-6.

(46) Lendzion-Bieluñ, Z.; Arabczyk, W.; Figurski, M. The Effect of the Iron Oxidation Degree on Distribution of Promotors in the Fused Catalyst Precursors and Their Activity in the Ammonia Synthesis Reaction. *Appl. Catal. Gen.* **2002**, *227* (1), 255–263. https://doi.org/10.1016/S0926-860X(01)00938-3.

(47) Pernicone, N.; Ferrero, F.; Rossetti, I.; Forni, L.; Canton, P.; Riello, P.; Fagherazzi, G.; Signoretto, M.; Pinna, F. Wustite as a New Precursor of Industrial Ammonia Synthesis Catalysts. *Appl. Catal. Gen.* **2003**, *251* (1), 121–129. https://doi.org/10.1016/S0926-860X(03)00313-2.

(48) Egeberg, R. C.; Dahl, S.; Logadottir, A.; Larsen, J. H.; Nørskov, J. K.; Chorkendorff, I. N2 Dissociation on Fe(110) and Fe/Ru(0001): What Is the Role of Steps? *Surf. Sci.* **2001**, *491* (1), 183–194. https://doi.org/10.1016/S0039-6028(01)01397-8.

(49) Mortensen, J. J.; Hansen, L. B.; Hammer, B.; Nørskov, J. K. Nitrogen Adsorption and Dissociation on Fe(111). *J. Catal.* **1999**, *182* (2), 479–488. https://doi.org/10.1006/jcat.1998.2364.

(50) Mortensen, J. J.; Ganduglia-Pirovano, M. V.; Hansen, L. B.; Hammer, B.; Stoltze, P.; Nørskov, J. K. Nitrogen Adsorption on Fe(111), (100), and (110) Surfaces. *Surf. Sci.* **1999**, *422* (1), 8–16. https://doi.org/10.1016/S0039-6028(98)00802-4.

(51) You, Z.; Inazu, K.; Aika, K.; Baba, T. Electronic and Structural Promotion of Barium Hexaaluminate as a Ruthenium Catalyst Support for Ammonia Synthesis. *J. Catal.* **2007**, *251* (2), 321–331. https://doi.org/10.1016/j.jcat.2007.08.006.

(52) Miyazaki, A.; Balint, I.; Aika, K.; Nakano, Y. Preparation of Ru Nanoparticles Supported on γ-Al2O3 and Its Novel Catalytic Activity for Ammonia Synthesis. *J. Catal.* **2001**, *204* (2), 364–371. https://doi.org/10.1006/jcat.2001.3418.

(53) Zhong, Z.; Aika, K. Effect of Ruthenium Precursor on Hydrogen-Treated Active Carbon Supported Ruthenium Catalysts for Ammonia Synthesis. *Inorganica Chim. Acta* **1998**, *280* (1), 183–188. https://doi.org/10.1016/S0020-1693(98)00202-3.

(54) Aika, K.; Kawahara, T.; Murata, S.; Onishi, T. Promoter Effect of Alkali Metal Oxides and Alkali Earth Metal Oxides on Active Carbon-Supported Ruthenium Catalyst for Ammonia Synthesis. *Bull. Chem. Soc. Jpn.* **1990**, *63* (4), 1221–1225. https://doi.org/10.1246/bcsj.63.1221.

(55) Raróg-Pilecka, W.; Miśkiewicz, E.; Jodzis, S.; Petryk, J.; Łomot, D.; Kaszkur, Z.; Karpiński, Z.; Kowalczyk, Z. Carbon-Supported Ruthenium Catalysts for NH3 Synthesis Doped with Caesium Nitrate: Activation Process, Working State of Cs–Ru/C. *J. Catal.* **2006**, *239* (2), 313–325. https://doi.org/10.1016/j.jcat.2006.01.035.

(56) Dahl, S.; Törnqvist, E.; Chorkendorff, I. Dissociative Adsorption of N2 on Ru(0001): A Surface Reaction Totally Dominated by Steps. *J. Catal.* **2000**, *192* (2), 381–390. https://doi.org/10.1006/jcat.2000.2858.

(57) Saadatjou, N.; Jafari, A.; Sahebdelfar, S. Ruthenium Nanocatalysts for Ammonia Synthesis: A Review. *Chem. Eng. Commun.* **2015**, *202* (4), 420–448. https://doi.org/10.1080/00986445.2014.923995.

(58) Jacobsen, C. J. H.; Dahl, S.; Hansen, P. L.; Törnqvist, E.; Jensen, L.; Topsøe, H.; Prip, D. V.; Møenshaug, P. B.; Chorkendorff, I. Structure Sensitivity of Supported Ruthenium Catalysts for Ammonia Synthesis. *J. Mol. Catal. Chem.* **2000**, *163* (1), 19–26. https://doi.org/10.1016/S1381-1169(00)00396-4.

(59) van Hardeveld, R.; van Montfoort, A. The Influence of Crystallite Size on the Adsorption of Molecular Nitrogen on Nickel, Palladium and Platinum: An Infrared and Electron-Microscopic Study. *Surf. Sci.* **1966**, *4* (4), 396–430. https://doi.org/10.1016/0039-6028(66)90016-1.

(60) Zambelli, T.; Wintterlin, J.; Trost, J.; Ertl, G. Identification of the "Active Sites" of a Surface-Catalyzed Reaction. *Science* **1996**, *273* (5282), 1688–1690. https://doi.org/10.1126/science.273.5282.1688.

(61) Hinrichsen, O.; Hornung, A.; Muhler, M. Modeling of Temperature-Programmed Surface Reactions. *Chem. Eng. Technol.* **1999**, *22* (12), 1039–1042. https://doi.org/10.1002/(SICI)1521-4125(199912)22:12<1039::AID-CEAT1039>3.0.CO;2-5.

(62) Hinrichsen, O.; Rosowski, F.; Hornung, A.; Muhler, M.; Ertl, G. The Kinetics of Ammonia Synthesis over Ru-Based Catalysts. *J. Catal.* **1997**, *165* (1), 33–44. https://doi.org/10.1006/jcat.1997.1447.

(63) Dietrich, H.; Geng, P.; Jacobi, K.; Ertl, G. Sticking Coefficient for Dissociative Adsorption of N2 on Ru Single-crystal Surfaces. *J. Chem. Phys.* **1996**, *104* (1), 375–381. https://doi.org/10.1063/1.470836.

(64) Aika, K.; Ohya, A.; Ozaki, A.; Inoue, Y.; Yasumori, I. Support and Promoter Effect of Ruthenium Catalyst: II. Ruthenium/Alkaline Earth Catalyst for Activation of Dinitrogen. *J. Catal.* **1985**, *92* (2), 305–311. https://doi.org/10.1016/0021-9517(85)90265-9.

(65) Aika, K.; Kumasaka, M.; Oma, T.; Kato, O.; Matsuda, H.; Watanabe, N.; Yamazaki, K.; Ozaki, A.; Onishi, T. Support and Promoter Effect of Ruthenium Catalyst. III. Kinetics of Ammonia Synthesis over Various Ru Catalysts. *Appl. Catal.* **1986**, *28*, 57–68. https://doi.org/10.1016/S0166-9834(00)82492-6.

(66) Rambeau, G.; Amariglio, H. Ammonia Synthesis on Ruthenium Powder from 100 to 500 °C and Hydrogenation of Preadsorbed Nitrogen down to −70 °C. *J. Catal.* **1981**, *72* (1), 1–11. https://doi.org/10.1016/0021-9517(81)90071-3.

(67) Aika, K. I. Ammonia Synthesis over Non-Iron Catalysts and Related Phenomena. In *Ammonia: Catalysis and Manufacture*; Nielsen, A., Ed.; Springer-Verlag: Berlin Heidelberg, 1995; pp 199–328.

(68) Urabe, K.; Aika, K.-I.; Ozaki, A. Activation of Nitrogen by Alkali Metal-Promoted Transition Metal: VI. Hydrogen Effect on Isotopic Equilibration of Nitrogen and Rate-Determining Step of Ammonia Synthesis on Potassium-Promoted Ruthenium Catalysts. *J. Catal.* **1976**, *42* (2), 197–204. https://doi.org/10.1016/0021-9517(76)90253-0.

(69) Kitano, M.; Inoue, Y.; Yamazaki, Y.; Hayashi, F.; Kanbara, S.; Matsuishi, S.; Yokoyama, T.; Kim, S.-W.; Hara, M.; Hosono, H. Ammonia Synthesis Using a Stable Electride as an Electron Donor and Reversible Hydrogen Store. *Nat. Chem.* **2012**, *4* (11), 934–940. https://doi.org/10.1038/nchem.1476.

(70) Kitano, M.; Kanbara, S.; Inoue, Y.; Kuganathan, N.; Sushko, P. V.; Yokoyama, T.; Hara, M.; Hosono, H. Electride Support Boosts Nitrogen Dissociation over Ruthenium Catalyst and Shifts the Bottleneck in Ammonia Synthesis. *Nat. Commun.* **2015**, *6*, 6731. https://doi.org/10.1038/ncomms7731.

(71) Inoue, Y.; Kitano, M.; Kishida, K.; Abe, H.; Niwa, Y.; Sasase, M.; Fujita, Y.; Ishikawa, H.; Yokoyama, T.; Hara, M.; Hosono, H. Efficient and Stable Ammonia Synthesis by Self-Organized Flat Ru Nanoparticles on Calcium Amide. *ACS Catal.* **2016**, *6* (11), 7577–7584. https://doi.org/10.1021/acscatal.6b01940.

(72) Kitano, M.; Inoue, Y.; Sasase, M.; Kishida, K.; Kobayashi, Y.; Nishiyama, K.; Tada, T.; Kawamura, S.; Yokoyama, T.; Hara, M.; Hosono, H. Self-Organized Ruthenium–Barium Core–Shell Nanoparticles on a Mesoporous Calcium Amide Matrix for Efficient Low-Temperature Ammonia Synthesis. *Angew. Chem.* **2018**, *130* (10), 2678–2682. https://doi.org/10.1002/ange.201712398.

(73) Fabbri, E.; Bi, L.; Pergolesi, D.; Traversa, E. Towards the Next Generation of Solid Oxide Fuel Cells Operating Below 600 °C with Chemically Stable Proton-Conducting Electrolytes. *Adv. Mater.* **2012**, *24* (2), 195–208. https://doi.org/10.1002/adma.201103102.

(74) Phair, J. W.; Badwal, S. P. S. Review of Proton Conductors for Hydrogen Separation. *Ionics* **2006**, *12* (2), 103–115. https://doi.org/10.1007/s11581-006-0016-4.

(75) Iwahara, H.; Esaka, T.; Uchida, H.; Maeda, N. Proton Conduction in Sintered Oxides and Its Application to Steam Electrolysis for Hydrogen Production. *Solid State Ion.* **1981**, *3–4*, 359–363. https://doi.org/10.1016/0167-2738(81)90113-2.

(76) Kochetova, N.; Animitsa, I.; Medvedev, D.; Demin, A.; Tsiakaras, P. Recent Activity in the Development of Proton-Conducting Oxides for High-Temperature Applications. *RSC Adv.* **2016**, *6* (77), 73222–73268. https://doi.org/10.1039/C6RA13347A.

(77) Eufinger, J.-P.; Schmidt, A.; Lerch, M.; Janek, J. Novel Anion Conductors – Conductivity, Thermodynamic Stability and Hydration of Anion-Substituted Mayenite-Type Cage Compounds C 12 A 7 :X (X = O, OH, Cl, F, CN, S, N). *Phys. Chem. Chem. Phys.* **2015**, *17* (10), 6844–6857. https://doi.org/10.1039/C4CP05442C.

(78) Fabbri, E.; Bi, L.; Tanaka, H.; Pergolesi, D.; Traversa, E. Chemically Stable Pr and Y Co-Doped Barium Zirconate Electrolytes with High Proton Conductivity for Intermediate-Temperature Solid Oxide Fuel Cells. *Adv. Funct. Mater.* **2011**, *21* (1), 158–166. https://doi.org/10.1002/adfm.201001540.

(79) Pergolesi, D.; Fabbri, E.; D'Epifanio, A.; Di Bartolomeo, E.; Tebano, A.; Sanna, S.; Licoccia, S.; Balestrino, G.; Traversa, E. High Proton Conduction in Grain-Boundary-Free Yttrium-Doped Barium Zirconate Films Grown by Pulsed Laser Deposition. *Nat. Mater.* **2010**, *9* (10), 846–852. https://doi.org/10.1038/nmat2837.

(80) Bohn, H. G.; Schober, T. Electrical Conductivity of the High-Temperature Proton Conductor BaZr0.9Y0.1O2.95. *J. Am. Ceram. Soc.* **2000**, *83* (4), 768–772. https://doi.org/10.1111/j.1151-2916.2000.tb01272.x.

(81) Schober, T.; Bohn, H. G. Water Vapor Solubility and Electrochemical Characterization of the High Temperature Proton Conductor BaZr0.9Y0.1O2.95. *Solid State Ion.* **2000**, *127* (3), 351–360. https://doi.org/10.1016/S0167-2738(99)00283-0.

(82) Kreuer, K. D.; Münch, W.; Traub, U.; Maier, J. On Proton Transport in Perovskite-Type Oxides and Plastic Hydroxides. *Berichte Bunsenges. Für Phys. Chem.* **1998**, *102* (3), 552–559. https://doi.org/10.1002/bbpc.19981020339.

(83) Laidoudi, M.; Talib, I. A.; Omar, R. Investigation of the Bulk Conductivity of BaZr0.95M0.05O3-α (M =Al, Er, Ho, Tm, Yb and Y) under Wet N2. *J. Phys. Appl. Phys.* **2002**, *35* (4), 397. https://doi.org/10.1088/0022-3727/35/4/316.

(84) Gorelov, V. P.; Balakireva, V. B.; Kuz'min, A. V. Ionic, Proton, and Oxygen Conductivities in the BaZr1 − XYxO3 − α System (x = 0.02−0.15) in Humid Air. *Russ. J. Electrochem.* **2010**, *46* (8), 890–895. https://doi.org/10.1134/S1023193510080057.

(85) Amsif, M.; Marrero-Lopez, D.; Ruiz-Morales, J. C.; Savvin, S. N.; Gabás, M.; Nunez, P. Influence of Rare-Earth Doping on the Microstructure and Conductivity of BaCe0.9Ln0.1O3−δ Proton Conductors. *J. Power Sources* **2011**, *196* (7), 3461–3469. https://doi.org/10.1016/j.jpowsour.2010.11.120.

(86) Zhang, C.; Zhao, H.; Zhai, S. Electrical Conduction Behavior of Proton Conductor BaCe1-XSmxO3-δ in the Intermediate Temperature Range. *Int. J. Hydrog. Energy* **2011**, *36* (5), 3649–3657. https://doi.org/10.1016/j.ijhydene.2010.12.087.

(87) Yoo, C.-Y.; Yun, D. S.; Joo, J. H.; Yu, J. H. The Effects of NiO Addition on the Structure and Transport Properties of Proton Conducting BaZr0.8Y0.2O3−δ. *J. Alloys Compd.* **2015**, *621*, 263–267. https://doi.org/10.1016/j.jallcom.2014.09.207.

(88) Cervera, R. B.; Oyama, Y.; Miyoshi, S.; Kobayashi, K.; Yagi, T.; Yamaguchi, S. Structural Study and Proton Transport of Bulk Nanograined Y-Doped BaZrO3 Oxide Protonics Materials. *Solid State Ion.* **2008**, *179* (7), 236–242. https://doi.org/10.1016/j.ssi.2008.01.082.

(89) Islam, Q. A.; Nag, S.; Basu, R. N. Electrical Properties of Tb-Doped Barium Cerate. *Ceram. Int.* **2013**, *39* (6), 6433–6440. https://doi.org/10.1016/j.ceramint.2013.01.071.

(90) Kuz'min, A. V.; Balakireva, V. B.; Plaksin, S. V.; Gorelov, V. P. Total and Hole Conductivity in the BaZr1 − XYxO3 − α System (x = 0.02−0.20) in Oxidizing Atmosphere. *Russ. J. Electrochem.* **2009**, *45* (12), 1351–1357. https://doi.org/10.1134/S1023193509120064.

(91) Yamazaki, Y.; Hernandez-Sanchez, R.; Haile, S. M. High Total Proton Conductivity in Large-Grained Yttrium-Doped Barium Zirconate. *Chem. Mater.* **2009**, *21* (13), 2755–2762. https://doi.org/10.1021/cm900208w.

(92) Babilo, P.; Uda, T.; Haile, S. M. Processing of Yttrium-Doped Barium Zirconate for High Proton Conductivity. *J. Mater. Res.* **2007**, *22* (05), 1322–1330. https://doi.org/10.1557/jmr.2007.0163.

(93) Fabbri, E.; Pergolesi, D.; Licoccia, S.; Traversa, E. Does the Increase in Y-Dopant Concentration Improve the Proton Conductivity of BaZr1−xYxO3−δ Fuel Cell Electrolytes? *Solid State Ion.* **2010**, *181* (21), 1043–1051. https://doi.org/10.1016/j.ssi.2010.06.007.

(94) Pasierb, P.; Wierzbicka, M.; Komornicki, S.; Rekas, M. Electrochemical Impedance Spectroscopy of BaCeO3 Modified by Ti and Y. *J. Power Sources* **2009**, *194* (1), 31–37. https://doi.org/10.1016/j.jpowsour.2009.01.098.

(95) Katahira, K.; Kohchi, Y.; Shimura, T.; Iwahara, H. Protonic Conduction in Zr-Substituted BaCeO3. *Solid State Ion.* **2000**, *138* (1), 91–98. https://doi.org/10.1016/S0167-2738(00)00777-3.

(96) Iwahara, H.; Yajima, T.; Hibino, T.; Ozaki, K.; Suzuki, H. Protonic Conduction in Calcium, Strontium and Barium Zirconates. *Solid State Ion.* **1993**, *61* (1), 65–69. https://doi.org/10.1016/0167-2738(93)90335-Z.

(97) Manthiram, A.; Kuo, J. F.; Goodenough, J. B. Characterization of Oxygen-Deficient Perovskites as Oxide-Ion Electrolytes. *Solid State Ion.* **1993**, *62* (3), 225–234. https://doi.org/10.1016/0167-2738(93)90376-E.

(98) Sawant, P.; Varma, S.; Wani, B. N.; Bharadwaj, S. R. Synthesis, Stability and Conductivity of BaCe0.8−xZrxY0.2O3−δ as Electrolyte for Proton Conducting SOFC. *Int. J. Hydrog. Energy* **2012**, *37* (4), 3848–3856. https://doi.org/10.1016/j.ijhydene.2011.04.106.

(99) Wang, W.; Virkar, A. V. Ionic and Electron–Hole Conduction in BaZr0.93Y0.07O3−δ by 4-Probe Dc Measurements. *J. Power Sources* **2005**, *142* (1), 1–9. https://doi.org/10.1016/j.jpowsour.2004.09.031.

(100) Park, H. J. Electrical Properties of the Protonic Conductor 1 Mol% Y-Doped $$ {\hbox{BaZr}}{{\hbox{O}}_{{3 - \delta }}} $$. *J. Solid State Electrochem.* **2011**, *15* (10), 2205–2211. https://doi.org/10.1007/s10008-010-1237-z.

(101) Kreuer, K. D. Proton-Conducting Oxides. *Annu. Rev. Mater. Res.* **2003**, *33* (1), 333–359. https://doi.org/10.1146/annurev.matsci.33.022802.091825.

(102) Kreuer, K. D. Aspects of the Formation and Mobility of Protonic Charge Carriers and the Stability of Perovskite-Type Oxides. *Solid State Ion.* **1999**, *125* (1), 285–302. https://doi.org/10.1016/S0167-2738(99)00188-5.

(103) Norby, T.; Widerøe, M.; Glöckner, R.; Larring, Y. Hydrogen in Oxides. *Dalton Trans.* **2004**, *0* (19), 3012–3018. https://doi.org/10.1039/B403011G.

(104) Malavasi, L.; Fisher, C. A. J.; Islam, M. S. Oxide-Ion and Proton Conducting Electrolyte Materials for Clean Energy Applications: Structural and Mechanistic Features. *Chem. Soc. Rev.* **2010**, *39* (11), 4370–4387. https://doi.org/10.1039/B915141A.

(105) Nyman, B. J. Proton Conductivity of Lanthanum and Barium Zirconate: Microscale Aspects on First-Principles Basis. Doctoral thesis, Chalmers University of Technology, 2012.

(106) Yamazaki, Y.; Hernandez-Sanchez, R.; Haile, S. M. High Total Proton Conductivity in Large-Grained Yttrium-Doped Barium Zirconate. *Chem. Mater.* **2009**, *21* (13), 2755–2762. https://doi.org/10.1021/cm900208w.

(107) Hempelmann, R.; Soetratmo, M.; Hartmann, O.; Wäppling, R. Muon Diffusion and Trapping in Proton Conducting Oxides. *Solid State Ion.* **1998**, *107* (3), 269–280. https://doi.org/10.1016/S0167-2738(97)00543-2.

(108) Malavasi, L.; Fisher, C. A. J.; Islam, M. S. Oxide-Ion and Proton Conducting Electrolyte Materials for Clean Energy Applications: Structural and Mechanistic Features. *Chem. Soc. Rev.* **2010**, *39* (11), 4370–4387. https://doi.org/10.1039/B915141A.

(109) Kreuer, K. D. On the Complexity of Proton Conduction Phenomena. *Solid State Ion.* **2000**, *136–137*, 149–160. https://doi.org/10.1016/S0167-2738(00)00301-5.

(110) Iguchi, F.; Sata, N.; Yugami, H. Proton Transport Properties at the Grain Boundary of Barium Zirconate Based Proton Conductors for Intermediate Temperature Operating SOFC. *J. Mater. Chem.* **2010**, *20* (30), 6265–6270. https://doi.org/10.1039/C0JM00443J.

(111) Kreuer, K. D.; Adams, St.; Münch, W.; Fuchs, A.; Klock, U.; Maier, J. Proton Conducting Alkaline Earth Zirconates and Titanates for High Drain Electrochemical Applications. *Solid State Ion.* **2001**, *145* (1), 295–306. https://doi.org/10.1016/S0167-2738(01)00953-5.

(112) Scholten, M. J.; Schoonman, J.; van Miltenburg, J. C.; Oonk, H. A. J. Synthesis of Strontium and Barium Cerate and Their Reaction with Carbon Dioxide. *Solid State Ion.* **1993**, *61* (1), 83–91. https://doi.org/10.1016/0167-2738(93)90338-4.

(113) Tanner, C. W.; Virkar, A. V. Instability of BaCeO3 in H 2 O -Containing Atmospheres. *J. Electrochem. Soc.* **1996**, *143* (4), 1386–1389. https://doi.org/10.1149/1.1836647.

(114) Coors, W. G.; Manerbino, A.; Ricote, D. M. and S. Fabrication of Yttrium-Doped Barium Zirconate for High Performance Protonic Ceramic Membranes. In *Perovskite Materials - Synthesis, Characterisation, Properties, and Applications*; 2016.

(115) Shipman, M. A.; Symes, M. D. Recent Progress towards the Electrosynthesis of Ammonia from Sustainable Resources. *Catal. Today* **2017**, *286*, 57–68. https://doi.org/10.1016/j.cattod.2016.05.008.

(116) Cui, X.; Tang, C.; Zhang, Q. A Review of Electrocatalytic Reduction of Dinitrogen to Ammonia under Ambient Conditions. *Adv. Energy Mater. 0* (0), 1800369. https://doi.org/10.1002/aenm.201800369.

(117) Kyriakou, V.; Garagounis, I.; Vasileiou, E.; Vourros, A.; Stoukides, M. Progress in the Electrochemical Synthesis of Ammonia. *Catal. Today* **2017**, *286*, 2–13. https://doi.org/10.1016/j.cattod.2016.06.014.

(118) Cao, N.; Zheng, G. Aqueous Electrocatalytic N<Subscript>2</Subscript> Reduction under Ambient Conditions. *Nano Res.* **2018**, *11* (6), 2992–3008. https://doi.org/10.1007/s12274-018-1987-y.

(119) Amar, I. A.; Lan, R.; Petit, C. T. G.; Tao, S. Solid-State Electrochemical Synthesis of Ammonia: A Review. *J. Solid State Electrochem.* **2011**, *15* (9), 1845–1860. https://doi.org/10.1007/s10008-011-1376-x.

(120) McPherson, I. J.; Sudmeier, T.; Fellowes, J.; Tsang, S. C. E. Materials for Electrochemical Ammonia Synthesis. *Dalton Trans.* **2019**, *48* (5), 1562–1568. https://doi.org/10.1039/C8DT04019B.

(121) Vayenas, C. G.; Bebelis, S. I. Electrochemical Promotion. *Solid State Ion.* **1997**, *94* (1–4), 267–277. https://doi.org/10.1016/S0167-2738(96)00511-5.

(122) Ouzounidou, M.; Skodra, A.; Kokkofitis, C.; Stoukides, M. Catalytic and Electrocatalytic Synthesis of NH3 in a H+ Conducting Cell by Using an Industrial Fe Catalyst. *Solid State Ion.* **2007**, *178* (1–2), 153–159. https://doi.org/10.1016/j.ssi.2006.11.019.

(123) Murakami, T.; Nishikiori, T.; Nohira, T.; Ito, Y. Electrolytic Synthesis of Ammonia in Molten Salts under Atmospheric Pressure. *J. Am. Chem. Soc.* **2003**, *125* (2), 334–335. https://doi.org/10.1021/ja028891t.

(124) McEnaney, J. M.; Singh, A. R.; Schwalbe, J. A.; Kibsgaard, J.; Lin, J. C.; Cargnello, M.; Jaramillo, T. F.; Nørskov, J. K. Ammonia Synthesis from N2 and H2O Using a Lithium Cycling Electrification Strategy at Atmospheric Pressure. *Energy Environ. Sci.* **2017**, *10* (7), 1621–1630. https://doi.org/10.1039/C7EE01126A.

(125) Licht, S.; Cui, B.; Wang, B.; Li, F.-F.; Lau, J.; Liu, S. Ammonia Synthesis by N2 and Steam Electrolysis in Molten Hydroxide Suspensions of Nanoscale Fe2O3. *Science* **2014**, *345* (6197), 637–640.

(126) Bale, C. W.; Belise, E.; Chartrand, P.; Decterov, S. A.; Eriksson, G.; Gheribi, A. E.; Hack, K.; Jung, I. H.; Kang, Y. B.; Melancon, J.; Pelton, A. D.; Peterson, S.; Robelin, C.; Sangster, J.; Van Ende, M.-A. FactSage Thermochemical Software and Databases, 2010-2016, Calphad, Vol. 54, Pp 35-53, 2016 <www.Factsage.Com>. *Calphad 54*, 35–53.

(127) Takeda, O.; Li, M.; Toma, T.; Sugiyama, K.; Hoshi, M.; Sato, Y. Electrowinning of Lithium from LiOH in Molten Chloride. *J. Electrochem. Soc.* **2014**, *161* (14), D820–D823. https://doi.org/10.1149/2.0871414jes.

(128) McPherson, I. J.; Sudmeier, T.; Fellowes, J. P.; Wilkinson, I.; Hughes, T.; Tsang, S. C. E. The Feasibility of Electrochemical Ammonia Synthesis in Molten LiCl–KCl Eutectics. *Angew. Chem. Int. Ed.* **2019**, *58* (48), 17433–17441. https://doi.org/10.1002/anie.201909831.

(129) Shi, M.-M.; Bao, D.; Wulan, B.-R.; Li, Y.-H.; Zhang, Y.-F.; Yan, J.-M.; Jiang, Q. Au Sub-Nanoclusters on TiO2 toward Highly Efficient and Selective Electrocatalyst for N2 Conversion to NH3 at Ambient Conditions. *Adv. Mater.* **2017**, *29* (17), 1606550. https://doi.org/10.1002/adma.201606550.

(130) Bao, D.; Zhang, Q.; Meng, F.-L.; Zhong, H.-X.; Shi, M.-M.; Zhang, Y.; Yan, J.-M.; Jiang, Q.; Zhang, X.-B. Electrochemical Reduction of N_2 under Ambient Conditions for Artificial N_2 Fixation and Renewable Energy Storage Using N_2 /NH_3 Cycle. *Adv. Mater.* **2017**, *29* (3), 1604799. https://doi.org/10.1002/adma.201604799.

(131) Wang, H.; Wang, L.; Wang, Q.; Ye, S.; Sun, W.; Shao, Y.; Jiang, Z.; Qiao, Q.; Zhu, Y.; Song, P.; Li, D.; He, L.; Zhang, X.; Yuan, J.; Wu, T.; Ozin, G. A. Ambient Electrosynthesis of Ammonia: Electrode Porosity and Composition Engineering. *Angew. Chem. Int. Ed.* **2018**. https://doi.org/10.1002/anie.201805514.

(132) Wang, X.; Wang, W.; Qiao, M.; Wu, G.; Chen, W.; Yuan, T.; Xu, Q.; Chen, M.; Zhang, Y.; Wang, X.; Wang, J.; Ge, J.; Hong, X.; Li, Y.; Wu, Y.; Li, Y. Atomically Dispersed Au1 Catalyst towards Efficient Electrochemical Synthesis of Ammonia. *Sci. Bull.* **2018**. https://doi.org/10.1016/j.scib.2018.07.005.

(133) Li, S.-J.; Bao, D.; Shi, M.-M.; Wulan, B.-R.; Yan, J.-M.; Jiang, Q. Amorphizing of Au Nanoparticles by CeOx-RGO Hybrid Support towards Highly Efficient Electrocatalyst for N2Reduction under Ambient Conditions. *Adv. Mater.* **2017**, *29* (33), 1700001. https://doi.org/10.1002/adma.201700001.

(134) Wang, J.; Yu, L.; Hu, L.; Chen, G.; Xin, H.; Feng, X. Ambient Ammonia Synthesis via Palladium-Catalyzed Electrohydrogenation of Dinitrogen at Low Overpotential. *Nat. Commun.* **2018**, *9* (1). https://doi.org/10.1038/s41467-018-04213-9.

(135) Liu, H.-M.; Han, S.-H.; Zhao, Y.; Zhu, Y.-Y.; Tian, X.-L.; Zeng, J.-H.; Jiang, J.-X.; Xia, B. Y.; Chen, Y. Surfactant-Free Atomically Ultrathin Rhodium Nanosheet Nanoassemblies for Efficient Nitrogen Electroreduction. *J. Mater. Chem. A* **2018**, *6* (7), 3211–3217. https://doi.org/10.1039/C7TA10866D.

(136) Shi, M.-M.; Bao, D.; Li, S.-J.; Wulan, B.-R.; Yan, J.-M.; Jiang, Q. Anchoring PdCu Amorphous Nanocluster on Graphene for Electrochemical Reduction of N $_2$ to NH $_3$ under Ambient Conditions in Aqueous Solution. *Adv. Energy Mater.* **2018**, *8* (21), 1800124. https://doi.org/10.1002/aenm.201800124.

(137) Manjunatha, R.; Schechter, A. Electrochemical Synthesis of Ammonia Using Ruthenium–Platinum Alloy at Ambient Pressure and Low Temperature. *Electrochem. Commun.* **2018**, *90*, 96–100. https://doi.org/10.1016/j.elecom.2018.04.008.

(138) Wang, D.; Azofra, L. M.; Harb, M.; Cavallo, L.; Zhang, X.; Suryanto, B. H. R.; MacFarlane, D. R. Energy-Efficient Nitrogen Reduction to Ammonia at Low Overpotential in Aqueous Electrolyte under Ambient Conditions. *ChemSusChem* **2018**, *0* (0). https://doi.org/10.1002/cssc.201801632.

(139) Abghoui, Y.; Garden, A. L.; Hlynsson, V. F.; Björgvinsdóttir, S.; Ólafsdóttir, H.; Skúlason, E. Enabling Electrochemical Reduction of Nitrogen to Ammonia at Ambient Conditions through Rational Catalyst Design. *Phys. Chem. Chem. Phys.* **2015**, *17* (7), 4909–4918. https://doi.org/10.1039/C4CP04838E.

(140) Lee, W. J.; Maiti, U. N.; Lee, J. M.; Lim, J.; Han, T. H.; Kim, S. O. Nitrogen-Doped Carbon Nanotubes and Graphene Composite Structures for Energy and Catalytic Applications. *Chem. Commun.* **2014**, *50* (52), 6818. https://doi.org/10.1039/c4cc00146j.

(141) Mukherjee, S.; Cullen, D. A.; Karakalos, S.; Liu, K.; Zhang, H.; Zhao, S.; Xu, H.; More, K. L.; Wang, G.; Wu, G. Metal-Organic Framework-Derived Nitrogen-Doped Highly Disordered Carbon for Electrochemical Ammonia Synthesis Using N 2 and H 2 O in Alkaline Electrolytes. *Nano Energy* **2018**. https://doi.org/10.1016/j.nanoen.2018.03.059.

(142) Vasileiou, E.; Kyriakou, V.; Garagounis, I.; Vourros, A.; Manerbino, A.; Coors, W. G.; Stoukides, M. Electrochemical Enhancement of Ammonia Synthesis in a BaZr0.7Ce0.2Y0.1O2.9 Solid Electrolyte Cell. *Solid State Ion.* **2016**, *288*, 357–362. https://doi.org/10.1016/j.ssi.2015.12.022.

(143) Vasileiou, E.; Kyriakou, V.; Garagounis, I.; Vourros, A.; Manerbino, A.; Coors, W. G.; Stoukides, M. Reaction Rate Enhancement During the Electrocatalytic Synthesis of Ammonia in a BaZr0.7Ce0.2Y0.1O2.9 Solid Electrolyte Cell. *Top. Catal.* **2015**, *58* (18–20), 1193–1201. https://doi.org/10.1007/s11244-015-0491-9.

(144) Vasileiou, E.; Kyriakou, V.; Garagounis, I.; Vourros, A.; Stoukides, M. Ammonia Synthesis at Atmospheric Pressure in a BaCe0.2Zr0.7Y0.1O2.9 Solid Electrolyte Cell. *Solid State Ion.* **2015**, *275*, 110–116. https://doi.org/10.1016/j.ssi.2015.01.002.

(145) Wang, W. B.; Cao, X. B.; Gao, W. J.; Zhang, F.; Wang, H. T.; Ma, G. L. Ammonia Synthesis at Atmospheric Pressure Using a Reactor with Thin Solid Electrolyte BaCe0.85Y0.15O3−α Membrane. *J. Membr. Sci.* **2010**, *360* (1–2), 397–403. https://doi.org/10.1016/j.memsci.2010.05.038.

(146) Zheng, J.; Liao, F.; Wu, S.; Jones, G.; Chen, T.-Y.; Fellowes, J.; Sudmeier, T.; McPherson, I. J.; Wilkinson, I.; Tsang, S. C. E. Efficient Non-Dissociative Activation of Dinitrogen to Ammonia over Lithium-Promoted Ruthenium Nanoparticles at Low Pressure. *Angew. Chem. Int. Ed.* **2019**, *58* (48), 17335–17341. https://doi.org/10.1002/anie.201907171.

Chapter 2 Experimental Methods & Characterisation

This chapter introduces the material synthesis and characterisation experiments that were used in producing this thesis. Specific details of individual experiments will be discussed in later experimental chapters.

2. 1 Synthetic Techniques

Material synthesis is at the heart of any experimental thesis in catalysis science. Synthesis choices will have a direct impact on the catalytic performance, both through physical and chemical phenomena. This section contains an overview of the types of synthetic techniques employed.

2. 1. 1 Ceramic Oxide Synthesis

While the synthesis of ceramic oxides has, at times, been referred to as "shake and bake chemistry", it would not be fair to suggest that this implies the chemistry is without complications, nor that improvements can be made. The shake and bake term originated from the first solid state syntheses developed, in which multi-component oxides are synthesised by mixing the constituent oxides, and heating to high temperatures.[1] Problems emerge due to slow solid-solid diffusion kinetics, and inhomogeneity of starting materials.

In a mixture of two oxides to be reacted, reactions can only occur at an interface between two particles, meaning further mixing relies on diffusion of ions. High temperatures and long reaction times are required to achieve homogeneity, although sometimes this is not enough; materials prepared through this route often suffer from oxide-phase inhomogeneity, including secondary phases, and uncontrolled (typically large) particle sizes.[1] While with appropriate preparation, such as rotary milling of reactants to improve homogeneity of mixing, and to reduce particle size, high quality oxide materials can be prepared; for some preparations it is more appropriate to consider solution-based techniques.[2]

Solution based synthetic techniques allow for significantly more uniform mixtures of precursors to be prepared prior to reaction.[3] Sol gel chemistry is one of several solution-based synthesis techniques that emerged in response to the limitations of traditional solid-state reactions. Traditionally, the term sol-gel refers to the reaction of alkoxide-based precursors, as a route to prepare a range of inorganic polymers and ceramics. Known in literature as far back as Ebelmen's work in 1846,[4] it has become an important process for the preparation of a range of solid-state materials.

By trapping the metal cations in a polymeric gel network, the randomness of the solution state is propagated into the material prior to calcination, allowing atomic level mixing. Complex and multicomponent oxides can be synthesised at lower temperatures with shorter reaction times. Most 'traditional' sol-gel chemistry can be classified as the formation of inorganic polymers or ceramics from the hydrolysis and condensation of metal alkoxide precursors via a polymeric network (gel). Several different methodologies have evolved over the development of this technique.

The method pioneered by Pechini in a patent in 1967 exploited the ability of several alpha-hydroxycarboxylic acids (citric, lactic, and glycolic acids) to form polybasic acid chelates with niobium, titanium, and zirconium.[5] The chelates undergo polyesterification reactions when heated in the presence of polyhydroxy alcohol. Removal of the solvent does not result in any crystallisation, instead yielding a resin intermediate. Subsequent calcination of the resin removes the organic components yielding the desired ceramic oxide material. By trapping the components in the resin, and preventing crystallisation, it is possible to maintain the solution-phase homogeneity during the calcination procedure.

Over the years, the Pechini process was modified in various ways. The polyol can be replaced by water (Marcilly et al. 1967; Marcilly et al. 1970; Courty et al. 1973), to give an amorphous gel instead of a resin.[6,7] Kakihana demonstrated in 1999 the use of alternate cation precursors, namely metal nitrate salts.[8] These modified Pechini syntheses were defined by Sunde et al. as:[9]

"The modified Pechini type of synthesis process to oxide materials starts with a homogeneous aqueous solution containing the desired cation precursors in stoichiometric ratio and selected additives, which by evaporation and reactions is converted to a rigid cross-linked polymer hindering segregation of the cations. The polymer is further converted to a homogeneous oxide powder or film by heat treatment."

For homogeneity to be achieved, a stable, aqueous chelated solution of all cation precursors is the first requirement. To achieve this, the precursors should be water-soluble, or soluble in an aqueous solution with the chelating agents. Commonly, hydroxides, alkoxides, acetates, chlorides, citrates, and nitrates fulfil this requirement.[9]

To ensure the correct stoichiometry in the final product, it must be carefully controlled at this stage, including through additional characterisation of the starting materials (e.g. thermogravimetric analysis).

The chelate compounds must remain soluble until formation of the polymeric like resin is achieved. This involves the expulsion of water through heating, which can lead to precipitation. To control for this, the pH can be modified, and chelating agents with higher affinity for the cations chosen. This is especially relevant in the case of basic cations, such as the alkaline earth metals, which form weak complexes with citric acid (CA). In the case of barium cations, Sletnes et al. found it necessary to use an additional ethylenediaminetetraacetic acid (EDTA) chelating agent to prevent the precipitation of barium compounds. [10]. A report by Chu and Dunn found that barium nitrate precipitated during the gelation stage, but would re-dissolve upon addition of ammonium hydroxide, and would not re-precipitate if the pH remained above ~6. [11]

Usually a polyalcohol, such as ethylene glycol, is added to promote the polyesterification reaction between carboxylic acid groups, giving rise to the desired polymeric resin. However following a report by Shao in which it was demonstrated the use of solely EDTA and CA to form the resin, [12] a number of reports have shown that the alcohol groups of citric acid are sufficient to promote the polyesterification reaction.[13–17]. This process has been referred to as the citrate-EDTA complexation method. Feldhoff et al. carried out a detailed characterisation of the intermediates of this process,

finding that a gel starts to form between 120 – 150 ºC, without the addition of extra polyalcohol. Transmission electron micrographs showed a high degree of separation of metal components within the gel. [14]

After gelling, a thermal treatment step follows; firstly, to remove unwanted components (organics) from the gelling procedure, and secondly to promote chemical process' to yield the desired ceramic oxide. This can be carried out in a one-step calcination, or with separate combustion and calcination steps.

Doped barium zirconate powders were synthesised by a citrate-EDTA complexation method. Metal nitrates were used as starting materials and were dissolved in water in the desired molar ratio under high stirring. EDTA was added, and the pH adjusted to ~10 using $NH_4OH_{(aq)}$. Citric acid was added, and the pH again adjusted to ~10 using $NH_4OH_{(aq)}$. The molar ratio between the chelating agents and the metal nitrate salts was fixed at 1.5:1.5:1 EDTA: CA: metal ions. This solution was heated in an oven, until it combusted, yielding a black ash with rigid, porous structure. The resulting ash was crushed into a fine powder and calcined in a furnace under high airflow (~ 200 mL min^{-1}), yielding an off-white powder.

2. 1. 2 Sintering of Ceramic Powders

After synthesis, almost all ceramics must be further processed via sintering. An exception to this is when powders are desirable. The goal of sintering is to change the microstructure of the ceramic, to adapt it to the chosen application. This normally focusses on changing the pores and grains within a ceramic structure, in turn affecting the density.

Rahaman wrote in 2003 that while some experimental parameters are easy to control, such as temperature, atmosphere, pressure and average particle size, are easy to control; others, such as particle packing and powder characteristics, are more difficult to account for.[18] This means sintering is a difficult and not always scientific process; new protocols must be established for each ceramic and application.

There are three main driving forces for sintering processes; chemical reactions, externally applied pressure, and the free energy of curved surfaces.[18] It is this last driving force that is the most fundamental, to see why we must first acknowledge that sintering is an irreversible chemical process, so therefore must result in a decrease of free energy. All materials have a specific surface free energy factor, energy per unit area. As sintering processes result in a decrease in surface area, the total surface free energy of a body of material will decrease upon sintering, providing an energetic driving force. The sintering process can then be assisted by externally applied pressure, and by designing systems that undergo a chemical reaction during the sintering process to provide an additional driving force.

Sintering is, fundamentally, controlled by diffusion within the crystalline solid, meaning it is a slow process even at the elevated temperatures required. The kinetics can be influenced by three factors; the temperature, oxygen partial pressure, and defect concentration.[18]

Barium zirconate was sintered using the following procedure. Prior to sintering, barium zirconate powder was uniaxially pressed into pellets using a 13 mm Specac IR pellet die and manual hydraulic press. Typically, 0.5 – 1 g was added to the press, and the load gradually increased up to 10 tonnes, and held for 1 minute. The pressure was then slowly released, and the pellet slowly ejected. After pressing pellets were placed in round crucibles and surrounded with sacrificial barium zirconate powder. At such extreme temperatures, barium can start to evaporate from the pellet, leaving a barium deficient lattice. Surrounding the pellet with sacrificial BZY20 powder creates a partial pressure of barium, preventing the formation of barium deficient phases. Pellets were sintered by slowly heating (5 ºC min^{-1}) to 1500 ºC, where they were held for 24 hours, before slowly cooling to room temperature. To ensure the pellets would have sufficient oxygen to properly form the oxide phase, custom endcaps were designed and manufactured in the University workshops, allowing high air flows to be passed through the furnace work tube at high temperatures. It was necessary to add alumina insulating blocks (Almath crucibles, custom design) to ensure the heat from the furnace did not decompose the silicone O-rings in the endcaps.

2. 1. 3 Ball Milling of Ceramic Powders for Size Reduction

Ball milling is a type of mechanochemical process, which are defined according to IUPAC as "chemical reactions that are induced by the direct absorption of mechanical energy". [19] In the case of size reduction, a fracture within a crystal is induced by the breaking of bonds.

A milling jar is rotated in some fashion (various designs exist) to generate Centrifugal forces. These forces generate kinetic energy in small milling balls made of a hard, inert material. At high kinetic energies, the impact and grinding forces will reduce the size of and mix any powders placed into the milling jar.

Ball milling of powders can be used to produce extremely fine powders, down to the nanoscale. Synthesis of these fine powders can be divided into single or multi-component starting powders. Milling with multiple components is known as mechanical-alloying, whereas the simpler size-reduction process when processing a single component powder is known as mechanical milling.[20] The objective of particle size reduction is to produce a powder with specified size distribution, to facilitate the subsequent material processing steps. Particle size reduction, during long term processing, often complicated by 'particle size enlargement' where smaller particles form larger particles in which the larger particles can still be identified. This effect, known as the 'equilibrium state of milling', is closely related to agglomeration or aggregation of particles. [21]

In this work, planetary ball milling was employed. Planetary mills operate by rotating the grinding bowl, and the grinding bowl support plate, in opposite directions (Figure 2-1a). The result of this is the application of centrifugal forces in the same, and opposite directions. This causes the milling balls to roll

around half the circumference of the grinding bowl, and then fly off to cause an impact effect on the opposite side (Figure 2-1b).

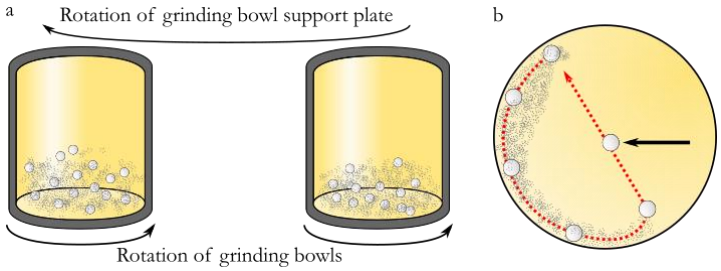


Figure 2-1: a) Grinding bowls, and the plate on which they are mounted rotate in opposite directions b) movement of grinding balls during operation (dashed red arrow), and the overall centrifugal force generated by the opposite rotations (solid black arrow)

Many factors can influence the outcome of the milling, including the ball and jar material, the ball size, ball-to-powder ratio, filling extent, milling atmosphere, milling speed, and milling time. In this work ZrO_2 balls and jars were employed, for the high hardness, and because contamination of the material with microscopic amounts of ZrO_2 would not be hugely problematic.

Calcined powders were milled in a Fristch P7 mill, in a ZrO_2 milling jar using 1mm ZrO_2 milling balls. The ball to powder ratio was initially determined from manufacturer's instructions and was eventually fixed at 5:12 mL of powder to solvent. This corresponded to a close to maximum filling level of the milling jar. Powders were milled in dry conditions and wet conditions, with both isopropanol and water lubricants. Milling was always conducted for 5 min at a time, with a 3-minute pause between cycles to dissipate excess heat. A relatively low maximum milling speed of 500 rpm was employed, as due to the use of solvents elevated pressures can build in the jar at higher speeds.

2. 1. 4 Wet-Impregnation Synthesis of Ruthenium Nanoparticles

Wet impregnation has become a popular technique in heterogeneous catalyst synthesis, as it allows with relative simplicity the introduction of an active catalyst phase into a support material. It has been popularised thanks to having relatively few steps, allowing for efficient use of often expensive precursors, and resulting in well-dispersed catalysts.[22] The basic experiment involves introducing a solvent containing a catalyst-phase precursor to a support material. Some precursor molecules will form seeds, which upon removal of the solvent will act as growth points for the crystalline phase. If the seeds and subsequent crystal form evenly across the surface, the catalyst phase obtained after drying and calcination should also be well dispersed.

Wet impregnation can be described as 'dry' or 'wet', referring to the initial state of the support. A 'wet' support has previously had water introduced into its pores, meaning that the catalyst precursor moves into the pores via diffusion. In 'dry' or 'incipient wetness' impregnation, ideally a support of pore volume V_{PT} is contacted with a precursor solution of volume $V=V_{PT}$. The solvent and precursor enter the pores via capillary action, leaving no excess.

Incipient wetness impregnation procedures for powder supports, however, often involve an excess of solution, which is then removed by a drying procedure.[23–25] This is particularly useful for precursors with low solubility.[22] The drying procedure only involves the removal of solvent from the system, leaving behind only the support and precursor. This is separate from later calcination procedures, in which previously dried precursor/support systems undergo thermal chemical processes, such as ligand decomposition or redox reactions.

Ruthenium nanoparticles were prepared from ruthenium (III) acetylacetonate via wet impregnation followed by a temperature-controlled chemical vapour deposition reduction. the following procedure. Typically, 100mg $Ru(acac)_3$ was dissolved in 1 mL acetone, and sonicated with the support material for 2 hrs, then stirred overnight and dried in an oven for 2 hrs to yield a red powder. Powder was reduced in a furnace under 30 mL min^{-1} 5% H_2:Ar flow heated to 150 C at 5 C min^{-1}, held for 24 hrs then heated to 350 C at 5 C min^{-1}, held for 24 hrs and cooled to room temperature. The catalyst was passivated for 2 hrs under 30 mL min^{-1} 2.5% O_2:He to yield a grey powder.

Ruthenium particles prepared from tri-ruthenium dodecacarbonyl were prepared as follows. Ru NPs were prepared from a ruthenium carbonyl ($Ru_3(CO_{12})$ precursor according to the method reported by Aika et al.[26] $Ru_3(CO)_{12}$ was dissolved in tetrahydrofuran (THF), to give an orange solution. 20 mL THF per 30 mg $Ru_3(CO)_{12}$ was used to reliably achieve complete dissolution without the need for heating. After dissolution of the precursor, barium zirconate support was added, with the ruthenium loading fixed at 10 wt.%. The resulting suspension was sonicated for 6 hours, at which point the solvent was removed by rotary evaporation, leaving an orange powder. $Ru_3(CO)_{12}$ was then decarboxylated to give supported Ru NPs. The orange powder was heated in a furnace under 50 mL min^{-1} Ar to 70 ºC, where it dwelled for 4 hours, and then to 350 ºC where it dwelled for 5 hours before cooling to room temperature. A ramp rate of 2 ºC min-1 was used when heating. A grey powder was obtained, typically with yields >90%. No passivation was employed for this preparation.

Caesium promoters were added to the barium zirconate-supported Ru catalysts using wet impregnation. Caesium nitrate ($CsNO_3$) was used as a precursor, with a loading of 5 wt. %. Ru barium zirconate catalyst was added to a small vial, then $CsNO_3$ was dissolved in the minimum volume of water (~ 2 – 3 mL for 200 mg of catalyst) under stirring, and the desired Ru barium zirconate catalyst was added to form a thick slurry. This mixture was stirred for 5 hrs, before drying in a vacuum oven at 70 ºC overnight. The $CsNO_3$ was reduced in-situ prior to testing.

2. 2 Electrochemical Characterisation Techniques

For any electro-catalytic system, electrochemical characterisation is of key importance, to give details about the electrochemical process both within the electrolyte, and at the electrodes.

Electrochemical cells were prepared as detailed in Chapters 3 and 4, and the electrodes connected to Ag wires. The cells were sealed in a furnace tube using custom-designed endcaps with electrical feedthroughs. Endcaps were designed and manufactured in the University workshops. Nitrogen and hydrogen were supplied to the cell, the ratio and flow rates of the gasses were controlled using mass flow controllers (Bronkhurst). The nitrogen was supplied from a cylinder of 5% H_2/N_2, which allowed the cell to be held under reducing atmosphere at all times, without needing to connect the reactor to the pure hydrogen cylinder used during testing.

2. 2. 1 Electrochemical Impedance Spectroscopy

Electrical resistance is normally defined by Ohm's law (Equation 2.1), however this only applies in the case of ideal resistors. This means that the law holds true for all values of potential (*R*) and current (*I*), is independent of the frequency for alternating currents (AC) signals, and that AC signals remain in phase when passing through a resistive element. Rarely do real word cells and cell elements meet these conditions, therefore impedance is commonly used to characterise cells.

$$V = IR \qquad \textit{Equation 2.1}$$

In this thesis potentiostatic AC impedance spectroscopy was used to investigate the conductivity of the cells. A current of fixed amplitude is applied as a sine wave. The magnitude (amplitude) and phase shift of the current are then recorded and used to calculate the magnitude and phase of the impedance. The amplitude of the applied signal is kept low to avoid significant polarisations in the cell and keep it at pseudo-steady state.

To look at how this can help investigate conductivity, it should be recognised that an AC current or voltage can be expressed as a vector rotating at an angular frequency of $\omega = 2\pi f$ rad s^{-1}. For an AC potential, the voltage or current at time t, V(t) and I(t), are given by Equation 2.2 and Equation 2.3 for the angular dependence of the voltage and current.

$$V(t) = V_0 \cos \omega t \qquad \textit{Equation 2.2}$$

$$I(t) = I_0 \cos \omega t + \varphi \qquad \textit{Equation 2.3}$$

To express the magnitude and phase of the input (voltage) and output (current) signals, complex exponentials are used. Euler's relationship (Equation 2.4) is used to express V(t) and I(t) as the real parts of Equation 2.5 and Equation 2.6 respectively.

$$e^{jx} = \cos x + j \sin x \qquad \textit{Equation 2.4}$$

$$V = V_0 . e^{j\omega t} \qquad \textit{Equation 2.5}$$

$$I = I_0 . e^{j\varphi\omega t} \qquad \textit{Equation 2.6}$$

This is convenient as the current can now be expressed with three terms expressing the magnitude (I_0), phase ($e^{j\varphi}$) and frequency ($e^{\omega t}$) information separately.

$$I = I_0 . e^{j\varphi} . e^{\omega t} \qquad \textit{Equation 2.7}$$

Impedance is then expressed as the ratio of voltage to current, with the frequency terms cancelling out, to give the complex representation of impedance

$$Z = \left({}^{V_0}/_{I_0}\right) . e^{-j\varphi} = |Z| . e^{-j\varphi} \qquad \textit{Equation 2.8}$$

This allows the magnitude of impedance ($|Z|$) and phase (φ) to be calculated from the input and output symbols. Impedance is then expressed as a sum of its real and imaginary parts. A plot of real vs imaginary impedance (called a Nyquist plot) can be fitted using an equivalent circuit model, representing areas of a cell with different electrical transport properties as simple components (i.e. resistors and capacitors).

Electrochemical impedance spectrums were recorded on an Ivium CompactStat in a four-electrode configuration (working and sense electrodes, and counter and reference electrodes were shorted together). A polarisation of 100 mV was applied between frequencies 10^6 – 10^{-1} Hz with 10 points collected per decade. Fitting of the collected spectra was carried out using the instrument's IviumStat software.

2. 2. 2 Voltammetry

Voltammetry is used to obtain information about an electrochemical cell by applying a current and sweeping the potential. This can be done as a linear sweep (linear sweep voltammetry – LSV), or cyclically where the potential is swept up and down repeatedly (cyclic voltammetry – CV). Time is also an important variable in voltammetry techniques.

In voltammetry techniques, unlike in potentiometric techniques, significant polarisations are applied to the cell, resulting in (desired) redox reactions. Experiments can be designed to monitor these redox processes, as well as adsorption and desorption processes, the kinetics and thermodynamics of electron transfer processes, and transport, speciation and thermodynamic properties of solvated species.[27]

A voltammetry experiment is conducted in a three electrode configuration; a working electrode at which the process of interest is measured, a reference electrode which passes no current but is used to determine the potential at the working electrode, and a counter electrode which passes current but is not directly measured.

Voltammetry experiments were carried out using an Ivium CompactStat potentiostat. Linear Sweep Voltammetry (LSV) was conducted on electrochemical cells at 600 ºC under 150 mL min^{-1} 3:1 H_2:N_2. The potential was swept from -2 to +2 V (vs Ag reference electrode), and the current response of the cell recorded. DC voltammetry was used to calculate conductivity of electrochemical cells. Potentials between 0 – 0.8 V were applied across the electrodes. Each pulse lasted for 60 s and the current was recorded.

2. 3 Material Characterisation

In catalysis science, characterisation of the physical and chemical properties of materials is of critical importance to understand which features are beneficial for the catalytic reactions, and which are detrimental.

2. 3. 1 Crystal Structure Determination via Diffraction Techniques

Determination of the crystal structure is of critical importance to materials and catalysis science. By studying crystal structures, we can identify materials, look at how structure influences chemistry, and even elucidate reaction mechanisms. Crystals can be single-phase, where only one crystalline chemical compound is present; or multi-phase, where multiple crystalline compounds can be identified. Through diffraction experiments the chemical compounds present in a crystal can be identified.

Since the discovery in 1912 by Max von Laue of the phenomenon of X-ray diffraction (XRD), diffraction has become the ubiquitous technique for crystal structure determination. That same year Lawrence Bragg formulated what is now known as Bragg's Law, describing the diffraction condition. For these efforts, the 1914 and 1915 Nobel prizes for Physics were awarded to von Laue and Bragg Jr & Sr for the discovery and explanation of XRD.[28,29]

However, diffraction experiments are not limited to the use of only X-ray waves, and have evolved into an entire field of science, with electrons and neutrons both commonly used as incident waves. These waves types can all be generated with wavelengths on the order of magnitude of the d-spacing of solid crystals. X-ray waves will interact with the electron cloud surrounding each atom, neutrons with nuclei or unpaired-spin electrons, and electrons also with the nuclei of atoms (due to its positive charge).[30]

Crystals are solids characterised by their repeating structures, which are referred to as lattice structures. The smallest repeat 3d unit of the crystal lattice is called the unit cell, which is a rhombohedral shape described by three vectors, the crystallographic axes, all starting from the same lattice point. The magnitudes and angles between these vectors exactly describe the unit cell and these quantities (magnitudes a, b, c and angles α, β, γ) are known as the lattice constants (Figure 2-2).[31]

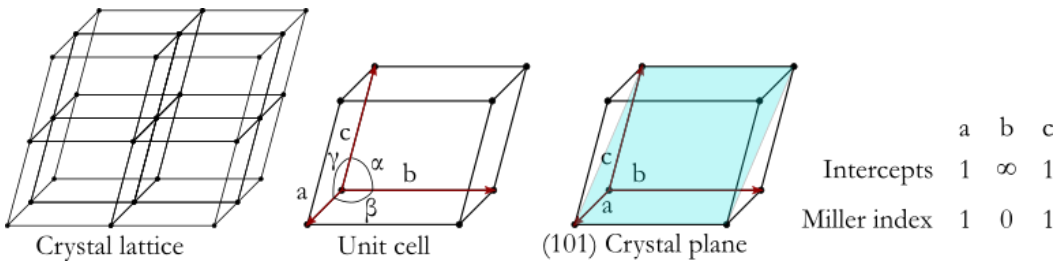


Figure 2-2: The crystal lattice is made up of individual unit cells, which are described using 3 vectors (a, b & c), and the angles between the vectors (α, β, γ). Crystal planes are characterised by their Miller indices

Any plane drawn through the crystal can be described using Miller indices, which are the agreed-upon notation for describing crystal planes. If each point of the lattice takes an integer value according to the crystal axes (a, b & c), and a crystal plane makes fractional intercepts of (1/h, 1/k & 1/l) with the

axes, taking the reciprocal of these intercepts will give the Miller index of the plane, (h, k, l), illustrated in Figure 2-2. A peak in a diffraction pattern corresponds to a crystal plane.

Over a whole lattice the same crystal plane will be repeated many times, and the distance between these planes is called the d-spacing. In total there are seven possible crystallographic systems, and for each system equations exist to relate all six lattice parameters to the d-spacing. Therefore, if we can find the d-spacing, we can calculate the lattice parameters for the entire crystal, or crystal phase.

The basic diffraction experiment works as follows; an incident wave is directed at a material to be studied, and the source or sample is moved to vary the angle of incidence. The detector is also moved to maintain an angle of 2 Theta (Figure 2-3a) with the incident beam, and the intensity of diffracted waves recorded. As incident waves hit the material, some will be elastically scattered by interaction with the target matter, preserving their energy. Due to the nature of waves, they will constructively and destructively interfere as a geometric function of the lattice points that scattered them.[31] The diffraction pattern is composed of coherent waves which interfered constructively and therefore reached the detector with significantly higher intensities. Atomic periodicities with long-range order in the crystal cause diffraction events at low scattering angles, and features with only short-range order (such as small interplanar spacings) cause diffraction at high angles.[30]

To understand how constructive interference leads to a diffraction pattern, we can derive Bragg's law from Figure 2-3a. Two waves of equal front striking atoms in adjacent crystal planes, with inter-planar spacing d, will be phase-shifted by the path length indicated in red. It can be shown with geometric proofs that the angle with which the incident beam strikes the surface, θ, is equal to the angle indicated within the small triangle. Using simple trigonometry, it can be demonstrated that the path length shift is equal to 2d sin θ.

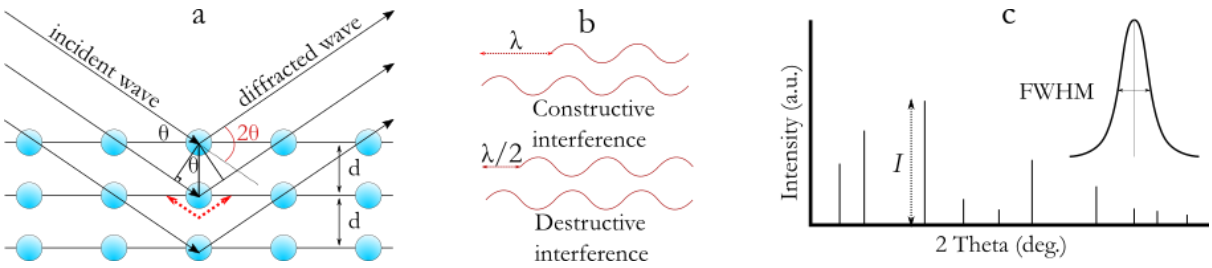


Figure 2-3: (a) Scattering of incident waves hitting a surface with angle θ, d corresponds to the spacing between crystal planes (d-spacing), red arrows indicate difference in path length between two scattered waves. (b) Constructive and destructive interference of waves with equal wavelength. (c) typical diffraction pattern showing perfect diffraction peaks; however, peaks are always subject to experimental broadening (inset).

For elastically scattered waves, which will have equal wavelengths, interference between waves is a function of the phase shift. As seen in Figure 2-3b, waves separated by an integer number of wavelengths, will constructively interfere. If separated by a half-integer wavelength, they will destructively interfere. Waves will be strongly diffracted when the reflected waves are coherent and constructive interference occurs.[30] Putting together the path shift and constructive interference, we can formulate the Bragg condition, Equation 2.9. Strong diffraction will occur when the path length shift is

equal to a whole number of wavelengths (the waves are coherent). Most commonly this occurs when n=1 (first-order reflection), however n may also take values greater than unity (n=2 or 3, second and third order reflections, respectively).

$$n\lambda = 2d\sin\theta \qquad \textit{Equation 2.9}$$

A perfect diffraction pattern will appear like that in Figure 2-3c, with the intensity of the peak proportional to the degree of reflection at these values of 2θ. However in practice peaks are subject to broadening due to inhomogeneity in the factors governing the diffraction of the peaks; imperfect crystal formations, atomic thermal vibrations, and the nature of the beam all lead to broadening, Figure 2-3c inset.[31] The broadening of the peaks is quantified by the width of the peaks at half of the maximum intensity recorded, the full-width half maximum (FWHM). The imperfections of the crystal can be caused by significant structural features, and so the analysis of the broadening phenomenon (known as lineshape analysis), is an important aspect of diffraction experiments.[30]

Diffraction experiments can be run with single crystal or powder samples, although in this work only powder diffraction was utilised. The diffraction pattern generated by polycrystalline samples is due to the incident beam encountering many different crystal planes on its path through the sample, due to sample inhomogeneity. A single crystal must be rotated many times to satisfy the Bragg condition for all crystal planes.

Collected diffraction patterns can be compared to a library of published patterns to determine which phase or phases are present in the sample. Many diffraction experiments end here, with sample identification, however much more quantitative information can be obtained from the data, if it is of high enough quality. The two types of analysis can be grouped into numerical methods, where the diffraction pattern is treated as a list of discrete diffraction peaks, each with a position, intensity, width and shape; and full pattern fitting methods in which a pattern is generated from a model, compared to the experimental pattern, and then refined until the differences between the two patterns are minimised.[32]

2. 3. 1. A X-Ray Diffraction

X-rays are scattered by interaction with the electron density of atoms; the oscillating electric field of the incident X-ray moves the atomic electrons and their acceleration generates a reflected wave.[30] Therefore, X-rays are sensitive to the atomic numbers (Z-numbers) of the target atoms. Atoms with low Z-numbers will not strongly scatter X-rays, and atoms with similar Z-numbers will be hard to differentiate.

The majority of XRD instruments utilise vacuum diode tubes to generate X-rays. Current is passed through a filament (typically biased to -40 kV), heating it to the point that it will thermoionically emit electrons, which are then accelerated into the anode, which is maintained at ground potential.[30] X-rays are then created when these energetic electrons lose energy, either through an inelastic scattering process,

leading to a continuum of what is termed 'bremsstrahlung' radiation; or by ionising a core electron, creating a hole that will be filled by an outer electron falling into it, simultaneously releasing either an Auger (secondary electron), or an X-ray photon of discrete energy related to the anode material. A typical X-ray intensity spectrum is shown in Figure 2-4, with the spectrum of wavelengths due to inelastic scattering, and discrete energy peaks due to ionisation processes both visible. Increasing the filament bias will increase the intensity of all X-ray wavelengths and allow some previously energetically forbidden processes to occur (demonstrated by the appearance of the 'K' peaks in the 30 & 40 kV spectrums).

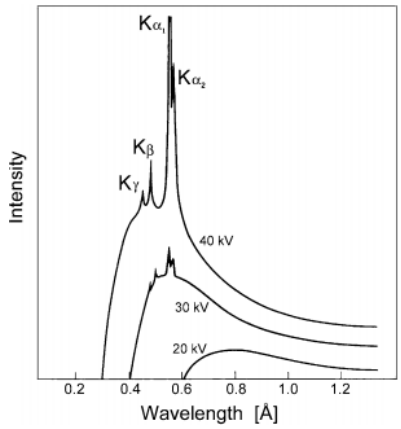


Figure 2-4: Intensity of X-ray radiation as a function of wavelength when generated from vacuum diode with a silver anode at 20, 30 & 40 kV acceleration voltage. Continuum of bremsstrahlung radiation, with discrete peaks due to ionisation of core electrons. Reproduced from Fultz and Howe.[30]

X-rays became the most popular choice of source for diffraction experiments due to the ease of generation, making them cheap and easy to access, also meaning high flux sources are easy to access, allowing small samples to be studied.

XRD patterns were collected on Philips Xpert and Bruker D8 diffractometers, both using a Cu 2-α source with 40 kV acceleration voltage. Patterns were typically recorded between 10 – 90 ^{0} 2Theta, with 0.017 step size and 0.5 s step^{-1}.

2. 3. 1. B Neutron Diffraction

Diffraction of neutrons was first demonstrated in 1936, independently by both Mitchell & Powers and von Halban & Preiswerk.[33,34] This just 4 years after Chadwick suggested the existence of the neutron.[35] For a long time neutron diffraction remained a relatively unused technique, until the publication of Rietveld's method for refinement of crystal structures from a model structure and powder diffraction data.[36,37] The renaissance of neutron diffraction has led to the development of a wide variety of new techniques, such as time-of-flight analysis and Larmor precession, and more accurate crystal structure determination.[38]

Neutrons can be diffracted thanks to wave-particle duality. Neutrons with sufficient energy, determined by their velocity, will behave as waves with a wavelength determined by the de Broglie relation

$$\lambda = \frac{h}{mv}$$ *Equation 2.10*

Where h is Planck's constant, m is the mass of the neutron, v is the velocity and λ the wavelength. As the mass of neutrons is fixed (in the energy ranges of interest), and h is a constant, the equation can be simplified to λ = 3.956/v. For a diffraction pattern to occur the Bragg condition must still be satisfied, therefore λ is of the same order as the d-spacing in the crystal.

Neutrons interact with the nuclear strong force generated by atomic nuclei, which acts over only very short distances (femtometre scales). Therefore, neutrons travel through mainly empty space, and the scattering event probability is low. Neutrons may penetrate mm into a sample before scattering, meaning large amounts of sample are required.[30] However, the nuclear interaction has a major advantage in that even light elements, such as hydrogen, have high scattering cross-sections. Although hydrogen presents new problems, as it has a high incoherent scattering cross-section. These incoherently scattered neutrons may still reach the detector, contributing to the background of the pattern, worsening the quality of the data. This problem is even worse for bound hydrogen, where the incoherent scattering cross-section is four times that of free hydrogen.[38] When chemically feasible, deuterium is often chosen as an analogous atom in place of hydrogen.

Neutrons experiments use either nuclear reactors or spallation as a source. Neutrons are freely available from nuclear reactors thanks to the fission of ^{235}U; spalled neutrons are generated by bombardment of a heavy metal target by a GeV proton beam. In both cases the initial high energy fast neutrons must be moderated, to produce lower energy thermal neutrons. Neutron sources produce beams with different and often wide spectrums of energies. This varies a lot between neutron sources and will not be discussed beyond the specific neutron source used in this work. A good summary of other types of source can be found in Kisi and Howard.[38]

Neutron powder diffraction patterns were recorded at the Paul Scherrer Institute (Switzerland). 3g of sample was used for measurement, and the patterns were collected at ambient temperatures.

2. 3. 2 Electron Microscopy

Electron microscopy is another ubiquitous technique in catalyst and materials science, providing measurements of size on a very localised area of the sample. Both transmission and scanning electron microscopy (TEM & SEM, respectively) were utilised in this work, and will be discussed in more depth in the following sections.

According to Equation 2.10 electrons can be accelerated to velocities where they display wave like behaviour. The resolution of a microscope is limited by the wavelength of the incident beam. In an optical microscope, this is on the hundred nanometre scale; a 200 kV electron beam has a corresponding wavelength of 0.00251 nm.[39].

Electrons striking a sample can undergo elastic (diffraction) or inelastic scattering; or be transmitted straight through the sample, Figure 2-5. Inelastic collisions also cause the production of another photon or electron. The electrons can be high-energy secondary electrons, or lower energy Auger electrons. Electrons can also be absorbed by the sample, leading to a build-up of current in the sample, which can lead to undesirable charging effects in images. Some electrons are scattered to such an extent that they emerge from the sample in the opposite direction to which they entered, these are known as back scattered electrons and may be elastic or inelastic.

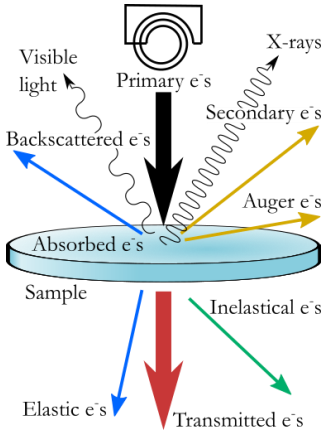


Figure 2-5: Electron scattering interactions when beam of primary electrons strikes a specimen. Interactions can be classified as elastic (blue) or inelastic (green). Electrons transmitted straight through thin samples (red) will have the same energy as elastically scattered electrons. Inelastic collisions also cause the emission of either X-ray & visible photons (black waves), or the emission of secondary & Auger electrons (gold). Additionally, electrons may be absorbed by the sample, leading to a charge build up, and currents within the sample.

Electrons are generated in electron microscopes through the process of thermionic emission; a filament is heated to temperatures such that electrons in the material have enough energy to overcome the work function of the material and escape into the vacuum of the microscope column. The filament is strongly negatively polarised with respect to the microscope column (-100 to -1000 kV),[39] so electrons are strongly repelled away from the filament and down the column. The rate of emission of electrons is proportional to the Boltzmann factor, $\exp(-\Phi/k_BT)$ where k_B is the Boltzmann constant, T is the temperature in Kelvin, and Φ is the work function of the filament.[30]

Once electrons have left the filament and passed through the sample, they must be focussed as in Figure 2-6. This is achieved using solenoids acting as magnetic lenses, which deflect electrons with a force proportional to the strength of the applied magnetic field and the velocity of the electrons, the Lorentz force:

$$F = -ev \times B \qquad \textit{Equation 2.11}$$

Where F is the force of the deflection, e is the charge of the electron, v is the velocity and B is the strength of the magnetic field.[30]

2. 3. 2. A Transmission Electron Microscopy

TEM allows the direct observation of nanostructures, lattices, and even individual atoms. Characterising the size, shapes, crystallinity, composition, and even elemental mapping are all possible in TEM experiments. While diffraction experiments are more representative of a whole sample, TEM has a key advantage in that it can be focussed, allowing observation of a specific section of a sample.

TEM works in a manner analogous to optical microscopy; a wave is passed through a sample material and focussed using a series of lenses. Image contrast, a variation in the intensity of the transmitted wave, is produced by differences in scattering of the wave across a sample.[40] To allow electrons to be transmitted entirely though the sample, without undergoing inelastic scattering events, samples must be extremely thin. Special preparations are necessary for TEM experiments, with powder samples being mounted on specialised metallic grids.

As seen in Figure 2-5, a variety of scattering interactions are possible, the most important of which in conventional TEM is diffraction of electrons. Bright field TEM focuses on the directly transmitted electrons, whereas dark field TEM forms an image from diffracted electrons, Figure 2-6. Other types of image and information can be collected from these diffracted electrons, such as selective area diffraction or diffraction contrast images.[30]

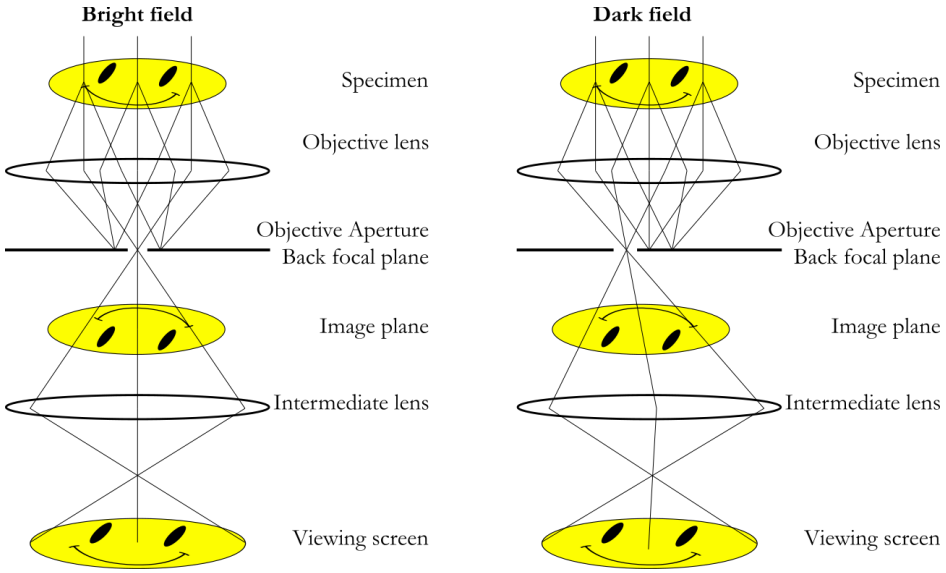


Figure 2-6: Bright and dark field modes of TEM imaging. Bright field image relies only on directly transmitted electrons, whereas dark field image is formed by adjusting the objective aperture to permit only diffracted electrons.

Electrons are lost from the image by large angle scattering outside of the objective aperture, or by inelastic interactions with the sample. Inelastically scattered electrons will have a lower velocity and so according to Equation 2.11 will experience less focussing force, meaning they are in a different focal plane to the elastic electrons and will only contribute to background noise in bright and dark field TEM experiments. Areas of the sample that strongly scatter electrons outside of the objective aperture will appear as a local intensity deficit and create image contrast.[40]

TEM images were collected on JEOL JEM 2010 and JEM 2100F microscopes, both operating at an acceleration voltage of 200 kV. HAADF-STEM images were collected on a JEOL ARM F300 operating at an acceleration voltage of 300 kV

2. 3. 2. B Scanning Electron Microscopy

SEM has a lower resolution than TEM, however has some advantages over it. Chief of these is the ability to better observe three-dimensional structures thanks to the higher depth of field of the images. A finely focussed beam of electrons is scanned across the surface and the intensity of the scattered electrons is used to generate an image. Sample preparation is also much more facile, with conductive samples able to be directly observed after mounting onto a microscope stage.

Both backscattered (BSEs) and secondary electrons (Figure 2-5) are commonly observed in SEM experiments to form images. BSEs are the most commonly observed electrons in SEM experiments, having a high flux/intensity giving a good depth of field to images, however as they come from deep within the sample, they have a lower resolution due to a high degree of scattering. Secondary electrons are emitted only around 5 – 50 nm from the surface, meaning they have a higher resolution as they have undergone relatively few scattering interactions.

SEM images were collected using a Hitachi S-520 microscope, operating at an acceleration voltage of 20 kV.

2. 3. 3 Thermo-Gravimetric Analysis

Thermo-gravimetric analysis (TGA) involves heating a sample to induce a thermal reaction, and monitoring the reaction using changes of weight, and time. Instruments are typically equipped with highly sensitive balances, capable of measuring very slight weight changes. A number of different reaction types may be monitored; physical reactions such as sorption processes, chemical reactions such as chemisorption or thermal decomposition, and reactions (chemical and physical) of only the sample, or between the sample and the atmosphere.[41] The chosen atmosphere allows different types of reactions to be promoted or supressed.

The precise weight changes of the sample over a temperature range and time are used to find temperatures (thermal processes) at which reactions occur, and the speed of the reactions (reaction dynamics). A typical output from an experiment will be a curve showing the differential of mass change over a temperature range, allowing weight change peaks to be observed.

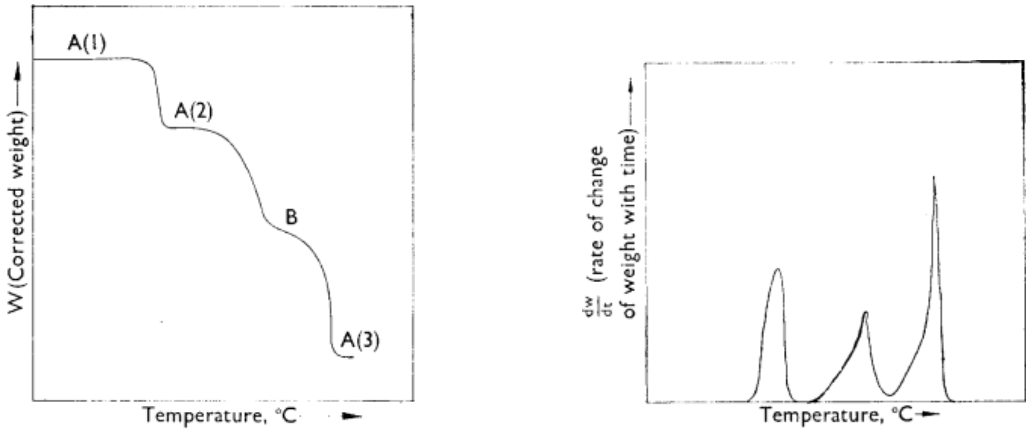


Figure 2-7: Typical raw TGA curve showing weight change with temperature, and the same data after differentiation, clearly showing weight change peaks. Flat sections of raw data (A1 – 3) correspond to plateaus on differential curve, and weight changes appear as peaks. Reproduced from Coats and Redfern.[41]

Hydration level of $ZrO(NO_3)_2$ xH_2O was determined via TGA. Approximately 10 mg samples were analysed under 100 mL min^{-1} N_2 flow, sample was purged for 10 min before heating to 500 ºC at 10 ºC min^{-1}. Decomposition of $Ru_3(CO)_{12}$ precursor on support was also analysed via TGA. Approximately 15 mg of sample was placed into the platinum pan, sealed in the instrument, and purged under 100 mL min^{-1} N_2 flow. Temperature was then ramped at 10 ºC min^{-1} to 600 ºC.

2. 3. 4 Temperature Programmed Reduction

Temperature programmed reduction or TPR was first reported in 1975 by Robertson et al.,[42] and has become a useful technique in determining synthetic procedures, and for determining the temperature at which a pre-catalyst requiring reduction should be treated at before starting the main catalytic reaction.

A gas mix of inert gas and hydrogen is passed over a sample at a constant rate and H_2 concentration. The consumption of hydrogen or the production of water is then measured as a function of the temperature, resulting in reduction peaks.

TPR was used to investigate the reduction of ruthenium nanoparticles on supports. Samples of approximately 30 mg were packed into a quartz tube and secured with quartz wool. Two instruments were used for analysis. For experiments conducted on a TPDRO 1100 ThermeQuest, samples were purged with 10 mL min^{-1} and heated to 150 ºC to remove surface adsorbates. After cooling to 40 ºC, gas flow was changed to 5% H_2/Ar, and the sample heated at 5 ºC min^{-1} to 600 ºC. The exhaust gas was flowed over a Thermal Conductivity Detector (TCD), and the signal in mV recorded. For experiments conducted on a Quantachrome ChemBET instrument equipped with a TCD, samples were heated under N_2 to 120 ºC to remove surface adsorbates. Samples were cooled to 40 ºC, the gas changed to 5% H_2/Ar and heated to 600 ºC at 10 ºC min^{-1}.

2. 3. 5 Laser Diffraction Particle Size Analysis

Particle size analysis is a key feature of ceramic preparations and preparation of heterogeneous catalysts. At a microscale and above, the use of laser diffraction is a useful technique for size distribution measurements.

A particulate sample is dispersed into a flowing stream (either liquid or in some special cases gas), and then the stream passed through a laser beam. The laser is scattered by solid particles; large particles scatter the laser at small angles, and small particles at large angles. The angular scattering intensity measured and is used to calculate the particle sizes, assuming spherical particles.

Laser diffraction Spectroscopy (LDS) experiments were carried out on a Malvern Mastersizer 3000. Powders were dispersed into a bath of DI water by sonicating for 60s before each size measurement was carried out. Each sample was measured 3 times independently and the average calculated from these three measurements.

2. 3. 6 Quantification of Dissolved Ammonia

Ammonia (NH_3) is a polar molecule composed of one nitrogen and three hydrogen atoms, with a nitrogen lone pair giving the molecule a distorted tetrahedral structure. Under standard conditions it is a gas with a vapour pressure of 9.59 bar.[43] Gaseous ammonia readily dissolves in water, with an aqueous solubility of 482 g L^{-1} at 24 ºC.[43] Once in solution it may form ammonium (NH_4^+), according to Scheme 4, with a pK_a value of 9.25 at 25 ºC.[43] The dominant species will depend on the pH of solution, at low pH values NH_3 will be more prevalent, and NH_4^+ more so at high pH values.

$$NH_{3(aq)} + H_2O_{(l)} \rightleftharpoons NH_4^+{}_{(aq)} + OH^-{}_{(aq)}$$

Scheme 4: Ammonia-ammonium equilibrium in water

Due to the high solubility, for quantification of ammonia produced in the gas phase, it is convenient to trap it by dissolution into aqueous solutions. Aqueous ammonia can be quantified using numerous techniques, however in this work quantification was carried out using an ammonium ion-selective electrode.

2. 3. 6. A Ammonium Ion-Selective Electrodes

Ion selective electrodes work in a manner analogous to pH metres, measuring the conductivity of a solution to determine the quantity of dissolved ammonia by comparison to a calibration curve. However, a key feature of these electrodes is the separation of the measured solution from the solution directly in contact with the electrode, avoiding changes in the solution conductivity due to other dissolved ionic species. This is achieved in ammonium ISEs using a hydrophobic PTFE membrane, which will allow neutral, gaseous phase NH_3 to pass through, but not water or other solvated ions. A diagram of a typical ISE is shown in Figure 2-8.

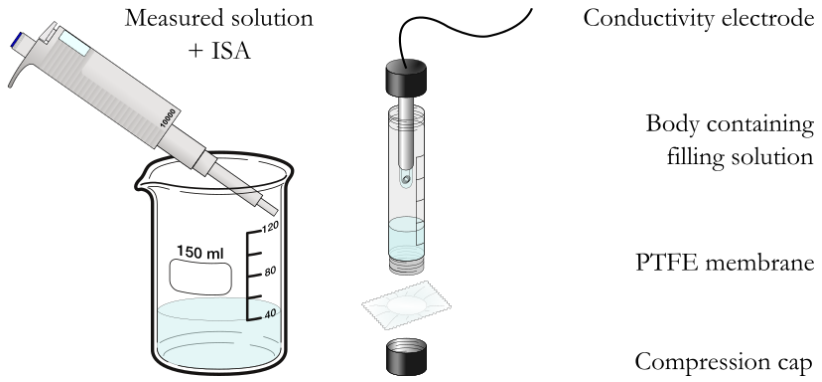


Figure 2-8: A typical ammonium ISE. Measured solution is made basic using an ionic strength adjuster (ISA) solution. Gaseous NH_3 can pass through PTFE membrane into filling solution, where conductivity changes are measured by the electrode. Compression cap ensures no measured solution can pass into electrode body.

First, a strongly basic ionic strength adjustor is added to the measured solution serving two purposes; to drive Scheme 4 to the left creating dissolved NH_3, and to alter the total ionic strength of the measured solution to a constant value, much higher than the original measured solution. The pKa of ammonia at 25 ºC is 9.25, which is equal to the pH when ammonia and ammonium have the same concentrations according to the Henderson-Hasselbach equations.[44,45] Above this pH NH_3 will be the dominant species and free to escape the solution, according to Henry's law. Henry's law states that the partial pressure of a gas dissolved in a liquid is proportional to its aqueous concentration. For ammonia the Henry's law constant has a value of ~59 moles per atmosphere at 25 ºC.[46]

Dissolved NH_3 can leave the solution as a gas, but the degree of dissolution will be dependent on the total ionic strength. Gaseous NH_3 can pass through the PTFE membrane into the filling solution surrounding the electrode, inducing changes in the solution conductivity, which are measured by the electrode. Solutions with unknown NH_3 concentrations are measured by comparison to a calibration curve.

The equilibrium constant for Scheme 4 equal to the concentration of product species by concentration of reactant species. However, the electrode filling solution contains high amounts of NH_4Cl dissolved in excess water, so the ammonium and water concentrations can be considered constant, and the ammonia and hydroxide concentrations are related by Equation 2.12.

$$[OH^-] = [NH_3] \times K \qquad \textit{Equation 2.12}$$

The change of $[OH^-]$ induces a potential change in the solution, which is compared to the potential of an internal reference electrode via the Nernst equation. This equation is used to relate cell potentials to the concentration of reactants and is derived from the expression for free energy and the expression cell potentials:

$$\Delta G = \Delta G^o + RTlnQ \qquad \textit{Equation 2.13}$$

Where R is the gas constant, ΔG is the free energy change, ΔG^0 is the free energy change under standard conditions, T is the temperature in kelvin, and Q is the reaction quotient (equivalent to the equilibrium constant under equilibrium conditions). Cell potential in terms of free energy is given by:

$$\Delta G = -nFE \qquad \textit{Equation 2.14}$$

Where n is the number of moles of electrons transferred in the reaction, F is Faradays constant, and E is the cell potential. It can also be written for standard conditions with ΔG^0 and E^0. Combining these two equations, fixing the temperature at 25 °C (298.15K) and converting the natural log to base 10 log, gives the Nernst equation in its most recognisable form:

$$E = E^o - \frac{59.2\ mV}{n} log\ (Q) \qquad \textit{Equation 2.15}$$

Applying this to the operation of the ammonia ISE, 1 electron is transferred in Scheme 4, therefore n = 1. Q is set equal to $[OH^-]$ and since $[OH^-]$ and $[NH_3]$ are proportional according to Equation 2.12, the metre has a Nernstian response to changes in $[NH_3]$. Therefore, at 25 °C each decade increase in ammonia concentration will induce a change in E of -59.2 mV. Practically, so long as the solution temperatures are close to 25 °C, and critically that the temperature is the same during calibration and measurement, the samples do not need to be held at 25 °C. It is also true that both the Henry's law constant and the pH of the equivalence point vary with temperature, underling the need to control the temperatures between calibration and measurement. The temperature of each solution was recorded during measurement to ensure that the variation remains low.

An Orion High-Performance ammonia-ion selective electrode (Thermo-Fischer) was used for analysis. Firstly, a calibration curve was constructed from a minimum of 3 points, using ammonia standards prepared by serial dilution (standards between 1000 and 0.01 ppm). Samples could be then be measured, however when analysing large batches of samples, it was important to periodically check the electrode response using the calibration solutions. The measurement of samples and standards followed the same procedure. 30 mL of solution to be measured was added to well-cleaned beaker for measurement, and heavily stirred. 300 μL of Ionic Strength Adjustor (ISA, 10M NaOH) was added, and the mV reading from the electrode was left to stabilise for up to a minute. Once stabilised, the mV reading was recorded, and the measured solution was discarded.

2. 3. 7 X-Ray Photoelectron Spectroscopy

X-ray photoelectron spectroscopy, or XPS, is a type of electron spectroscopy. In these types of techniques, materials are studied by inducing the ejection of an electron from a solid. Of the electron spectroscopy techniques, XPS is by far the most utilised.

Electrons in solids are bound to the nucleus by strong electrostatic and nuclear forces, and the magnitude of the total energy holding the electrons in their orbitals is called the binding energy. In atoms the deep core electrons have binding energies magnitudes corresponding to photon energies of the same

order as X-rays. By exposing a surface to an X-ray beam, the ejection of core electrons can be induced, and the kinetic energy of these photoelectrons is related to the energy of the photon. Deep core electrons do not participate in bonding, and therefore are elementally specific, leading to the use of XPS as an elemental analysis technique. XPS can also be used quantitatively, as XPS peak areas are proportional to the amount of material present.[47]

Ejected electrons that reach the detector will have their kinetic energy, E_K, measured. Therefore, the binding energy can be calculated according to:

$$E_B = h\nu - E_K \qquad \textit{Equation 2.16}$$

XPS is a surface sensitive technique, due to the nature of the inelastic mean free path of electrons (how far they will travel through a solid before losing energy). It is strongly dependant on the energy of the electron. Seah and Dench reported that for inorganic solids it follows a function of the form:

$$\lambda_m = \frac{x}{E^2} + y(aE)^{1/2} \qquad \textit{Equation 2.17}$$

Where x and y are average constants determined by examining many types of material. For inorganic solids x and y are 2170 and 0.72 respectively, and for elemental solids they are 538 and 0.41. λ_m is the inelastic mean free path in monolayers, a is the monolayer thickness in nanometres, and E is the electron energy in electron volts.[48] λ_m is converted to nm simply by multiplying again by a, which typically takes a value of 2 – 3 Å.[47] Expressed graphically in Figure 2-1 using data from Seah and Dench, it can be see that in the range of electron energies measured in a typical XPS experiment, the inelastic mean free path is often less than 1nm, meaning only those electrons emitted from electrons close to the surface will be detected.

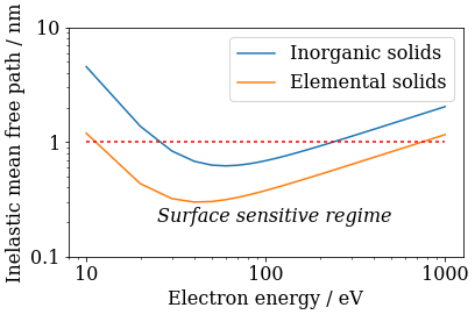


Figure 2-9: Equation 2.17 expressed graphically using data from Seah and Dench.[48] Inorganic compounds and elemental solids behave differently.

The short mean free path of the electrons also means that most XPS experiments are conducted under UHV conditions, otherwise the attenuation of signal by the atmosphere is simply too high. However recent advances in the field have made the development of near-ambient pressure XPS systems (NAP-XPS) a reality. These systems rely on differential pumping of various experimental chambers, allowing the sample chamber to be placed under low atmosphere values, while maintaining the analysis chamber under close-to-UHV levels.

Near-ambient pressure XPS was carried out at the B07 beamline at Diamond Light Source (Didcot, UK). Ruthenium on barium zirconate samples to be measured were first reduced under 1 barH_2 at 450 ºC for 2 hours. Next, photoemission spectrums were recorded under ~40 mbar H_2, then under ~10 mbar Ar, and finally again under H_2. First a survey scan was taken, before narrow energy scans were carried out to record changes in the Ru3d and O1s bands, at 720 and 900 eV photon energy, respectively. At each photon energy a spectrum of the Fermi edge was also recorded for charge-correction purposes.

2. 3. 8 Gas Adsorption Techniques

Adsorption can be defined as the formation of a layer of gas, liquid, or solid on the surface of a solid, or less frequently, a liquid. Two main types of adsorption can occur, classified by the type of bonds formed during the interaction. Chemisorption is the formation of chemical bonds between the surface and the adsorbate, whereas in physisorption the adsorbate bonds to the surface via much weaker Van der Waals forces.[47]

The adsorption of gases to surfaces is of critical important in catalysis science. Understanding how gases adsorb to surfaces is often the key to determining reaction mechanisms and pathways. It is also of great use in characterising materials and surfaces. Two adsorption characterisation techniques were employed in this work.

2. 3. 8. A Pulsed-Titration Chemisorption Analysis

Unlike physisorption, chemisorbed molecules can only form a monolayer, due to the short-range nature of chemical bonds. This can be exploited to measure surface areas using pulsed titration. After preparation of the surface to be studied by desorption and sometimes reduction, the surface is exposed small amounts of a specific adsorbate gas, which is injected or 'pulsed' into a stream of inert gas flowing over the surface. Eventually, the surface will be saturated with adsorbate molecules, and will be unable to adsorb anymore.

By measuring the amount of adsorbate-gas in the gas stream after flowing over the sample, the point of saturation can be determined, and by using a known injection volume, the total amount of adsorbed gas can be calculated. This is then used to find the number of relevant adsorbate sites. This technique can be expanded by exploiting the reactivity of surfaces and adsorbates to selectively probe one type of surface in a material. I.e. a gas can be chosen that will selectively adsorbed to a metal surface, but not to an oxide one, therefore probing only the surface area of the metal.

Pulse titration analysis was used to determine the exposed Ru surface area. Analysis was conducted on a ChemBET Pulsar equipped with a TCD and an automatic injection loop, with a measured volume of 68.25 μL. ~100 mg of catalyst was used for each test and secured in a quartz tube with quartz wool. Catalysts were heated to 450 ºC under 5% H2/Ar to remove surface oxide, then the gas changed to He and purged for an hour before cooling down still under He flow to remove adsorbates from the Ru surface. Temperature was held at 40 ºC for the duration of all pulse titration experiments.

2. 3. 8. B BET Surface Area Analysis

Adsorption isotherms are mathematical models which predict the adsorption of molecules to a surface. The simplest of these is the Langmuir isotherm. The surface coverage by adsorbate molecules is dependent on the temperature and pressure of the system, and the chemical potential difference between the adsorbate and the surface, which arises due to the adsorption energy. The kinetics of the reaction are not accounted for by this model, affecting only the time taken to reach equilibrium.

Two major assumptions are made in forming the equations that come together to make the Langmuir isotherm. Firstly, that the surface can only accept a monolayer of adsorbate molecules, and that once every surface site has been saturated, adsorption stops. Secondly, that the adsorbates behave as ideal gas molecules, and are non-interacting between themselves meaning the adsorption energy does not change as a function of coverage.

By removing the assumption that coverage will stop at one monolayer, the Brunauer-Emmett-Teller (BET) model can be used to estimate total surface coverage. This model is now used in the ubiquitous technique of BET surface area measurements. BET analyses were carried out on a micromimetics TriStar in the Oxford Chemistry Surface Analysis Facility.

2. 4 References

(1) Ecija, A.; Vidal, K.; Larrañaga, A.; Ortega-San-Martín, L.; Arriortua, M. I. Synthetic Methods for Perovskite Materials; Structure and Morphology. *Adv. Cryst. Process.* **2012**. https://doi.org/10.5772/36540.

(2) E. Danks, A.; R. Hall, S.; Schnepp, Z. The Evolution of 'Sol–Gel' Chemistry as a Technique for Materials Synthesis. *Mater. Horiz.* **2016**, *3* (2), 91–112. https://doi.org/10.1039/C5MH00260E.

(3) Cushing, B. L.; Kolesnichenko, V. L.; O'Connor, C. J. Recent Advances in the Liquid-Phase Syntheses of Inorganic Nanoparticles. *Chem. Rev.* **2004**, *104* (9), 3893–3946. https://doi.org/10.1021/cr030027b.

(4) Ebelman, J. Mémoire Sur de Nouvelles Combinaisons de l'acide Borique Avec Les Éthers, et Sur l'éther Sulfureux. In *Annales de chimie et de physique*; 1846; Vol. 57, p 331.

(5) Pechini, M. P. Method of Preparing Lead and Alkaline Earth Titanates and Niobates and Coating Method Using the Same to Form a Capacitor. US3330697A, July 11, 1967.

(6) Marcilly, C.; Delmon, B.; Sugier, A. New Process for Obtaining Finely Divided Homogeneous Oxides of Many Elements. *Fr. Pat. PV* **1967**, *110*.

(7) Marcilly, C.; Courty, P.; Delmon, B. Preparation of Highly Dispersed Mixed Oxides and Oxide Solid Solutions by Pyrolysis of Amorphous Organic Precursors. *J. Am. Ceram. Soc.* **1970**, *53* (1), 56–57.

(8) Kakihana, M.; Arima, M.; Yoshimura, M.; Ikeda, N.; Sugitani, Y. Synthesis of High Surface Area LaMnO3+ d by a Polymerizable Complex Method. *J. Alloys Compd.* **1999**, *283* (1–2), 102–105.

(9) Sunde, T. O. L.; Grande, T.; Einarsrud, M.-A. Modified Pechini Synthesis of Oxide Powders and Thin Films. In *Handbook of Sol-Gel Science and Technology*; Klein, L., Aparicio, M., Jitianu, A., Eds.; Springer International Publishing: Cham, 2016; pp 1–30.

(10) Sletnes, M.; Skjærvø, S. L.; Lindgren, M.; Grande, T.; Einarsrud, M.-A. Luminescent Eu3+-Doped NaLa(WO4)(MoO4) and Ba2CaMoO6 Prepared by the Modified Pechini Method. *J. Sol-Gel Sci. Technol.* **2016**, *77* (1), 136–144.

(11) Chu, C.; Dunn, B. Preparation of High-Tc Superconducting Oxides by the Amorphous Citrate Process. *J. Am. Ceram. Soc.* **1987**, *70* (12), C-375-C–377.

(12) Shao, Z. Investigation of the Permeation Behavior and Stability of a Ba0.5Sr0.5Co0.8Fe0.2O3−δ Oxygen Membrane. *J. Membr. Sci.* **2000**, *172* (1–2), 177–188.

(13) Shao, Z.; Haile, S. M. A High-Performance Cathode for the next Generation of Solid-Oxide Fuel Cells. *Nature* **2004**, *431* (7005), 170–173.

(14) Feldhoff, A.; Arnold, M.; Martynczuk, J.; Gesing, Th. M.; Wang, H. The Sol–Gel Synthesis of Perovskites by an EDTA/Citrate Complexing Method Involves Nanoscale Solid State Reactions. *Solid State Sci.* **2008**, *10* (6), 689–701.

(15) Ding, X.; Liu, Y.; Gao, L.; Guo, L. Synthesis and Characterization of Doped LaCrO3 Perovskite Prepared by EDTA–Citrate Complexing Method. *J. Alloys Compd.* **2008**, *458* (1), 346–350.

(16) Patra, H.; Rout, S. K.; Pratihar, S. K.; Bhattacharya, S. Effect of Process Parameters on Combined EDTA–Citrate Synthesis of Ba0.5Sr0.5Co0.8Fe0.2O3−δ Perovskite. *Powder Technol.* **2011**, *209* (1), 98–104.

(17) Jeong, C.; Ryu, J.; Noh, T.; Kim, Y.-N.; Lee, H. Structural Analysis and Electrode Performance of Ce Doped SrMnO3 Synthesised by EDTA Citrate Complexing Process. *Energy Mater.* **2013**, *8* (4), 494–498.

(18) Rahaman, M. N. *Ceramic Processing and Sintering*, 2nd ed.; Materials engineering (Marcel Dekker, Inc.); M. Dekker: New York, 2003.

(19) IUPAC. Compendium of Chemical Terminology, 2nd Ed. (the "Gold Book"). Compiled by A. D. McNaught and A. Wilkinson. Blackwell Scientific Publications, Oxford (1997). XML on-Line Corrected Version: Http://Goldbook.Iupac.Org (2006-) Created by M. Nic, J. Jirat, B. Kosata; Updates Compiled by A. Jenkins. ISBN 0-9678550-9-8. Https://Doi.Org/10.1351/Goldbook.

(20) Koch, C. C. Structural Nanocrystalline Materials: An Overview. *J. Mater. Sci.* **2007**, *42* (5), 1403–1414.

(21) Baláž, P.; Achimovičová, M.; Baláž, M.; Billik, P.; Cherkezova-Zheleva, Z.; Criado, J. M.; Delogu, F.; Dutková, E.; Gaffet, E.; Gotor, F. J.; Kumar, R.; Mitov, I.; Rojac, T.; Senna, M.; Streletskii, A.; Wieczorek-Ciurowa, K. Hallmarks of Mechanochemistry: From Nanoparticles to Technology. *Chem. Soc. Rev.* **2013**, *42* (18), 7571–7637.

(22) Jong, K. P. de. *Synthesis of Solid Catalysts*; John Wiley & Sons, 2009.

(23) Wang, Z.; Liu, B.; Lin, J. Highly Effective Perovskite-Type BaZrO3 Supported Ru Catalyst for Ammonia Synthesis. *Appl. Catal. Gen.* **2013**, *458*, 130–136.

(24) Shimoda, N.; Kimura, Y.; Kobayashi, Y.; Kubota, J.; Satokawa, S. Ammonia Synthesis over Yttrium-Doped Barium Zirconate and Cerate-Based Perovskite-Type Oxide Supported Ruthenium Catalysts. *Int. J. Hydrog. Energy* **2017**, *42* (50), 29745–29755.

(25) Li, W.; Wang, S.; Li, J. Highly Effective Ru/BaCeO3 Catalysts on Supports with Strong Basic Sites for Ammonia Synthesis. *Chem. – Asian J. 0* (0).

(26) Aika, K.; Takano, T.; Murata, S. Preparation and Characterization of Chlorine-Free Ruthenium Catalysts and the Promoter Effect in Ammonia Synthesis: 3. A Magnesia-Supported Ruthenium Catalyst. *J. Catal.* **1992**, *136* (1), 126–140.

(27) Settle, F. A. Handbook of Instrumental Techniques for Analytical Chemistry; Prentice Hall PTR, 1997.

(28) The Nobel Prize in Physics 1914 https://www.nobelprize.org/prizes/physics/1914/summary/ (accessed Jul 8, 2019).

(29) The Nobel Prize in Physics 1915 https://www.nobelprize.org/prizes/physics/1915/summary/ (accessed Jul 8, 2019).

(30) Fultz, B.; Howe, J. M. *Transmission Electron Microscopy and Diffractometry of Materials*, 4th ed.; Graduate texts in physics; Springer: Heidelberg ; New York, 2013.

(31) He, B. B. *Two-Dimensional X-Ray Diffraction*; Ebook central; Wiley: Hoboken, NJ, 2009.

(32) Speakman, S. A. Introduction to X-Ray Powder Diffraction Data Analysis. *Cent. Mater. Sci. Eng. MIT* **2013**.

(33) Mitchell, D. P.; Powers, P. N. Bragg Reflection of Slow Neutrons. *Phys. Rev.* **1936**, *50* (5), 486–487.

(34) Mason, T. E.; Gawne, T. J.; Nagler, S. E.; Nestor, M. B.; Carpenter, J. M. The Early Development of Neutron Diffraction: Science in the Wings of the Manhattan Project. *Acta Crystallogr. A* **2013**, *69* (Pt 1), 37–44.

(35) Chadwick, J. The Existence of a Neutron. *Proc. R. Soc. Math. Phys. Eng. Sci.* **1932**, *136* (830), 692–708.

(36) Rietveld, H. M. Line Profiles of Neutron Powder-Diffraction Peaks for Structure Refinement. *Acta Crystallogr.* **1967**, *22* (1), 151–152.

(37) Rietveld, H. M. A Profile Refinement Method for Nuclear and Magnetic Structures. *J. Appl. Crystallogr.* **1969**, *2* (2), 65–71.

(38) Kisi, E. H.; Howard, C. J. *Applications of Neutron Powder Diffraction*; Oxford University Press, 2008.

(39) *Transmission Electron Microscopy Characterization of Nanomaterials*; Kumar, C. S. S. R., Ed.; Springer Berlin Heidelberg: Berlin, Heidelberg, 2014.

(40) Spence, J. C. H.; Spence, J. C. H. *High-Resolution Electron Microscopy*, 3rd ed.; Oxford University Press, 2008; Vol. 9780199552757.

(41) Coats, A. W.; Redfern, J. P. Thermogravimetric Analysis. A Review. *Analyst* **1963**, *88* (1053), 906–924.

(42) Robertson, S. D.; McNicol, B. D.; De Baas, J. H.; Kloet, S. C.; Jenkins, J. W. Determination of Reducibility and Identification of Alloying in Copper-Nickel-on-Silica Catalysts by Temperature-Programmed Reduction. *J. Catal.* **1975**, *37* (3), 424–431.

(43) *Lange's Handbook of Chemistry*, 15. ed.; Dean, J. A., Lange, N. A., Eds.; McGraw-Hill handbooks; McGraw-Hill: New York, NY, 1999.

(44) Lide, D. R.; Baysinger, G.; Chemistry, S.; Berger, L. I.; Goldberg, R. N.; Kehiaian, H. V. CRC Handbook of Chemistry and Physics. 2661.

(45) Henderson, L. J. Concerning the Relationship between the Strength of Acids and Their Capacity to Preserve Neutrality. *Am. J. Physiol.-Leg. Content* **1908**, *21* (2), 173–179.

(46) Sander, R. Compilation of Henry's Law Constants (Version 4.0) for Water as Solvent. *Atmospheric Chem. Phys.* **2015**, *15* (8), 4399–4981.

(47) Kolasinski, K. W. *Surface Science [Electronic Resource] : Foundations of Catalysis and Nanoscience*, 3rd ed.; Ebook central; Wiley: Chichester, West Sussex, 2012.

(48) Seah, M. P.; Dench, W. A. Quantitative Electron Spectroscopy of Surfaces: A Standard Data Base for Electron Inelastic Mean Free Paths in Solids. *Surf. Interface Anal.* **1979**, *1* (1), 2–11.

Chapter 3 Synthesis of Barium Zirconate Powders & Preparation of Ammonia Synthesis Cells

3. 1 Background

As discussed in Chapter 1, barium zirconate is an ABO_3 perovskite-structured oxide. When the B site is doped with an aliovalent cation, the material may display appreciable proton conductivity, and good chemical stability.[1] This makes it an attractive candidate for application to both high-temperature protonic fuel cells, and electrolytic cells. From here-on, the pure $BaZrO_3$ will be referred to as 'barium zirconate', and the general class of materials, including the doped structures, referred to as 'barium zirconate materials'.

The discussion of proton conducting ceramics in Chapter 1 examined the choices available in terms of parent oxide and dopants. From this, it was concluded that 20% Y-doped barium zirconate (BZY20) was the best candidate for preparation of a proton-conducting membrane for ammonia synthesis. The key reasons behind this decision were 1) high total proton conductivity and 2) good chemical stability.

The synthesis of these materials, however, presents some significant challenges. For application as fuel cells and electrolytic cells, the most important consideration is the total ionic conductivity of the cell. In barium zirconate materials, the conductivity of the cell is dependent on two factors; the ease with which protonic currents can pass through the solid grains of materials, and at the edges of the grains, or grain boundaries.[2] It is accepted that the conductivity through grains (the bulk/intra-grain) conductivity is much faster than the conductivity across grain boundaries (inter-grain).

The nature of barium zirconate means high sintering temperatures are required to prepare the dense, compact cells required for use as electrolytes. An investigation by Tong et al. found that even at temperatures as high as 1600 ºC, pellets prepared from sol-gel synthesised powders only reached 80% of the theoretical density.[3] Some articles report temperatures as high as 2200 ºC are required to significantly reduce the presence of grain boundaries in the final pellet.[4] The presence of grain boundaries in sintered pellets results in significant resistances to ionic currents. At such high sintering temperatures, it is possible for barium to evaporate from the lattice, and during the sintering step pellets should be surrounded with sacrificial powder to generate a partial pressure of barium.[2]

To reduce the sintering temperatures of these materials, the addition of many sintering aids has been investigated. These materials reduce the overall sintering temperature by creating a glass-like mixed phase at the edges of growing grains, in which the diffusion of barium and zirconium ions is more rapid.[5] Park et al. investigated the addition of various transition metal sintering aids, finding CuO to be the most effective, resulting in an increase of the pellet density versus sintering aid-free samples, at sintering temperatures of 1670 ºC.[6] It was found, however, that all sintering aids reduced the conductivities of the cells. Biswas et al. used a eutectic mix of BaO-CuO and were able to achieve densification at sintering

temperatures as low as 1300 ºC.[7] However, other papers have found that NiO sintering aids perform better than CuO, and this has become the standard. Due to the decrease in conductivity observed with sintering aids, which has been ascribed to the reaction of the non-invasive NiO particles to metallic Ni particles which disrupt the structure, some reports have added an additional Ni extraction step.[5] By adding a secondary sintering procedure, in which the NiO diffuses into sacrificial barium zirconate powders, the content of NiO in the sample can be dramatically reduced.

An alternative procedure to prepare dense compacts without the need for sintering aids is solid reactive sintering. The idea is that the heat of formation of the barium zirconate material provides intense, localised heating within the pellet. Yamazaki et al. reported that BZY20 powders deliberately calcined at low temperatures to retain $BaCO_3$ in the structure, had larger grain sizes and higher total conductivities than powders calcined at higher temperatures.[8] Coors et al. reported a solid-state reactive sintering method, where no calcination of powders is carried out, and the precursors are mixed, pressed into pellets, and sintered.[5] High conductivities and dense pellets can be obtained using this method. Other methods have been proposed for low (relatively speaking) temperature sintering, such as microwave sintering, and flash grain welding using high current power sources to provide a spark capable of sintering the pellets.[9,10]

Once powders have been prepared, they must be formed into dense compacts. The simplest way to achieve this is via uniaxial pressing in an IR pellet die, which can achieve hundreds of MPa.[2] However often it is reported that an additional, isostatic pressing step is required to form sinterable compacts.[4,7,11] To achieve dense compacts it is also required to mill powders prior to pressing. The presence of large particles, and highly disperse size ranges is detrimental for achieving dense compacts. Small particles will have shorter distances for ions to diffuse and react, and uniform particle size distributions form closer-packed structures upon pressing.[7,12]

The preparation of dense pellets of barium zirconate is a multi-step process, with the individual steps all contributing to the density and conductivity of the final pellets. Identical materials prepared with slightly differing conditions or procedures may produce radically different results. Optimising each individual step is critical for a successful preparation.

3. 2 Objectives

The investigations presented in this chapter had three key aims:

1. Develop synthetic procedures for preparation of dense, conductive BZY20 membranes.

2. Measure the conductivity of cells prepared from synthesised membranes, and silver electrodes.

3. Measure rates of ammonia synthesis in these cells.

3. 3 Sol-Gel Synthesis of Barium Zirconate Powders & Processing into Dense Pellets

$BaZr_{0.8}Y_{0.2}O_{3-\delta}$ (BZY20) powders were synthesised using a sol-gel method. The effect of calcination temperature on phase purity was explored. Dense membranes were then prepared by milling, pressing, and sintering steps. Results of milling on the physical characteristics of BZY20 powders, and on the final membrane morphology were investigated. Utilised techniques are discussed in more detail in Chapter 2, and a schematic overview of the process is presented in Figure 3-1.

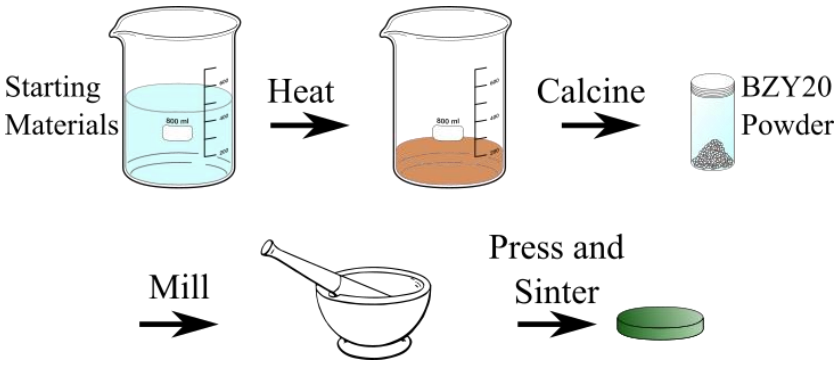


Figure 3-1: Schematic overview of whole pellet preparation process

3. 3. 1 Sol-Gel Synthesis

Yttrium-doped barium zirconate ceramic powders were synthesised by a citrate-EDTA complexation method. Yttrium (III) nitrate hexahydrate ($Y(NO_3)_3 \bullet 6H_2O$), barium nitrate ($Ba(NO_3)_2$), and Zirconium (IV) oxynitrate hydrate ($ZrO(NO_3)_2 \bullet xH_2O$) (Sigma Aldrich) were used as starting materials. Hydration of zirconium oxynitrate was determined by thermogravimetric analysis (TGA) analysis (shown below), with x between 2 - 2.5.

In a typical procedure, $BaZr_{1-x}Y_xO_{3-\delta}$ was synthesised by dissolving the metal nitrate salts in water in stoichiometric ratios under high stirring. EDTA was added and the pH adjusted to ~10 using aqueous NH_4OH. Citric acid was added, and the pH again adjusted to ~10 using $NH_4OH_{(aq)}$. The molar ratio between the chelating agents and the metal nitrate salts was fixed at 1.5:1.5:1 EDTA: CA: metal ions. This solution is heated in an oven, until it combusts, yielding a black ash with rigid, porous structure.

The resulting ash was crushed into a fine powder and calcined in a furnace under high airflow (~ 200 mL min^{-1}), yielding an off-white powder. The temperature and time of calcination was investigated up to 1300 ºC for 4 hours, yielding an off-white powder. Complete calcination was confirmed by powder XRD phase analysis

3. 3. 1. A Thermogravimetric Analysis

Hydration level of $ZrO(NO_3)_2$ xH_2O was determined to ensure correct stoichiometry for desired barium zirconate material was set from the initial reactant amounts. TGA was run under 100 mL min-1 N_2 flow, sample was purged for 10 min before heating to 500 ºC at 10 ºC min^{-1}. ~10 mg of $ZrO(NO_3)_2$ .xH_2O was tested.

Three distinct decomposition peaks were observed around 130, 190, and 240 ºC. Campbell et al. also observed 3 distinct decomposition peaks, although two decomposition peaks were observed at much higher temperatures (270 and 350 ºC).[13] They reported that after the final decomposition only ZrO_2 remained. Initial and final weights were used to calculate the mass loss and using known relative formula masses of ZrO_2 and anhydrous $ZrO(NO_3)_2$, hydration levels were calculated (between 2 and 2.5 for tested samples).

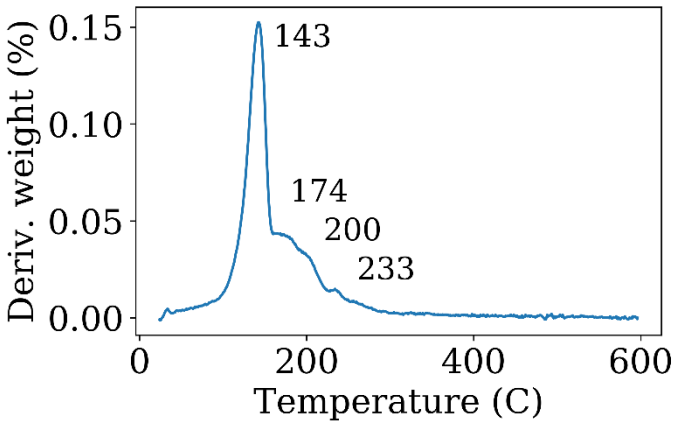


Figure 3-2: Typical TGA plot of $ZrO(NO_3)_2$ xH_2O

3. 3. 1. B XRD Phase analysis

The successful synthesis of $BaZrO_3$ materials was confirmed by X-ray diffraction experiments. XRD patterns were collected on Philips Xpert and Bruker D8 diffractometers, both using a Cu 2-α source with 40 kV acceleration voltage. Patterns were typically recorded between 10 – 90 ^{0} 2Theta, with 0.017 step size and 0.5 s $step^{-1}$.

The effect of calcination time and temperature on the phase purity was investigated and the results are shown in Figure 3-3. Three samples from the same batch of BZY20 ash were calcined at 1100 ºC for 5 hrs, and 1300 ºC for 3 and 4 hours. The same heating rates and volumetric air flows were used for all samples. All peaks in the collected patterns were indexed to $BaZrO_3$ reported by Peña and Fierro, or to $BaCO_3$ reported by Holl et al.[14,15] A 50-point moving average smoothing was applied to the collected patterns, allowing clearer differentiation of diffraction peaks from background noise. In all collected patterns the [110] peak of $BaZrO_3$ was the most prominent.

After 5 hours at 1100 ºC, $BaCO_3$ peaks were clearly visible in the diffraction pattern, showing an incomplete conversion of reactants. However, when raising the temperature to 1300 ºC, just 3 hours

was sufficient to ensure complete conversion to pure $BaZrO_3$ phase. Calcining for 4 hours at 1300 ºC did not result in any increase or sharpening in the diffraction peaks, indicating the crystallinity of the sample was not increased further with longer times.

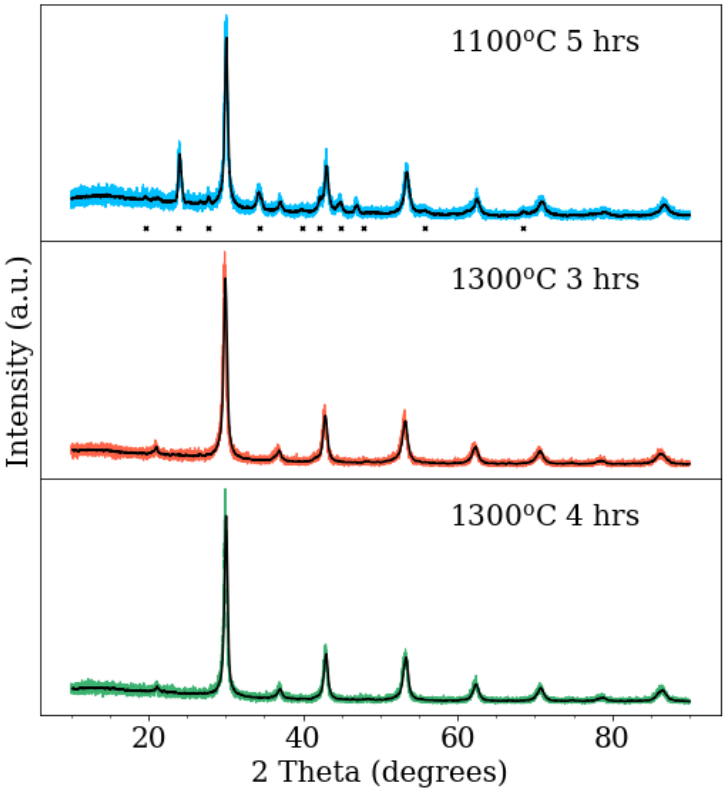


Figure 3-3: XRD patterns of BZY20 ash calcined under different conditions. Marked peaks are indexed to orthorhombic aragonite $BaCO_3$, and all other peaks indexed to cubic perovskite $BaZrO_3$. Black line indicates 50 point moving average smoothing.

Peak fitting for all samples was carried out in X-pert Highscore (Panalytical). Results are shown in Table 3-1 - Table 3-3. All peaks were successfully indexed to hkl planes of barium zirconate or carbonate phases (pdf numbers 01-074-1299 and 01-074-2663).

Table 3-1: XRD peaks of BZY20 calcined at 1100 ºC for 5 hrs. Indexed to $BaZrO_3$, and $BaCO_3$ pdf numbers 01-074-1299 and 01-074-2663 respectively. [14,15]

Pos. (2θ)	FWHM (2θ)	Rel. Int. (%)	Zirconate [hkl]	Carbonate [hkl]
19.6	0.5	2.3		101
21.1	0.8	1.3	100	
23.9	0.1	28.2		111
27.7	0.3	4.1		002
30.0	0.2	100.0	110	
34.3	0.5	10.3		022
37.0	0.4	5.5	111	
39.9	0.9	1.2		220

42.2	0.3	9.2		221
43.0	0.3	28.6	200	
44.9	0.4	6.4		132
47.0	0.6	4.6		113
53.4	0.3	25.8	211	
55.7	0.8	1.4		151
62.6	0.3	9.9	220	
68.4	0.6	1.2		204
71.1	0.8	6.3	311	
79.0	1.1	1.9	222	
86.7	1.1	5.7	321	

Table 3-2: XRD peaks of BZY20 calcined at 1300 ºC for 4 hrs. Indexed to $BaZrO_3$ phase (pdf number 01-074-1299).[15]

Pos. (2θ)	FWHM (2θ)	Rel. Int. (%)	Zirconate [hkl]
21.0	0.3	3.9	100
29.9	0.2	100.0	110
37.0	0.4	5.6	111
42.8	0.2	25.5	200
48.3	0.8	0.3	211
53.2	0.1	25.1	220
62.2	0.5	8.5	310
70.7	0.5	6.4	311
78.5	0.3	2.8	222
86.4	0.9	5.5	321

Table 3-3: XRD peaks of BZY20 calcined at 1300 ºC for 3 hrs. Indexed to $BaZrO_3$ phase (pdf number 01-074-1299).[15]

Pos. (2θ)	FWHM (2θ)	Rel. Int. (%)	Zirconate [hkl]
21.0	0.25	4.1	100
29.9	0.11	100.0	110
36.8	0.38	5.4	111
42.7	0.35	23.7	200
53.1	0.19	21.1	211
62.3	0.38	7.9	220

70.6	0.76	6.0	310
74.7	0.92	0.7	311
78.5	0.06	3.0	222
86.4	0.02	7.3	321

3. 3. 2 Milling of Powders

Calcined powders were milled in a Fristch P7 mill, in a ZrO_2 milling jar using 1mm ZrO_2 milling balls. The ball to powder ratio was initially determined from manufacturer's instructions and was eventually fixed at 5:12 mL of powder to solvent. This corresponded to a close to maximum filling level of the milling jar. Powders were milled in dry conditions and wet conditions, with both isopropanol and water lubricants. Phase changes during milling were characterised using XRD. The effect of milling speed and time were investigated with laser diffraction spectroscopy (LDS) and Brunauer-Emmett-Teller (BET) surface area analysis. Milling was always conducted for 5 min at a time, with a 3-minute pause between cycles to dissipate excess heat. A relatively low maximum milling speed of 500 rpm was employed, as due to the use of solvents elevated pressures can build in the jar at higher speeds.

3. 3. 2. A Brunauer-Emmett-Teller Surface Area Analysis

The surface areas of powder samples milled at 500 rpm were calculated by using the BET isotherm to analyse uptake of dinitrogen into the samples after evacuation of other gases. Experiments were carried out on a micromimetics TriStar in the Oxford Chemistry Surface Analysis Facility. Results are shown in Table 3-4. Calculated surface areas increased with milling time, with the area almost doubling after 30 min milling. Babilo reported areas of BZY powders of 8 $m^2\ g^{-1}$ after milling at 550 rpm for 2 hrs. That the same result can be obtained in less time under less slightly lower milling speeds is a sign that the sol-gel synthesis produced higher surface area particles, in comparison to the glycine nitrate combustion method reported.[12] It must be noted that such low surface area values are subject to a high degree of uncertainty. While the trend of increasing surface area with increased milling time is clear from these measurements, a more detailed study with repeat measurements should be carried out to establish if the trend is truly statistically significant.

Table 3-4: BET surface areas of milled samples

Sample	BET surface area ($m^2\ g^{-1}$)
BZY20 0 min	4.6
BZY20 5 min	5.4
BZY20 30 min	8.0

3. 3. 2. B XRD Phase Analysis

To investigate milling time on the crystalline phase of the material, samples were periodically removed from the milling jar, dried in an oven at 120 ºC, and analysed. The changes during milling in IPA and water are shown in Figure 3-4a & b respectively.

Under both lubricants it was observed that the relative intensity of all peaks decreased in samples with longer milling times. As increasing milling times result in particle size reduction, this reduction is expected to lead to a loss of XRD intensity. Due to the decreases in aligned crystal faces, smaller crystals have shorter X-ray path lengths therefore the chance of a scattering event is reduced. This effect was found to not increase after milling periods greater than 10 min. It was also observed that increased milling times resulted in a large increase in the low angle background scattering. Again, this change appeared complete after 10 min of milling.

It was surprisingly found that when milling BZY20 powders with water, a significant phase change occurs. There is a significant loss of $BaZrO_3$ peaks compared to samples milled for a similar time in IPA. Another phase, which could not be reliably identified, becomes the dominant structure. It is speculated this is due to some oxide or hydroxide phase, formed under the high energy impacts that occur during milling.

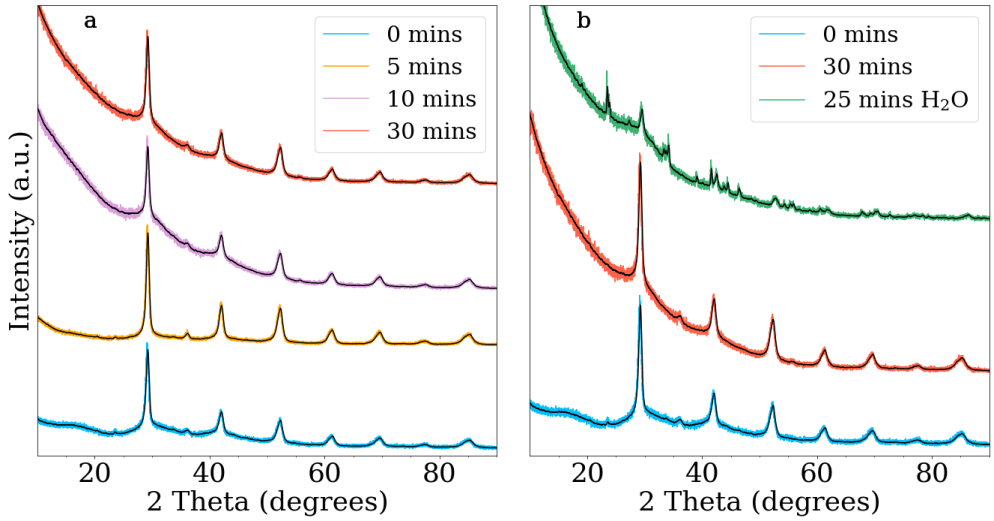


Figure 3-4: XRD patterns recorded during milling experiments; a) shows changes with IPA lubricant and b) with water

3. 3. 2. C Laser Diffraction Spectroscopy

Average particle sizes determined by Laser diffraction Spectroscopy (LDS) are shown in Figure 3-5. Experiments were carried out on a Malvern Mastersizer 3000. Powders were dispersed into a bath of DI water by sonicating for 60s before each size measurement was carried out. Each sample was measured 3 times independently and the average calculated from these three measurements. The results of milling with no lubricant versus an IPA lubricant were investigated at milling speeds of 300 and 500 rpm.

Prior to milling the mean particle size is found to be around 26 µm. After dry milling this powder with no lubricant at 300 rpm, peak at 26 µm is reduced and the presence of a new peak around 2.5 µm is noted (Figure 3-5a). Milling times longer than 15 min do not seem to significantly increase the size reduction effect. Increasing the milling speed results in a greater reduction of the peak at 26 µm, and a broadening of the distribution of the peak centred at 2.5 µm (Figure 3-5c). Both samples milled with no lubricant are still dominated by particles in the size regime of the 26 µm peak.

Adding an IPA lubricant is seen to significantly affect the distribution of particle sizes. Figure 3-5b shows powders wet milled at 300 rpm for times up to 15 min. The peak particle size reduces, and the count increases with longer milling times. Wet milling at 500 rpm has a similar effect to milling at 300 rpm, although the relative peak intensity is lower after milling at higher speeds, suggesting a broader distribution of particle sizes.

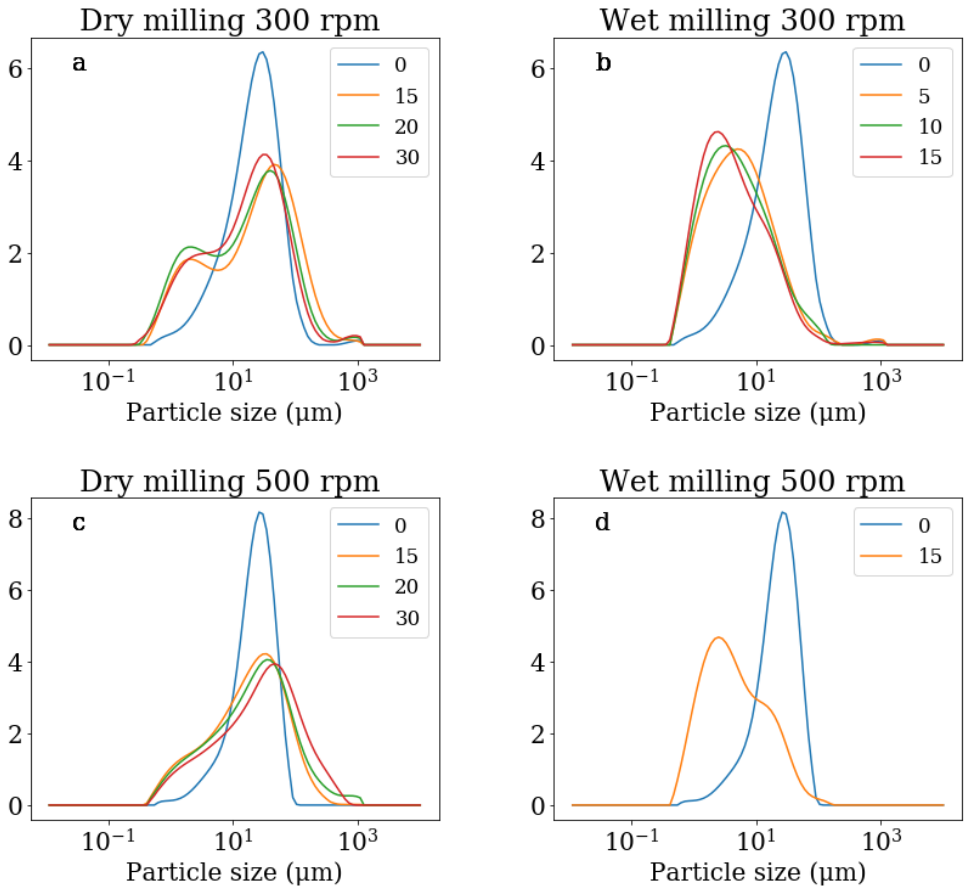


Figure 3-5: Particle sizes versus arbitrary particle counts as measured by laser diffraction spectroscopy, and the results of different speeds and lubricants. All legend values represent time in min.

3. 3. 3 Sintering of Powders

Prior to sintering, barium zirconate powder was uniaxially pressed into pellets using a 13 mm Specac IR pellet die and manual hydraulic press. Typically, 0.5 – 1 g was added to the press, and the load gradually increased up to 375 MPa, and held for 1 minute. The pressure was then slowly released, and the pellet slowly ejected. BET surface areas of BZY20 powder before and after uniaxial pressing into a compact pellet are shown in Table **3-5**. Conditions for measurement were the same as above. The clear reduction in surface area indicates successful compaction. While these low surface area values are subject to the same areas as the values discussed in section 3. 3. 2. A, the order of magnitude difference between the numbers mean it can be said with higher confidence that pressing results in a clear decrease in surface area.

Table 3-5: BET surface areas of pelletised samples

Sample	BET surface area ($m^2\ g^{-1}$)
BZY20 powder	4.7
BZY20 pellet	0.6

Pellets were prone to cracking upon ejection. Tests using binders mixed into the powder, and lubricants for the pellet die were unsuccessful. Greatest success was had using 0.8 g of powder and ensuring that when adding or removing load from the pellet, this was done gradually. Some pellets would totally splinter on ejection from the press, whereas more commonly others would undergo 'endcapping' whereby a thin ring of material breaks away from the outer edge of one of the faces of the pellet (Figure 3-6b).

After pressing pellets were placed in round crucibles and surrounded with sacrificial barium zirconate powder (Figure 3-6a). At such extreme temperatures, barium can start to evaporate from the pellet, leaving a barium deficient lattice. Surrounding the pellet with sacrificial BZY20 powder creates a partial pressure of barium, preventing the formation of barium deficient phases. The sacrificial powder was observed to take on a green colour, and the crucible developed a blue hue after sintering, both thought to be due to the evaporation of barium from within the barium zirconate lattice (Figure 3-6d). Pellets were sintered by slowly heating (5 ºC min^{-1}) to 1500 ºC, where they were held for 24 hours, before slowly cooling to room temperature. To ensure the pellets would have sufficient oxygen to properly form the oxide phase, custom endcaps were designed and manufactured in the University workshops, allowing high air flows to be passed through the furnace work tube at high temperatures. It was necessary to add alumina insulating blocks (Almath crucibles, custom design) to ensure the heat from the furnace did not decompose the silicone O-rings in the endcaps.

Pellets were prepared from both unmilled and milled powders. Post sintering, pellets were often found to have not formed into one cohesive mass and instead formed into thin, fragile layers, partially

attached to each other (Figure 3-6c). This made the subsequent application of Ag paste to form a cell extremely challenging. The pellet microstructure was investigated using scanning electron microscopy (SEM).

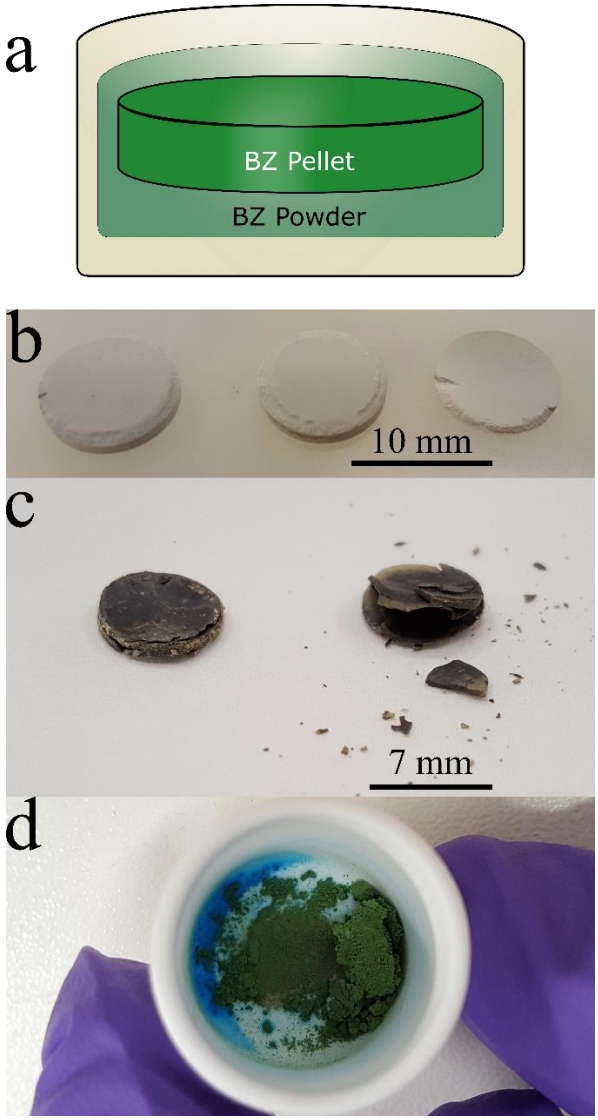


Figure 3-6: Photos showing a) pellet surrounded by BZY20 powder in a crucible, b) Compact pellets before sintering, c) densified pellets after sintering (prepared from milled powder), and d) sacrificial powder in crucible after sintering

3. 3. 3. A Scanning Electron Microscopy

Microstructures of sintered pellets were investigated using a Hitachi S-520 scanning electron microscope. The effects of milling powders prior to sintering on the microstructure of the pellets is presented below.

Figure 3-7 shows a sintered pellet prepared from un-milled powders, after the application of Ag paste ready for electrochemical testing. Ag layer was found to have a thickness of around 85 μm (Figure 3-7a)and to be highly porous. Close contact was formed between the Ag layer and the BZY20 electrolyte, although a small gap was still obvious (Figure 3-7b & c). Pellets prepared from un-milled powder showed

high presence of pores in the structure. Pores fell into two distinct size regimes with average sizes of approximately 30 and 1 nm Figure 3-7d, f & h). BZY20 grain sizes were measured and found to be around 2 μm (Figure 3-7e & g).

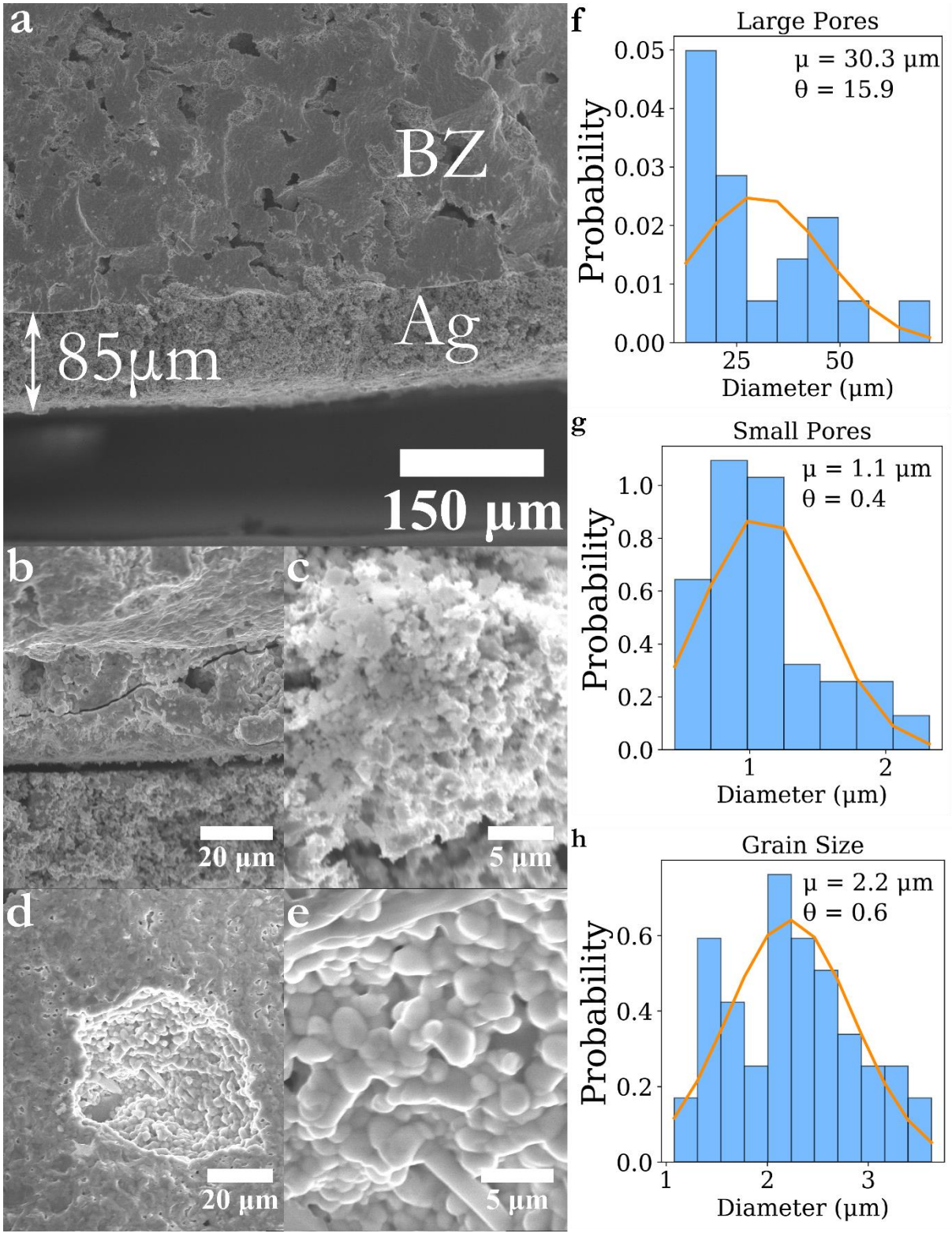


Figure 3-7: a & b) microstructure of sintered BZY20 cell after application of Ag paste c) Close up of Ag paste d) Close up of pore in BZY20 pellet e) Microstructure of BZY20 grains f - h) Measurements of large & small pores, and grain size in BZY20 pellet. μ = mean, θ = standard deviation

Figure 3-8 shows a sintered pellet prepared from BZY20 powder milled for 30 min in IPA at 500 rpm. Large pores were eliminated from the sample (Figure 3-8a). Small pores were still present but in lower concentrations than for pellets made from un-milled powder (Figure 3-8b). The average grain size of the sample was significantly reduced to around 600 nm (Figure 3-8c).

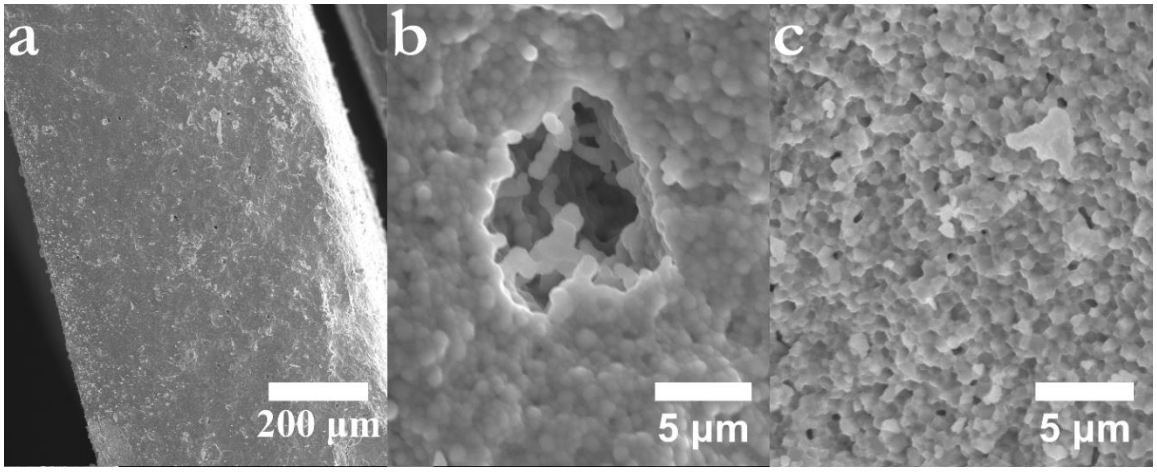


Figure 3-8: a) Structure of BZY20 pellet prepared from milled powder b) Close up of pore in BZY20 pellet c) Microstructure of BZY20 grains.

3. 4 Electrochemical Testing

Cells for electrochemical testing were prepared by application of conductive Ag paste (Sigma Aldrich). A thin layer was applied to each face using a scalpel blade, and then Ag wires were secured to the Ag electrode using additional paste. Ag paste was cured by heating in air up to 150 ºC.

After preparation, cells were placed into a quartz furnace tube, with custom designed endcaps allowing both gas and electrical connections to be made. Cells were then heated up under humidified gases and tested for protonic conductivity using both direct current (DC) voltammetry and alternating current (AC) impedance techniques. All experiments were performed using an Ivium CompactStat Potentiostat at elevated temperatures.

Electrolytic conductivity is defined as the thickness of the cell (distance between the two electrodes) divided by the resistance (or impedance) and area of electrolyte in contact with the electrode, Equation 3.1.[2] In the case of solid electrolytes, the separation of electrodes is equal to the thickness of pellets, and the area to the area of a single face of the pellet.

$$\sigma = \frac{L}{R \times A} \qquad \textit{Equation 3.1}$$

3. 4. 1 Conductivity in Cells Prepared from Unmilled Powders

DC voltammetry techniques rely on the application of Ohm's law to calculate resistance from current-potential (I-V) curves. AC impedance techniques typically apply a smaller polarisation (~100 mV) and measure current responses to this potential stimulus at a range of frequencies. Use of AC impedance to determine the conductivity of cells is preferable, as the use of small polarisations mean the system is more likely to be at steady state. The current response of real circuits to changes in potentials is well known to be non-linear. However, over small potential ranges, the response can be considered pseudo-linear.

The conductivity of a BZY20 cell prepared by sintering of un-milled powder, and application of Ag electrodes was investigated. It was not possible to obtain AC-impedance data of this sample due to high signal to noise ratios. For this reason, DC voltammetry was employed to investigate the conductivity.

Figure 3-9 shows the I-V curves obtained by applying 60s pulses of increasing potential and measuring the response currents. Potentials between 0 – 0.8 V, with steps of 100 mV were measured.

A 10-point moving average smoothing was applied to raw data and is presented in Figure 3-9a & b. Even with smoothing, the data under nitrogen and at temperatures below 700 ºC has a high degree of uncertainty and it is difficult to see clear trends.

Taking the average current at each potential and plotting against potential is more illuminating (Figure 3-9c & d). Except for I-V curve recorded under wet 5% H_2 / N_2 at 550 ºC, all curves show increasing current with potential. Curves recorded under wet nitrogen show a non-linear relationship between

current and potential. Curves recorded under wet 5% H_2 show a linear relationship at high potentials, taking the gradient of this linear region gives the conductivity. Scaling these conductivities by the cell geometries gives the conductivities in S cm^{-1} (Table **3-6**). Constructing an Arrhenius plot from these values gives an activation energy of 135 kJ mol^{-1}. This does not correspond to any ionic conduction processes in the cell, showing DC conductivity is not a valid way to measure this.

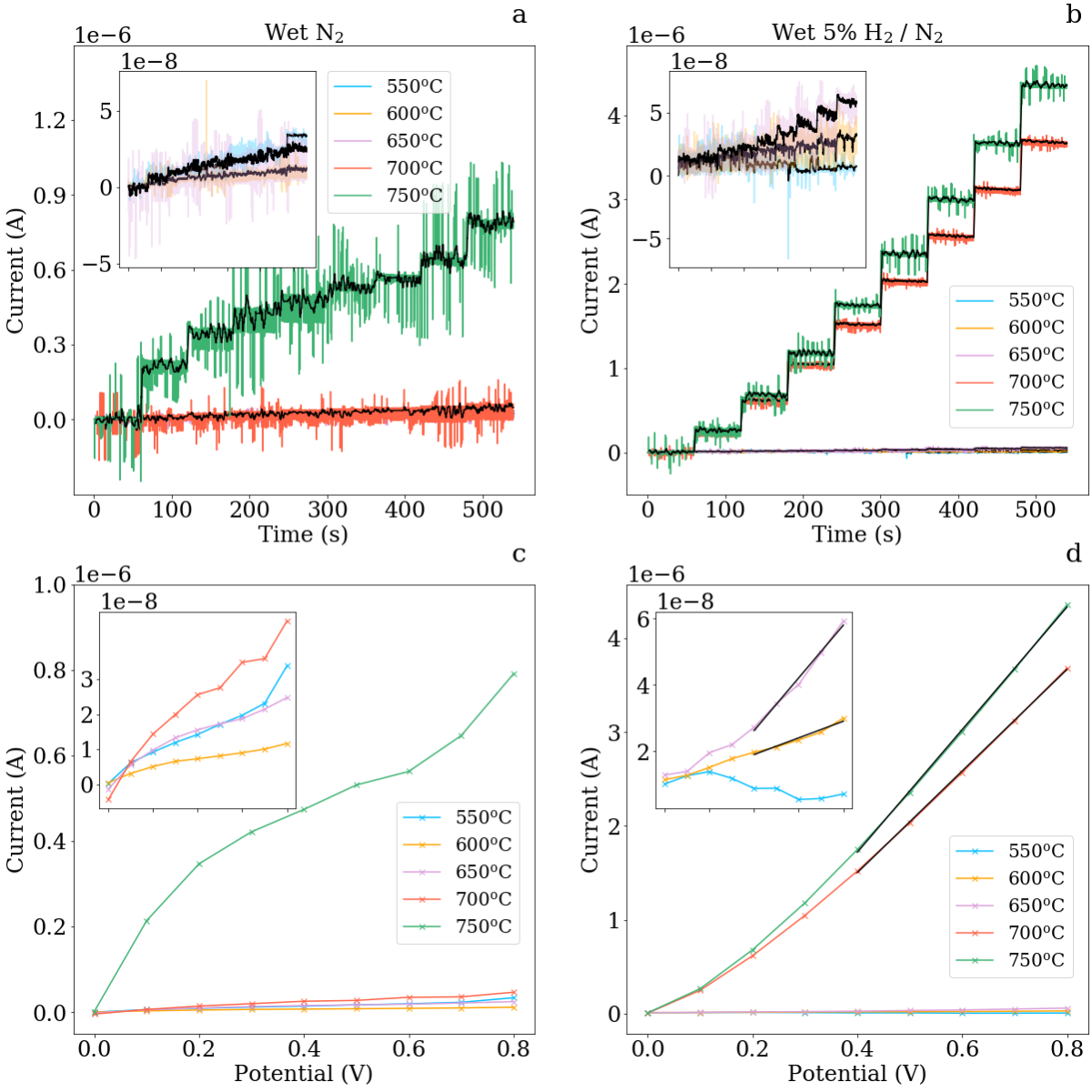


Figure 3-9: I-V curves obtained under humidified N_2 and 5% H_2 / N_2 at varying temperatures. a & b) show raw data obtained when measuring current under a changing electrical potential. Potential is held at values ranging from 0 – 0.8V for 60 seconds. Black lines represent a 10-point moving average smoothing. c & d) show average current at each potential value. Black lines represent linear fit of data between selected points. Axes of main plots are all in values of 10^{-6} A and subplots are all in values of 10^{-8} A.

Table 3-6: Recorded conductivity values from I-V curve gradients

Temperature (°C)	Conductivity (μS cm^{-1})
600	0.025
650	0.079
700	5.4
750	6.5

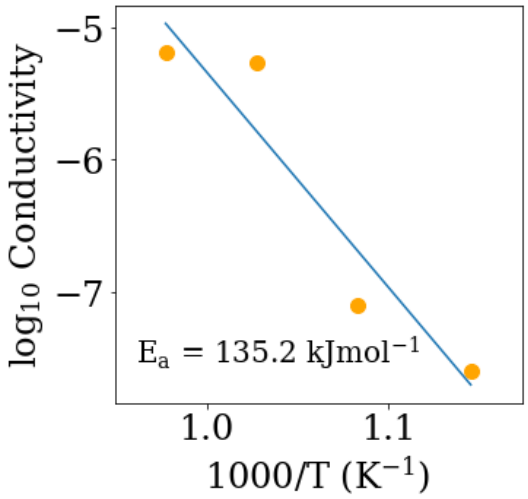


Figure 3-10: Conductivities of cell under humidified 5% H_2 / N_2 at various temperatures, calculated from gradients of I-V curves. Graph shows conductivities and temperatures plotted as an Arrhenius plot.

3. 4. 2 Conductivity in Cells Prepared from Milled Powders

AC Impedance spectroscopy was employed to study the conductivity of cell BZY20 cell composed of a sintered BZY20 pellet prepared from milled powder, and Ag electrodes. A spectrum was recorded at 430 °C, a polarisation of 100 mV was applied at frequencies from 10^6 to 10^{-2} Hz, and the current response recorded. The data is presented as Nyquist and Bode plots Figure 3-11.

Data was fitted using an equivalent circuit model composed of two Randles circuits in series, preceded by a series resistor (Figure 3-12). The Randels circuits, consisting of a resistor in parallel with a Constant Phase Element (CPE), represent the two ionic transfer processes (intra- and inter-grain transfer of protons) within the electrolyte. A CPE is used to account for the non-ideal behaviour of capacitive processes in the cell. Equation 3.2 shows the relationship between the impedance and capacitance. When n = 1, Q_0 is equal to the capacitance; when n takes values less than 1 the arc of the semicircle is reduced, giving a depressed semicircle.

In addition to collecting bulk-conductivity data, AC impedance spectroscopy can be used to find values of intra- and inter-grain transport processes in the cell. Intra-grain transport is easier and faster

than inter-grain transport, therefore at high frequency values the recorded impedance data will be dominated by intra-grain transport. At low frequencies, the inter-grain transport process will dominate the impedance data. By modelling the data as two separate transport process, separated by frequency, values of the intra- and inter-grain conductivity are calculated.

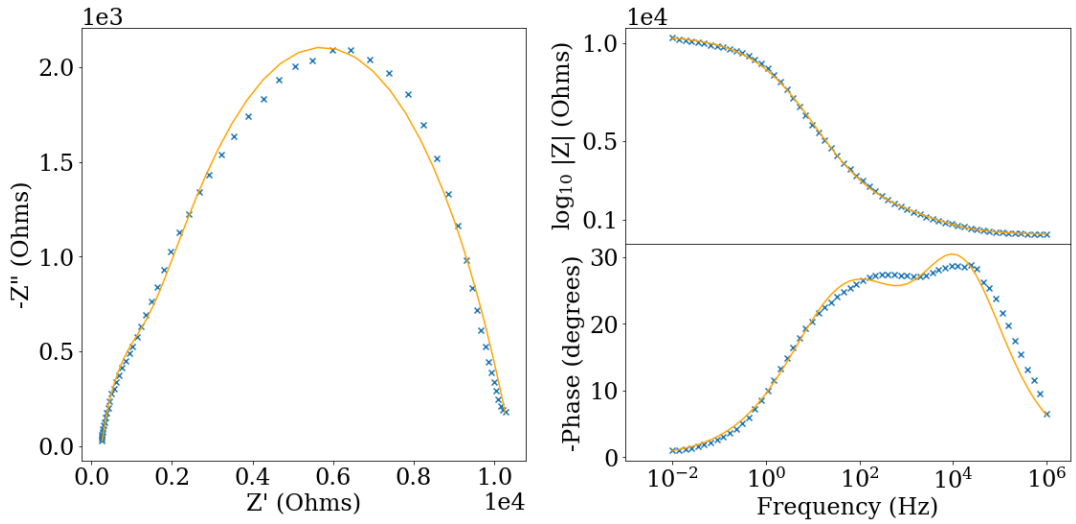


Figure 3-11: Nyquist (left) and Bode (right) plots recorded at 430 °C on cell constructed from BZY20 pellet formed from milled BZY20 powder.

Fitted values for each component are displayed in Table **3-7**. A series resistor is used to account for circuit resistances such as contact resistance between the electrode and the electrolyte. This is calculated to be approximately 250 Ω. Resistances to intra- and inter-grain transport are calculated to be 860 Ω (2.6 x10^{-4} S cm^{-1}) and 9.3 kΩ (2.4 x10^{-5} S cm^{-1}).

$$Z = \frac{1}{Q^{\circ}(j\omega)^{n}} \qquad \textit{Equation 3.2}$$

Table 3-7: Fitted values for equivalent circuit components

Component	Resistance (Ω)	Capacitance (F)	N
R_1	248.3	-	-
R_2	863.2	-	-
R_3	9326	-	-
CPE_1	-	1.100 x10^{-6}	6.882 x10^{-1}
CPE_2	-	1.252 x10^{-5}	5.370 x10^{-1}

Calculated bulk conductivity value (260 μS cm^{-1}, 400 ºC, wet hydrogen) are comparable to literature values, given in section 1. 3. 1 (Chapter 1). Fabbri et al. reported a BZY20 material displaying a bulk conductivity of 900 μS cm^{-1} (350 ºC, wet hydrogen), Gorelov et al. reported a BZY15 cell with a total conductivity of 600 μS cm^{-1} (425 ºC, wet air), and Manthiram et al. measured a total conductivity of 300 μS cm^{-1} for a BZY20 membrane (425 ºC, wet nitrogen).[16–18] Much higher conductivity values are reported (Sawant et al., Yamazaki et al., Babilo et al.),[2,8,19] but given the problems encountered with the sintering stage, it is not surprising these high values cannot be measured.

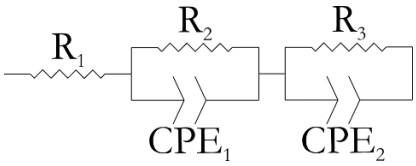


Figure 3-12: Equivalent circuit model used for AC impedance spectroscopy analysis

3. 4. 3 Electrochemical Ammonia Synthesis

Using the cell described above from milled powders, the rates of ammonia synthesis were recorded under open circuit and applied potentials up to 1.0 V (Figure 3-13). The full electrochemical testing setup is described in detail in chapter 4, where the sources of thermal ammonia in these cells are also explored. For now, it is enough to say that thermal ammonia is expected, and the extent of electrochemical ammonia production is defined as the total rate less the open circuit rate under the same conditions. Produced ammonia was trapped in 0.1 M H_2SO_4 and measured using an ion-selective electrode. Experiments were conducted at 430 ºC, under humidified 5% H_2 / N_2 (50 mL min^{-1}). Measurement times were long, with most run overnight to accumulate sufficient ammonia. Rates were normalised to the measurement time, and the geometric surface area of the electrolyte pellet. Current density is calculated from the total current passed during the measurement, normalised to the geometric surface area of the electrolyte pellet. Current efficiency is calculated by dividing the purely electrochemical rate of ammonia by the theoretical ammonia rate if all passed electrons are converted into ammonia.[20] All values from Figure 13 are tabulated in Table 3-8.

Rates of ammonia synthesis varied between 2 x10^{-11} mols s^{-1} cm^{-2}, and 6 x10^{-13} mols s^{-1} cm^{-2}. A comparable rate is reported by Yun et al, who measured 4.9 x10^{-11} mols s^{-1} cm^{-2} in a BZY20 cell with Ag electrodes operating at 550 ºC, with water as the proton source (30 mL min^{-1} humidified N_2).[21] Nonetheless, the recorded values are below other literature reports.[22] A low rate of electrochemical ammonia production is likely dependant on the issues with producing dense electrolyte pellets. A low rate of thermal ammonia synthesis could be due to the presence of water in the gas stream, preferentially adsorbing to metal surface sites and blocking the adsorption of dinitrogen.

The rates did increase with applied potential, with a large spike in the rate at 0.8 V, before subsequently dropping. However, the low rate at 0.6 V applied potential does not fit this trend. As the measurement times were long, the ammonia synthesis rates are subject to interference from extraneous

sources of ammonia, as covered in a recent article by Greenlee et al.[23] While the rates and trends are promising, they should be treated with a degree of caution due to the low overall values, which will be subject to uncertainties.

All closed-circuit rates exceeded the open circuit rate by an order of magnitude, therefore current efficiencies could be calculated. These are consistent with literature reports, and (as expected) follow the same trend as the ammonia synthesis rates. Current densities show a linear increase with applied potential but are extremely low. The linearity of the response is not expected for ionic currents and could indicate an electrical short circuit somewhere in the cell. BZY materials are expected to show some electrical conductivity, but not at this temperature or under this gas atmosphere.[24]

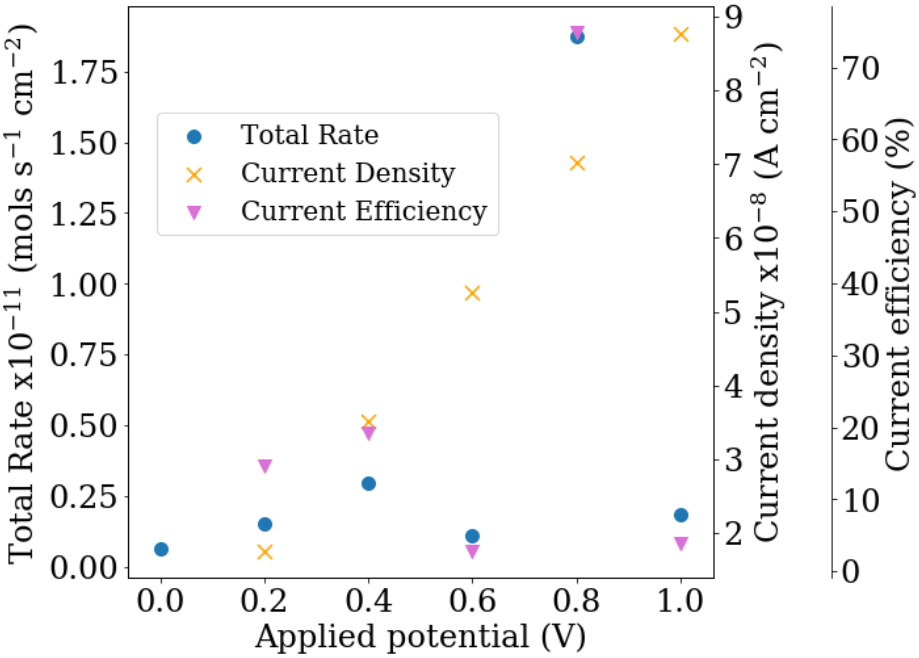


Figure 3-13: Rates, current densities and current efficiencies vs applied potential

Table 3-8: Tabulated values from Figure 3-13

Potential	Rates	Current Density	Faradaic Efficiency
0	6.3 E-13	-	-
0.2	1.5 E-12	1.8 E-08	14.6
0.4	3.0 E-12	3.5 E-08	19.2
0.6	1.1 E-12	5.3 E-08	2.7
0.8	1.9 E-11	7.0 E-08	74.8
1	1.8 E-12	8.8 E-08	3.9

3. 5 Conclusions

Proton conducting barium zirconate cells were successfully synthesised and characterised. Various synthetic parameters were optimised, and the conductivity values were investigated using DC and AC techniques. The rates of electrochemical ammonia synthesis were recorded.

It was found that phase pure barium zirconate could be synthesised by a sol-gel method followed by calcination at 1300 ºC for 3 hours. Milling these powders resulted in a decrease in average particle size, as measured by LDS, and an increase in the BET surface areas. The best milling results came when using IPA as a lubricant. Milling at 500 rpm for 30 min was sufficient to obtain good particle size reduction and surface area increase.

After preparation of the powders, they were pressed and sintered into dense pellets. The sintering step presented significant challenges, and almost all samples resulted in badly formed, cracked pellets, making subsequent preparation of electrochemical cells difficult. Nonetheless, cells were successfully prepared from both unmilled and milled powders.

These pellets were characterised using DC and AC techniques. It was found that DC characterisation of conductivity does not give reliable values of the conductivity within the cell, but that using AC techniques the intra- and inter-grain conductivities could be calculated. These were within the range of reported values in the literature.

The rates of ammonia synthesis were recorded as a function of applied potential. These were found to be comparable to some of the lowest reports in literature, and to show some increase in rates with increasing potential, although this trend was far from clear.

The objectives stated at the beginning of this chapter were to:

1. Develop synthetic procedures for preparation of dense, conductive BZY20 membranes.

2. Measure the conductivity of cells prepared from synthesised membranes, and silver electrodes.

3. Measure rates of ammonia synthesis in these cells.

All these objectives were realised, however given the significant problems encountered during the preparation of BZY20 ceramics this section of work was concluded. The proton mobility in the prepared electrolytes did not reach the highest values reported in literature, and it was suggested that this was limiting the electrochemical ammonia production.

The recent availability of commercial ultra-thin, highly conductive, electrode supported, high-temperature proton-conducting electrolytes seemed a better avenue of research than continuing to make the electrolytes inhouse. As the initial focus of this project was on testing catalysts for electrochemical ammonia synthesis, these commercial samples provided a more consistent base from which to test and optimise electrochemical ammonia synthesis cells.

3. 6 References

(1) Bi, L.; Traversa, E. Synthesis Strategies for Improving the Performance of Doped-BaZrO3 Materials in Solid Oxide Fuel Cell Applications. *J. Mater. Res.* **2014**, *29* (1), 1–15.

(2) Babilo, P.; Uda, T.; Haile, S. M. Processing of Yttrium-Doped Barium Zirconate for High Proton Conductivity. *J. Mater. Res.* **2007**, *22* (05), 1322–1330.

(3) Tong, J.; Clark, D.; Hoban, M.; O'Hayre, R. Cost-Effective Solid-State Reactive Sintering Method for High Conductivity Proton Conducting Yttrium-Doped Barium Zirconium Ceramics. *Solid State Ion.* **2010**, *181* (11–12), 496–503.

(4) Duval, S. B. C.; Holtappels, P.; Vogt, U. F.; Pomjakushina, E.; Conder, K.; Stimming, U.; Graule, T. Electrical Conductivity of the Proton Conductor BaZr0.9Y0.1O3−δ Obtained by High Temperature Annealing. *Solid State Ion.* **2007**, *178* (25), 1437–1441.

(5) Coors, W. G.; Manerbino, A.; Ricote, D. M. and S. Fabrication of Yttrium-Doped Barium Zirconate for High Performance Protonic Ceramic Membranes. In *Perovskite Materials - Synthesis, Characterisation, Properties, and Applications*; 2016.

(6) Park, K.-Y.; Seo, Y.; Kim, K. B.; Song, S.-J.; Park, B.; Park, J.-Y. Enhanced Proton Conductivity of Yttrium-Doped Barium Zirconate with Sinterability in Protonic Ceramic Fuel Cells. *J. Alloys Compd.* **2015**, *639*, 435–444.

(7) Biswas, M.; An, H.; Choi, S. M.; Son, J.-W.; Lee, J.-H.; Kim, B.-K.; Lee, H.-W.; Yoon, K. J. Low-Temperature Sintering of Ba(Zr,Y)O3-Based Proton Conducting Oxides Using BaO–CuO Eutectic Flux as Sintering Aid. *Ceram. Int.* **2016**, *42* (8), 10476–10481.

(8) Yamazaki, Y.; Hernandez-Sanchez, R.; Haile, S. M. High Total Proton Conductivity in Large-Grained Yttrium-Doped Barium Zirconate. *Chem. Mater.* **2009**, *21* (13), 2755–2762.

(9) Nuernberg, R. B.; Morelli, M. R.; Nuernberg, R. B.; Morelli, M. R. Microwave Assisted Synthesis and Sintering of Ba0.5Sr0.5Co0.8Fe0.2O3-δ Perovskite. *Mater. Res.* **2015**, *18* (1), 85–91.

(10) Muccillo, R.; Muccillo, E. N. S.; Kleitz, M. Densification and Enhancement of the Grain Boundary Conductivity of Gadolinium-Doped Barium Cerate by Ultra Fast Flash Grain Welding. *J. Eur. Ceram. Soc.* **2012**, *32* (10), 2311–2316.

(11) Dahl, P. I.; Lein, H. L.; Yu, Y.; Tolchard, J.; Grande, T.; Einarsrud, M.-A.; Kjølseth, C.; Norby, T.; Haugsrud, R. Microstructural Characterization and Electrical Properties of Spray Pyrolyzed Conventionally Sintered or Hot-Pressed BaZrO3 and BaZr0.9Y0.1O3−δ. *Solid State Ion.* **2011**, *182* (1), 32–40.

(12) Babilo, P. Processing and Characterization of Proton Conducting Yttrium Doped Barium Zirconate for Solid Oxide Fuel Cell Applications. phd, California Institute of Technology, 2007.

(13) Campbell, P. F.; Ortner, M. H.; Anderson, C. J. Differential Thermal Analysis and Thermogravimetric Analysis of Fission Product Oxides and Nitrates to 1500 C. *Anal. Chem.* **1961**, *33* (1), 58–61.

(14) Holl, C. M.; Smyth, J. R.; Laustsen, H. M. S.; Jacobsen, S. D.; Downs, R. T. Compression of Witherite to 8 GPa and the Crystal Structure of BaCO3II. *Phys. Chem. Miner.* **2000**, *27* (7), 467–473.

(15) Peña, M. A.; Fierro, J. L. G. Chemical Structures and Performance of Perovskite Oxides. *Chem. Rev.* **2001**, *101* (7), 1981–2018.

(16) Fabbri, E.; Pergolesi, D.; Licoccia, S.; Traversa, E. Does the Increase in Y-Dopant Concentration Improve the Proton Conductivity of BaZr1−xYxO3−δ Fuel Cell Electrolytes? *Solid State Ion.* **2010**, *181* (21), 1043–1051.

(17) Gorelov, V. P.; Balakireva, V. B.; Kuz'min, A. V. Ionic, Proton, and Oxygen Conductivities in the BaZr1 − XYxO3 − α System (x = 0.02−0.15) in Humid Air. *Russ. J. Electrochem.* **2010**, *46* (8), 890–895.

(18) Manthiram, A.; Kuo, J. F.; Goodenough, J. B. Characterization of Oxygen-Deficient Perovskites as Oxide-Ion Electrolytes. *Solid State Ion.* **1993**, *62* (3), 225–234.

(19) Sawant, P.; Varma, S.; Wani, B. N.; Bharadwaj, S. R. Synthesis, Stability and Conductivity of BaCe0.8−xZrxY0.2O3−δ as Electrolyte for Proton Conducting SOFC. *Int. J. Hydrog. Energy* **2012**, *37* (4), 3848–3856.

(20) Ouzounidou, M.; Skodra, A.; Kokkofitis, C.; Stoukides, M. Catalytic and Electrocatalytic Synthesis of NH3 in a H+ Conducting Cell by Using an Industrial Fe Catalyst. *Solid State Ion.* **2007**, *178* (1), 153–159.

(21) Yun, D. S.; Joo, J. H.; Yu, J. H.; Yoon, H. C.; Kim, J.-N.; Yoo, C.-Y. Electrochemical Ammonia Synthesis from Steam and Nitrogen Using Proton Conducting Yttrium Doped Barium Zirconate Electrolyte with Silver, Platinum, and Lanthanum Strontium Cobalt Ferrite Electrocatalyst. *J. Power Sources* **2015**, *284*, 245–251.

(22) Giddey, S.; Badwal, S. P. S.; Kulkarni, A. Review of Electrochemical Ammonia Production Technologies and Materials. *Int. J. Hydrog. Energy* **2013**, *38* (34), 14576–14594.

(23) Greenlee, L. F.; Renner, J. N.; Foster, S. L. The Use of Controls for Consistent and Accurate Measurements of Electrocatalytic Ammonia Synthesis from Dinitrogen. *ACS Catal.* **2018**, *8* (9), 7820–7827.

(24) Coors, W. G. Co-Ionic Conduction in Protonic Ceramics of the Solid Solution, BaCe(x)Zr(y-x)Y(1-y)O3- Part I: Fabrication and Microstructure. **2011**.

Chapter 4 Electrochemical Ammonia Synthesis in Barium-Cerate-Zirconate Cells

4. 1 Background

Electrochemical ammonia synthesis offers a promising alternative to the energy and carbon intensive Haber-Bosch process. Significant challenges remain for the development of electrochemical ammonia synthesis, however. The highly inert nature of the dinitrogen molecule towards reduction presents the most difficult one. As the most common electrochemical solvent, water, is much more easily reduced than dinitrogen, this presents a major challenge for synthetic routes using aqueous electrolytes. Molten salt cells have shown promising rates, but present many complications to design, build, and operate. Many different types of electrochemical cells have been considered in literature and are reviewed in Chapter 1.

Ceramic electrolytes operating at temperatures at which H^+ or O^{2-} ion conduction is possible have been demonstrated for NH_3 synthesis. The high temperatures permit fast reaction kinetics, while the solid-state geometry permits easy separation of the cathode and anode gas feeds if desired. Cells with isolated anode and cathode feeds are referred to as two-chamber reactors, and those with no separation, single chamber reactors.

Among the first reports of electrochemical ammonia synthesis, was one by Marnellos and Stoukides in 1998. They demonstrated that an electrochemical cell prepared from a proton conducting $SrCe_{0.95}Yb_{0.05}O_{3-\delta}$ perovskite electrolyte and palladium electrodes could produce ammonia electrochemically operating at atmospheric pressure and 570 ºC, at rates of 5×10^{-9} mol cm^{-2} s^{-1} with 78% efficiency.[1] Since this report, a large number of electrolytes have been tested and the maximum rate remains on the order of 10^{-9} mol cm^{-2} s^{-1} for most, regardless of the material.[2,3] Predictably, the highest rates are observed when H_2 and N_2 are used, although the reaction has been demonstrated with humidified nitrogen, and even methane as a hydrogen source.[4,5] When H_2O is used the rates and efficiencies are much lower; a study using $BaZr_{0.8}Y_{0.2}O_{3-\delta}$ electrolytes at 550 ºC with a range of electrodes found rates of around 10^{-11} mol cm^{-2} s^{-1} at efficiencies <0.5%. [6] This was recently increased to 1.5×10^{-10} mol cm^{-2} s^{-1} at a much lower temperature (400 ºC) using a $Ce_{0.8}Gd_{0.18}Ca_{0.02}O_{2-\delta}$/carbonate composite electrolyte and a $La_{0.6}Sr_{0.4}Co_{0.2}Fe_{0.8}O_{3-\delta}$-composite cathode, but the efficiency remained low (0.2%).[7]

The possible pathways for decomposition of dinitrogen and dihydrogen and the subsequent reaction to ammonia in single chamber reactors are presented below. Figure 4-1a shows the ideal case for the electrochemical reduction of dinitrogen to ammonia; at the anode hydrogen reacts to protons and electrons, which travel through the electrolyte and external circuit to the cathode, where they react with nitrogen to form ammonia. The reduction of dinitrogen may take place via an associative or dissociative

mechanism, Figure 4-1b. Once adsorbed to the surface, nitrogen or dinitrogen may form hydrogenated or protonated species via reaction with hydrogen, or protons (Figure 4-1d). Adsorbed hydrogen may be formed by dissociation of dihydrogen, or by a one electron reduction of protons from the electrolyte (Figure 4-1c).

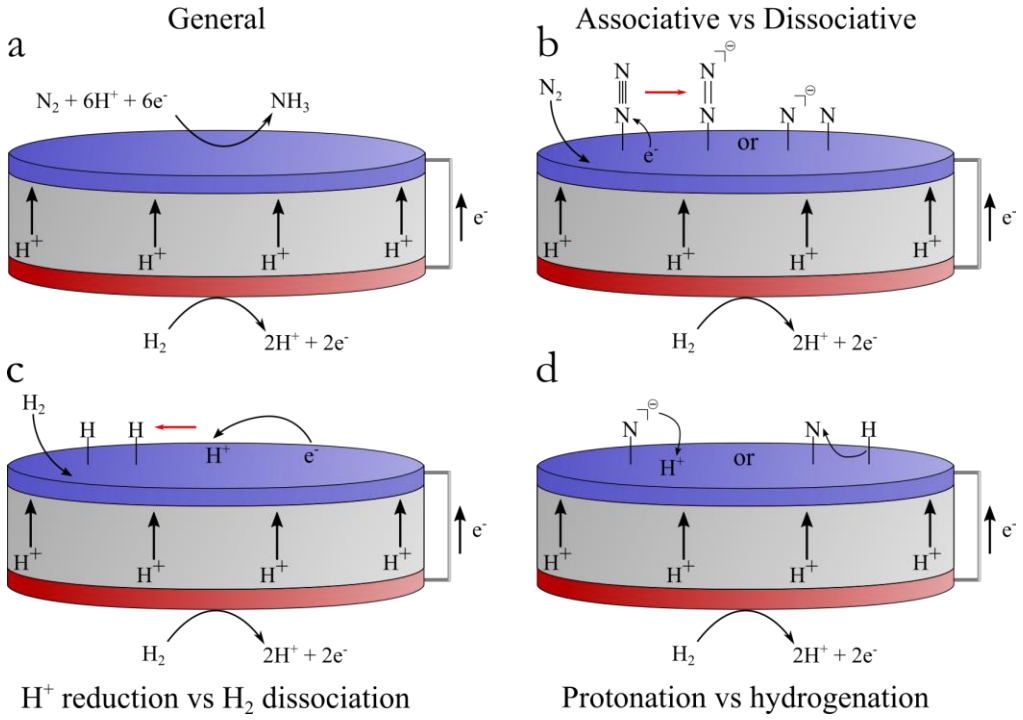


Figure 4-1: Possible pathways for decomposition of N_2 and H_2 molecules in single chamber reactors, and subsequent formation of NH_3. a) Ideal electrode reactions for oxidation of hydrogen at the anode and electrochemical reduction of dinitrogen at the cathode

The presence of adjacent adsorbed hydrogen atoms presents a loss pathway- hydrogen evolution reaction may occur at the cathode. This extent of this loss process is measured by calculating the current efficiency. As both nitrogen and hydrogen are present at both electrodes, gaseous adsorption and thermal reaction can occur. For this reason, the pure electrochemical rate is defined as the rate at applied potential minus the rate at open circuit. Electrochemical NH_3 production at higher temperatures is significantly affected by non-electrochemical reactions. For example, at 620 °C over a Ni-BCZY cathode co-fed with N_2 and H_2, the net electrochemical rate (i.e. the rate at closed circuit minus the rate at open circuit) was 40% greater than the open circuit rate.[8] The reverse reaction is also possible and NH_3 production rates start to drop above 600 °C due to NH_3 decomposition.[8–10]

Another challenge facing ceramic cells is the small area at which reactions can occur. As the electrolyte is solid and flat even on the microscale, the area at which the electrode and electrolyte meet is determined by the dimensions of the electrode. Liquid electrolytes, which can flow around microstructured electrodes, have a much higher surface area where reactions can occur. The low surface area can be somewhat compensated for by spillover of ions from the electrolyte into the electrode. This effect, often reported as Non-Faradaic Modification of Catalytic Activity (NEMCA),[11] can lead to dramatic enhancements in the rate of catalytic reactions at electrode surfaces, several orders of

magnitude greater than the rate expected for a thermal process.[12] However this effect is reported to be small for the electrochemical synthesis of ammonia.[13]

For the successful electrochemical synthesis of ammonia, reduced nitrogen, protons, and electrons must all meet in the same area, known as the triple-phase boundary (Figure 4-1). If electrodes can be formulated such that they conduct protons and electrons, this will extend the area of the triple phase boundary to the entire microstructured area of the electrode. [2,14]

Further challenges are presented by the low conductivity of ceramic electrolytes, and challenging, high temperature syntheses. Considering the limitations of solid-electrolyte cells, the aims for the efficient reduction of dinitrogen to ammonia should be to fabricate electrodes with proton conductivity and containing catalysts which can efficiently reduce dinitrogen. Furthermore, the conductivity of the electrolyte should be maximized.

4. 1. 1 Objectives

The aims of this chapter were as follows:

1. Prepare electrochemical cells and characterise their physical and electrochemical properties
2. Test new electrode catalysts for electrochemical ammonia synthesis
3. Test a different cell geometry to allow easier quantification of electrochemical ammonia

Electrode supported proton conductive BCZY membranes were provided by CoorsTek. These were characterised by their physical and electrochemical properties. New electrode catalysts were then applied to the cells and tested for their activity for electrochemical ammonia synthesis. Changes in electrochemical properties were also explored. Finally, to highlight electrochemical production of ammonia, a two-chamber cell was constructed, to allow separation reactants and products.

4. 2 Experimental

4. 2. 1 Cell & Electrode Preparations

Cells were supplied by CoorsTek. A diagram of typical test cell is shown in Figure 4-3c. The supplied cells consisted of a dense membrane of $BaZr_{0.7}Ce_{0.2}Y_{0.1}O_{3-d}$ (BCZY) 25 μm thick on a 0.7 mm Ni-BCZY (70% Ni) ceramic-metallic (cermet) support with OD 10 mm. The Ni phase of the cermet makes it electronically conductive, therefore it can be used directly as an electrode. The cermet was always connected as the working electrode. A variety of anode systems were tested; the area was always fixed at 3.14 cm2 (1 cm wide on tube of 1 cm diameter, area = π). Carbon felt (C-felt) was used as a current collector for the electrodes, as it is highly conductive and porous, thus allowing gas diffusion. C-felt was either packed into the inner cell cavity or wrapped around the outer face and secured with a length of Ag wire. The rough ends of the cylindrical cells (Figure 4-3e) were polished to smooth surfaces (Figure 4-3a) using 600 grit sandpaper to the same lengths. This was done to ensure that the mass of support (known to be an active thermal ammonia synthesis catalyst, 8) was roughly equal, however it was difficult to achieve uniform results and cells differed by up to 1 mm in length.

Ag counter electrodes were first tested to benchmark the system against literature, then new systems were explored, including Pt nanoparticles and Ru nanoparticle impregnated electrodes. Under these conditions, there will be thermal ammonia produced on the surfaces of the cell. The extent of the electrochemical contribution is defined as the difference between the open and closed-circuit rates. Ag was chosen as an appropriate choice for benchmarking, as it has a very low expected rate of thermal ammonia synthesis- the volcano plot for ammonia synthesis activity compared to atomic number of various d-metals peaks at Ru and declines thereafter (Chapter 1).[15]

To prepare Ag electrodes, a fixed area on the outer face of a BCZY cell was masked using Parafilm. Ag paste was brush painted onto the outer electrode surface with a loading of ~10 mg cm^{-2}. After application the Ag paste was cured in an oven at 130 ºC for 2 hrs and was ready to use (Figure 4-2a).

Platinum electrodes were prepared from a Pt ink (Sigma Aldrich), brush painted over an area of exposed electrolyte. An initial test used a low loading of 2.5 mg cm^{-2}, this was subsequently increased to match the 10 mg cm^{-2} used for Ag electrodes. Pt ink was cured at 450 ºC in a furnace under air flow for 2 hrs.

To prepare an impregnated porous electrode, a saturated solution of $Ru(acac)_3$ (Sigma Aldrich) in acetone was added dropwise to the electrode, while slowly rotating the cell during solvent evaporation. This process was repeated until the desired loading was reached. The total mass of Ni/BCZY cermet was estimated using known values for the density (6.498 g cm^{-3}, [16]) and calculated volume of the BCZY electrolyte, and the loading of Ru fixed at 5 wt. %. Reduction of $Ru(acac)_3$ was carried out in a furnace at 350 ºC under 5% H_2 / Ar flow. Post-reduction, a metallic film was observed on the impregnated electrodes and on the outer electrolyte layer (Figure 4-2b). This Ru film was undesirable as it could result

in electrical shorts between electrodes. Therefore, it was removed by wiping the surface with a NaClO soaked tissue. The cell was then thoroughly rinsed with DI water.

Finally, a cell with Ru-impregnated cathode was modified by Pt impregnation of the Ag electrode, and addition of a reference electrode. Initially this was attempted using a dual layer of Pt followed by Ag paste, but ultimately a wet impregnation procedure was settled on. The reference electrode was applied by brush painting Ag paste over a secondary area of the electrolyte. The Ag electrode was found to have poor wettability with a contact angle estimated from Figure 4-2c to be around 145 °, indicative of a hydrophobic surface.[17] however a solution of H_2PtCl_6 $6H_2O$ in EtOH (12.5 mg mL^{-1}) was successfully impregnated. Solution was applied over the masked Ag surface (Figure 4-2d) to give a final Pt loading of 0.1 mg cm^{-2}. Addition of acidic platinum source resulted in darkening of Ag layer, which remained even after in-situ reduction during testing (Figure 4-2e). All tested cells are listed in Table 4-1.

Table 4-1: All tested cells, and the anode & cathode formulations for each.

Cell	Anode	Cathode
Ag | BCZY | Ni/BCZY	Ag	Ni/BCZY cermet
Pt | BCZY | Ni/BCZY	Pt	Ni/BCZY cermet
Ag | BCZY | Ru/Ni/BCZY	Ag	Ru impregnated Ni/BCZY
Ag/Pt | BCZY |Ru/ Ni/BCZY	Pt impregnated Ag	Ru impregnated Ni/BCZY

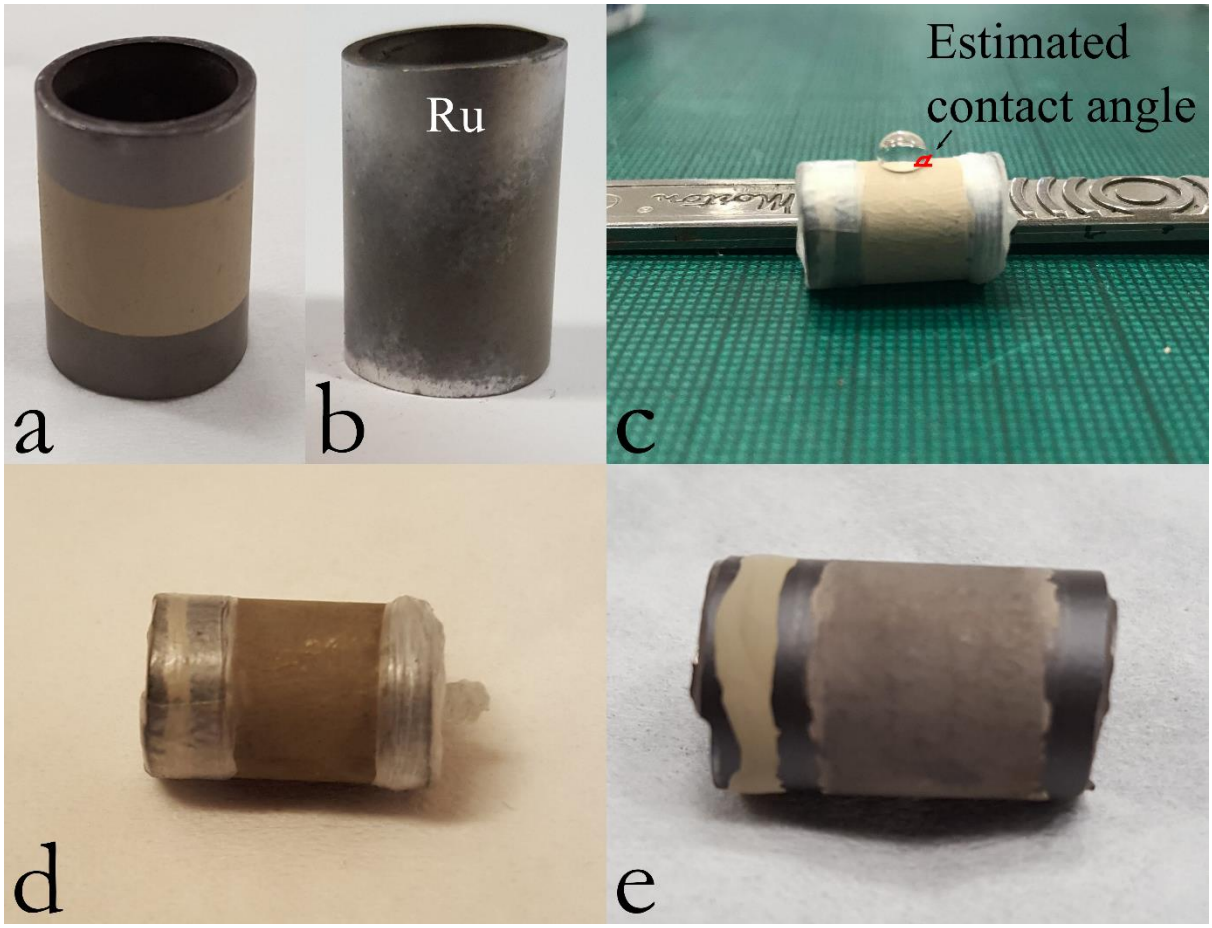


Figure 4-2: Photos of cells during electrode preparations. a) Ag anode b) Ru film after impregnation and reduction c) Water droplet on Ag film anode, estimate of contact angle between droplet and surface illustrated d) Impregnation of Pt maintaining pure Ag reference electrode e) Differences between Ag and Ag / Pt electrodes.

4. 2. 2 Testing of Electrochemical Cells

A single chamber geometry was employed for all tests. Cell test apparatus shown in Figure 4-3a. Pure hydrogen is mixed with 5% H2/N2 using a pair of mass-flow controllers, then flowed through a quartz test tube, which is sealed with custom built endcaps encompassing electrical feedthroughs. This allows for various ratios of H_2:N_2 to be tested, but the cell can still be safely held in a reducing atmosphere unattended under 5% H_2 flow, due to the flammability of pure hydrogen. The outflow gas is then bubbled through a 0.1 M H_2SO_4 an acid trap. Gaseous ammonia dissolves in the acid trap and is quantified using an ion-selective electrode (ISE). Unless stated otherwise, all tests were carried out under the same conditions; 600 °C, 150 mL min^{-1} 3:1 H_2:N_2. A potential was applied to the cell, typically either 2 V or open circuit, for 1 hr, the current was measured. For electrochemical ammonia (EC NH_3) synthesis, many reports show a plateau or even decrease in rate after a certain potential as the cathode surface becomes saturated with H adatoms.[18–20] -2V is reported as the optimum potential for NH_3 production in BCZY72 cells.[8–10]

Three important parameters for characterising the cells are the current density in mA cm^{-2}, the rate in mols s^{-1} cm^{-2}, and the current efficiency. Current density is calculated from the average of the

measured current over the course of testing, divided by the geometric surface area of the electrode applied to the outer face of the cylindrical cell. Rate is determined by converting the measured ppm values determined via ISE, and then divided by the measurement time, and the geometric surface area in the same manner current density. Current efficiency is defined as the purely electrochemical rate divided by the rate at which ammonia would be produced if 100% of the current passed through the cell was converted into ammonia.

Gas and electrical connections are supplied through custom built endcaps (Figure 4-3b). Endcaps were designed using Autodesk Inventor and machined in the universities workshop. Potentials were applied, and currents measured, using an Ivium Compactstat with 4 electrodes, where the working & sense, and reference & counter electrodes were shorted together. Working & sense electrodes were always connected to the Ni/BCZY cermet electrode, meaning under positive cell polarisation the cermet is acting as the cathode.

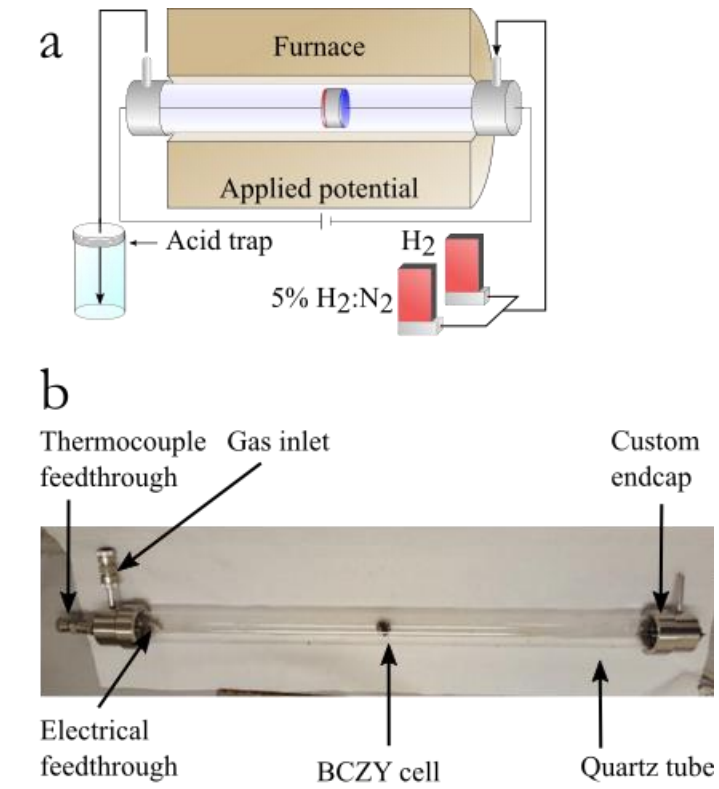


Figure 4-3: a & b) Cell testing apparatus c) Electrochemical cell design

4. 3 Characterisation

Morphologies of the measured cell electrodes and electrolytes were investigated using scanning electron microscopy. Analysis was conducted in the University Surface Analysis Facilities, on a Hitachi S-520 with 20 kV acceleration voltage. Firstly, the morphology of a Ag | BCZY | Ni/BCZY cell is presented. The BCZY electrolyte is observed to be a dense and well sintered, with no major pores or defects, Figure 4-4a. The thickness of the electrolyte was measured to be between 25 – 30 μm, Figure 4-4c. The individual grains of BCZY are clearly observable in Figure 4-4c, d, g & h, and have a diameter of around 5 μm (Figure 4-4d). The electrolyte is directly supported on a 1 mm thickness cermet composed of 70% Ni and 30% BCZY ceramic by weight. In Figure 4-4a, the presence of dense ceramic grains and highly porous structures is apparent. A higher magnification image of the cermet in Figure 4-4e shows the dense ceramic grains have a high coverage of Ni particles on the order of hundreds of nm in diameter.

The Ag paste electrode after heat curing, forms a porous structure layer, with the presence of large and small particles observable. The boundary of the Ag layer is shown in Figure 4-4b & d, with high porosity in the Ag layer apparent. A side on view of the Ag electrode (Figure 4-4f) shows that the Ag appears to form into distinct layers, with conjoined particles of ~ 1 μm in diameter. Higher magnification images of the electrolyte grains directly adjacent to the Ag layer in Figure 4-4g & h shows the presence of larger Ag particles ~ 1 μm in diameter, but also a high coverage of smaller particles hundreds of nanometres in diameter.

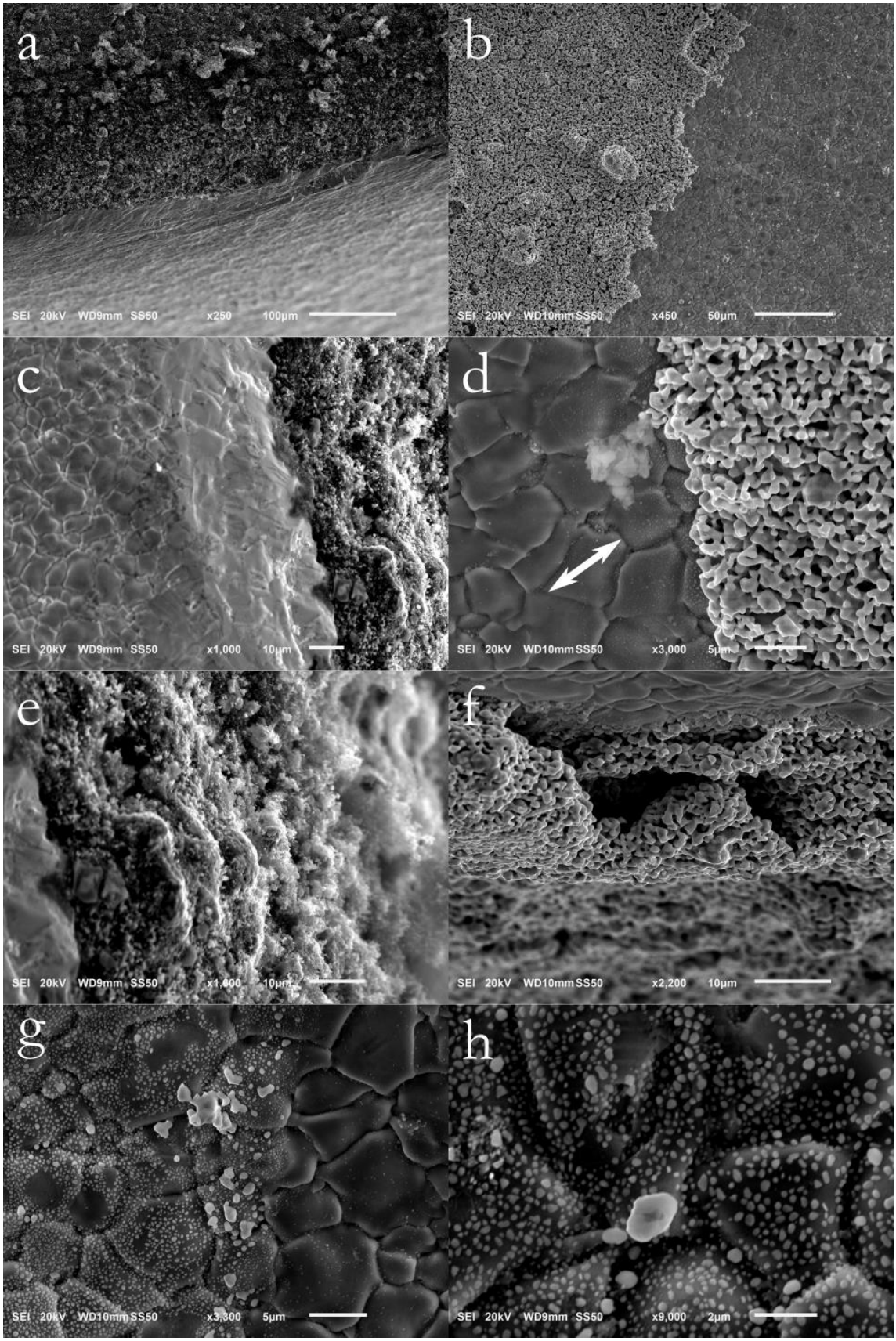


Figure 4-4: SEM images of Ag | BCZY | Ni/BCZY cell. Ag electrode forms in a porous layer-like structure, with smaller Ag particles directly covering electrolyte grains. Electrolyte is a dense and well sintered with grains ~ 5 µm and thickness of ~ 25 µm. Cermet support is observed to be highly porous structure. Scale bars represent 100, 50, 10, 5, 10, 10, 5, and 2 µm for images a – h, respectively.

Next is presented the analysis of a cell with a platinum electrode, Pt | BCZY | Ni/BCZY. Electrolyte was observed to have the same dense, well sintered morphology, Figure 4-5a. The boundary between the electrode and electrolyte is less obvious than in the Ag cell, but still observable, Figure 4-5b. Higher magnification images of the Pt electrode show two distinct Pt structures; small particles on the scale of hundreds of nanometres directly on the BCZY grains, and large layer-like Pt clusters. Figure 4-5c & d show high coverage of small Pt particles directly on the BCZY grains. Figure 4-5e – g show high electrolyte coverage by large, sheet-like Pt clusters, which were observed to be microporous. The total electrolyte coverage by Pt structures was lower than for the Ag cell.

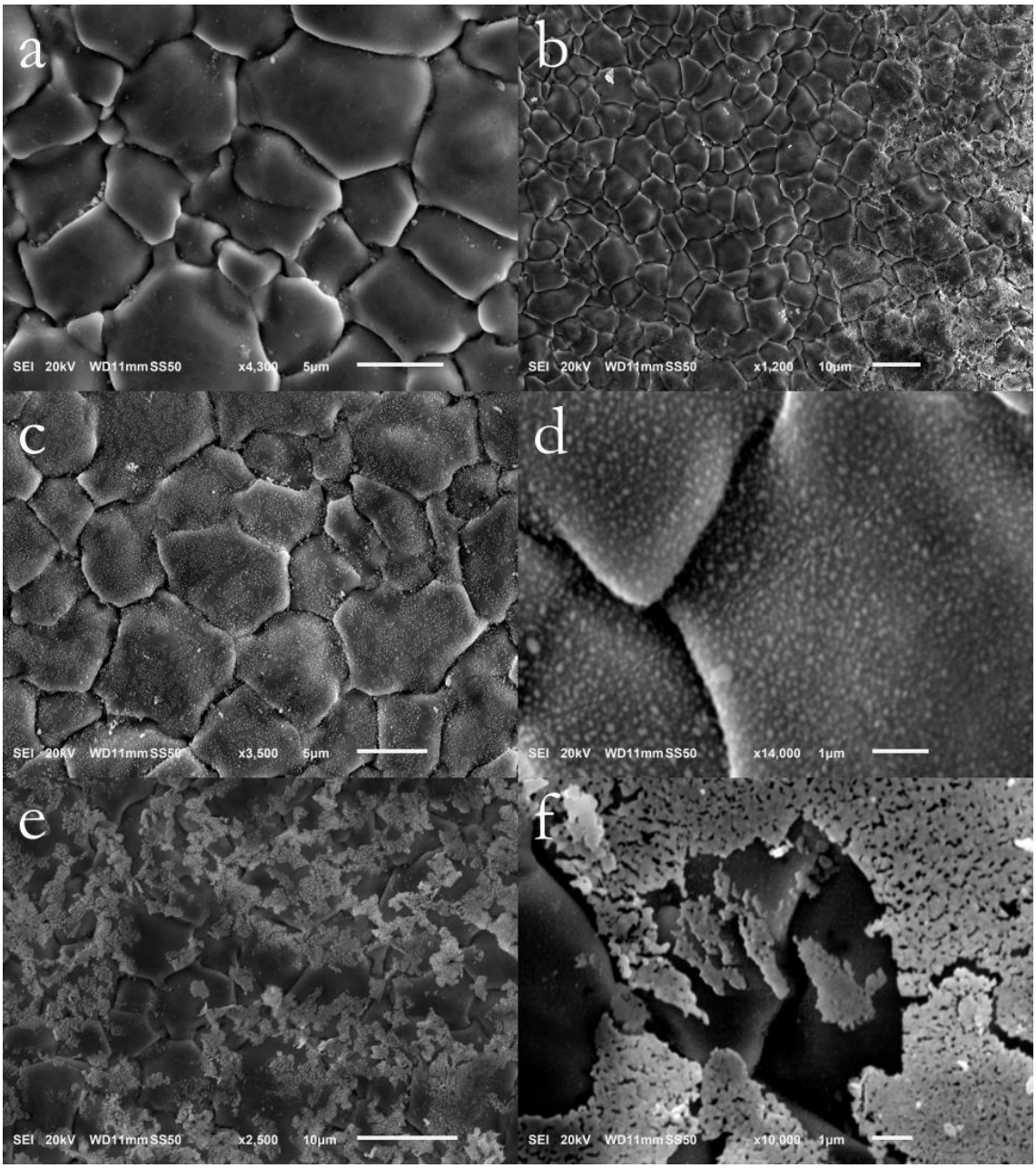


Figure 4-5: SEM images of Pt | BCZY | Ni/BCZY cell. Two distinct types Pt structures are observed. Scale bars represent 5, 10, 5, 1, 10, and 1 µm for images a – f, respectively.

Finally, a cell with a Ru impregnated cermet is presented. Analysis was conducted after the removal of excess Ru from the electrolyte as discussed in section 4. 2. 1. Also presented is an image of the cermet prior to impregnation (Figure 4-6a). After impregnation, both smooth BCZY grains and rough Ni surfaces are identifiable in the cermet. No Ru particles are apparent in any of the SEM images, indicating the Ru has formed nanoparticles not visible at the magnification achievable in this microscope.

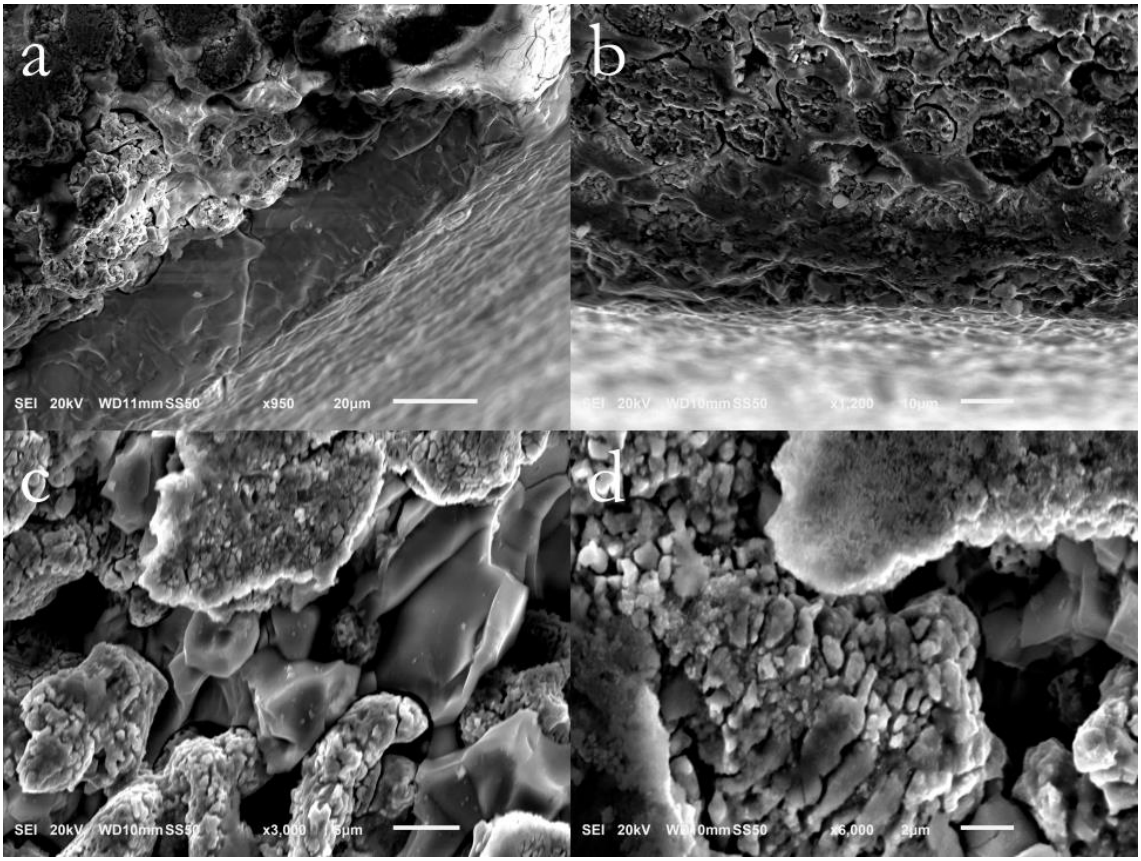


Figure 4-6: Ni/BCZY cermet before (a) and after (b-d) impregnation and reduction of $Ru(acac)_3$. Scale bars represent 20, 10, 5, and 2 µm for images a – d, respectively.

4. 4 Electrochemical Ammonia Synthesis

The results are presented in an order to show the progression of the cell development. As a greater understanding of the system was developed, the electrode materials and conditions were adapted. A variety of measurements were made on each cell, namely voltammetry, electrochemical impedance spectroscopy, and transient measurements of current at constant applied potential during which the EC NH_3 synthesis rate was measured. Measured currents are normalised to the surface area of the counter electrode. Between each measured sample the reactor was allowed to purge for ~ 10 min to allow rates to return to steady state rate (~200 mL furnace tube, 50 – 150 mL min^{-1} gas flow, 4 – 1.3 min purge time).

Open circuit results are obtained with no applied potential, meaning no current can flow, and produced ammonia is purely thermal. Closed circuit results are recorded under an applied potential of 2V with current flowing according to the conductivity of the electrolyte. Electrochemical ammonia is possible under these conditions. The rate values are obtained by measuring the accumulation of ammonia in an acid trap over a set period (usually 1 hr). Gas is constantly flowing through the reactor and over the cell, then a potential is applied (if required), and an acid trap is filled with 10 mM H_2SO_4. The outflow gas is bubbled through this trap for the duration of measurement.

For the figures in this section, errors were accounted for in the following two ways. Firstly, accumulated uncertainty for rate measurements (calculated from concentration, surface-area, and time) was found to be on the order of 10^{-12} mols s^{-1} cm^{-2}. Secondly, standard deviations of repeat ISE measurements were calculated wherever possible and found not to exceed 10^{-11} mols s^{-1} cm^{-2}. Neither of these two calculated errors can be displayed meaningfully on the plots. Nor do they explain the differences in observed rate at ostensibly the same reaction conditions.

Firstly, the effect of applied potential was investigated. As discussed previously, EC NH_3 synthesis in these BCZY cells has been reported to peak at around 2 V applied potential. Both positive (Ni/BCZY cathode) and negative (Ag cathode) polarisations were investigated. The poor catalytic activity of metallic Ag for ammonia synthesis means that polarising the electrodes such that Ag is working as a cathode should result in a lower EC NH_3 rate than with a Ni/BCZY cathode. Figure 4-7a shows the rates and current densities recorded with a Ag cathode. Samples were collected using alternating closed and open circuit conditions. All samples showed a constant rate, with no difference in rate between open and closed-circuit. The first recorded sample had a noticeably higher current density than later closed-circuit samples. This could be due to poor H_2 oxidation kinetics at the anode leading to a depletion of charge carriers (protons) from the BCZY electrolyte, decreasing the conductivity.

Figure 4-7b shows the rates and current densities recorded with a Ni/BCZY cathode. To account for the possibility of a 'lag' effect, closed circuit samples were recorded consecutively. A lag effect may occur when rate of ammonia synthesis under closed circuit conditions does not return to its steady state 'thermal' rate in the 10 min between recordings, resulting in a convolution of rates between adjacent

recorded samples. The current densities were notably higher than with a Ag cathode. Rates were unaffected by current flowing through the cell (ruling out a lag effect), and were similar to those in Figure 4-7a. Therefore, the ammonia synthesis rates are heavily dominated by thermal ammonia synthesis, and the electrochemical rate cannot be resolved.

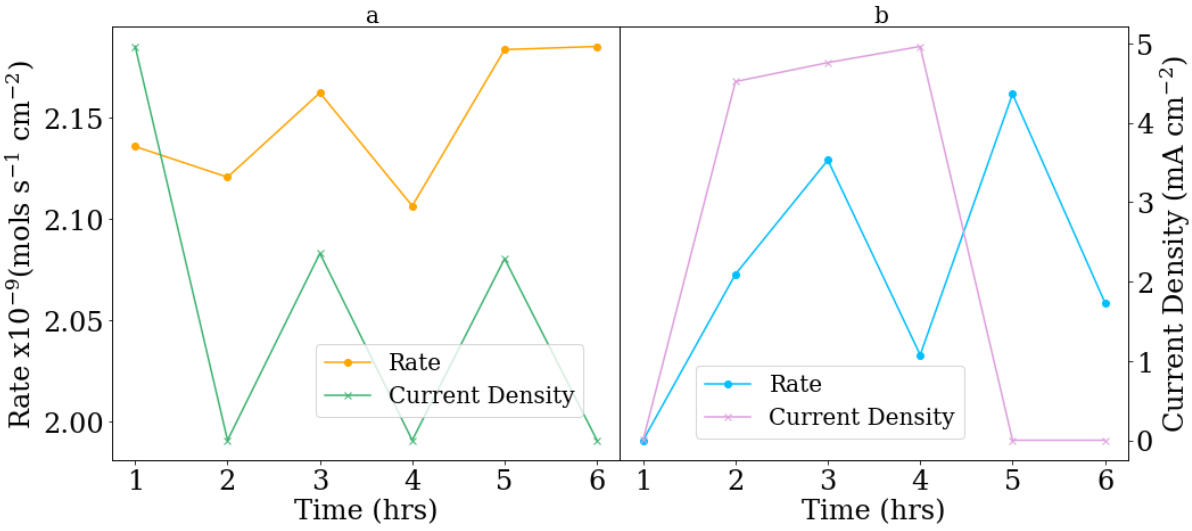


Figure 4-7: Ammonia synthesis rates & current densities. Recorded at 600 °C under 50 mL min^{-1} using Ag | BCZY | Ni/BCZY cell configuration. a) Rates & current densities (CDs) under +2 V applied potential (Ag cathode). Recorded using alternating closed and open circuits. b) Rates & CDs under -2 V applied potential (Ni/BCZY cathode). All closed-circuit samples recorded concurrently.

Next, the operating conditions of the cell were optimised (Ag | BCZY | Ni/BCZY cell) to look for conditions under which EC NH_3 could be demonstrated. Rates of EC NH_3 synthesis at temperatures between 300 – 600 °C were recorded under open circuit and an applied potential of -2 V. Current densities were calculated from measured currents under applied potential. Open circuit current density is 0 for all samples by definition but is shown for illustrative purposes. Both rates and current densities rose exponentially with temperature, indicative of an Arrhenius relationship, which is expected for a thermally activated process (Figure 4-8a). Rates at 300 and 400 °C had measured ammonia concentration values close to the detection limit of the ISE (0.01 ppm). Average rate and standard deviations in the ammonia concentrations were determined by averaging three independent measurements of the same solution, with uncertainties of around 1% recorded for the low-level measurements. Taking the rate at 400 °C to be equal to the detection limit yields a linear Arrhenius plot (Figure 4-8a, inset). From this activation energies are calculated to be -58.5 and -53.5 kJ mol^{-1} under closed and open circuit conditions respectively, suggesting the reaction is not mass transport limited. At all temperatures, rates under applied potential did not significantly exceed the rates under open circuit conditions.

It was postulated that increasing the total flow rate of gas through the reactor may highlight differences between the open and closed-circuit rates. At 600 °C, significant thermal decomposition of ammonia is expected, therefore perhaps the ammonia concentration approaches the thermal equilibrium as it exits the furnace hot zone. Increasing the flow rate will reduce dwell time of ammonia in the hot

zone. Rates of NH_3 synthesis at total flow rates between 50-150 mL min^{-1} were recorded (Figure 4-8b). It is observed that increasing the flow rate does increase the rate of ammonia synthesis, and slightly more significantly for measurements under open circuit conditions than closed. It also appears that the rate increase starts to plateau at 150 mL min^{-1}.

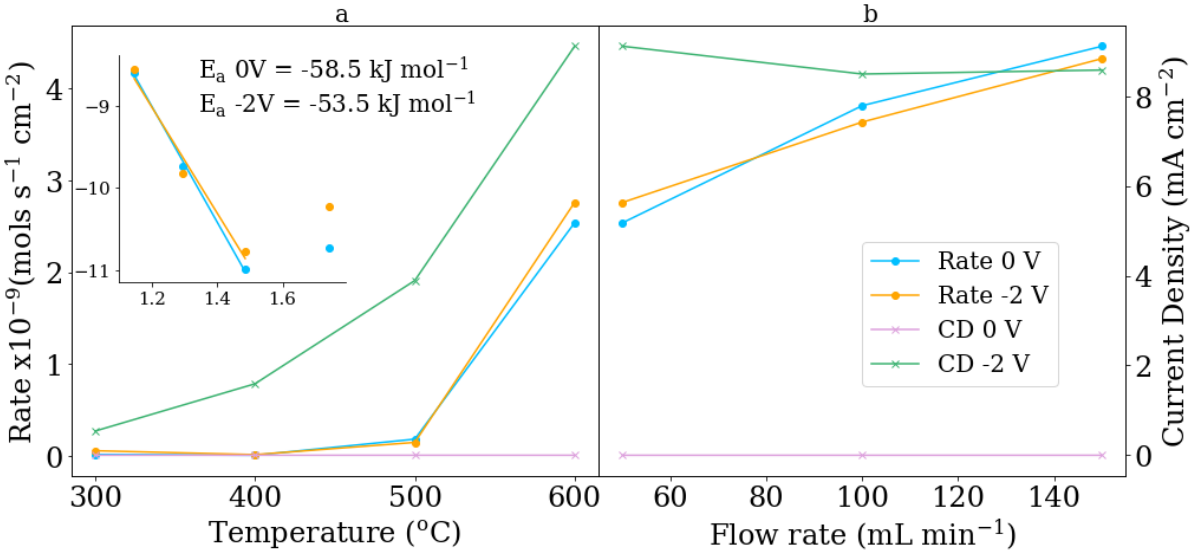


Figure 4-8: Rates and CDs of ammonia synthesis from Ag | BCZY | Ni/BCZY cell. a) Effect of temperature. Inset shows Arrhenius plot, with linear fit applied to points recorded at 400 – 600 °C b) Effect of total flow rate.

None of the Ag-anode cells investigated were able to demonstrate an electrochemical contribution to reduction of dinitrogen to ammonia. As previously discussed, Ag has a poor ability to reduce dinitrogen, therefore the thermal ammonia measured is attributed to the Ni/BCZY cermet. This cermet has been previously reported to have a significant ability to thermally reduce dinitrogen.[8]

The next step was to investigate how changing the anode catalyst would affect the NH_3 rates and currents. Previous reports were able to demonstrate EC NH_3 synthesis in M | BCZY | Ni/BCZY cells where M = Rh, Cu, Pt.[8–10] Therefore, as the metal with the fastest hydrogen reaction kinetics, Pt was chosen as a good candidate for an anode catalyst. Two Pt | BCZY | Ni/BCZY cells were prepared, one with a Pt loading of 2.5 mg cm^{-2} and the other with a loading of 10 mg cm^{-2} (as with Ag cells). Both positive (Pt cathode) and negative (Ni/BCZY cathode) potentials were investigated. As with Ag, Pt is not expected to have a high ability to reduce nitrogen so Pt cathodes should produce less EC NH_3 (Chapter 1).

In both tested cells the rate is independent of applied potential and of current density and produced NH_3 appears to be purely thermal, although the rates are twice those observed for previous Ag cells (Figure 4-8). In both Figure 4-9a & b, the rate slightly decreases over the course of testing. The cause of this decrease has not yet been identified.

The current densities were also observed to decrease over the course of testing, although interestingly this decrease only occurred under positive polarisations, where the Pt is acting as a cathode. Current

densities are also noticeably lower at negative polarisations. The higher current densities under positive polarisation vs negative, are attributed to the faster kinetics of the HER on Pt surfaces versus on the Ni/BCZY cermet. The fast kinetics of the HER can also explain the rapid decrease in current over the course of testing at positive polarisation. Rapid reaction at the Pt cathode of protons stored in the electrolyte may be faster than the Ni/BCZY anode can repopulate the lattice, leading to a decrease in conductivity.

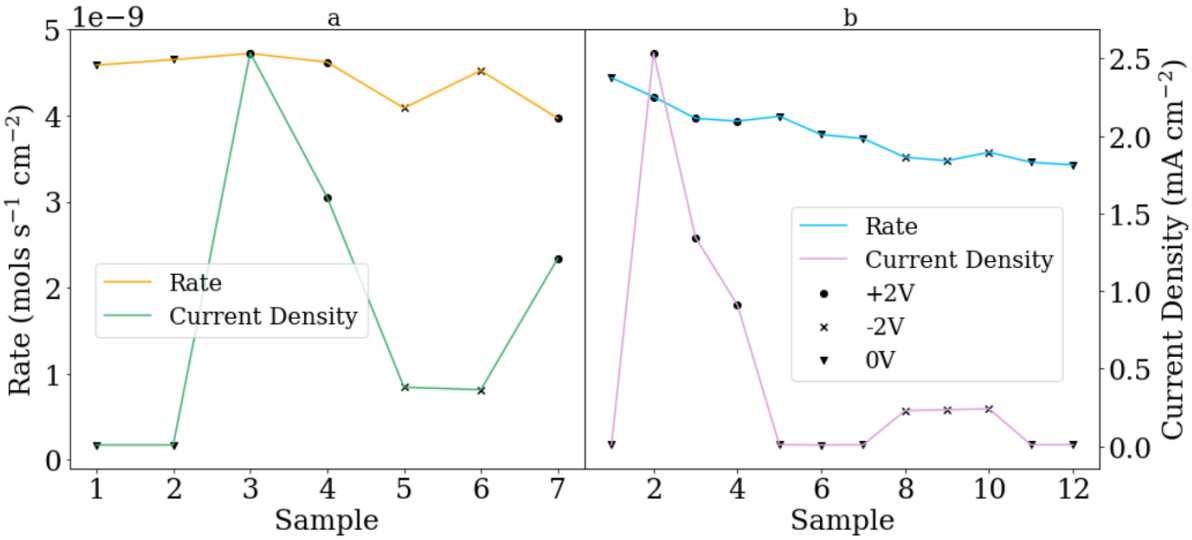


Figure 4-9: Rates & CDs in Pt | BCZY | Ni/BCZY cells. Different symbols are used to indicate the applied potential for each sample. a) Cell with 2.5 mg cm^{-2} Pt. b) Cell with 10 mg cm^{-2} Pt.

Modification of the anode catalyst did not highlight any significant EC NH_3 synthesis, therefore new cells were prepared with modified cathode catalysts. Ru is established as the most active metal for reduction of dinitrogen to ammonia, as discussed in Chapter 1, and was therefore used to prepare wet-impregnated cermet supports, with the lack of observable Ru particles in Figure 4-6 showing particles were on the nanoscale. Rates and CDs for a Ag | BCZY | Ru/Ni/BCZY cell are presented in Figure 4-10. Application of -2 V to the cell (Ru-cermet cathode) did not result in any consistent increase in production of NH_3 relative to open circuit conditions. Surprisingly, the addition of Ru did not appear to increase the rate of ammonia synthesis at all, relative to the previously presented Pt cells. One explanation for this is that the cell was geometrically smaller, therefore has a lower mass of cermet on which dinitrogen reduction to ammonia can occur. Taking the estimate of uncertainty in size given in section 4. 2. 1, and the known density of the cermet support (electrolyte is so thin the contribution is negligible) it can be calculated that the mass may vary by around 100 mg between samples, 6 – 8 % of the total mass. Therefore, the difference in mass of the cermet support will not entirely account for an ~ 20% decrease observed between the peak rates in Pt cells vs the peak rates in Ru cells. This suggests that the high surface of the Pt particles is somewhat responsible for the rate difference. It is also noteworthy that the rate of ammonia production decreases over the course of testing. This is again attributed to sintering of metallic ruthenium particles resulting in a reduction of total surface area.

Modification of the cermet resulted in a dramatic increase of the current densities relative to unmodified cathodes. The order of magnitude increase is attributed to the presence of Ru nanoparticles facilitating proton reduction and hydrogen evolution within the cermet electrode. For such a dramatic increase to occur it is suggested that the Ru nanoparticles must be in intimate contact with the cermet electrode. Therefore, it was determined likely that the synthesis of Ru nanoparticles within the cermet was successful. It is surprising that this novel material, which results in a dramatic increase in electrochemical activity, does not result in any observable increase in the rates of EC NH_3 synthesis.

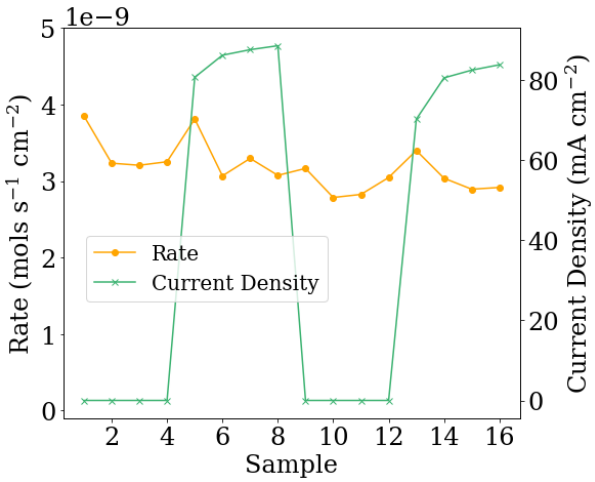


Figure 4-10: Rates & CDs of Ag | BCZY | Ru/Ni/BCZY cell, recorded under open circuit and -2 V applied potential.

4. 5 Impedance & Voltammetry Characterisation

The electrochemical characteristics of the different cells were investigated using voltammetry and impedance spectroscopy.

The effects of modifying electrodes were explored by addition of a Ag reference electrode. This unpolarised electrode provides a constant reference point against the relative potentials of the anode and cathode. In a two-electrode setup, it is not known how much of the applied voltage is dropped at each electrode, and therefore what the driving force for the electrochemical half-cell reactions are. Adding a reference electrode allows the measurement of the potential at each electrode and, when using a reference electrode of known potential, the potential of the working electrode to be determined (Figure 4-11). It should be noted that reference electrodes for solid electrolytes prepared in this manner do not give a true representation of the electrode potentials. A true reference electrode should be placed in the centre of the electrolyte, or more accurately at a point where it can measure the midpoint of the potential drop across the electrolyte (Figure 4-11).[22–24] It can, however, still be informative to use a reference electrode of the type used in this work to look at changes in a sample.

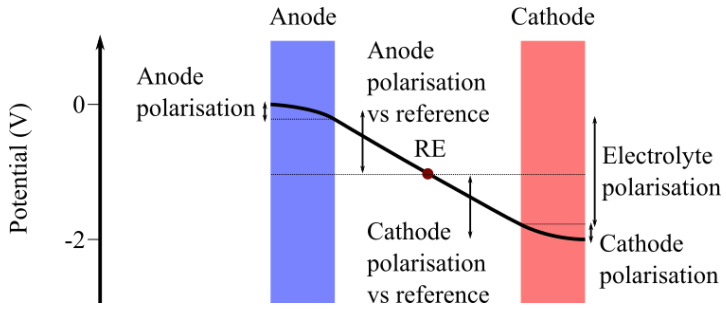


Figure 4-11: Diagram of ideal reference electrode. Redrawn and simplified from Finklea et al. [24]

Figure 4-12 shows the results of cyclic-voltammetry (CV) investigations. A Ag | BCZY | Ru/Ni/BCZY cell was investigated before and after the addition of Pt to the Ag electrode. CVs in Figure 4-12 show the cell currents when polarising the Ag electrode (working electrode of the potentiostat is connected to the Ag electrode). Under positive polarisation of Ag & Ag/Pt electrodes, the onset potential of the hydrogen oxidation reaction shifts from 1.1 V to 600 mV, accompanied with a two-fold increase of cell current. When polarising negatively polarising the Ag & Ag/Pt electrodes, no change was observed between them. This is a noteworthy observation: the Ag/Pt electrode oxidises hydrogen to protons faster than the Ag electrode (expected given the fast reaction kinetics for hydrogen on Pt surfaces), however when reducing protons to hydrogen, no change is observed between the two electrodes, even at large polarisations. The possibility of a more efficient Hydrogen Evolution Reaction on Ag surfaces over Pt surfaces has previously been explored by other members of our group.[25] However, for the purposes of EC NH_3 synthesis, it can be concluded that the faster hydrogen oxidation kinetics observed on the Ag/Pt electrode means this electrode should have a higher performance for this, and other electrolytic cell operations.

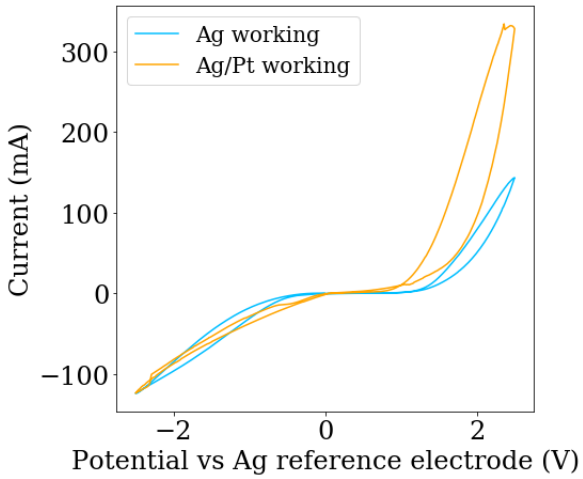


Figure 4-12: Voltammetry of Ag | BCZY | Ru/Ni/BCZY cell before and after impregnation of Ag electrode with Pt. 600 °C, 150 mL min^{-1} 3:1 H_2:N_2, 50 mV s^{-1}. Currents recorded vs Ag reference electrode

Impedance spectroscopy was carried out for each tested electrode configuration. The temperature ramp was paused while heating the cells prior to EC NH_3 testing, and an impedance spectrum recorded at a range of temperatures. A polarisation of 100 mV was applied at frequencies from 10^6 to 10^{-1} Hz, and the current response recorded.

Each spectrum showed inductive behaviour at high frequencies (negative values of -Z"). This behaviour was not observed with the cell discussed in Chapter 3, despite the overall setup remaining the same. Therefore, this was attributed to an aspect of cell preparation. Inductive elements can be caused by instrument artefacts,[26] however most instruments automatically correct for this. While even straight pieces of wire have an associated inductance, the inductance effect is proportional to the square of the number of turns in a coil of wire.[27] Therefore the inductance is attributed to the formation of carbon-felt current collectors secured by tight loops of Ag wire. With the addition of this inductive element, the previously used equivalent circuit model is modified, as shown in Figure 4-13. This circuit has been used in literature for modelling Solid Oxide Fuel Cells (SOFCs).[22] The rest of the equivalent circuit model was the same; Two R-CPE elements represent two ionic transfer processes within the electrolyte. The first process appears in data collected at high frequency and is representative of intragrain protonic transport. The second is apparent at lower frequencies and is assigned to intergrain protonic transport.

R_1 is representative of the contact resistance between electrodes and the electrolyte, and the two R-CPE circuits represent the intra- (high frequency) and inter- (low frequency) grain boundary transport resistances. Equivalent circuit modelling was carried out using IviumSoft software. Raw impedance data is displayed as a scatter plot, and equivalent circuit modelling is shown as a solid line. The resistance values were converted to conductivities (in S cm^{-1}) by dividing the electrolyte thickness (25 μm) by the resistance and Ag or Pt electrode areas, according to the equation reported by Babilo et al.[28] The calculated values for each circuit component are given below in Table 4-2.

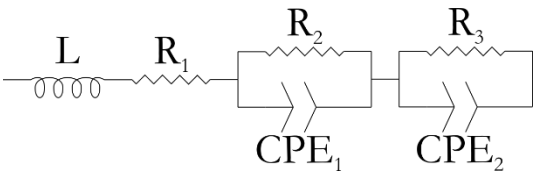


Figure 4-13: Equivalent circuit model utilised for modelling.

The Nyquist and Bode plots for a Ag | BCZY | Ni/BCZY cell are shown in Figure 4-14. The Nyquist plot shows a decrease in the total resistance (arc x-intercept) with increasing temperature. Two distinct arcs were observed and are more clearly seen in the Bode plot of frequency vs phase. The decreasing resistance with increasing temperature is typical for ion-conducting behaviour. Intra- and inter-grain conductivities are 4.0, 21 & 52 $x10^{-5}$ and 8.9, 19, 37 $x10^{-6}$ S cm^{-1} for temperatures of 470, 520 & 570 °C, respectively. These values are lower than those reported in literature, but the order of magnitude difference between the intra- and inter-grain boundaries is typical.[28] It is noteworthy that the values at 470 °C are similar to the values measured in Chapter 4 for the milled BZY20 pellet; intra- and inter- grain conductivities of 2.6 $x10^{-4}$ and 2.8 $x10^{-5}$. It is unexpected that the homemade pellet from the previous investigations should show higher conductivities than the well sintered BCZY electrolyte. This could be indicative of two things. Firstly, the conductivities under water are notably higher than under dry hydrogen nitrogen mixes, or secondly that the previous BZY20 measurements were affected by an electrical short circuit. Further investigations are needed to find the truth of this matter.

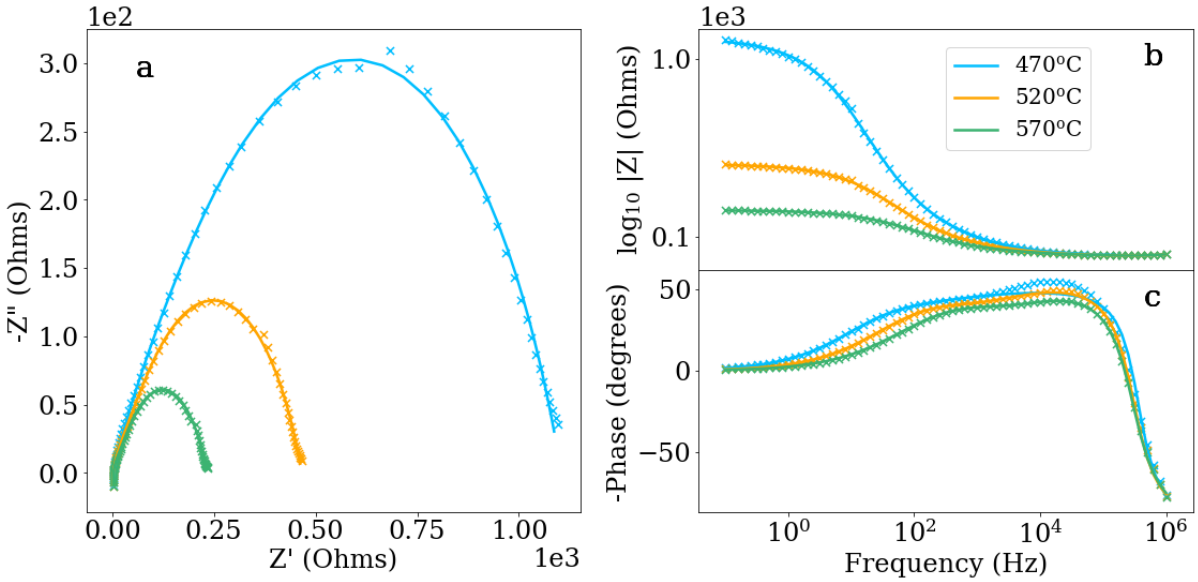


Figure 4-14: EIS data from Ag | BCZY | Ni/BCZY cell. Raw data shown as scatter and fitted data as solid line. a) Nyquist plot b) Impedance Bode plot c) Phase Bode plot.

Figure 4-15 shows the EIS data recorded from a cell with a Pt counter electrode. The total impedance decreased with increasing temperature. Between 400 – 500 °C, the same trend of decreasing impedance with increasing temperature is observed. However, there was a dramatic increase in the high frequency impedance between 500 and 600 °C, indicative of a sudden increase in the contact resistance (R_1). This is attributed to one of two possibilities; firstly, that the sintering of Pt particles previously proposed starts

or rapidly accelerates between these two temperature points, or secondly that a thermal expansion led to a loosening of physical contact between circuit elements. The sintering of particles will cause a reduction of total Pt metal in contact with the electrolyte, effectively leading to an increase in contact resistance. A thermal expansion of the cell could lead to poor contact between the carbon felt current for the cermet electrode, and therefore an increase of resistance.

The increase in contact resistance is also accompanied by an increase of resistance of all other R components relative to the spectrum recorded at 500 °C, Table 4-2 lines 6 & 7. There is obviously a significant change in the cell causing a spike in all impedance values. Due to outlying data points, visible in Figure 4-15b, the fit of the experimental data recorded at 500 and 600 °C was poor, and is reflected by outlier values in Table 4-2.

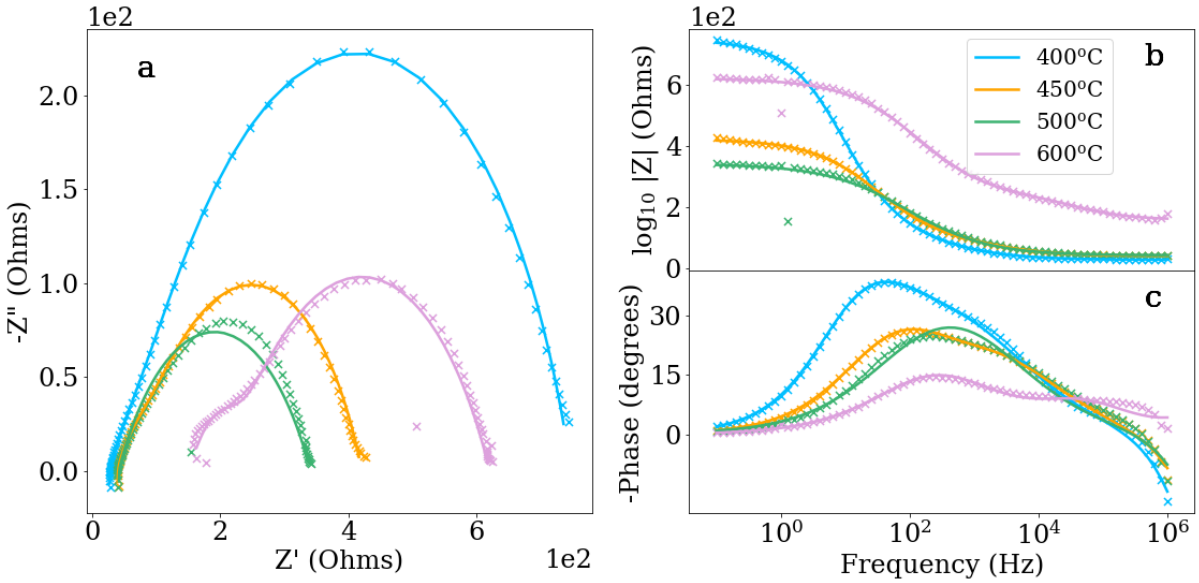


Figure 4-15: EIS data from Pt | BCZY | Ni/BCZY cell. Raw data shown as scatter and fitted data as solid line. a) Nyquist plot b) Impedance Bode plot c) Phase Bode plot.

Figure 4-16 shows the EIS data for a Ag | BCZY | Ru/Ni/BCZY cell. Some issues were had getting a good fit of the data at low temperature, as can be seen in Figure 4-16c. The same decrease in total impedance with increasing temperature is observed, however in this case the extent is much more dramatic. The impedance at 400 °C is much higher than for previous samples, Table 4-2 line 8. Increasing the temperature to 500 °C resulted in a return to typical values of resistance for this temperature. However, when increasing the temperature further to 600 °C, a dramatic decrease in impedance was observed. The Measured values for R_2 and R_3 at this point are 1.7 & 53.3, corresponding to conductivities of 4.6 x10^{-4} and 1.5 x10^{-5} S cm^{-1}. This is consistent with the increase in current density shown in Figure 4-10. The initially high impedance values dropping to the lowest recorded values is a curious phenomenon; it is suggested that this is due to a reduction process of Ru particles within the cermet electrode. As shown in Chapter 5, the reduction of ruthenium nanoparticles prepared from $Ru(acac)_3$ is only just completed at 400 °C and depends on the nature of the support material. Therefore, it is

suggested that the EIS plot recorded at 400 °C is limited by the presence of ruthenium oxide species. Once reduced, the ruthenium dramatically boosts the electrochemical activity.

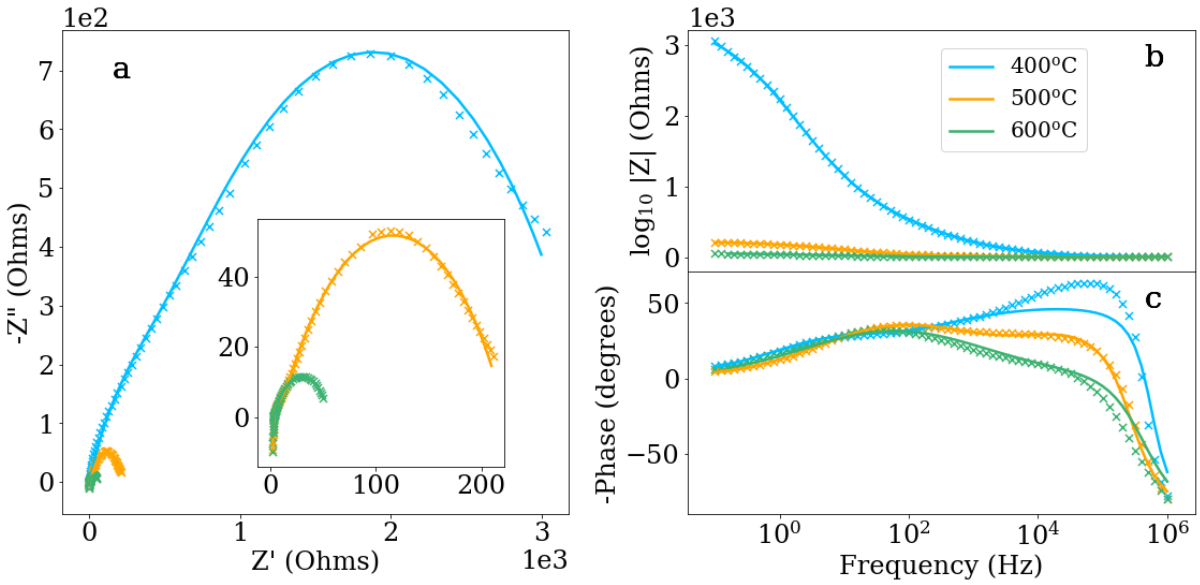


Figure 4-16: EIS data from Ag | BCZY | Ru/Ni/BCZY cell. Raw data shown as scatter and fitted data as solid line. a) Nyquist plot. Inset shows 500 and 600 °C curves in more detail b) Impedance Bode plot c) Phase Bode plot.

The calculated conductivity values for the intra- and inter-grain proton transport processes (R_1 & R_2) were plotted as Arrhenius plots, and are shown in Figure 4-17. All values except for the final points recorded in the Pt cell showed the expected trend of increasing conductivity, which is excluded from the activation energy fitting. The issues with the Pt cell at 600 °C are expected given the EIS plots in Figure 4-15. The Pt cell Arrhenius plots also show much lower activation energies than the other two cells, and indeed are in an energy regime indicative of a diffusion limited process. Given the previous discussions about Figure 4-5 & Figure 4-17, it is suggested that poor Pt coverage over the electrolyte limits the rate at which protons can be supplied to the cell, resulting in a diffusion limited process. Both the Ag and Ru cells show similar values for the activation energy for intra-grain conduction, of 58.1 and 60.4 kJ mol^{-1}. These values are significantly higher than the value of 43.4 kJ mol^{-1} reported by Babilo et al.[28] in a study of BZY20 conductivity. The activation energies of the inter-grain (ground boundary) are unexpectedly lower than the values for the intra-grain conduction for the Ag and Ru cells, values of 32.3 and 42.9 kJ mol^{-1}, respectively. Babilo et al. reported a value of 68.5 kJ mol^{-1}. These activation energy values are quite unexpected, and indeed differ to those reported for an identical material by Coors et al., who found values of 45.3 and 75.3 kJ mol^{-1} for the intra- and inter-grain conductivity, respectively. The cause of the discrepancy is unknown at this time, but it is known that changes in atmosphere can significantly affect the conductivity, and that this study used significantly higher amounts of hydrogen gas (75% H_2 /N_2, due to the ammonia synthesis goal) than is typical in the literature. A systematic study of the conductivities in the different cells under different atmospheres should be conducted to elucidate the cause of this result.

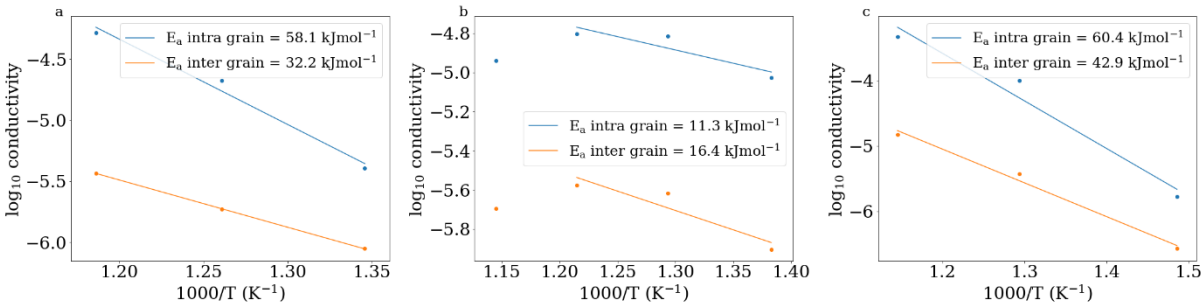


Figure 4-17: Arrhenius plots showing activation energies of intra- and inter-grain conduction for a) Ag cell, b) Pt cell, and c) Ru cell

Table 4-2: EIS fitting parameters for all cells, at all temperatures.

Row	Cell	R_1	R_2	R_3	L_1	Q_1	N_1	Q_2	N_2
1	Ag 470	2.8	197.5	896.0	1.6 x10^{-6}	7.4 x10^{-5}	0.6	5.3 x10^{-5}	0.7
2	Ag 520	1.7	38.0	426.4	1.6 x10^{-6}	5.3 x10^{-5}	0.6	6.0 x10^{-5}	0.7
3	Ag 570	1.9	15.3	216.0	1.6 x10^{-6}	4.7 x10^{-5}	0.7	8.0 x10^{-5}	0.6
4	Pt 400	26.9	65.0	657.0	1.1 x10^{-6}	1.3 x10^{-4}	0.6	9.1 x10^{-5}	0.7
5	Pt 450	38.8	52.1	330.5	1.1 x10^{-6}	7.4 x10^{-5}	0.6	1.1 x10^{-4}	0.7
6	Pt 500	40.9	50.6	300.0	1.0 x10^{-6}	2.6	0.6	9.7 x10^{-5}	0.6
7	Pt 600	156.8	69.5	394.8	8.1 x10^{-7}	1.9 x10^{-6}	0.7	4.6 x10^{-5}	0.6
8	Ru 400	2.0	474.7	2931.7	2.3 x10^{-6}	4.0 x10^{-5}	0.5	9.7 x10^{-5}	0.6
9	Ru 500	1.9	8.1	213.0	1.4 x10^{-6}	1.3 x10^{-4}	0.6	6.1 x10^{-4}	0.6
10	Ru 600	1.0	1.7	53.3	1.5 x10^{-6}	1.0 x10^{-4}	0.5	4.8 x10^{-3}	0.5

4. 6 Two-Chamber Cell

To address the issues of EC NH_3 detection, it was decided to try and manufacture a two-chamber cell. An initial test cell was developed and machined from Macor ceramic in the University workshop. In the absence of gaseous hydrogen at the cathode, ammonia may only be produced via protons transported electrochemically through the electrolyte and therefore the 'thermal rate' should be zero. The cell design is shown in Figure 4-18, with the Macor pieces bonded together using zirconia cement. Current connections were made in the same manner as before i.e. a carbon felt plug inside and C-felt wrapped around the outer electrode. A Ru impregnated cell was utilised.

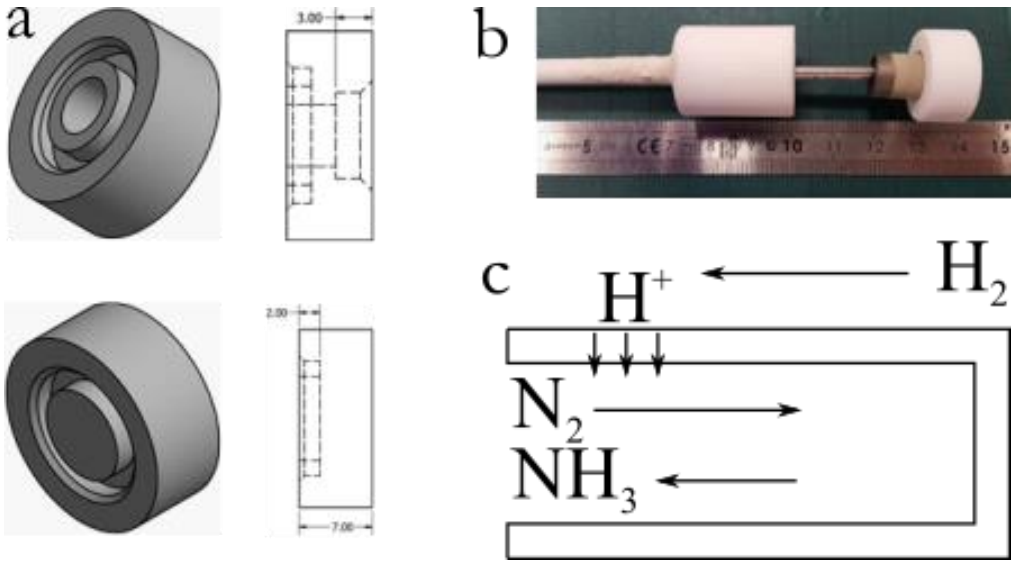


Figure 4-18: design (a) and construction (b) of two-chamber cell for ammonia synthesis c) schematic showing theory of operation, and separation of anode and cathode gas feeds.

Critical to the cell is the efficient sealing of the ceramic onto the tubing to prevent mixing of the anode and cathode gas feeds. The leak rate of the cell was therefore examined by flowing He through the anode chamber, and N_2 through the cathode chamber, then examining the exhaust gas from the cathode chamber with mass-spectrometry. Figure 4-19a shows the results of a leak rate test with 10 mL min^{-1} He flow, and 10, 20 & 40 mL min^{-1} flow. Significant leakage of He into the cathode chamber is observed, however it can be slightly depressed by increasing cathode chamber flow rate.

For electrochemical testing, the cathode chamber was purged with 10 mL min^{-1} N_2, and 50 mL min^{-1} 5% H_2 in Ar flowed around the anode. The cell was then heated to 450 °C and testing conducted. The electrochemical synthesis rates of the cell showed significant thermal rates, and it was not possible to separate this contribution from the purely electrocatalytic rate, consistent with significant leaking between compartments (Figure 4-19b). Indeed, it was observed that the thermal rates increased with time, suggesting the leak worsened during the experiment, perhaps as differential expansion of the cement increased the size of existing holes. Ultimately, this testing was postponed in favour of other investigations

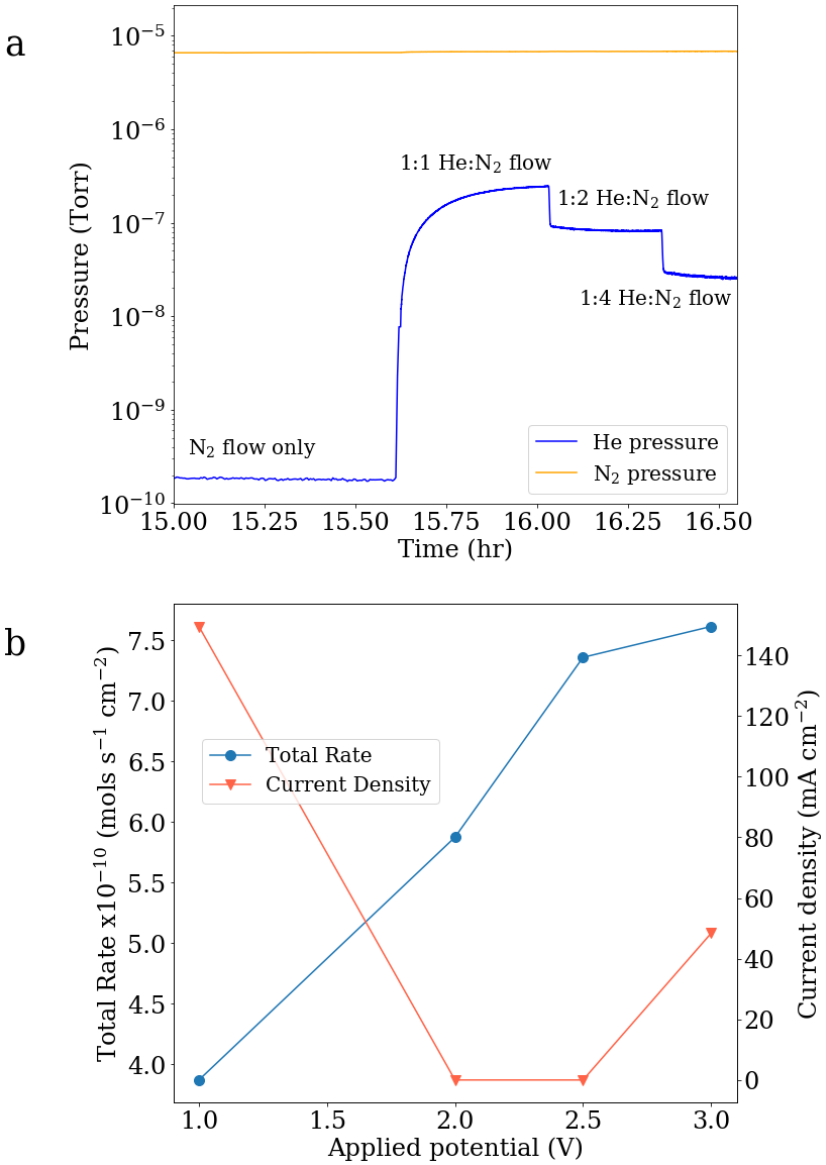


Figure 4-19: (a) Mass trace of He and N_2 in cathode chamber exhaust (b) Current densities and rates for two chamber cell

4. 7 Conclusion

The stated objectives of this chapter were:

1. Prepare electrochemical cells and characterise their physical and electrochemical properties
2. Test new electrode catalysts for electrochemical ammonia synthesis
3. Test a different cell geometry to allow easier quantification of electrochemical ammonia

EIS studies showed conductivity followed expected trend of increasing conductivity with temperature. The activation energies for the intra- and inter-grain conduction were calculated but disagree with literature values. The cause of this discrepancy is unknown currently. The morphology of the cell electrodes and electrolyte were characterised using SEM.

Voltammetry was used to characterise the electrochemical redox behaviour of cells with Ag or Pt electrode catalysts. The addition of Pt resulted in a clear increase in the kinetics of electrochemical hydrogen oxidation to protons at the Ag/Pt surface. Interestingly, the hydrogen evolution reaction proceeds at the same rate at a Ag electrode as at a Ag/Pt one. This noteworthy observation is consistent with previous work by our group and warrants further investigation.[25]

A range of catalysts were tested for the electrochemical reduction of dinitrogen to ammonia. After extensive investigations, it can be concluded that it is not possible to measure electrochemical ammonia from any of the cells discussed in the setup discussed in section 4. 2. 2 This contrasts with previous reports using similar cells.[8–10] Several cells using differing electrode catalysts were unable to highlight any electrochemical contribution to the rate. A novel ruthenium impregnated cermet was prepared and tested, with evidence that nanoparticles were formed within the electrode structure. While this dramatically increased the kinetics of hydrogen oxidation and proton reduction within the cell, it did not affect the rate of ammonia synthesis.

The total uncertainty in rate due to measurement uncertainties was calculated, as was the standard deviation in ISE measurements. These did not explain variance in rate at the same reaction conditions, therefore an unaccounted-for variable is responsible. A good summary of the controls that should be carried out during experiments measuring low rates of ammonia production can be found in a review by Greenlee et al.[21]

It is proposed ammonia produced in the single chamber reactor, from either thermal or electrochemical reactions, is limited by the thermal equilibrium. As the gas stream is not directed over the electrodes, but rather the passes around the cell as it sits in the tube, it is possible that while total flow rates are high, localised flows over the electrode surfaces are low. This will lead to low localised GHSV values, and high conversions which are limited by equilibrium. The conversion was calculated for the highest recorded rate and found to be two orders of magnitude less than the equilibrium conversion (at 150 mL min^{-1} total flow, 3:1 H_2:N_2, 600 ºC, 1 atm. pressure: 0.006 % experimental

conversion, 0.1 % equilibrium conversion as calculated using FactSage education). Therefore, to meaningfully measure the conversion and investigate this theory, a new reactor design ensuring gas flow is directed over the electrode catalysts is required.

To avoid thermal ammonia production obscuring any electrochemical ammonia, a two-chamber reactor geometry was designed and constructed. However, the challenges with manufacturing a gas tight cell were immediately apparent, and thermal ammonia was still observed. It is suggested that this will be a major issue for most two-chamber reactors, and that any reports claiming ammonia synthesis in two-chamber reactors should also report measured leak rates.

Electrochemical cells were successfully prepared and characterised, fulfilling the first objective of this chapter. However, it was not possible to realise either the second or third objective; electrochemical ammonia could not be observed for any of the prepared cells in a single chamber reactor geometry, nor in a two-chamber reactor.

While the electrochemical synthesis of ammonia could not be measured in this work, it is noteworthy that the Cermet support displayed high rates of thermal ammonia synthesis. Indeed, when adding a highly active ammonia synthesis catalyst (Ru nanoparticles), no significant increase in the thermal rates was detected. Therefore, it was decided to investigate the thermal rates of ammonia synthesis over catalysts derived from barium zirconate proton conductors.

4. 8 Acknowledgements

CoorsTek are acknowledge for providing the BCZY cells, free of charge.

4. 9 References

(1) Marnellos, G.; Stoukides, M. Ammonia Synthesis at Atmospheric Pressure. *Science* **1998**, *282* (5386), 98–100.

(2) Amar, I. A.; Lan, R.; Petit, C. T. G.; Tao, S. Solid-State Electrochemical Synthesis of Ammonia: A Review. *J. Solid State Electrochem.* **2011**, *15* (9), 1845–1860.

(3) Kyriakou, V.; Garagounis, I.; Vasileiou, E.; Vourros, A.; Stoukides, M. Progress in the Electrochemical Synthesis of Ammonia. *Catal. Today* **2017**, *286*, 2–13.

(4) Skodra, A.; Stoukides, M. Electrocatalytic Synthesis of Ammonia from Steam and Nitrogen at Atmospheric Pressure. *Solid State Ion.* **2009**, *180* (23), 1332–1336.

(5) Wang, B. H.; Wang, J. D.; Liu, R.; Xie, Y. H.; Li, Z. J. Synthesis of Ammonia from Natural Gas at Atmospheric Pressure with Doped Ceria–Ca3(PO4)2–K3PO4 Composite Electrolyte and Its Proton Conductivity at Intermediate Temperature. *J. Solid State Electrochem.* **2007**, *11* (1), 27–31.

(6) Yun, D. S.; Joo, J. H.; Yu, J. H.; Yoon, H. C.; Kim, J.-N.; Yoo, C.-Y. Electrochemical Ammonia Synthesis from Steam and Nitrogen Using Proton Conducting Yttrium Doped Barium Zirconate Electrolyte with Silver, Platinum, and Lanthanum Strontium Cobalt Ferrite Electrocatalyst. *J. Power Sources* **2015**, *284*, 245–251.

(7) Amar, I. A.; Lan, R.; Humphreys, J.; Tao, S. Electrochemical Synthesis of Ammonia from Wet Nitrogen via a Dual-Chamber Reactor Using La0.6Sr0.4Co0.2Fe0.8O3−δ-Ce0.8Gd0.18Ca0.02O2−δ Composite Cathode. *Catal. Today* **2017**, *286*, 51–56.

(8) Vasileiou, E.; Kyriakou, V.; Garagounis, I.; Vourros, A.; Stoukides, M. Ammonia Synthesis at Atmospheric Pressure in a BaCe0.2Zr0.7Y0.1O2.9 Solid Electrolyte Cell. *Solid State Ion.* **2015**, *275*, 110–116.

(9) Vasileiou, E.; Kyriakou, V.; Garagounis, I.; Vourros, A.; Manerbino, A.; Coors, W. G.; Stoukides, M. Electrochemical Enhancement of Ammonia Synthesis in a BaZr0.7Ce0.2Y0.1O2.9 Solid Electrolyte Cell. *Solid State Ion.* **2016**, *288*, 357–362.

(10) Vasileiou, E.; Kyriakou, V.; Garagounis, I.; Vourros, A.; Manerbino, A.; Coors, W. G.; Stoukides, M. Reaction Rate Enhancement During the Electrocatalytic Synthesis of Ammonia in a BaZr0.7Ce0.2Y0.1O2.9 Solid Electrolyte Cell. *Top. Catal.* **2015**, *58* (18–20), 1193–1201.

(11) Ladas, S.; Kennou, S.; Bebelis, S.; Vayenas, C. G. Origin of Non-Faradaic Electrochemical Modification of Catalytic Activity. *J. Phys. Chem.* **1993**, *97* (35), 8845–8848.

(12) Vayenas, C. G.; Bebelis, S. I. Electrochemical Promotion. *Solid State Ion.* **1997**, *94* (1–4), 267–277.

(13) Garagounis, I.; Kyriakou, V.; Stoukides, M. Electrochemical Promotion of Catalytic Reactions: Thermodynamic Analysis and Calculation of the Limits in Faradaic Efficiency. *Solid State Ion.* **2013**, *231*, 58–62.

(14) Giddey, S.; Badwal, S. P. S.; Kulkarni, A. Review of Electrochemical Ammonia Production Technologies and Materials. *Int. J. Hydrog. Energy* **2013**, *38* (34), 14576–14594.

(15) HoÌˆskuldsson; B, A.; Abghoui; Younes; GunnarsdoÌ• ttir; B, A.; SkuÌ• lason; Egill. Computational Screening of Rutile Oxides for Electrochemical Ammonia Formation. *ACS Sustain. Chem.* **2017**.

(16) Coors, W. G.; Manerbino, A. Characterization of Composite Cermet with 68 Wt.% NiO and BaCe0.2Zr0.6Y0.2O3−δ. *J. Membr. Sci.* **2011**, *376* (1–2), 50–55.

(17) Förch, R.; Schönherr, H.; Jenkins, A. T. A. *Surface Design: Applications in Bioscience and Nanotechnology*; John Wiley & Sons, 2009.

(18) Wang, W. B.; Cao, X. B.; Gao, W. J.; Zhang, F.; Wang, H. T.; Ma, G. L. Ammonia Synthesis at Atmospheric Pressure Using a Reactor with Thin Solid Electrolyte BaCe0.85Y0.15O3−α Membrane. *J. Membr. Sci.* **2010**, *360* (1–2), 397–403.

(19) Otomo, J.; Noda, N.; Kosaka, F. Electrochemical Synthesis of Ammonia with Proton Conducting Solid Electrolyte Fuel Cells at Intermediate Temperatures. *ECS Trans.* **2015**, *68* (1),

(20) Li, Z.; Liu, R.; Xie, Y.; Feng, S.; Wang, J. A Novel Method for Preparation of Doped Ba3(Ca1.18Nb1.82)O9−δ: Application to Ammonia Synthesis at Atmospheric Pressure. *Solid State Ion.* **2005**, *176* (11–12), 1063–1066.

(21) Greenlee, L. F.; Renner, J. N.; Foster, S. L. The Use of Controls for Consistent and Accurate Measurements of Electrocatalytic Ammonia Synthesis from Dinitrogen. *ACS Catal.* **2018**, *8* (9), 7820–7827.

(22) Jørgensen, M. J.; Primdahl, S.; Mogensen, M. Characterisation of Composite SOFC Cathodes Using Electrochemical Impedance Spectroscopy. *Electrochimica Acta* **1999**, *44* (24), 4195–4201.

(23) Jørgensen, M. J.; Mogensen, M. Impedance of Solid Oxide Fuel Cell LSM/YSZ Composite Cathodes. *J. Electrochem. Soc.* **2001**, *148* (5), A433–A442.

(24) Finklea, H.; Chen, X.; Gerdes, K.; Pakalapati, S.; Celik, I. Analysis of SOFCs Using Reference Electrodes. *J. Electrochem. Soc.* **2013**, *160* (9), F1055–F1066.

(25) Mo, J.; Stefanov, B. I.; Lau, T. H. M.; Chen, T.; Wu, S.; Wang, Z.; Gong, X.-Q.; Wilkinson, I.; Schmid, G.; Tsang, S. C. E. Superior Performance of Ag over Pt for Hydrogen Evolution Reaction in Water Electrolysis under High Overpotentials. *ACS Appl. Energy Mater.* **2019**, *2* (2), 1221–1228.

(26) Rodgers, R. Impedance Measurements with Real Potentiostats: Corrections for Potentiostat Response. In *Extended Abstracts, 2nd Int. Symp. Electrochemical Impedance Spectroscopy (University of California-Santa Barbara*; 1992.

(27) *Inductance : Loop and Partial*, 1st ed.; Wiley-IEEE Press, 2009.

(28) Babilo, P. Processing and Characterization of Proton Conducting Yttrium Doped Barium Zirconate for Solid Oxide Fuel Cell Applications. phd, California Institute of Technology, 2007.

Chapter 5 Barium Zirconate Supported Ruthenium Nano-Catalysts for Heterogeneous Ammonia Production

5. 1 Background

Development of the Haber-Bosch process, and the associated catalysts has been a century-long project. It is now known that ruthenium is the most active pure metal catalyst capable of reducing dinitrogen to ammonia in a thermal reactor setup. The high activity of ruthenium catalysts at low temperatures are attractive for an agile heterogeneous ammonia process. Poisoning of the metal surface is a major concern for Ru nanocatalysts; there is no activation barrier for the dissociative adsorption of H_2 on Ru surfaces, meaning the surface can become saturated with hydrogen atoms, retarding the adsorption of dinitrogen.[1] A number of studies have looked at ways to alleviate hydrogen poisoning by modification of supports.[2–4]

Reduction of dinitrogen to ammonia over ruthenium catalysts follows a dissociative reaction pathway (Section 1.2.3). Once a dinitrogen species has adsorbed to the surface, electron donation into the 2p π^* orbitals causes a dissociation to adsorbed nitrogen atoms which can be easily hydrogenated to ammonia. Alkali metal promoters increase the electron density in the ruthenium d-band, facilitating this donation. The dissociative adsorption of dinitrogen occurs at B5 sites on the surface. The concentration of these surface sites is dependent on the size and distribution of ruthenium particles on the support.

The choice of Ru source can affect the structure and distribution of the crystals. $RuCl_3$ is a convenient and cheap precursor, however the chloride ions are difficult to remove from the metal surface, and poison the catalyst.[5] However, Zhong and Aika reported that on active-carbon supports, the ionic precursors $Ru(acac)_3$ and $RuCl_3$ had better activities than the neutral precursor $Ru_3(CO)_{12}$. $Ru(acac)_3$ gave smaller particles with higher dispersion than $Ru_3(CO)_{12}$.[6] After a high temperature reduction in the presence of $Ba(NO_3)_2$, chloride could be removed from the metal giving much improved activities. On metal oxide supports, a different relationship was found, with $Ru_3(CO)_{12}$ precursor giving the smallest particles, highest dispersion, and best rates of ammonia synthesis.[5]

Catalyst support can have a dramatic impact on the rate of dinitrogen reduction, and even on the mechanism. Most reported supports are either carbon or metal-oxide based. A systematic study by Aika et al. looked at the differences between Ru based catalysts supported on different metal oxides, and found dramatic differences.[7] The differences were attributed to the basicity (electron donating ability of the support), with the most effective being MgO. A subsequent study by Niwa and Aika found differences between lanthanide oxide supports.[8] The differences were attributed to differing degrees of reduction of the support, leading to a donation of electron density from the support to the Ru. The same

group then published work on carbon supports.[6] Activated carbon has a much larger Brunauer-Emmett-Teller (BET) surface area than metal oxide supports.

Cisneros & Lunsford prepared zeolites impregnated with Ru nanocrystals, and tested the activity for ammonia synthesis.[9] They found that the more negative the partial oxygen charge of the zeolite support, the better the catalyst performed, suggesting donation of electron density from the support to the catalyst. The zeolite, however, limited the size of the Ru crystals (up to 0.25 nm in diameter), resulting in low rates compared to other supported catalysts. Zeolite supports were also studied by Fishel et al., when they showed that the rate of ammonia synthesis is limited by the size of the Ru clusters.[10] In this paper, several different promoters were compared, and it was surprisingly found that a potassium promoter would outperform a caesium one.

Kitano et al. synthesised an electride ($C12A7:e^-$), which showed remarkably high rates of ammonia synthesis when used as a support for Ru nanocrystals.[3] The support can both absorb hydrogen and donate excess electrons in the lattice to the Ru particles, boosting the rate of dinitrogen reduction. In a follow up study, it was proposed that the hydrogen absorbing and electron donating properties of the support change the mechanism.[11] The rate determining step is the hydrogenation of N-atoms on the Ru surface, rather than the dissociative adsorption of dinitrogen.

Kitano et al. also investigated calcium amide as a support material for Ru/Ba particles, and found significant improvements over Mitassch iron, and Ru/MgO catalysts at low temperatures (340 and 260 ºC respectively).[2] For the Ru/Ba-$Ca(NH_2)_2$ catalyst, positive reaction orders were observed for both nitrogen and hydrogen, but a negative order for ammonia, suggesting the surface is mostly covered by N-H species. The Ru/MgO catalyst showed more usual behaviour with a negative reaction order for hydrogen, suggesting a poisoning effect. They attributed the unique qualities of the Ru/Ba-$Ca(NH_2)_2$ catalyst to a reversible exchange reaction between electrons and hydride ions at interfaces between the nanoparticles and the support.

Promoters are a key component of Ru-based ammonia synthesis catalysts. Aika et al. tested 14 different metal ions as promoters, from the alkali, alkali earth, and rare earth metal groups. Cs was found to be the most effective promoter among those tested, attributed to its high electropositivity.[7] Siporin and Davis examined the role of base promoters for ammonia synthesis using a Ru/MgO catalyst.[12] The mechanism of the reaction was examined using kinetic models. They found that Ba and La promoters functioned by decreasing hydrogen poisoning, whereas a Cs promoter increased hydrogen poisoning, but also increased the rate of dinitrogen reduction. They concluded that promoters can have dual effects, both affecting the coverage of the Ru surface, and the ability of the metal to reduce dinitrogen. We have recently published work showing how lithium can act as a more effective promoter than the more electropositive metals, via an alternative reaction pathway.[13] Li occupies the stepped terrace sites, causing dinitrogen to adsorb in an end-on mode due to a strong polarisation effect, forcing the reaction to proceed through an associative mechanism.

ABO_3 perovskite materials have previously been studied as supports for Ru nanocatalysts for ammonia synthesis. Wang et al. tested Ru nanoparticles on a range of supports, and found $BaZrO_3$ (BZ) support gave the highest rate.[14] They concluded that a transfer of electrons from the BZ support to the Ru particles via a strong metal-support interaction, increasing the ability of Ru particles to reduce dinitrogen. H_2 TPD profiles showed little difference between bare BZ and Ru/BZ, so they concluded the BZ support supresses H_2 poisoning. Yang et al. reported that a $Ru/BaCeO_3$ catalyst showed superior reactivity in comparison to other common supports at lower temperatures (300 – 350 °C). This was attributed to electronic promotion from the support. Shimoda et al. tested Y-doped barium zirconate and barium cerate as supports. Y-doping was found to be detrimental for barium cerate-based catalysts, but 10% Y-doped barium zirconate was found to boost the rate of ammonia synthesis. Further doping was detrimental to the rate. The mechanism for the promotion of the rate (peaking at 10% doping) was not elucidated.

5. 2 Objectives

The aim of this work was to investigate how proton conduction can influence the rate of thermal ammonia synthesis on metal surfaces in proximity to proton-conducting supports. Barium zirconate (BZ) ceramics were chosen as the target support material and ruthenium metal was chosen as the target metal phase to investigate this effect.

It is known that the proton conductivity of BZ ceramics is highly dependent on the doping of the Zr-sublattice (Section 1.3.1). Both the nature of the dopant, and the percentage substitution influence the conductivity of the material.

The aims of this chapter were as follows:

4. Investigate how changing dopant cation of a BZ ceramic effects the ammonia synthesis activity over Ru/BZ catalysts.
5. Investigate how the yttrium doping level of a BZ support can affect activity of ammonia synthesis.
6. Investigate the spillover of protons from Ru particles to a BZ support.

To investigate how the dopant cation influenced catalytic rates, a range of lanthanide-doped barium zirconate materials were synthesised and tested for activity as supports for Ru-based ammonia synthesis catalysts.

Next it was investigated how doping level could influence rate. BZ supports with Y-doping levels between 0 and 50% were synthesised and tested as catalyst supports, and the relationship between conductivity and activity was established.

Catalysts were characterised using XRD, TEM & HRTEM, TGA, TPR, ICP-MS, and Chemisorption analysis.

Finally, evidence was sought for a spillover mechanism between ruthenium particles and the barium zirconate support. This was achieved through in-situ characterisation of ruthenium oxidation states under changing hydrogen pressure, and ex-situ characterisation of the concentration of lattice deuterons.

5. 3 Experimental

5. 3. 1 Preparation of Barium Zirconate Powders

Yttrium-doped barium zirconate ceramics were synthesised by a citrate-EDTA complexation method. Yttrium (III) nitrate hexahydrate ($Y(NO_3)_3 \bullet 6H_2O$), barium nitrate ($Ba(NO_3)_2$), and Zirconium (IV) oxynitrate hydrate ($ZrO(NO_3)_2 \bullet xH_2O$) (Sigma Aldrich) were used as starting materials. Hydration of zirconium oxynitrate was determined by TGA analysis, with x between 2 – 2.5. Lanthanide-doped barium zirconate ceramics were synthesised via the same procedure, but with the yttrium dopant replaced by a lanthanide (III) ion. Doping level was fixed at 20% for all lanthanide samples and was varied from 0 – 50 % for the yttrium samples. Lanthanide sources were as follows: erbium nitrate pentahydrate ($Er(NO_3)_3\ 5H_2O$), holmium nitrate pentahydrate ($Ho(NO_3)_3\ 5H_2O$), and ytterbium nitrate pentahydrate ($Yb(NO_3)_3\ 5H_2O$). **Table** 5-1 shows the acronyms and formulae for all synthesised ceramics.

In a typical procedure, $BaZr_{1-x}Y_xO_{3-\delta}$ was synthesised by dissolving the metal nitrate salts in water in stoichiometric ratios under high stirring. EDTA was added and the pH adjusted to ~10 using aqueous NH_4OH. Citric acid was added, and the pH again adjusted to ~10 using $NH_4OH_{(aq)}$. The molar ratio between the chelating agents and the metal nitrate salts was fixed at 1.5:1.5:1 EDTA: CA: metal ions. This solution is heated in an oven, until it combusts, yielding a black ash with rigid, porous structure.

The resulting ash was crushed into a fine powder and calcined in a furnace under high airflow to 1300 ºC for 4 hours, yielding an off-white powder. Complete calcination was confirmed by powder XRD phase analysis.

The powders were then wet milled in a Fristch P7 mill, in a ZrO_2 milling jar using 1mm ZrO_2 milling balls. The ball to powder ratio was initially determined from manufacturer's instructions and was eventually fixed at 5:12 mL of powder to 8 mL isopropanol. This corresponded to a close to maximum filling level of the milling jar. Powders were milled for 30 min @ 500 rpm, broken into 5-minute milling cycles with a 3 minute pause in between to dissipate excess heat.

Table 5-1: Formulas of investigated lanthanide and yttrium doped ceramics.

Acronym	Formula
BZEr20	$BaZr_{0.8}Er_{0.2}O_{3-\delta}$
BZHo20	$BaZr_{0.8}Ho_{0.2}O_{3-\delta}$
BZYb20	$BaZr_{0.8}Yb_{0.2}O_{3-\delta}$
BZ	$BaZrO_3$
BZY10	$BaZr_{0.9}Y_{0.1}O_{3-\delta}$
BZY20	$BaZr_{0.8}Y_{0.2}O_{3-\delta}$
BZY30	$BaZr_{0.7}Y_{0.3}O_{3-\delta}$
BZY50	$BaZr_{0.5}Y_{0.5}O_{3-\delta}$

5. 3. 2 Synthesis of Supported Ruthenium Nanocatalysts

Supported Ru nanoparticles (NPs) were synthesised by a wet-impregnation procedure. Both ruthenium (III) acetylacetonate ($Ru(acac)_3$) and tri-ruthenium dodecacarbonyl ($Ru_3(CO)_{12}$) sources were investigated. While most reports on wet-impregnation synthesis utilise stirring to achieve uniform distribution of the precursor onto the support, it was found that with stirring alone, the barium zirconate supports would clump at the bottom of the reaction flask. Sonication was employed instead, resulting in a much better dispersion of the reaction mixture

5. 3. 2. A Preparation of Ruthenium Nanoparticles from Ru(III) Acetylacetonate

Ru NPs were synthesised by wet impregnation, followed by temperature controlled chemical vapour deposition reduction. Typically, 100mg $Ru(acac)_3$ was dissolved in 1 mL acetone, and sonicated with the support material for 2 hrs, then stirred overnight and dried in an oven for 2 hrs to yield a red powder. Powder was reduced in a furnace under 30 mL min^{-1} 5% H_2:Ar flow heated to 150 ºC at 5 ºC min^{-1}, held for 24 hrs then heated to 350 ºC at 5 ºC min^{-1}, held for 24 hrs and cooled to room temperature. The catalyst was passivated for 2 hrs under 30 mL min^{-1} 2.5% O_2:He to yield a grey powder.

5. 3. 2. B Preparation of Ruthenium Nanoparticles from Tri-Ruthenium Dodecacarbonyl

Ru NPs were prepared from a ruthenium carbonyl ($Ru_3(CO_{12})$ precursor according to the method reported by Aika et al.[7] $Ru_3(CO)_{12}$ was dissolved in tetrahydrofuran (THF), to give an orange solution. 20 mL THF per 30 mg $Ru_3(CO)_{12}$ was used to reliably achieve complete dissolution without the need for heating. After dissolution of the precursor, barium zirconate support was added, with the ruthenium loading fixed at 15 wt%. The resulting suspension was sonicated for 6 hours, at which point the solvent was removed by rotary evaporation, leaving an orange powder.

$Ru_3(CO)_{12}$ was then decarboxylated to give supported Ru NPs. The orange powder was heated in a furnace under 50 mL min^{-1} Ar to 70 ºC, where it dwelled for 4 hours, and then to 350 ºC where it dwelled for 5 hours before cooling to room temperature. A ramp rate of 2 ºC min^{-1} was used when heating. A grey powder was obtained, typically with yields >90%. No passivation was employed for this preparation.

5. 3. 3 Addition of Caesium Promoter

Caesium promoters were added to the Ru barium zirconate catalysts using wet impregnation. Caesium nitrate ($CsNO_3$) was used as a precursor, with a loading of 5 wt %. Ru barium zirconate catalyst was added to a small vial, then $CsNO_3$ was dissolved in the minimum volume of water (~ 2 – 3 mL for 200 mg of catalyst) under stirring, and the desired Ru barium zirconate catalyst was added to form a thick slurry. This mixture was stirred for 5 hrs, before drying in a vacuum oven at 70 ºC overnight. The $CsNO_3$ was reduced in-situ prior to testing; reports suggest it is reduced to sub-symmetric oxide, Cs_xO_y, $x/y = 2.7 – 3.6$.[15]

5. 3. 4 Catalytic Testing

Catalyst activity was evaluated in a differential, fixed-bed, single pass reactor, operating at low conversions. Gas flow was controlled by mass flow controllers (Bronkhurst), with all tests utilising a total flow rate of 200 sccm. Nitrogen and hydrogen were supplied from cylinders (BOC, 99.999%). Pressure was controlled by means of a backpressure regulator set at 10 or 50 bars, giving a total pressure of 11 or 51 bars. A heating element at the centre of the reactor (at the same level as the catalyst bed) was controlled using a PID controller.

Typically, 100 mg of catalyst was loaded into a quartz tube (7 mm internal diameter) and secured in place using quartz wool plugs. The sample was then sealed in the reactor and reduced under 50 sccm H_2 flow at 450 ºC. For testing, the gas flow was fixed at a ratio of 3:1 H_2:N_2 (200 sccm total flow), and the reactor was pressurised to the desired level. Once at pressure, the reaction was left stabilise for at least an hour before measurement started. The rate was determined by bubbling exhaust gases through an

acid trap (10 mM H_2SO_4) of exact volume, recording the time, and then measuring the concentration of the trap using an ammonium ion-selective electrode.

The volume of the catalyst bed was 0.1 cm^3, and from this the residence time could be calculated as 0.29 s at standard pressure, 2.9s at 10 bar, and 14.5s at 50 bar.. The GHSV of the reactor was calculated to be 10,900 mL g^{-1} h^{-1}, or based on the density of the catalyst bed, 12,400 h^{-1}. Reaction order measurements were carried out under the same conditions as the rate measurements, but the hydrogen partial pressure was reduced, while maintaining a total flow of 200 sccm using Ar balance gas.

5. 4 Characterisation

5. 4. 1 Ruthenium Nanocatalysts Derived from $Ru(acac)_3$ on Lanthanide-Doped Barium Zirconate Supports

Barium zirconate ceramics with 20 mol % of the lattice doped with a lanthanide (III) ion were prepared for use as supports for Ru NPs. 5 wt% Ru was then added by wet impregnation of $Ru(acac)_3$ as discussed in section 5. 3. 2. The formulas of all investigated materials are shown in **Table** 5-1.

X-ray diffraction (XRD) was used to investigate the crystal structure of the ceramics and confirm the formation of phase-pure barium zirconate materials based on a reference literature pattern. XRD patterns recorded after the wet impregnation and reduction of $Ru(acac)_3$ still showed only phase-pure barium zirconate. The lack of peaks for Ru is presumably due to high dispersion and small size of particles.

Transmission Electron Microscopy (TEM) images in Figure 5-2 confirmed Ru NPs were successfully synthesised by wet-impregnation and reduction of $Ru(acac)_3$. A BZEr20 support pre- (top left) and post- (bottom left) synthesis of Ru nanoparticles showed the appearance of nanoparticles on the BZEr20 particles.

TEM also gave an insight into the porous structure of the support with pore diameters around 100 nm in the BZY20 support of a RuBZY20 catalyst. (Figure 5-2, top right). Higher magnification image showed the dispersion of Ru NPs on the same catalyst (bottom right). TEM images were used to generate histograms of the average particle size. An average of 50 measurements were used to generate each histogram using several images taken at different parts of the sample (

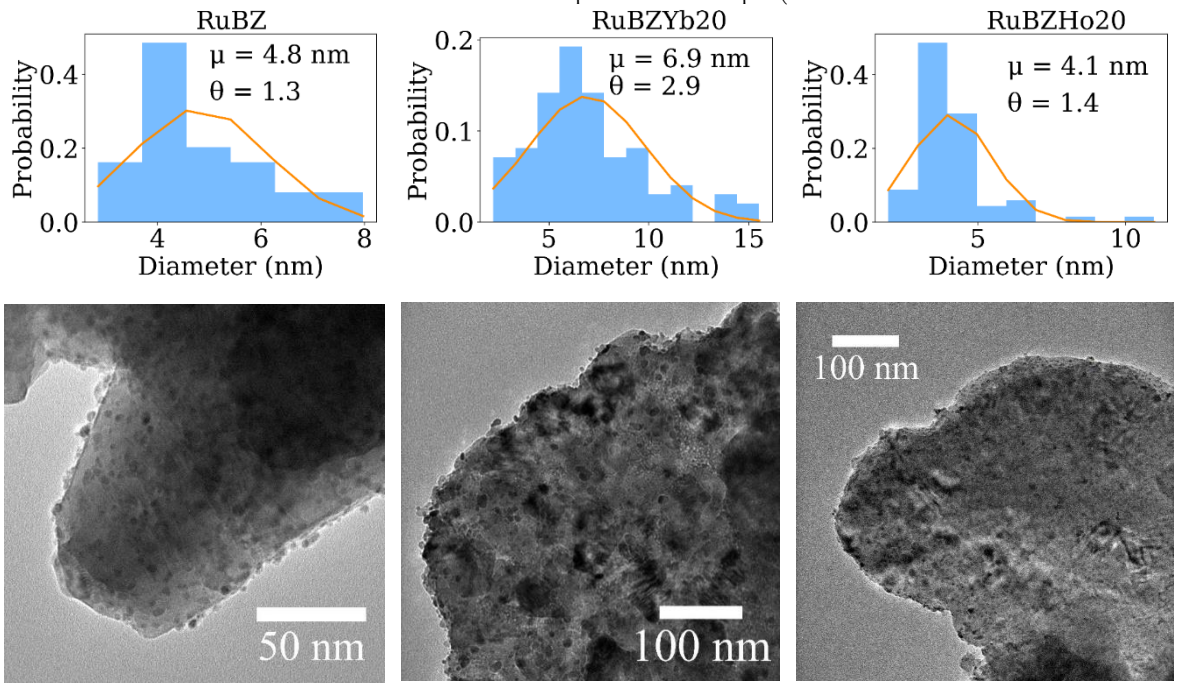


Figure 5-3).

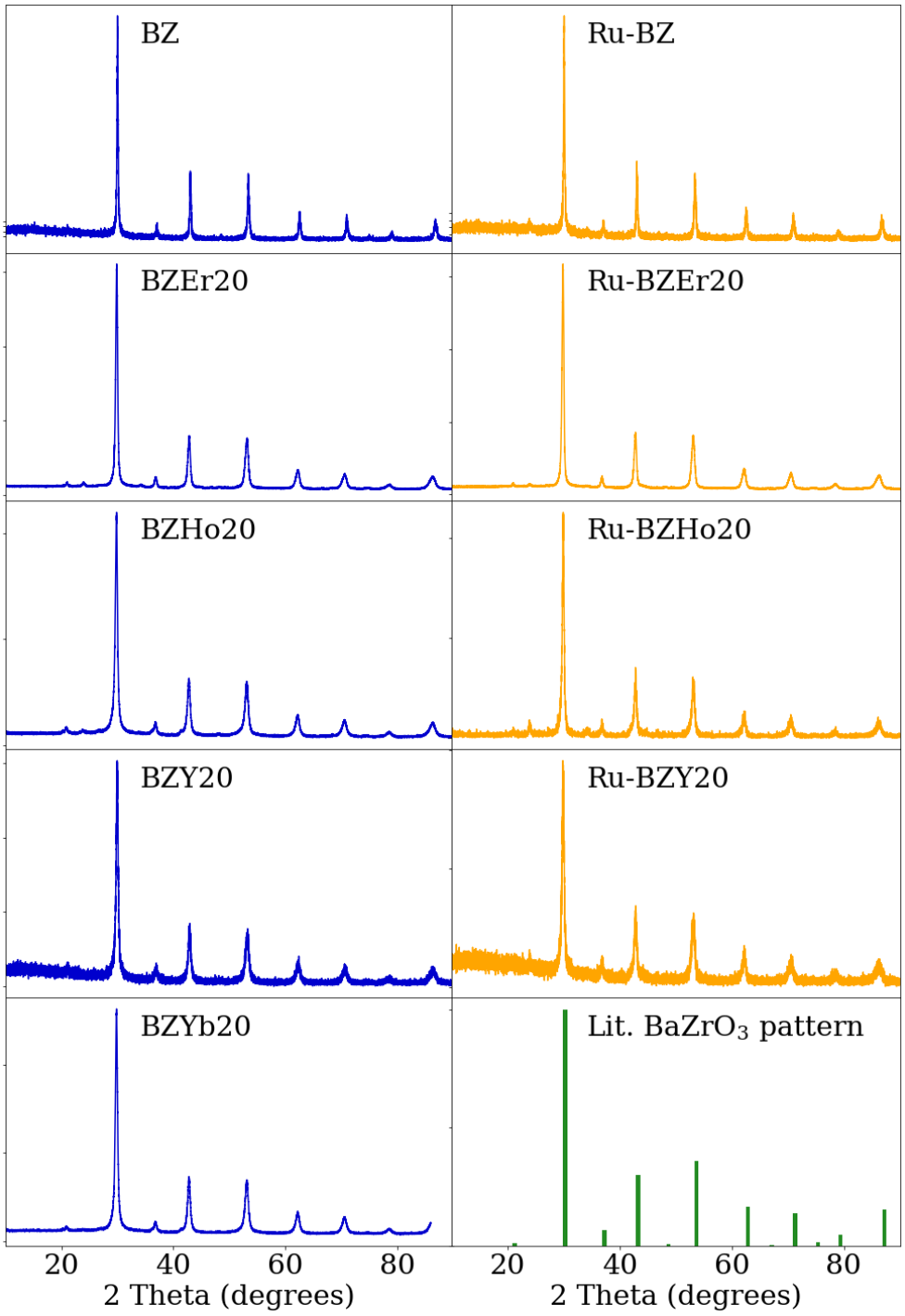


Figure 5-1: XRD patterns of lanthanide-doped supports before (left column) and after (right column) Ru impregnation and reduction. Bottom right shows a literature $BaZrO_3$ pattern. All peaks were indexed to pure $BaZrO_3$ as discussed in chapter 3.

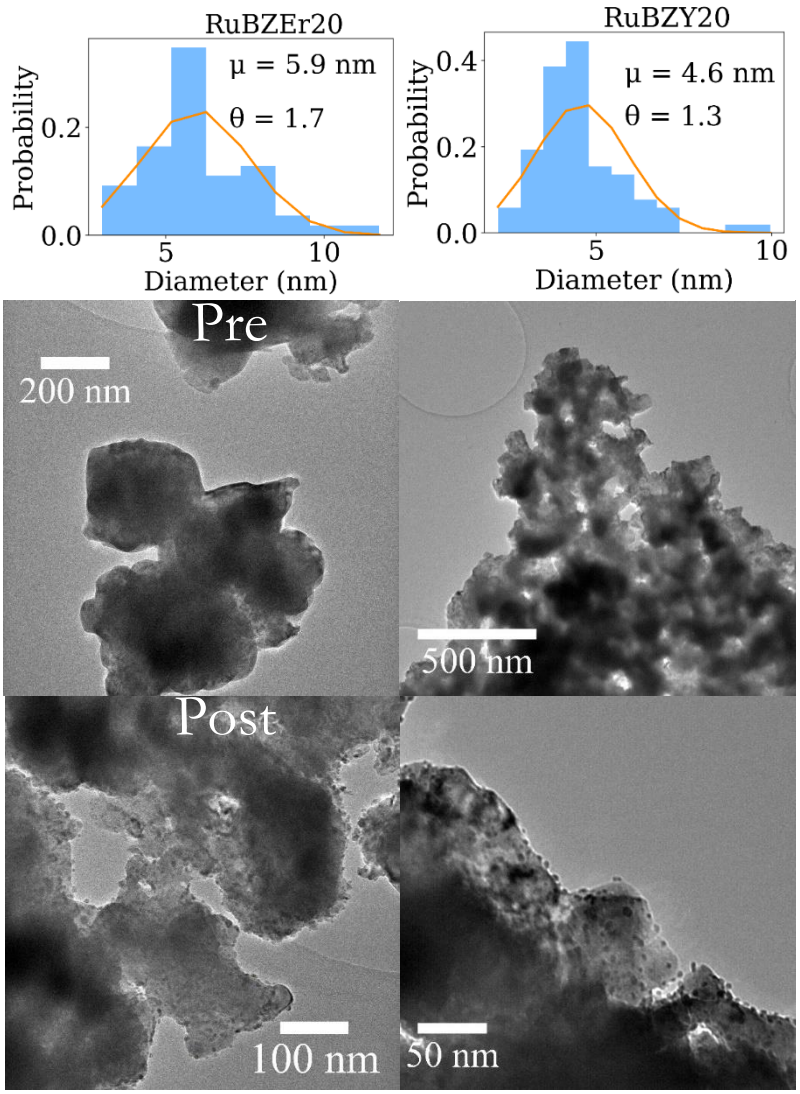


Figure 5-2: RuBZEr20 (left) and RuBZY20 (right) TEM data. Histograms show average Ru diameter as measured from the images. Left column shows RuBZEr20; images show BZEr20 support pre- and post-synthesis of Ru NPs. Right column shows RuBZY20 catalyst; top image shows the porosity of the support and bottom the presence of Ru NPs.

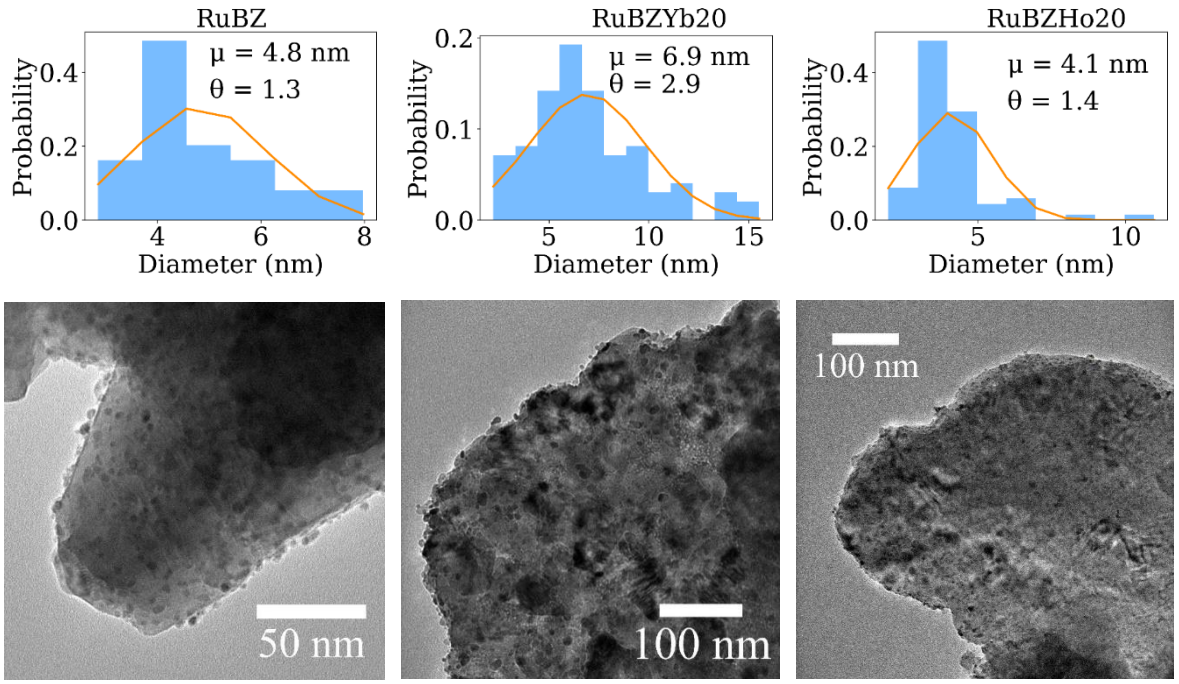


Figure 5-3: TEM images and Ru particle size histograms of RuBZ, RuBZYb20 & RuBZHo20 catalysts. Histograms were produced from average of 50 measurements of Ru particle diameter across multiple images for each sample. Inset of histogram gives mean (μ) and standard deviation (θ) of particle size.

Temperature programmed reduction (TPR) was used to investigate the reduction of Ru NPs on barium zirconate supports. After ex-situ reduction of the Ru precursor, ~ 30 mg of sample was packed into a quartz tube. The tube was purged with He (10 mL min^{-1}), and heated to 150 °C to remove surface adsorbates. After cooling to 40 °C, the gas was changed to 5% H_2 in Ar, and the sample heated at 5 °C min^{-1} to 600 °C. The exhaust gas was flowed over a thermal conductivity detector (TCD), and the signal in mV recorded.

Figure 5-4 shows temperature reduction profiles of BZY20 and BZYb20 supports in the absence and presence of Ru NPs (passivated by O_2). Where the supports themselves did not reveal an obvious H_2 consumption peak, a sharp peak at low temperature, and a broad peak between 215 and 370 °C, which looks to be two overlapping, broad peaks, were immediately apparent in Ru containing samples. The symmetric low temperature peaks are consistent with the reduction behaviour of RuO_2.[16] The broad, complex reduction peaks in the range 215 – 370 °C indicate some Ru species exist in heterogeneous chemical environments (variations in size and structure), leading to the different peak maxima.

There were clear differences between the Ru reduction behaviour on the two supports, with peaks occurring at lower temperatures on the Yb-doped support than on the Y-doped which might indicate that Yb doping can facilitate the reduction of ruthenium oxide species. Reduction of Ru was complete at temperatures below 400 °C in both cases, meaning the selected reduction temperature (450 °C) of catalysts prior to catalytic testing is sufficient to reduce all Ru oxides.

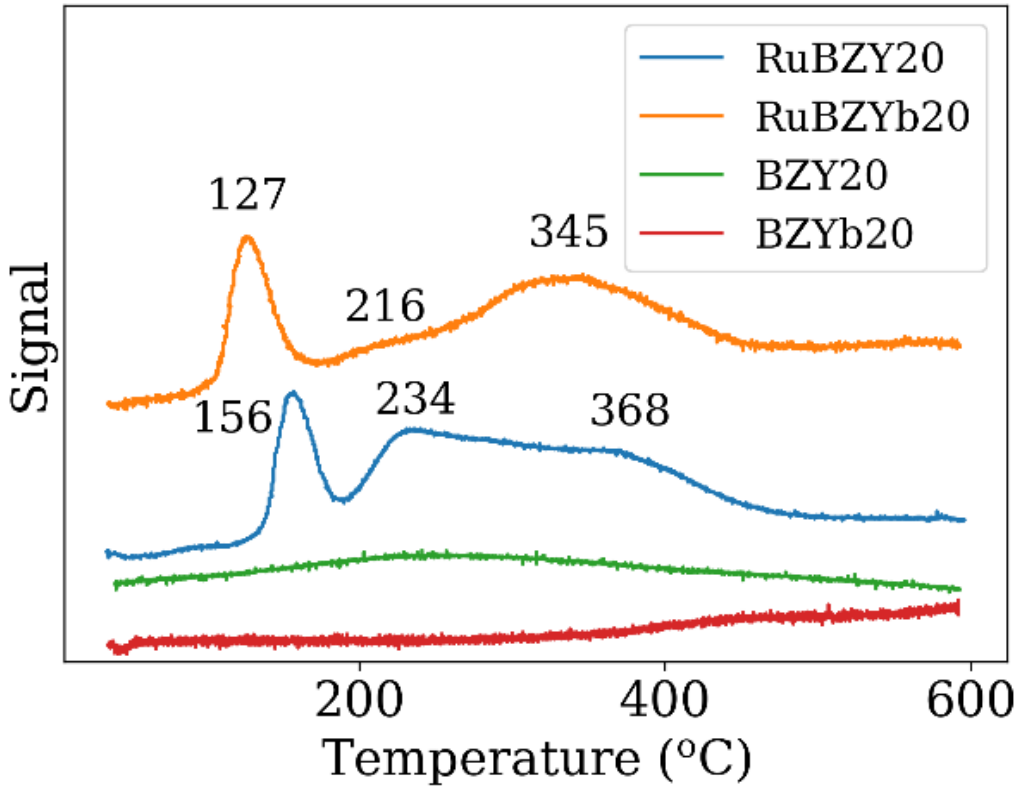


Figure 5-4: TPR plots of BZY20 and BZYb20 supports before and after synthesis of Ru NPs.

5. 4. 2 Ruthenium Nanocatalysts Derived from $Ru_3(CO)_{12}$ on Yttrium-Doped Barium Zirconate supports

Ruthenium nanocatalysts (10 wt.%) derived from ruthenium dodecacarbonyl were prepared on yttrium doped barium zirconate (BZY) supports. The Y-doping level was varied between samples, and the formulas of all investigated materials are shown in **Table** 5-1.

Elemental analysis was conducted through The Hong Kong Polytechnic University. An Optima 8300DV ICP-AES system was used to determine the concentrations of Ru and Y in a batch of RuBZY20 catalyst, before and after catalytic testing, and a batch of RuBZ catalyst prior to any testing.

Table 5-2: Weight percent values as determined from ICP-AES analysis.

Sample	Element	Weight %	Calculated Weight %
RuBZY20	Ru	9.974	-
Post-reaction	Y	5.896	5.856
RuBZY20	Ru	8.203	-
Pre-reaction	Y	5.732	5.952
RuBZ	Ru	6.569	-
Pre-reaction	Y	0.005	-

Table 5-2 shows the weight % values; Ru weight % varies between ~6 – 10 for the tested catalysts. To compare reported Y wt% to the stoichiometric BZY20 formula, a theoretical Y wt% was calculated:

Theoretical stoichiometric formula of BZY20 = $BaZr_{0.8}Y_{0.2}O_3$

Stoichiometric mass (m) = 1/137.27 + 0.8/91.224 + 0.2/88.905 + 3/15.999

Stoichiometric mass after Ru synthesis = m + (m x Ru wt%)

Calculating a theoretical weight % of Y based on the measured values of Ru wt% gives a value close to that reported by the data. Therefore, the values are regarded to be reliable estimates of the wt% of all components. Some assumptions must be made in calculating these values; the real oxygen stoichiometry will be lower than 3 due to oxygen vacancies, and error in the Ru wt% values will carry through to the yttrium values. Also, the pre- and post- testing BZY20 samples were from the same catalyst batch, so the Y wt% values should be identical, the discrepancy is experimental error. These ICP-AES results confirm that the doping level of ytrrium in the support is approximately 20%, although are not truly accurate measures of this value. They also show that the level of Ru loading may vary between catalysts by at least 3.4%.

Thermogravimetric analysis (TGA) was used to investigate the decomposition of $Ru_3(CO)_{12}$ precursor on a BZY20 support. After the wet impregnation and removal of solvent, ~15 mg of the

$Ru_3(CO)_{12}$-BZY20 sample was placed into a platinum pan, sealed in the instrument and the atmosphere purged with 100 mL min^{-1} N_2 flow. The temperature was then ramped at 10 ºC min^{-1} to 600 ºC, and the mass change recorded. Figure 5-5a shows the derivative of the mass plotted against temperature. A sharp mass change peak at 143 ºC with shoulders at 174, 200, and 233 ºC was observed. Complete decomposition of the $Ru_3(CO)_{12}$ precursor is observed, in agreement of the results of Gutiérrez et al.[17].

TPR was carried out to investigate the conditions for reduction of catalysts prior to catalytic testing. ~30 mg of a RuBZY20 catalyst (after the ex-situ decomposition of the precursor) was placed into a quartz tube and secured with quartz wool before placing into a Quantachrome ChemBET pulsar, equipped with a TCD detector. Sample was heated under N_2 to 120 ºC to remove surface adsorbates, before cooling the sample, changing the gas to 5% H_2/Ar and heating at 10 ºC min^{-1} to 600 ºC.

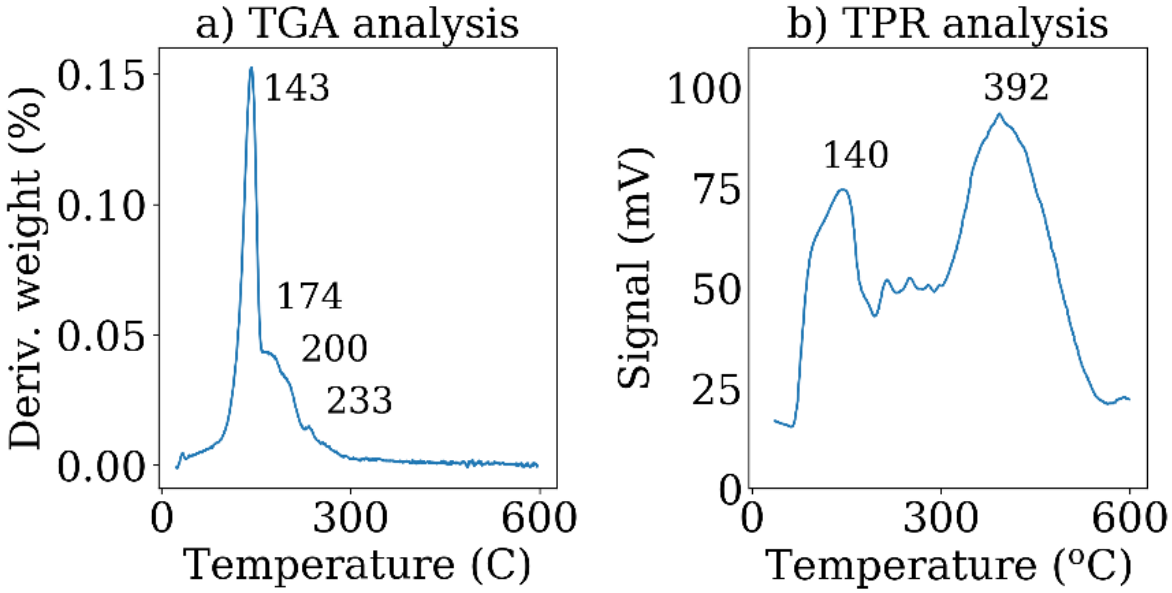


Figure 5-5: a) TGA plot showing decomposition of $Ru_3(CO)_{12}$ precursor on a BZY20 support. b) TPR plot showing reduction of RuBZY20 catalyst up to 600 ºC

Two reduction peaks were observed, at 140 and 392 ºC. The low temperature peak is consistent with the previous TPR results and assigned to the reduction of RuO_2. The high temperature peak is considerably different to the previous TPR results, and much sharper (although still a broad peak), suggesting more homogeneity in the Ru structures. This could be due to this preparation yielding more consistent Ru particles. It could also be the case that removing the passivation step from the synthesis causes a more substantial bulk oxidation of the ruthenium structures to occur. This would explain the change in relative intensity between the two peaks, with the low temperature peak representative of the surface RuO_2 species, and the high temperature one arising from the reduction of oxide species in the bulk structure.

Pulse titration analysis was used to determine the exposed Ru surface area, conducted on a ChemBET Pulsar equipped with a TCD and an automatic injection loop, with a measured volume of 68.25 µL. 100

mg of catalyst was used for each test and secured in a quartz tube with quartz wool. Catalysts were heated to 450 ºC under 5% H_2/Ar to remove surface oxide, then the gas changed to He and purged for an hour before cooling down to remove adsorbates from the Ru surface. Temperature was held at 40 ºC for the duration of all pulse titration experiments. Carbon monoxide held in the injection loop was injected into stream of He flowing over the catalyst surface, causing peaks in the TCD, as seen in the left column of Figure 5-6. After ~4 peaks, the Ru surface was saturated with CO, and the peaks had constant areas. The change in peak area is shown in the right column of Figure 5-6. The total adsorbed CO was calculated by recognising that the area of the peaks once saturated corresponded to 68.25 μL. Therefore, the difference between the saturated peak areas and the peaks below this threshold is equal to the total amount of CO adsorbed to the catalyst surface. Converting these area values into cm^3 and moles gives the values in Table 5-3 (shown per gram of catalyst used for each test).

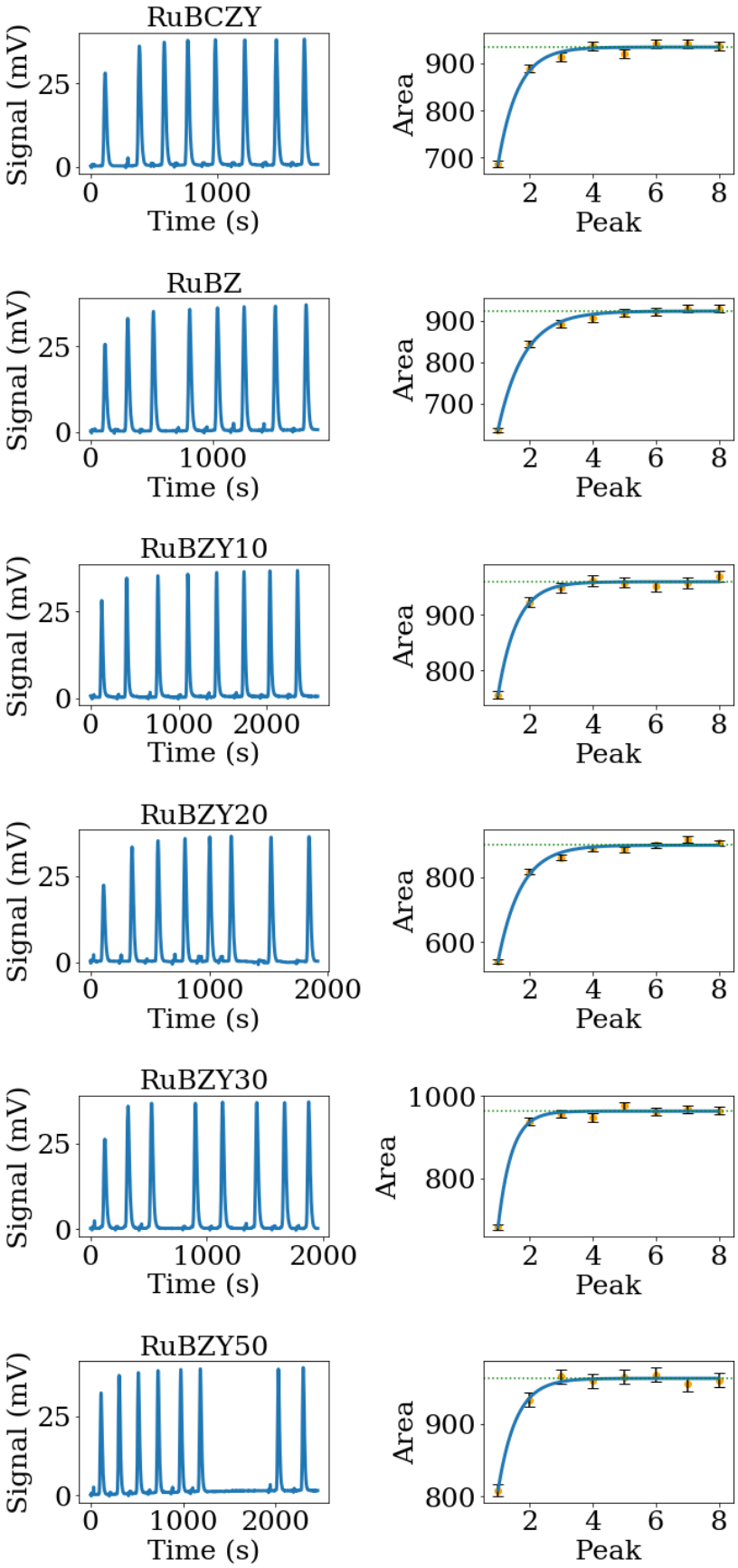


Figure 5-6: Pulse titration analysis of Ru barium zirconate catalysts. Left column shows signal from TCD detector against time. Each peak represents a pulse of CO released into the gas stream flowing over the catalyst surface. Right columns show the increase of peak areas as Ru surface becomes saturated with CO molecules.

It is reported that CO adsorbs to Ru atoms in a 1:1 ratio,[18] therefore the moles of adsorbed CO g^{-1} catalyst should be roughly equivalent to the moles of exposed Ru surface atoms. The moles of CO adsorbed per gram of catalyst are quite consistent, suggesting the amounts of exposed Ru atoms is similar across samples. RuBCZY showed the highest adsorption of CO, however this catalyst did not show promising rates so was excluded from further characterisations. RuBZY50 showed the lowest CO adsorption and was also phased out of further testing in favour of supports with better characterised crystal structures. The other catalysts showed quite consistent amounts of adsorbed CO. How the exposed Ru surface atoms impacted the synthesis rates will be discussed in section 0

Table 5-3: Total volume and moles of CO adsorbed to each catalyst during pulse-titration analysis.

Catalyst	Adsorbed CO (cm^3 g^{-1})	Adsorbed CO (mols g^{-1})
RuBCZY	0.389	2.23×10^{-5}
RuBZ	0.312	1.79×10^{-5}
RuBZY20	0.365	2.09×10^{-5}
RuBZY30	0.232	1.33×10^{-5}
RuBZY50	0.167	9.56×10^{-6}
RuBZY10	0.226	1.29×10^{-5}

TEM images were recorded at the Hong Kong Polytechnic University. Images of samples pre and post catalytic testing were recorded. The image resolution was high enough such that lattice fringe measurements could be taken. These were clearly identified as ruthenium, which displays lattice fringes between 0.21 and 0.23 nm.[19] After identifying Ru metal, nanoparticles could be identified. To most clearly illustrate the presence of particles and lattice fringes, the best available images of a sample of RuBZ post-catalytic testing is presented first (Figure 5-7). Later discussed are the changes of the catalysts pre and post testing.

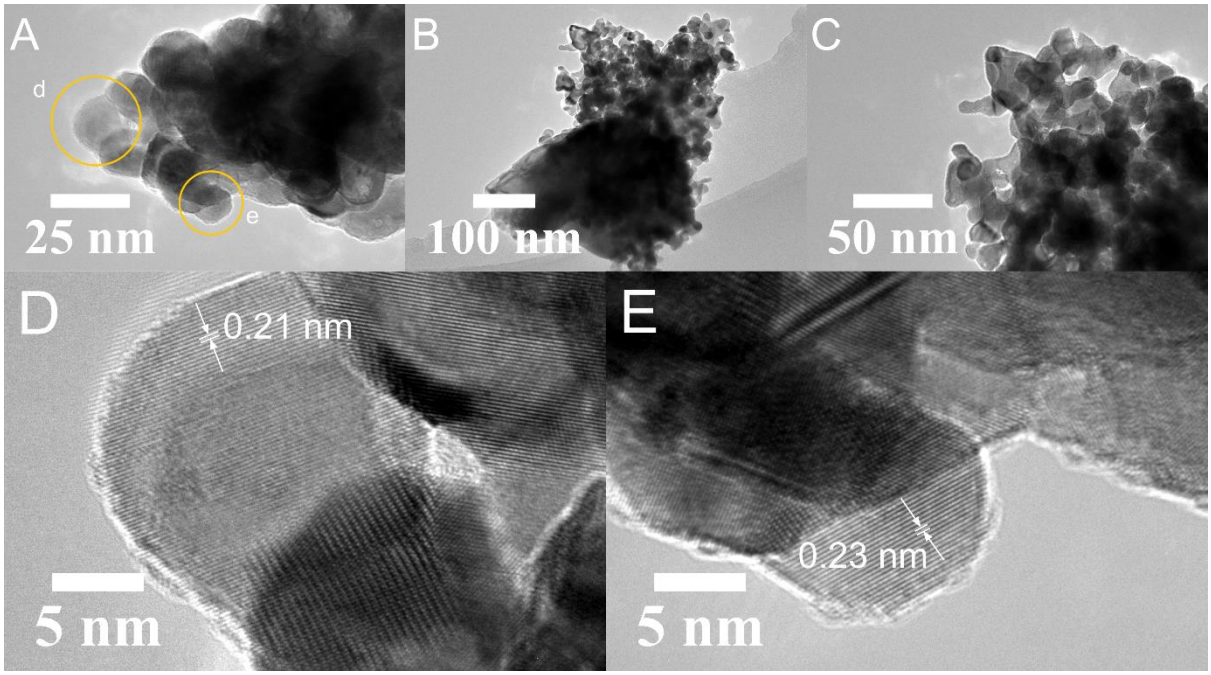


Figure 5-7: TEM images of RuBZ catalyst post catalytic testing; a) Presence of nanoparticles ~13 nm in diameter, circles indicate particles used for lattice fringe measurements. b) and c) show a high coverage of nanoparticles on support. Resolution of images was high enough to observe lattice fringes, measured to be between 0.21 and 0.23 nm (d & e).

Particles were typically larger than those synthesised from $Ru(acac)_3$ precursor previously presented, often above 10 nm. The coverage of particles on support was also much higher, with particles at times appearing to grow on one another rather than the support. There were also significant differences between the samples pre and post catalytic testing. For a RuBZ sample, average nanoparticle size increased from around 5 nm (Figure 5-8a) to 13 nm (Figure 5-7) after catalytic testing. In a RuBZY20 sample post testing, the growth of large, metallic ruthenium structures was observed (Figure 5-8b). Particle sizes of RuBZY20 prior to catalytic testing could not be reliable measured. A sample of RuBZY50 pre catalytic testing showed Ru NPs with a diameter of around 10 nm (Figure 5-8d).

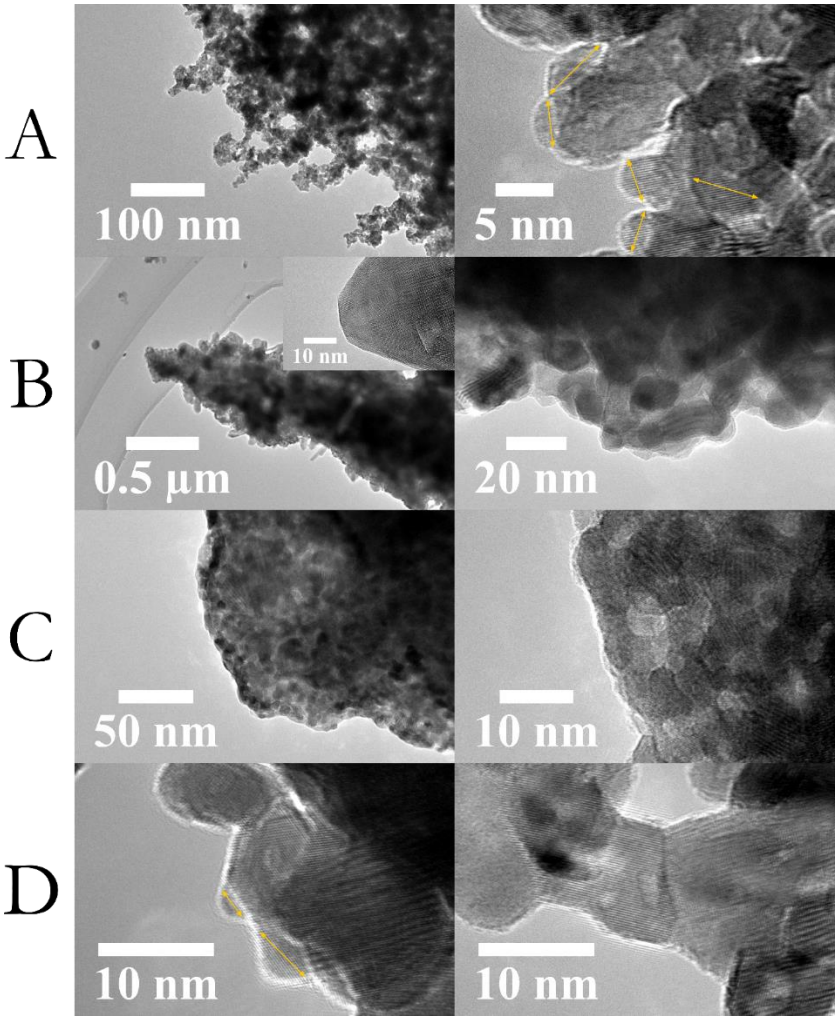


Figure 5-8: TEM images of Ru barium zirconate catalysts before and after catalytic testing; A) RuBZ pre-, B) RuBZY20 post-, C) RuBZY20 pre-, & D) RuBZY50 pre-reaction.

To better elucidate the dispersion of nanoparticles on the barium zirconate supports, Scanning Transmission Electron Microscopy-High Angle Annular Dark Field (STEM-HAADF) images of a RuBZY10 catalyst (pre-reaction) were collected, shown in Figure 5-9. High dispersion of Ru nanoparticles on barium zirconate supports was clearly observed, with Ru particle sizes ranging from 5 – 15 nm.

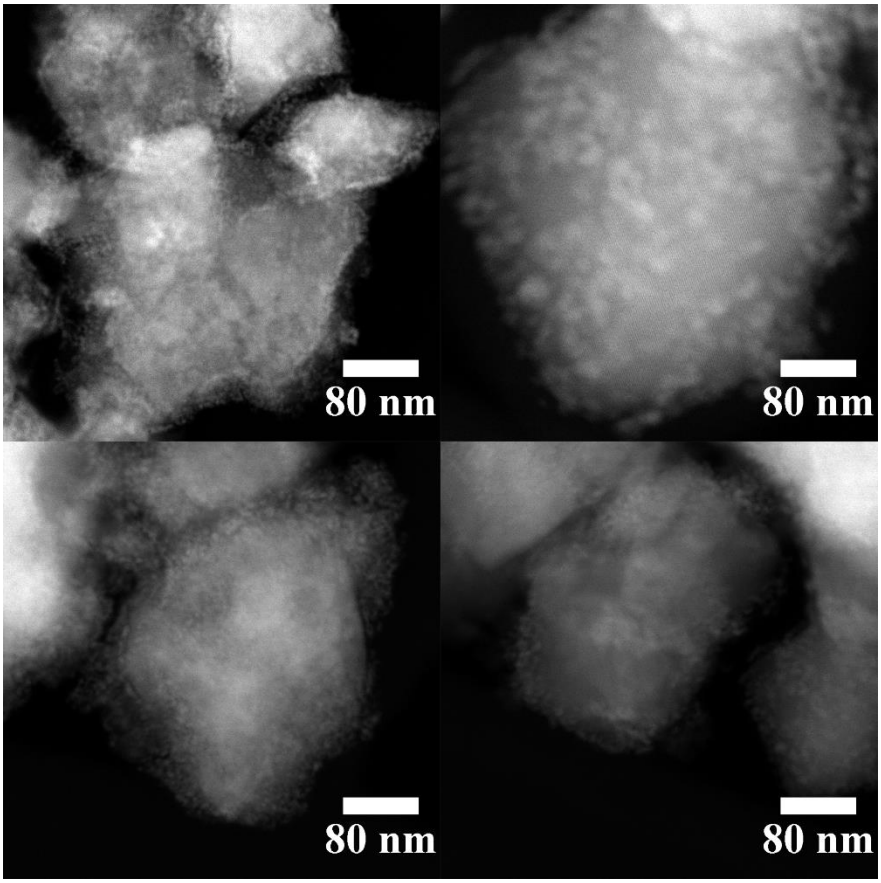


Figure 5-9: STEM-HAADF images of RuBZY10 catalyst. Brighter Ru particles observed on top of support. Ru particle sizes between 5 – 15 nm were measured, however resolution was too low to accurately calculate an average.

5. 5 Catalytic Testing

5. 5. 1 Catalysts Derived from Lanthanide-Doped Supports

The ammonia synthesis rates over Ru NP catalysts on lanthanide doped supports (RuBZLn) were investigated in a fixed bed reactor. A catalyst prepared from yttrium-doped barium zirconate (RuBZY20) was included as a benchmark, known to display high proton conductivity. The conditions for each test were fixed at 51 bar total pressure, 50 mL min^{-1} flow of 75:25 % H_2:N_2, and 450 °C. After reduction and stabilisation steps, exhaust gas was bubbled through an acid trap, and the trap periodically changed and measured to determine the rates of ammonia synthesis.

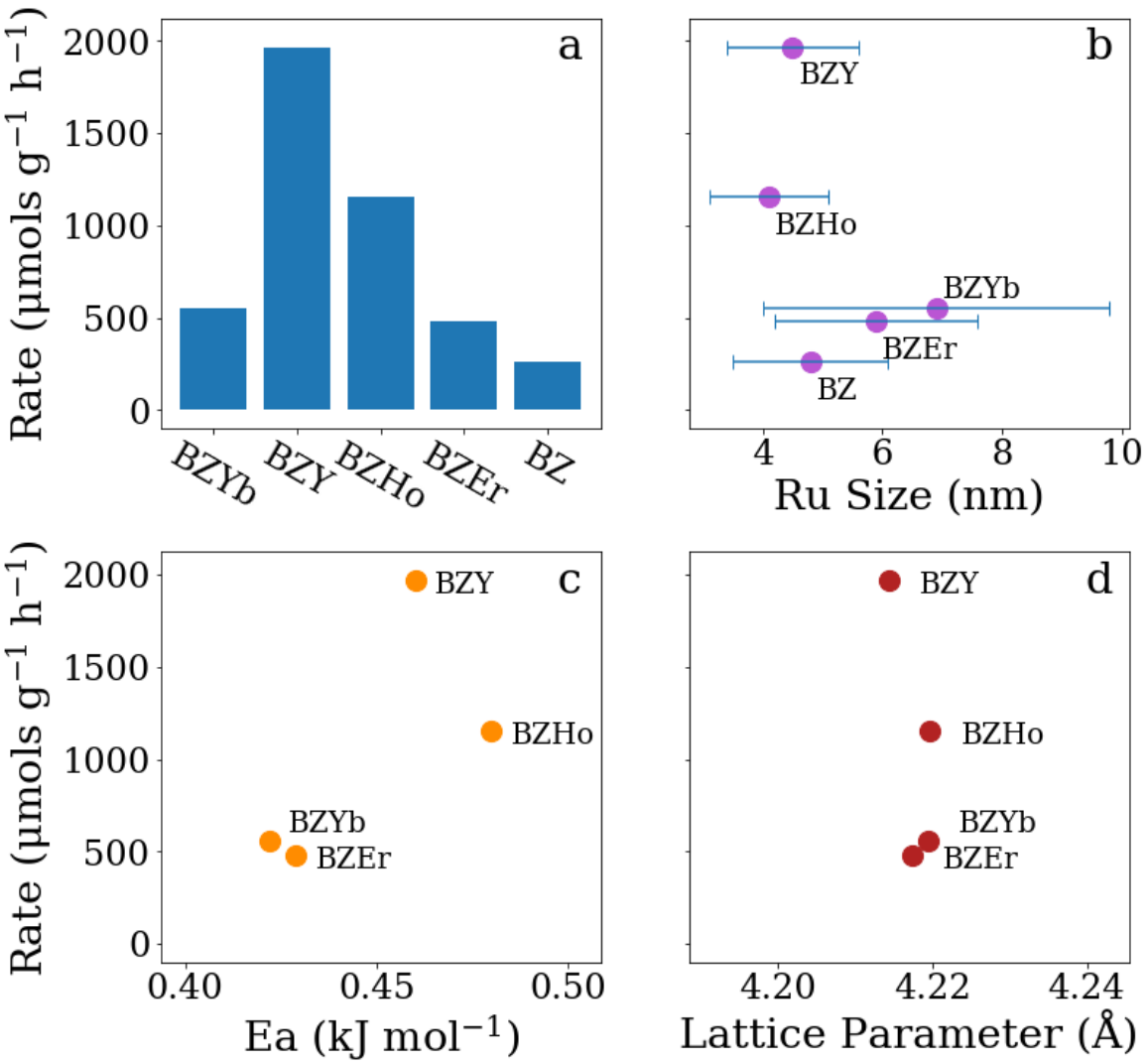


Figure 5-10: a) Rates of ammonia synthesis over RuBZLn and RuBZY20 catalysts b) Size of Ru nanoparticles measured from TEM against rate of ammonia synthesis c) activation energy for intragrain proton transport, from reference [20] d) lattice parameters calculated from XRD patterns

It was observed that a change of support had a dramatic effect on the rate of ammonia synthesis (Figure 5-10a). The yttrium doped support gave the highest overall rate, and the support with no doping

the lowest. The lanthanide doped catalysts all showed modest rates. As previously discussed, Ru particle size has a significant effect on the rate of ammonia synthesis over Ru nanocatalysts. Figure 5-10b shows the rates of ammonia synthesis against Ru particle size as measured from TEM, error bars represent the standard deviation of the measurements. Plotting rates against average TEM particle size showed no correlation, suggesting the difference in rates are not due to particle size effects.

The rates could not simply be explained by examining the proton mobility of the supports either. Activation energy of the intra-grain proton transport is representative of the ease with which protons can move within the support; a support with lower activation energy may promote 'spillover' of hydrogen atoms to the support, discussed later in more detail. A paper by Han et al. measured the rates of proton uptake and transport in lanthanide-doped barium zirconate supports.[20] They reported values of activation energy for the intragrain transport of protons in the lattice, as measured by electrochemical impedance spectroscopy. The differences in proton mobility do not seem to correlate with the rates, Figure 5-10c. In another paper by Han et al., they correlated the lattice parameter to the concentration of protons per unit cell [21]. Higher lattice parameters allowed a greater degree of hydration of the lattice. Lattice parameters were calculated from XRD patterns in Figure 5-1. Calculated parameters are similar to those reported by Han et al., but do not correlate with observed reaction rates (Figure 5-10d).

An investigation of lanthanide doped supports for Ru nanocatalysts for the reduction of dinitrogen to ammonia did not yield any definitive correlation; neither Ru size, proton mobility, nor lattice parameter influenced the rates of ammonia synthesis. However, the benchmark catalyst (RuBZY20) emerged as the most active candidate. Comparing the 20% yttrium doped (BZY20) and undoped BZ supports showed a change in doping level can have a dramatic influence on the rate. For this reason, a new experiment was designed to instead investigate the effect of doping level on catalytic rates.

5. 5. 2 Catalysts Derived from Yttrium-Doped Supports

A series of yttrium doped barium zirconate supports was synthesised; undoped BZ, 10% yttrium-doped BZY10, 20% yttrium-doped BZY20, and 50% yttrium-doped BZY50. According to literature, the BZY10 and BZY20 supports show high proton conductivity (of the same order of magnitude), BZY50 shows a noticeably lower proton conductivity, and BZ does not show any real proton conductivity at the temperatures of interest for catalytic testing.

In addition, a Ce & Y co-doped barium zirconate ceramic was synthesised with the overall formula $BaZr_{0.7}Ce_{0.2}Y_{0.1}O_{3-d}$. This ceramic is reported to have a very high total proton conductivity, as the presence of Ce increases the inter-grain transport of protons, thanks to promotion of grain growth during sintering.[22]

Ru was added to these catalysts using the $Ru_3(CO)_{12}$ precursor as described in section 1.3 in detail. Catalytic testing was carried out in a fixed-bed flow reactor at temperatures of 450 °C, 10 bar pressure, and 200 mL min^{-1} total flow rate. Around 100 mg of catalyst is used for each reaction. An initial screen of catalytic rates showed that RuBZY20 still has the highest rate by a factor of 2. The rates then descend in the order RuBZY10, RuBZY50, and RuBZ (Figure 5-11a). RuBCZY had a rate greater than RuBZY50, but less than RuBZY10. BCZY was excluded from further tests to focus on the how specifically levels of yttrium-doping affected synthesis rates. The volume of CO adsorbed during chemisorption experiments, Table 5-3, is plotted against the measured rates for the 5 catalysts (Figure 5-11b). It is shown that the difference in rates is not simply due to differences in the levels of Ru loading on the support. Plotting the intra-grain proton conductivities reported by Fabbri et al (BZY20 and BZY50, 450 °C, wet 10% H_2/Ar atmosphere), and Iwahara et al. (BZ, 870 °C, pure H_2 atmosphere) against rate, showed an increase in rate with increasing proton conductivity (Figure 5-11c). [23,24]

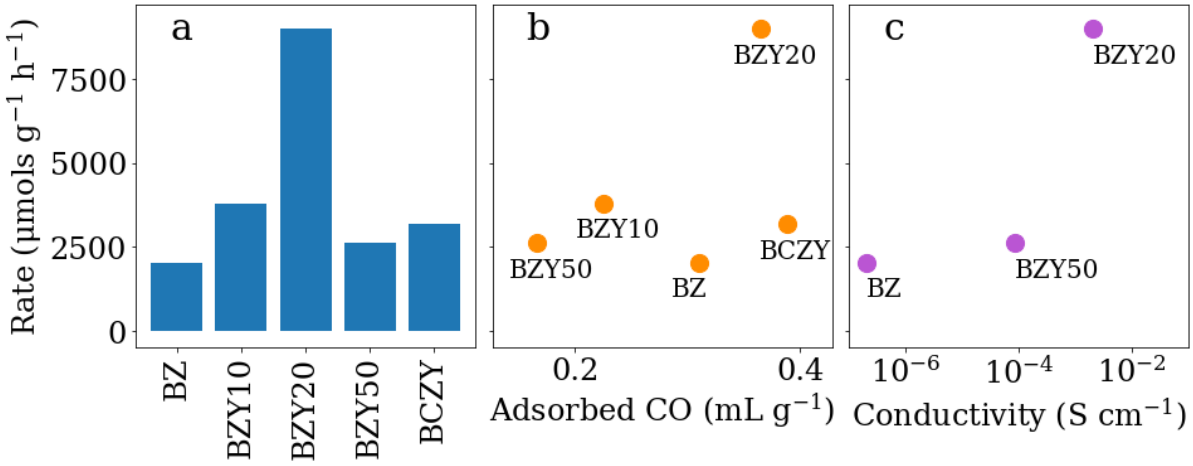


Figure 5-11: a) Rates of catalytic tests using different support materials b) Rates against adsorbed CO volume (measured from chemisorption) c) Rate vs conductivity for RuBZY10, RuBZY20 and RuBZY50 catalysts

It should be noted that comparing reported values of proton conductivities across different reported works is challenging. Proton conductivity measured by impedance is affected by the testing conditions

(temperature, atmosphere, electrode materials), and ceramic preparation (synthesis of oxide, pressing of pellets, sintering). This means there can be large variations in the conductivities not arising from fundamental material differences. In the case of the data used to construct Figure 5-11c, this is also true. However, the conductivities of undoped barium zirconates is so low as to effectively be zero for the purposes of the experiment. The conductivity of 10^{-7} S cm^{-1} from Iwahara et al. is representative of this but is not an accurate value under the conditions of the catalytic test.

It was observed in the catalytic tests, that the rates of ammonia synthesis would initially rise as the activation of the catalyst occurred, but then sharply drop off as the time on stream increased (Figure 5-12a). This is explained by the TEM images discussed earlier (Figure 5-7 & Figure 5-8), in which the growth of large Ru-nanostructures was observed during the course of catalytic testing. This sintering effect will cause a loss of Ru surface area, and a loss of the catalytically active stepped sites for dinitrogen reduction. To address this, an additional catalyst element was added; a Cs promoter. Alkali metal promoters are known to have a dual effect for Ru nanocatalysts for dinitrogen reduction; the donation of electrons into the Ru bands facilitating reduction of N_2, and structural promotion to hinder the sintering of Ru nanostructures. Indeed, after the addition of Cs-promoter, the promoted catalyst was dramatically stabilised compared to the unpromoted one. Rates for the promoted catalyst are an order of magnitude higher than the unpromoted one.

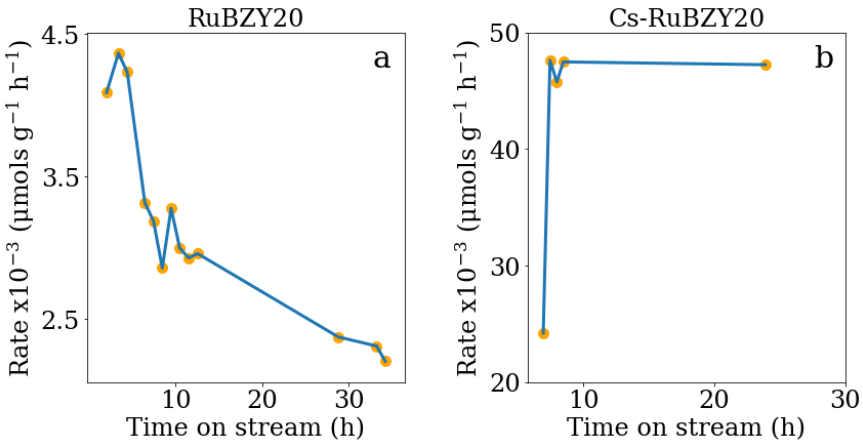


Figure 5-12: a) Rate change over 34 hours continual testing (RuBZY20 catalyst) b) Rate change over 24 hours continual testing (Cs-RuBZY20 catalyst)

5. 5. 3 Caesium Promoted Catalysts: Rates and Conversions

A range of caesium-promoted catalysts on barium zirconate supports were synthesised. The supports were doped with yttrium at a level of 0, 10, 20, and 30 %.

As with previous testing, a high GHSV value (12,400 h^{-1})was used, to minimise the residence time over the catalyst bed and stop the reaction being limited by equilibrium (i.e. back reaction of ammonia to nitrogen and hydrogen).

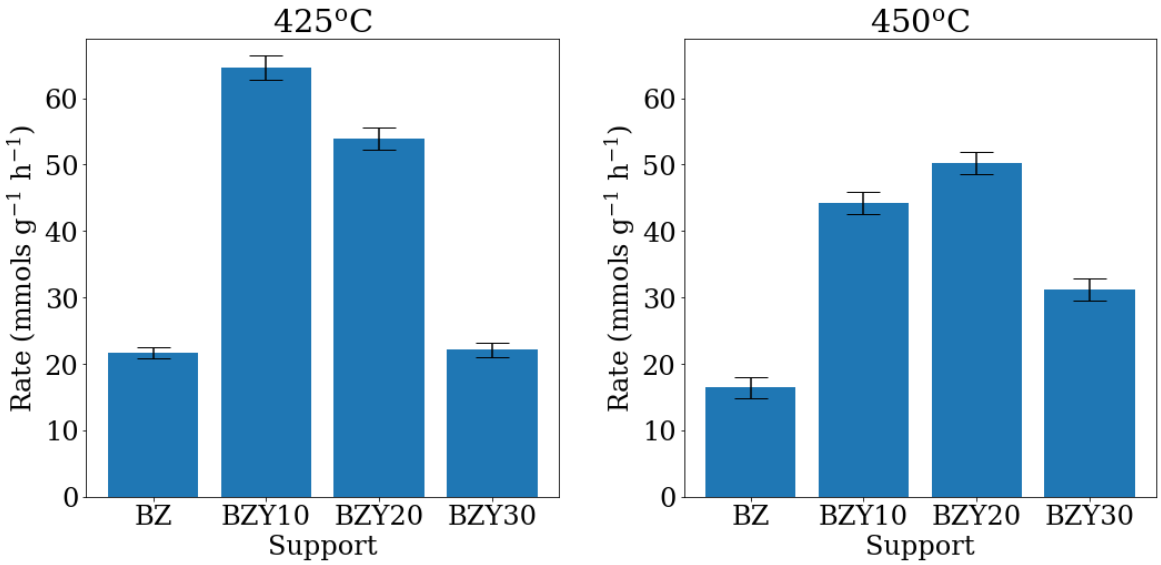


Figure 5-13: Reaction rates for Cs-Ru catalysts on Y-doped barium zirconate supports at indicated temperature. 10 bar total pressure, 3:1 H_2N_2, GHSV = 12,400 h^{-1}

Figure 5-13 shows the rates of reaction over the various catalysts at 425 and 450 °C. Two things are notable about the data, firstly BZY10 and BZY20 supports give much more active catalysts than BZ, or BZY30 supports. Secondly, rates over all catalysts, except for BZY30, decrease with increasing temperature, suggesting the reaction is being limited by equilibrium.

Temperature dependant studies were then carried out with the two most active catalysts. To examine the limiting effect of equilibrium on catalytic rates, reaction conversion values were calculated from the molar flow of nitrogen (50 sccm), and the observed moles of ammonia in the acid trap, as determined by ammonium ISE.

The equilibrium conversion under the experimental test conditions (10 bar total pressure, 3:1 H_2:N_2) was calculated using FactSage Education software. Plotted in Figure 5-14 are the equilibrium conversion, as calculated assuming ideal gas behaviour, and 20% of this equilibrium value.

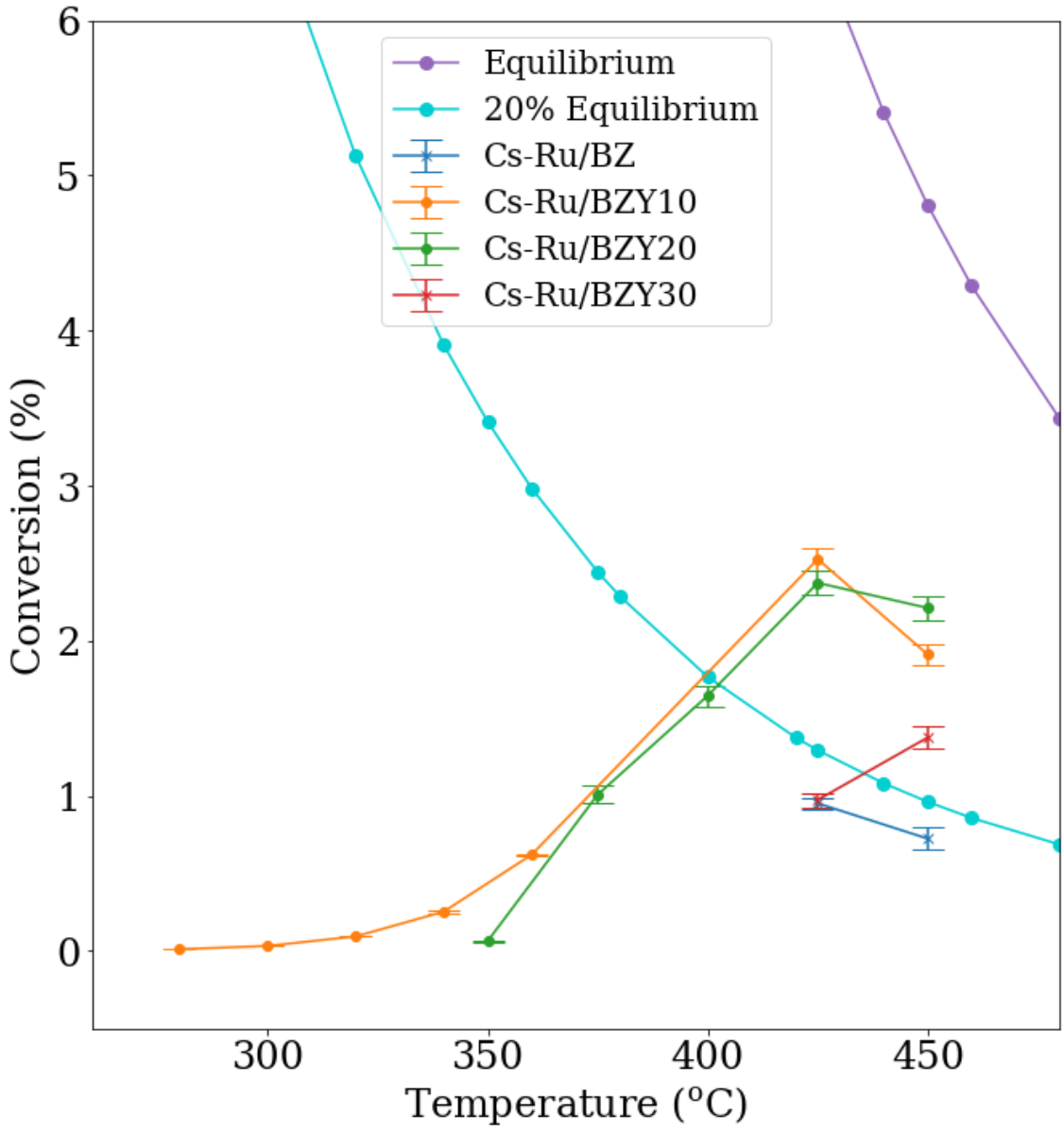


Figure 5-14: Conversion of reactant gases to ammonia for indicated catalysts vs temperature. Error bars represent the standard deviation across at least 3 independent rate measurements. Also plotted are equilibrium and 20% equilibrium values as calculated using FactSaage software. All experiments carried out with 0.1 g catalyst, 3:1 H_2:N_2, GHSV = 12,400 h^{-1}.

The conversion values for all recorded temperature points for all catalysts are presented in Figure 5-14. Indeed, most rate values recorded at temperatures of 425 and 450 °C have conversion values greater than 20% of the equilibrium value, where the conversion is expected to be partially limited by decomposition of ammonia. The data for BZY20 and BZY10 catalysts confirm that the conversion values rise with increasing temperature before being limited by back reaction of ammonia to nitrogen and hydrogen.

As discussed in Section 5. 1, the dissociative adsorption of dinitrogen to ruthenium catalysts is inhibited by the preferential adsorption of hydrogen. As the critical B5 sites upon which dinitrogen

adsorption takes place become saturated with hydrogen atoms, the rate of ammonia synthesis will drop. This poisoning effect is more pronounced at both low temperatures and high hydrogen partial pressures.

The extent of hydrogen poisoning can be determined by looking at the order of reaction with respect to hydrogen. If increasing the partial pressure of hydrogen results in a decrease in rate, the catalyst is being poisoned. The rate equation for ammonia synthesis is:

$$r = k \,.\, P_{N2}^{\alpha} \,.\, P_{H2}^{\beta} \,.\, P_{NH3}^{\gamma}$$

Equation 1.I

Where r is the rate, k is the rate constant, Px is the partial pressure of component x, and the exponents are the order of reaction with respect to each component.

For the BZY20 catalyst, investigations on the effect of hydrogen partial pressure on the rate were carried out. Only temperatures where the conversion values are less than or equal to 20% of the equilibrium are considered. Plotted in Figure 5-15 are the log values of rate vs the log of partial pressure. A linear fit of the data is made, and the gradient of this fit is taken as the hydrogen order.

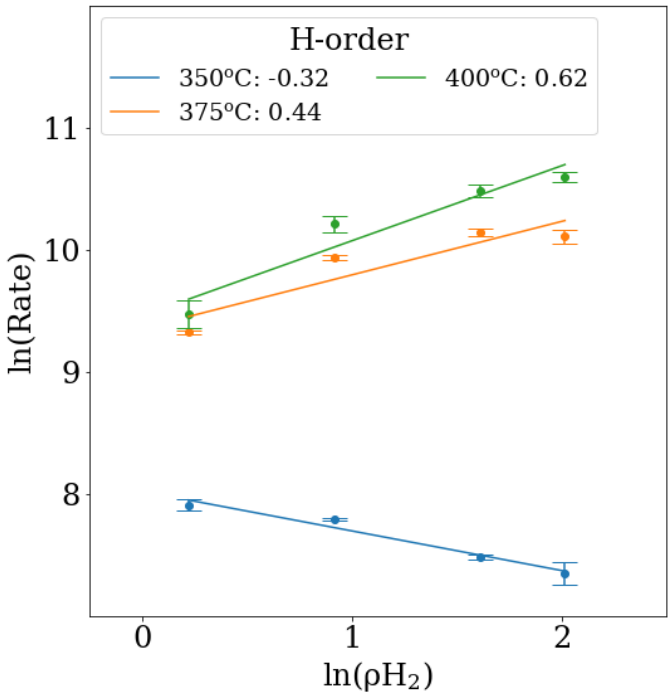


Figure 5-15: Effect of changing partial pressure on rate, at indicated temperatures. Gradients of linear fits of each dataset indicated in the legend.

At the lowest temperature (350 °C), increasing the hydrogen partial pressure decreases the rate, showing a negative order of reaction with respect to hydrogen. At higher temperatures, the hydrogen reaction order becomes positive, showing the hydrogen poisoning is no longer limiting the rate. All rate points at each temperature fall at or below the 20% equilibrium conversion line of Figure 5-14. The data at 375 and 400 °C is not perfectly linear, showing hydrogen poisoning starts to limit the rate again at higher hydrogen partial pressures.

5. 6 Investigation of Hydrogen Spillover

It was postulated that the unusual kinetic behaviour and higher rates that were observed when using 10 and 20% yttrium doped barium zirconate supports could be due to their higher proton conductivities. Therefore, experiments were designed and undertaken to look for evidence of an interaction or 'spillover' of hydrogen atoms from the ruthenium particles to the support. This spillover effect is summarised in Figure 5-16. Hydrogen atoms occupying active B5 sites can react with surface oxide groups on the BZY support to form protons, liberating an electron into the ruthenium band, and creating an adsorption site for dinitrogen. It is proposed that the reverse mechanism should also be possible; either hydrogen re-occupying the B5 site, or directly protonating a dissociated nitrogen atom. The liberation of electrons into the band structure of Ru NPs reduces the oxidation state of the metal, allowing the Ru to reduce dinitrogen more easily in a manner analogous to adding an alkali metal promoter.

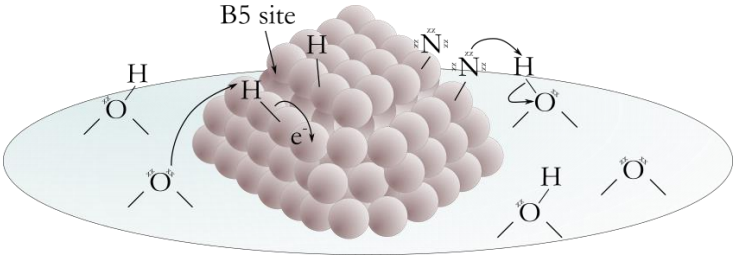


Figure 5-16: Proposed mechanism for reversible hydrogen spillover process.

5. 6. 1 Neutron diffraction

The spillover of protons from Ru particles to the BZY20 lattice was investigated by comparing the level of deuteration that could be achieved in samples with and without ruthenium metal. Four samples for neutron diffraction were prepared. Two were pure BZY20, and two were synthesised with 10 wt% Ru. One of each type was deliberately deuterated by heating in D_2O saturated argon, while two were heated under pure argon. If additional deuterium could be detected in the perovskite lattice of the RuBZY20 lattice, this is analogous to the spillover of hydrogen from Ru to BZY20.

Catalysts samples were prepared using the typical synthesis procedure. The catalysts were then reduced at 450 ºC, under 50 mL min^{-1} 5% H_2/Ar flow. A gas manifold was constructed such that after reduction, the gas flow could be swapped to an Ar line passed through a bubbler filled with D_2O without exposing the catalysts to atmosphere. After reduction, each sample was heated to 600 ºC under Ar, either dry or D_2O saturated. Samples were then sealed in tubes in a glove box and measured soon after preparation to limit exchange with atmospheric water.

Neutron powder diffraction patterns of each sample were collected of each sample at the Paul Scherrer Institute (Switzerland). 3g of each sample was used for measurement, and the patterns were collected at ambient temperatures. The raw data and calculated patterns for BZY20 and RuBZY20 samples are shown in Figure 5-17.

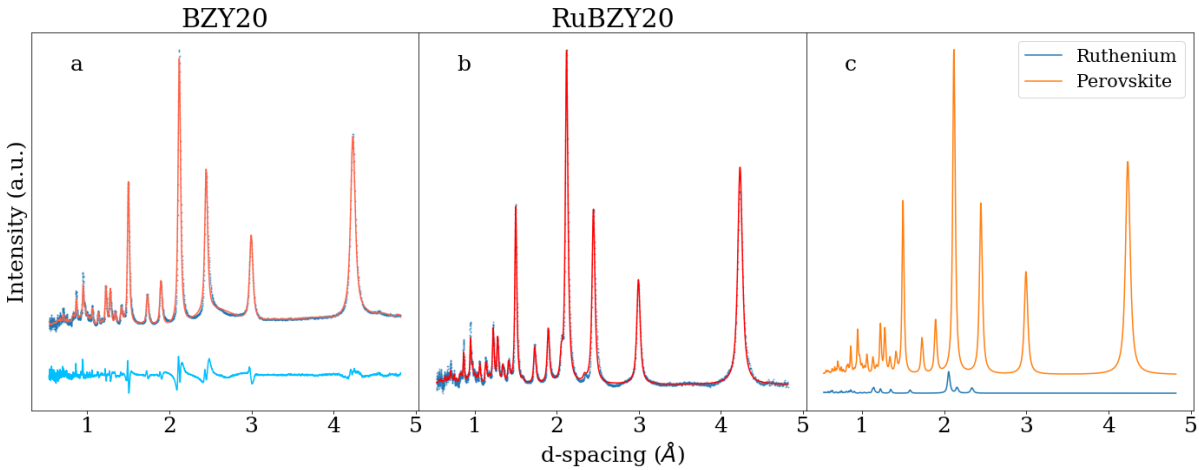


Figure 5-17: Neutron diffraction data of BZY20 (a) and RuBZY20 (b) samples. Raw data is shown as scatter plot, and result of fitting overlaid as line plot. a) also shows the subtraction of calculated pattern from raw data. c) Calculated perovskite and ruthenium patterns after subtraction of background.

A Pawley refinement was carried out on the pure, undeuterated BZY20 sample using known perovskite space group Pm-3m. Refinement was then applied to the deuterated BZY20 sample. Patterns for samples containing ruthenium were very similar but contained additional peaks, which were indexed to metallic Ru, present at ~ 1 wt % (Figure 5-17). Ruthenium samples were modelled using separate Ru and perovskite patterns (Figure 5-17c).

A structure solution was sought using Rietveld refinement of the ABO_3 perovskite structure. Occupancy values for the A and B sites were restricted to those predicted from stoichiometry ($BaZr_{0.8}Y_{0.2}O_{3-\delta}$). This was necessary due to the very similar neutron scattering path lengths of the metals. Taking the Fourier transform of the observed structural elements revealed additional neutron scattering cross-section density in an interstitial site in the centre of an octahedron composed of 2 A-site Ba atoms and 4 O atoms, Figure 5-18. Fourier heat maps show the appearance of neutron scattering density in this position in the D-BZY20 sample (Figure 5-18b & c).

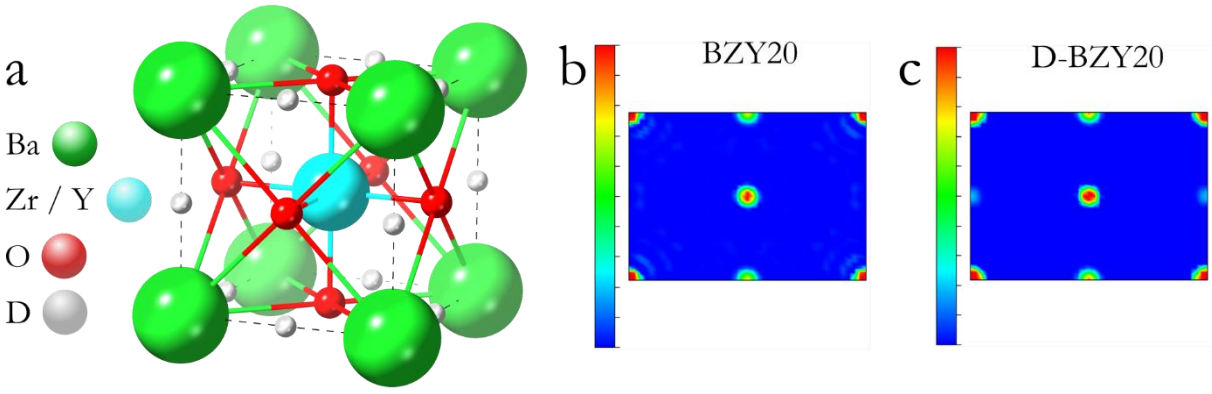


Figure 5-18: a) Solved structure showing location of deuterium ions b) Neutron scattering density heat map of BZY20 samples c) Neutron scattering density heat map of deuterated BZY20 sample.

Rietveld refinement was then applied to Ru samples. Ruthenium and perovskite patterns were calculated independently and are shown in Figure 5-17c. The refinement showed a higher degree of

neutron scattering density in the BZY20 lattice, attributed to deuterium ions. Fitted parameters for all samples are shown below in Table 5-4.

Table 5-4: Fitted parameters for all samples. R_{wp} values for Ru samples are average values, calculated the from individual ruthenium and perovskite patterns.

Sample	BZY20	D-BZY20	RuBZY20	D-RuBZY20
R_{wp} (%)	4.183	4.573	2.985	3.932
Lattice parameter (Å)	4.2259	4.2340	4.2229	4.2303
Ru wt. %	-	-	1.41	1.46
D-occupancy (%)	-	3.43	-	4.54

The weighted-profile R (R_{wp}) values for all samples are reasonably low. Both samples with and without Ru metal show a lattice parameter expansion after deuteration of around 0.008 Å. Calculated weight percentages are around 1.4 %, in disagreement with the values from ICP analysis. The ICP weight % values are considered to be more reliable. The discrepancy in the Ru wt % values determined from neutron diffraction is attributed to the small size of the Ru particles. These were not visible at all in the powder XRD measurements reported in section 5. 4. 1. As the neutrons pass through small particles, there will be a low chance of a scattering event occurring before they exit the Ru lattice. This results in a low signal for Ru peaks and after subtraction of the background pattern may introduce artefacts into the calculated pattern (Figure 5-17c). However low Ru signal should not affect the barium zirconate pattern.

The calculated values for deuterium occupancy show approximately 1 % more deuterium is incorporated into the BZY20 lattice in the presence of Ru. If the mechanism referred to in Figure 5-16 is operative, it is anticipated that the incorporation of D_2O into the lattice should be more facile, and therefore extensive than samples without Ru on the surface. Once D^+ ions are present on the surface of the perovskite, they can percolate into the bulk structure via the proton conductivity mechanism discussed in Chapter 1.

Some literature works found deuterium positions closely associated with oxygen atoms. Azad & Irvine found D-ions closely associated with the oxygen ion (1.06 Å), located on the face of the unit cell of a $BaCe_{0.4}Zr_{0.4}Sc_{0.2}O_3$ ceramic. In this paper they also deuterated the lattice using D_2O at high temperature and found a deuterium occupancy of around 10%. Sata et al. investigated proton positions in $SrTi_{0.98}Sc_{0.02}O_3$ using neutron diffraction and found protons located 1.2 Å away from the oxygen in a similar position to that reported by Azad and Irvine.[25] However, Ito et al. found a different proton site.[26] They reported the proton as located at coordinates (0, 0.28, 0.5), 1.0 Å away from the oxygen. The calculated spread of deuterium positions in our work showed a much greater distance between the oxygen and deuterium atoms (x, y, z = 0, 0, 0.5 and O-D distance of 2.11 Å). After carefully checking

the refinement, this was determined to be the best interpretation of the data, additional neutron scattering density was clearly located in this position.

A study looking into the dynamic mechanism of proton conduction in BZY20 ceramics found that the proton will pass through the calculated spread of deuterium positions as it moves between adjacent oxygen atoms (Figure 5-19).[27] In this study they found that the protons are primarily trapped along the edges of YO_6 octahedra, particularly at low temperatures. This agrees with both molecular quantum dynamics simulations and quasi-elastic neutron scattering studies, reporting the existence of both strong and weak proton traps.[28] Therefore, it is proposed that the deuterium becomes trapped at yttrium dopants within the BO_6 octahedra sublattice, and the calculated spread of deuterium positions is due to an unknown spatial arrangement of the deuterium ion when bonded to YO_6 octahedra in the lattice.

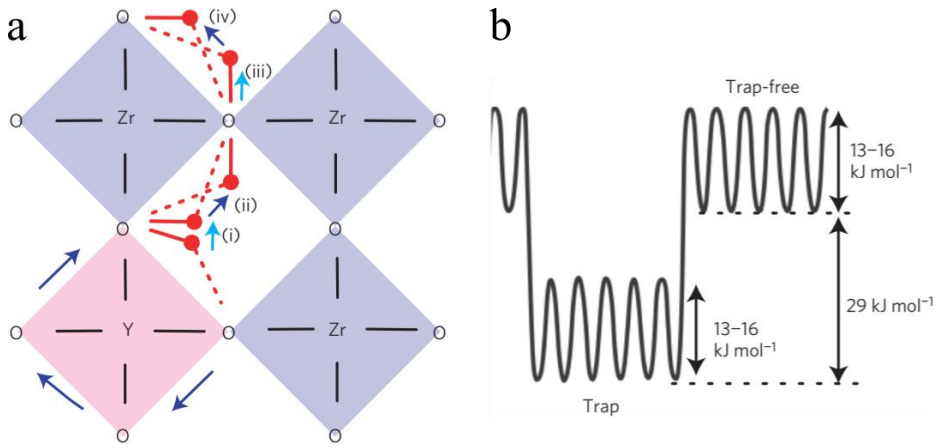


Figure 5-19: Proton dynamics in BZY20 structure, measured by in-situ NMR studies, reproduced from Yamazaki et al.[27] a) motion of proton within and between YO_6 and ZrO_6 octahedra (i) shows spatial rearrangement of proton in trap site (shared Y/Zr octahedra) to form a bond along the ZrO_6 octahedra before (ii) forming a new hydrogen bond attached to a ZrO_6 octahedra and then (iii & iv) continue long-range motion within the oxygen sublattice. b) shows the calculated energies associated with the trap escape mechanism.

5. 6. 2 In-situ XPS

To elucidate the spillover of hydrogen from Ru particles to the support, Near-Ambient Pressure (NAP) XPS was used to characterise the oxidation states of the catalysts in-situ. The B07 beamline at diamond light source (Didcot, UK) can achieve high enough x-ray photoemission fluxes that they may still be detected under near ambient pressures.

Four catalyst samples were tested; RuBZ, RuBZY10, RuBZY20, and RuBZY30. Prior to testing, all samples were reduced under 1 bar hydrogen at 450 °C for 2 hours. After this, the x-ray photoemission spectrums were recorded under ~40 mbar H_2, then under ~10 mbar Ar, and finally again under H_2. First a survey scan was taken, before narrow energy scans were carried out to record changes in the Ru3d and O1s bands, at 720 and 900 eV photon energy respectively. At each photon energy a spectrum of the Fermi edge was also recorded for charge-correction purposes. Spectrums were modelled using Casa XPS software. Shirley backgrounds were used for all regions, and two 5-point moving average smoothing operations were applied to each scan.

If a spillover mechanism is operative, it is expected to see a reduction in binding energy (BE) of the Ru3d band as hydrogen on the Ru surface reacts with oxide species in the barium zirconate lattice, forming -OH species, and leaving an electron behind in the Ru3d band. An increase of electron density in the Ru3d band will facilitate excitation of photoelectrons away from the surface, observed as a reduction of binding energy in the XPS.

The Ru3d peak is split into two spin-orbit coupled peaks from the $Ru3d_{5/2}$ and $Ru3d_{3/2}$ bands, with bandgap 4.17 eV, and area ratio of 3:2. For many samples the presence of satellite peaks, likely from trace ruthenium oxide or carbonate on the surface, was observed. The Ru3d photoemission region strongly overlaps with the C1s region, meaning the $Ru3d_{3/2}$ peak is not directly observable, and the quantification of binding energy changes was done using the $Ru3d_{5/2}$ peak. The carbon peaks were modelled using 3 separate sources of carbon photoemission; adventitious or graphitic carbon (C-C and C-H bonds), alcohol species, and carbonate species. Ruthenium and carbon peaks were modelled with asymmetric Lorentzian functions.

The intensity of all samples was found to increase under Ar atmospheres, as expected given the difference in pressures. Higher gas pressures mean a higher total absorption cross-section leading to low signals, Figure 5-20. Hydrogen has a much lower electron total scattering cross-section than Ar, therefore can be used at higher pressures (2.625 vs 30.464, values from NIST electron elastic-scattering cross-section database). It was decided to use the highest possible pressures for each gas in order to enhance the effect of changing atmosphere.

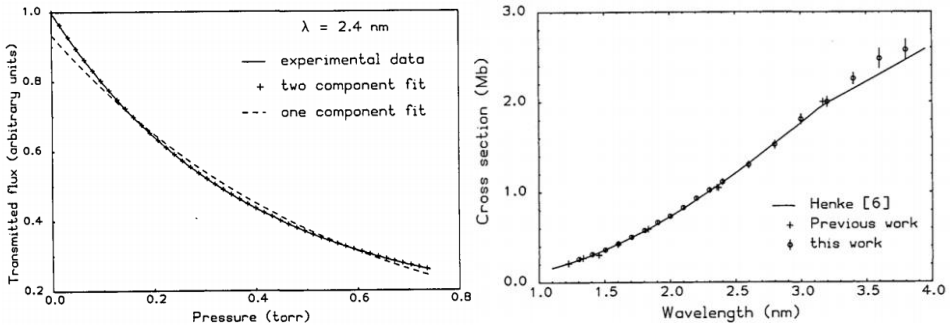


Figure 5-20: Variation of transmitted X-ray flux with changes in Ar pressure. X-ray absorption cross section of Ar varying with wavelength. Reproduced from Yang and Kirz (1987)[29]

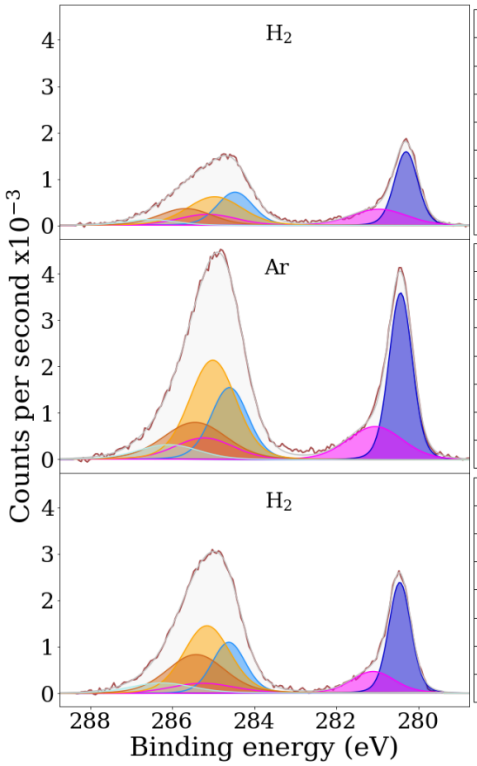
For the RuBZ sample, $Ru3d_{5/2}$ peak increased from 280.3 to 280.43 eV when changing from H_2 to Ar atmosphere but did not show any decrease upon returning to H_2, with a peak centre of 280.45 eV.

Scans under hydrogen for the RuBZY10 could not be properly modelled due to low overall ruthenium signal. Furthermore, high signal to noise ratio in the 720 eV Fermi edge scans made the energy calibration unreliable (appendix). The scan under Ar had a $Ru3d_{5/2}$ binding energy of 280.62 eV.

Interestingly, RuBZY20 showed the most pronounced increase in binding energy from 280.23 to 280. 73 eV when changing from hydrogen to argon, returning to a binding energy of 280.14 eV under hydrogen atmosphere.

RuBZY30 $3d_{5/2}$ peak showed a slight decrease over the three scans with binding energies of 280.64, 280.6, and 280.53 eV being recorded under first hydrogen, argon, and second hydrogen scans respectively.

RuBZ

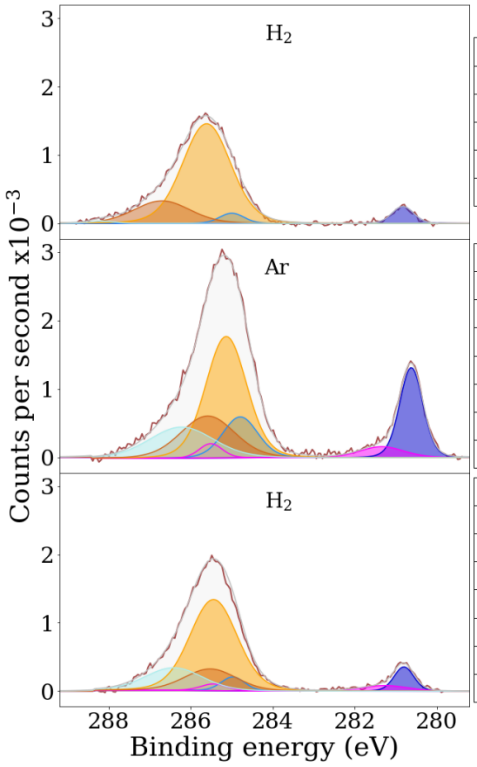


Name	Position	FWHM	Raw Area	%At Conc
$Ru3d_{5/2}$	280.3	0.67	1,181	4.5
$Ru3d_{3/2}$	284.47	1.03	815	3.1
$Ru3d_{5/2(sat)}$	280.96	1.61	622	2.4
$Ru3d_{3/2(sat)}$	285.13	1.65	429	1.6
C-C, C-H	284.96	1.57	1,070	51.0
C-OH	285.67	1.51	596	28.4
C=O	286.51	1.41	188	9.0

Name	Position	FWHM	Raw Area	%At Conc
nan	280.43	0.67	2,666	3.6
$Ru3d_{3/2}$	284.6	1.07	1,839	2.5
$Ru3d_{5/2(sat)}$	281.05	1.57	1,246	1.7
$Ru3d_{3/2(sat)}$	285.22	1.68	860	1.2
C-C, C-H	285.01	1.34	3,178	53.8
C-OH	285.44	1.81	1,599	27.1
C=O	286.08	1.73	602	10.2

Name	Position	FWHM	Raw Area	%At Conc
$Ru3d_{5/2}$	280.45	0.64	1,678	3.0
$Ru3d_{3/2}$	284.62	0.95	1,158	2.1
$Ru3d_{5/2(sat)}$	281.1	1.22	625	1.1
$Ru3d_{3/2(sat)}$	285.27	1.82	431	0.8
C-C, C-H	285.15	1.33	2,149	48.5
C-OH	285.42	1.65	1,525	34.4
C=O	286.26	1.8	447	10.1

RuBZY10

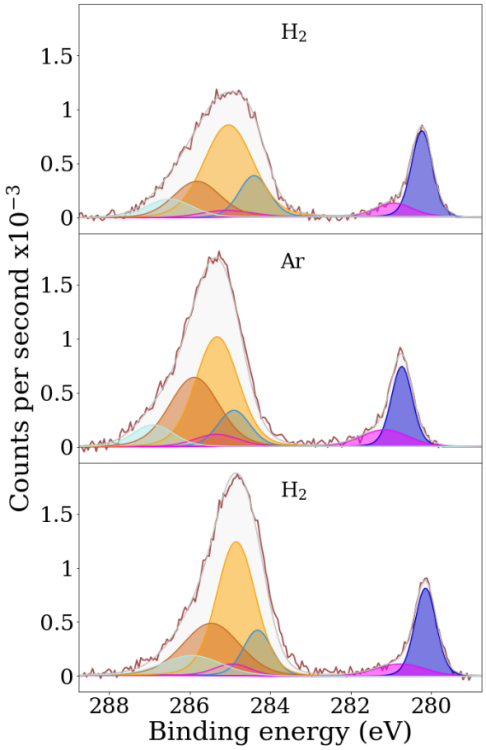


Name	Position	FWHM	Raw Area	%At Conc
$Ru3d_{5/2}$	280.83	0.62	170	0.5
$Ru3d_{3/2}$	285.0	0.7	117	0.3
C-C, C-H	285.61	1.38	2,239	77.9
C-OH	286.7	1.61	588	20.4
C=O	288.15	0.65	25	0.9

Name	Position	FWHM	Raw Area	%At Conc
$Ru3d_{5/2}$	280.62	0.67	974	1.7
$Ru3d_{3/2}$	284.79	1.01	672	1.2
$Ru3d_{5/2(sat)}$	281.34	1.27	226	0.4
$Ru3d_{3/2(sat)}$	285.51	0.66	156	0.3
C-C, C-H	285.13	1.18	2,321	51.8
C-OH	285.59	1.55	1,060	23.7
C=O	286.23	1.85	934	20.8

Name	Position	FWHM	Raw Area	%At Conc
$Ru3d_{5/2}$	280.8	0.57	224	0.6
$Ru3d_{3/2}$	284.97	0.68	155	0.4
$Ru3d_{5/2(sat)}$	281.26	1.33	121	0.3
$Ru3d_{3/2(sat)}$	285.43	0.76	83	0.2
C-C, C-H	285.44	1.36	2,016	63.2
C-OH	285.52	1.49	527	16.5
C=O	286.41	1.64	601	18.8

RuBZY20

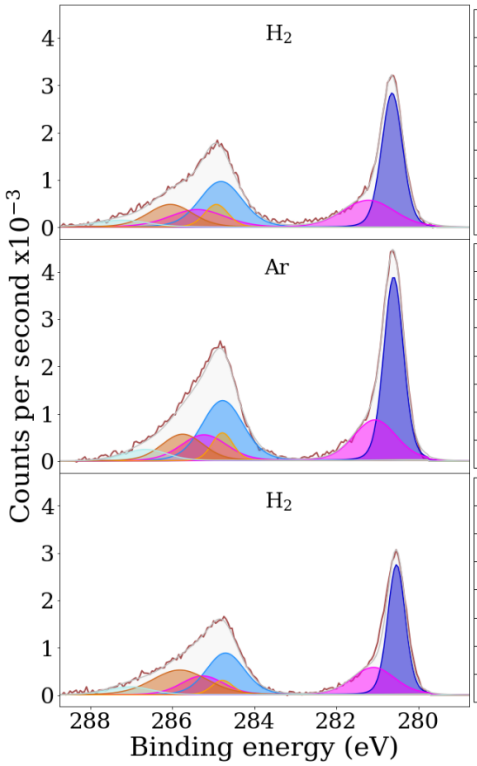


Name	Position	FWHM	Raw Area	%At Conc
$Ru3d_{5/2}$	280.23	0.62	543	2.0
$Ru3d_{3/2}$	284.4	0.88	375	1.3
$Ru3d_{5/2(sat)}$	280.93	1.07	150	0.5
$Ru3d_{3/2(sat)}$	285.1	1.48	104	0.4
C-C, C-H	285.04	1.45	1,370	61.4
C-OH	285.82	1.37	509	22.8
C=O	286.51	1.35	257	11.5

Name	Position	FWHM	Raw Area	%At Conc
$Ru3d_{5/2}$	280.73	0.62	509	1.4
$Ru3d_{3/2}$	284.9	0.95	351	1.0
$Ru3d_{5/2(sat)}$	281.16	1.36	234	0.7
$Ru3d_{3/2(sat)}$	285.33	1.29	161	0.5
C-C, C-H	285.32	1.26	1,417	50.4
C-OH	285.89	1.45	1,031	36.6
C=O	286.91	1.19	266	9.5

Name	Position	FWHM	Raw Area	%At Conc
$Ru3d_{5/2}$	280.14	0.63	573	1.6
$Ru3d_{3/2}$	284.31	0.84	395	1.1
$Ru3d_{5/2(sat)}$	280.77	1.46	185	0.5
$Ru3d_{3/2(sat)}$	284.94	1.06	128	0.4
C-C, C-H	284.85	1.14	1,575	54.0
C-OH	285.46	1.66	888	30.5
C=O	285.94	1.72	349	12.0

RuBZY30



Name	Position	FWHM	Raw Area	%At Conc
$Ru3d_{5/2}$	280.64	0.6	1,894	9.2
$Ru3d_{3/2}$	284.81	1.23	1,307	6.4
$Ru3d_{5/2(sat)}$	281.21	1.49	936	4.6
$Ru3d_{3/2(sat)}$	285.38	1.59	646	3.2
C-C, C-H	284.92	0.68	358	21.8
C-OH	286.04	1.28	674	41.0
C=O	287.23	1.46	229	13.9

Name	Position	FWHM	Raw Area	%At Conc
$Ru3d_{5/2}$	280.6	0.56	2,415	9.9
$Ru3d_{3/2}$	284.77	1.19	1,666	6.8
$Ru3d_{5/2(sat)}$	281.06	1.22	1,153	4.7
$Ru3d_{3/2(sat)}$	285.23	1.31	795	3.2
C-C, C-H	284.78	0.61	393	20.1
C-OH	285.75	1.2	747	38.1
C=O	286.65	1.25	337	17.2

Name	Position	FWHM	Raw Area	%At Conc
$Ru3d_{5/2}$	280.53	0.51	1,540	7.4
$Ru3d_{3/2}$	284.7	1.09	1,062	5.1
$Ru3d_{5/2(sat)}$	281.09	1.22	771	3.7
$Ru3d_{3/2(sat)}$	285.26	1.21	532	2.6
C-C, C-H	284.78	0.61	203	12.2
C-OH	285.82	1.59	917	55.0
C=O	287.03	1.25	235	14.1

The scans of the O1s photoemission region were recorded with a higher photon energy of 900 eV. The resulting peak was resolved as two Gaussian-Lorentzian peaks, representing contributions to the XPS from lattice oxide and hydroxide species with similar binding energies. The FWHM of the two peaks was fixed to be identical. The same trend as observed in the Ru scans of higher intensity under Ar atmospheres was observed in the oxygen spectrum. Changes in peak shapes were immediately apparent when looking at the oxygen spectrum; the strong overlap between the two peaks means a change in area ratio will create a broad peak, with a shoulder at high or low binding energy.

RuBZ sample showed similar contributions to the spectrum from lattice oxide and hydroxide species under H_2, but changed to a being dominated by the lattice oxide under Ar, maintaining the same state when returning to hydrogen atmosphere.

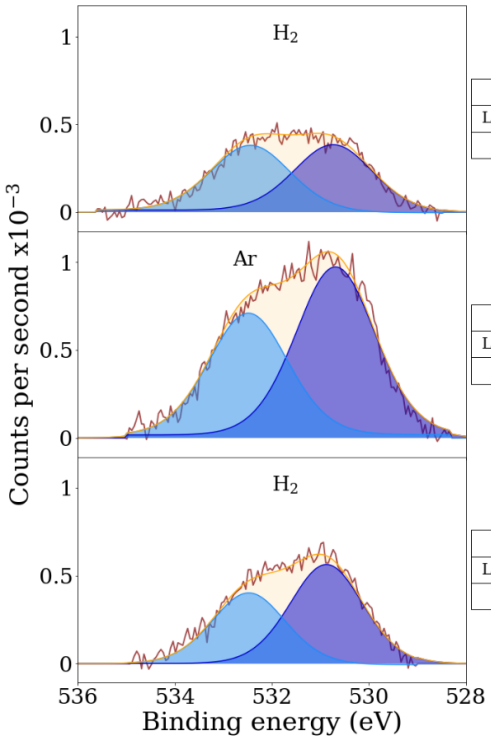
The combined peak width of the RuBZY10 under hydrogen atmosphere was much lower than for other samples. This could be due to lower overall signal, or lower separation of the two peaks, which for other all other samples was above 1.5 eV. Under Ar atmosphere, a peak was observed at high binding energy, with a shoulder at low binding energy, indicating a slightly higher area of the hydroxide peak.

For RuBZY20, all gas conditions showed a peak dominated by hydroxyl species, with greatest peak intensity coming at high binding energies and the oxide shoulder clearly apparent.

RuBZY30 under all conditions showed a broad peak, with the highest intensity coming at lower binding energy values. The area ratios of the oxide and hydroxide species were close to equal, with the lattice oxide just emerging as the largest component.

The change in peak area of oxide with reference to hydroxide over these samples may reflect changes in the concentration of oxygen vacancies on the materials' surface. Yttrium doping deliberately introduces oxygen vacancies into the perovskite structure, as discussed in Chapter 1. Interaction of these vacancies with hydrogen will generate hydroxide and can explain the increasing hydroxide/oxide ratio observed in the O1s XPS. Interestingly, the RuBZY20 sample shows the highest percentage of surface hydroxide amongst the three samples.

RuBZ

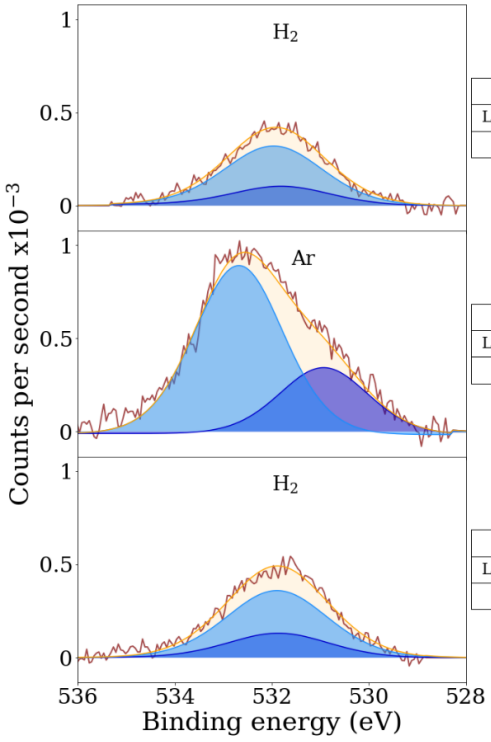


Name	Position	FWHM	Raw Area	%At Conc
Lattice oxide	530.73	1.92	799	50.7
Hydroxides	532.44	1.92	776	49.3

Name	Position	FWHM	Raw Area	%At Conc
Lattice oxide	530.69	1.93	1,994	58.0
Hydroxides	532.49	1.93	1,447	42.0

Name	Position	FWHM	Raw Area	%At Conc
Lattice oxide	530.87	1.78	1,095	58.5
Hydroxides	532.47	1.78	777	41.5

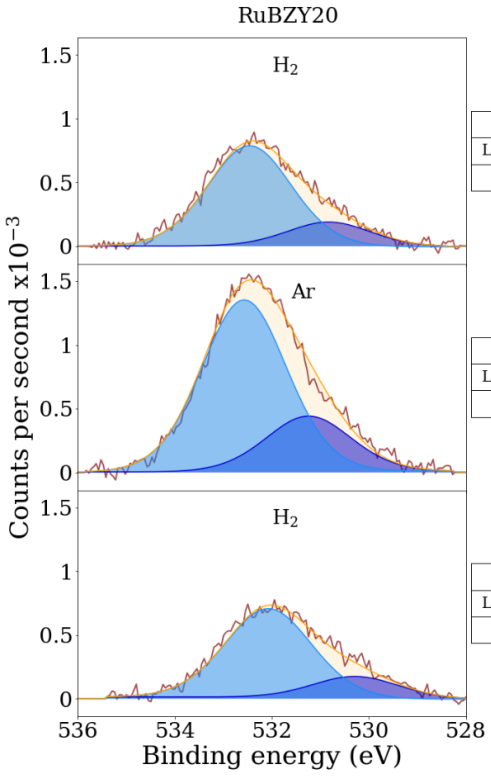
RuBZY10



Name	Position	FWHM	Raw Area	%At Conc
Lattice oxide	531.78	2.39	262	24.2
Hydroxides	531.96	2.39	819	75.8

Name	Position	FWHM	Raw Area	%At Conc
Lattice oxide	530.93	2.16	838	28.4
Hydroxides	532.68	2.16	2,112	71.6

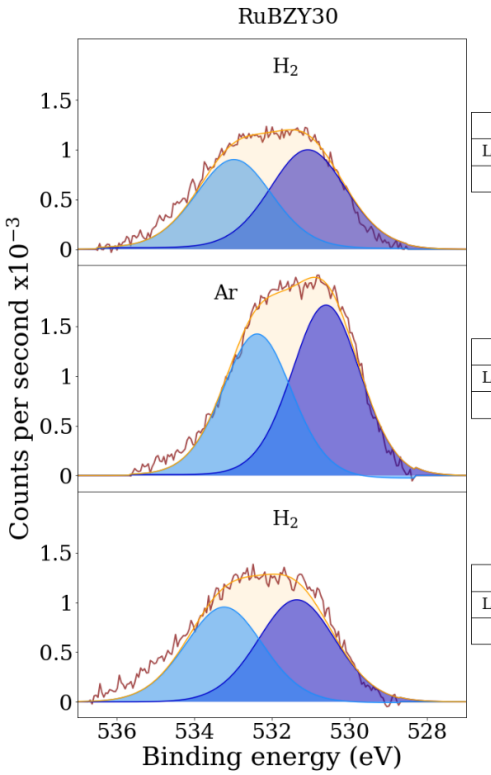
Name	Position	FWHM	Raw Area	%At Conc
Lattice oxide	531.86	2.46	352	26.8
Hydroxides	531.89	2.46	962	73.2



Name	Position	FWHM	Raw Area	%At Conc
Lattice oxide	530.83	2.04	428	19.7
Hydroxides	532.46	2.04	1,746	80.3

Name	Position	FWHM	Raw Area	%At Conc
Lattice oxide	531.24	2.07	968	24.3
Hydroxides	532.57	2.07	3,017	75.7

Name	Position	FWHM	Raw Area	%At Conc
Lattice oxide	530.28	2.11	406	20.2
Hydroxides	532.07	2.11	1,604	79.8



Name	Position	FWHM	Raw Area	%At Conc
Lattice oxide	531.07	2.31	2,480	52.7
Hydroxides	532.98	2.31	2,228	47.3

Name	Position	FWHM	Raw Area	%At Conc
Lattice oxide	530.6	2.09	3,921	54.9
Hydroxides	532.38	2.09	3,224	45.1

Name	Position	FWHM	Raw Area	%At Conc
Lattice oxide	531.36	2.37	2,647	51.9
Hydroxides	533.23	2.37	2,450	48.1

In summary, changes in BEs of Ru $3d_{5/2}$ and O1s peaks are observed when samples are under hydrogen or argon atmosphere. Switching from H_2 to Ar results in an increase in surface oxide species, with a corresponding decrease in hydroxides. This is also associated with an increase in $Ru3d_{5/2}$ binding energy, for RuBZ and RuBZY20 samples, indicating an increase in Ru oxidation state. The phenomena is reversible when switching back to H_2 for the RuBZY20 sample, where this phenomena is especially pronounced. A clear increase in binding energy of Ru $3d_{5/2}$ from 280.23 to 280. 73 eV is observed,

returning to 280.14 eV under hydrogen atmosphere. The content of hydroxide in the O1s region decreases from 80.3% to 75.7% when changing from hydrogen to argon, returning to 79.8% under hydrogen atmosphere. Furthermore, the surface hydroxide concentration is higher than in any other sample. It is suggested that the high proton conductivity of the BZY20 support facilitates spillover of hydrogen to the support surface according to the mechanism in Figure 5-16. The low $Ru3d_{5/2}$ binding energy under H_2 atmosphere is indicative of electron donation into the Ru3d band, and the high presence of hydroxide species on the support suggests efficient spillover. It is unfortunate that the RuBZY10 sample was unable to be properly analysed due to low signals, as this would provide even better evidence for the theory that hydrogen spillover from the Ru particles to the catalyst can be promoted using proton conducting supports.

Evidence for a hydrogen spillover mechanism was found using in-situ XPS and neutron diffraction experiments. The differences in rates observed between catalysts on different supports and the unusual kinetic behaviour of Cs-Ru/BZY20 are attributed to this spillover mechanism.

5. 7 Discussion

5. 7. 1 Catalyst Development

Screening a number of barium zirconate-supported ruthenium catalysts identified Y-doped barium zirconate (BZY) as producing the most active catalysts. As discussed in Chapter 1, yttrium dopants are established in the literature as producing barium zirconate ceramics with the highest proton conductivity versus other dopants. However, as seen in Figure 5-10, the difference in activity in the catalysts could not be linked to the activation energy for proton transfer within the BZY lattice, a measure of the conductivity in this case.

BZY materials were explored in more detail, with a range of differently doped BZY supported catalysts. Figure 5-11 shows how increasing conductivity of the support led to an increase in activity. However due to deactivation of the catalyst during testing, the activity could not be explored in more detail. Addition of a caesium promoter produced a catalyst which was both more active and more stable, as shown in Figure 5-12. The most likely explanation for this is the caesium acts as a structural promoter, preventing sintering of the ruthenium particles. Exposed ruthenium surface atoms were quantified using CO pulse titration, as shown in Figure 5-6. The exposed ruthenium surface area was determined for each BZY catalyst, and found to be similar between samples and not responsible for variations in rates between catalysts (Figure 5-11). Ruthenium particles of 5-15 nm in diameter were identified through TEM studies (Figure 5-7 & Figure 5-9).

5. 7. 1. A Comparison to Literature

Recorded rates of Cs-Ru/BZY catalysts were compared against recent highlights from the literature (Table 5-5), with a focus on metal oxide supported ruthenium catalysts. Also included are the ruthenium free catalysts reported by Wang et al.[30] Only measured rates with equivalent conversions below 20% of the equilibrium value were used for comparison.

At 400 ºC, the Cs-Ru/BZY20 catalyst performs better than most in literature, with the exception of the reports by Kitano et al. (2018) and Ogura et al. (2018).[2,31] Critically, it outperforms the barium zirconate-based catalysts of Wang et al. and Shimoda et al.[14,32]

Comparing the rates per mol of ruthenium (based on the reported wt.% loadings), the Cs-Ru/BZY20 catalyst performs better than many metal oxide supported catalysts, and at a similar level to the $Ru/BaZrO_3$ and Ru/Pr_2O_3 catalysts.[14,33] Other supports such as $La_{0.5}Ce_{0.5}O_{1.75}$ and MgO(111) give more active catalysts when considered on a per mole ruthenium basis.[31,34]

Table 5-5: Test conditions and ammonia synthesis rates of literature, and investigated catalysts. Literature data taken from references [2,3,14,30–35] All literature rates are from tests recorded at 3:1 H_2:N_2 and at 1.0 MPa, except (a) (3.0 MPa) and (b) (0.9 MPa). WHSV could not be determined for the Ru/$BaZrO_3$ catalyst, so the reported GHSV is given instead.[14]

Catalyst	Ru wt. %	Temperature / ºC	WHSV /mL h^{-1} g^{-1}	Rate /μmol g^{-1} h^{-1}	Rate /mol mol_{Ru}^{-1} h^{-1}	Reference
Cs-Ru/BZY10	***10***	***360***	***120,000***	***14,100***	***14.2***	***This work***
Cs-Ru/BZY20	***10***	***375***	***120,000***	***22,900***	***23.1***	***This work***
Cs-Ru/BZY20	***10***	***400***	***120,000***	***37,400***	***37.8***	***This work***
Ru/C12A7:e^-	1.2	400	18,000	8200	69.1	Kitano et al. 2012
Ru-Ba/AC	9.1	400	18,000	8300	9.2	Kitano et al. 2012
Ru-Cs/MgO	6.0	400	18,000	12,100	20.4	Kitano et al. 2012
Ru/$BaZrO_3$[(a)]	4	375	(10,000 h^{-1})	10,200	25.8	Wang et al. 2013
Ru/$BaZrO_3$[(a)]	4	400	(10,000 h^{-1})	15,300	38.7	Wang et al. 2013
Ru/Pr_2O_3	5	400	18,000	19,000	38.4	Sato et al. 2016
Co-LiH	-	350	60,000	11,500	-	Wang et al. 2017
Fe-LiH	-	350	60,000	10,800	-	Wang et al. 2017
Ru/BZY10	2	400	36,000	4,000	20.2	Shimoda et al. 2017
Ru/$La_{0.5}Ce_{0.5}O_{1.75}$[(b)]	5	400	72,000	65,000	131.4	Ogura et al. 2018
Ru/$La_{0.5}Ce_{0.5}O_{1.75}$[(b)]	5	350	72,000	32,000	64.7	Ogura et al. 2018
Ru/Ba-Ca$(NH_2)_2$	10	360	36,000	60,000	60.6	Kitano et al. 2018
Ru/CeO_2	10	400	60,000	18,000	18.2	Lin et al. 2018
Cs−Ru/MgO(111)	3.7	400	72,000	34,300	93.7	Wu et al. 2020

5. 7. 2 Relationship Between Support Conductivity and Activity

It is helpful to establish the expected trends in proton conductivity of BZY materials, according to the literature. Figure 5-21 shows two graphs reproduced from Fabbri et al. (a) and Han et al. (b).

The mechanisms of proton conduction in BZY ceramics are established in Chapter 1, however briefly: hydrogen reacts with oxygen vacancies in the BZY lattice (vacancies are created by doping Zr sublattice with yttrium). These protonic defects move through the lattice via a proton-hopping mechanism, until they reach a grain boundary. This bulk and grain boundary conductivity each have an associated energy barrier, and the bulk conduction is notably higher than the grain boundary.

Figure 5-21 (a) shows an Arrhenius plot of conductivity, as reported by Fabbri et al.[23] It is obvious from the plot that increasing temperature leads to higher proton conductivity. Total and grain boundary conductivity show almost an order of magnitude increase in conductivity between 350 and 450 ºC. Bulk conductivity is less sensitive to temperature, increasing by an approximate half-order of magnitude in the same temperature range. When considering the effect of support conductivity on hydrogen spillover from ruthenium particles to the BZY surface, it is likely that due to the small size of ruthenium particles the bulk conductivity will be most relevant as the number of Ru particles in close proximity to grain boundaries will be much lower than those close to the bulk. It can also be said that if support conductivity influences the spillover of hydrogen from the Ru particles, this effect will increase at higher temperatures. As demonstrated in Figure 5-15, the hydrogen order of reaction over a Cs-Ru/BZY20 increases with increasing temperature, indicating that the reaction is not limited by hydrogen poisoning at higher temperatures.

Figure 5-21 (b) shows the change in bulk and grain boundary conductivity with increasing Y-dopant concentration, reproduced from Han et al.[21] The bulk conductivity rapidly increases with increasing Y-dopant concentration, showing peaks at 10 and 20%. The grain boundary conductivity on the other hand peaks at 20% concentration. Both bulk and grain boundary conductivity are effectively 0 at 0% doping and decrease after 20%. Testing of Cs-Ru/BZY catalysts showed 10 and 20% BZY formulations gave significantly more active catalysts, Figure 5-13. It is proposed that the high activity of the BZY10- and 20-based catalysts is thanks to the high bulk proton conductivity of these materials.

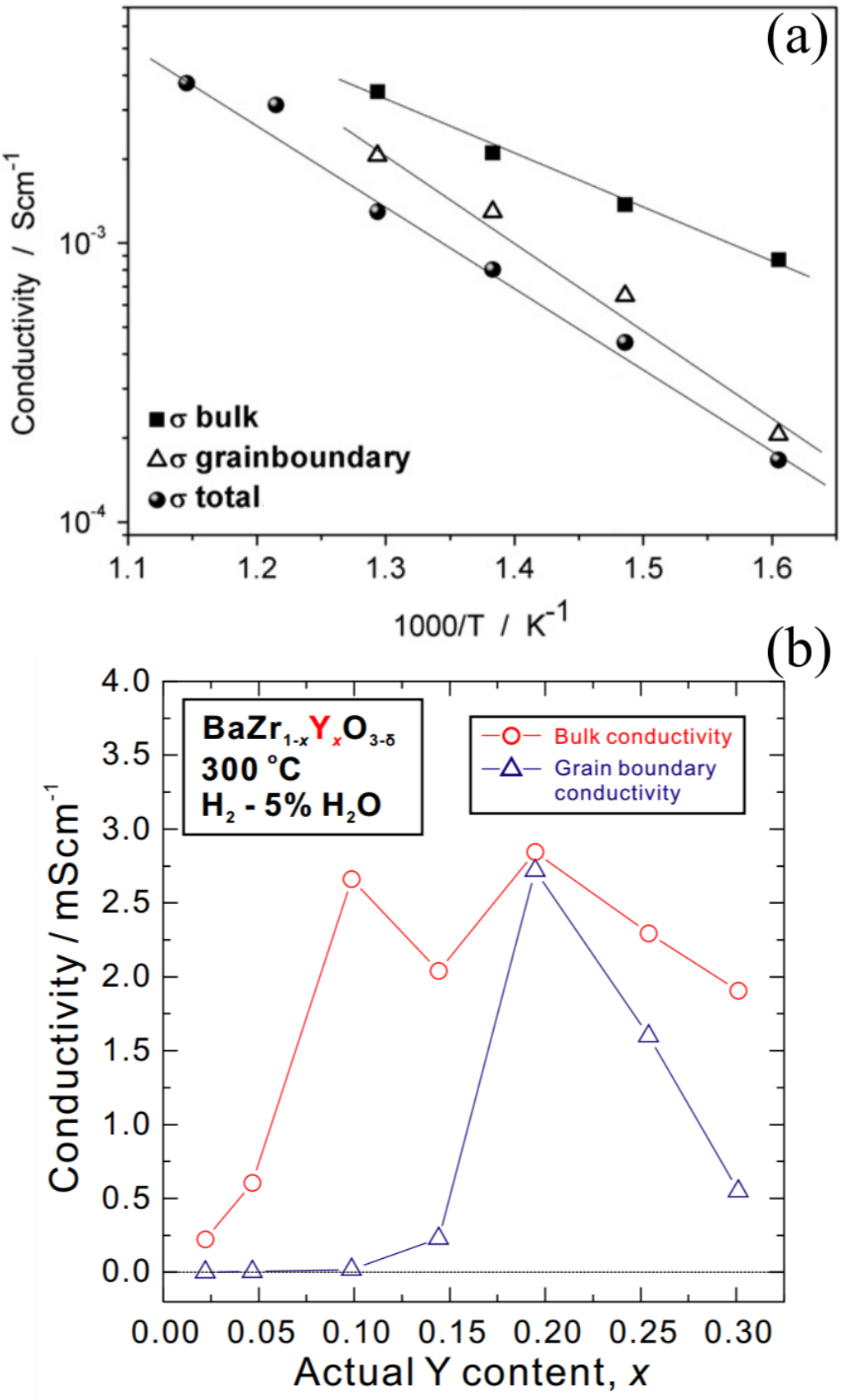


Figure 5-21: (a) Temperature dependence of conductivity of a BZY20 sample, recorded in a wet 10% H_2 atmosphere. Reproduced from Fabbri et al.[23] (b) Bulk and grain boundary conductivity dependence on doping level of Y-doped barium zirconate. Recorded at 300 °C in a wet 5% H_2 atmosphere. Y content determined by ICP-AES. Reproduced from Han et al.[21]

5. 7. 3 Spillover of Hydrogen

Spillover of hydrogen from BZY based catalysts was quantified using neutron diffraction, and in-situ XPS. The level of deuteration of a BZY20 ceramic after a high temperature treatment was examined via neutron diffraction. Ruthenium particles in the presence of BZY20 ceramic do cause an increased deuteration level of the ceramic. It is proposed that splitting of D_2O to deuterium atoms on the Ru surface creates adsorbed D species which can spillover to the BZY20 support.

Changes in ruthenium oxidation state at the temperature for ammonia synthesis reaction were characterised by in-situ near-ambient pressure XPS analysis. The binding energy of ruthenium was observed to increase when moving from a hydrogen to argon atmosphere, with this effect being most noticeable for the RuBZY20 catalyst, with which the same reduced state could be recovered when returning to hydrogen atmosphere. It is suggested that the higher proton mobility in the BZY20 support permit faster hydrogen spillover kinetics. Additionally, changes in the O1s binding energy region were observed. The ratio of hydroxide to oxide was observably higher under hydrogen atmospheres. Again, this effect was most pronounced in the RuBZY20 sample, which had a much greater level of surface hydroxide than either the RuBZ or RuBZY30 samples. The results of this study appear to show that a BZY20 support promotes a greater degree of hydrogen spillover, and faster kinetics than BZ or BZY30 supports. While unfortunate that this effect could not be confirmed with the BZY10 sample due to low signal, the results are nonetheless promising.

Characterisation of the hydrogen spillover using neutron diffraction gave evidence for spillover of deuterium from ruthenium particles to the support. In-situ XPS studies showed how oxidation state changes in the ruthenium can be explained by spillover of hydrogen atoms to the support also.

Therefore, it is proposed that the observed differences in rate between supports discussed in Section 5. 7. 2, can be explained by spillover of hydrogen occurring to a greater degree on the more conductive supports. This causes an increase in catalyst activity thanks to a reduction of hydrogen poisoning, also discussed section 5. 7. 2.

5. 8 Conclusions

This work aimed to look at how the proton conductivity of barium zirconate (BZ) supports might be used to promote rates of ammonia synthesis over ruthenium particles in contact with the support. Changing the dopant cation of the BZ supports did not show any clear trend of increasing catalyst activity with support conductivity. It is concluded that the differences in conductivity were simply too small to have any effect on catalyst activity. It was however established that Y-dopants gave much more active catalysts.

A range of Y-doped barium zirconate (BZY) supports with varying dopant levels were synthesised. In this case, increasing activity could be linked to increasing conductivity of the support. Long term catalyst stability studies established that a caesium promoter was necessary to prevent catalyst activity degrading over time.

Cs-promoted catalysts were screened for activity, and it was found that 10 and 20% Y-doped supports gave much more active catalysts than 0 or 30% doped supports. To explain this high activity, it was noted in the discussion (section 5. 7) that these BZY formulations have much higher proton conductivity than the other two samples. Kinetic studies demonstrated that at higher temperatures, hydrogen poisoning was no longer the limiting process in the reaction over a Cs-Ru/BZY20 catalyst. Therefore, it was proposed that spillover of adsorbed hydrogen from the ruthenium particles to the support reduces hydrogen poisoning to such an extent that it no longer limits the ammonia synthesis reaction.

Evidence for this spillover process was sought using in neutron diffraction and in-situ XPS studies. Neutron diffraction showed how ruthenium particles promote deuteration of a BZY20 support. In-situ XPS characterisation of ruthenium oxidation states showed a reduction in Ru oxidation state under hydrogen atmosphere, consistent with the spillover mechanism proposed in section 5. 6

All three stated aims of this work were realised. The efficacy of proton conducting ceramics as catalyst supports has been established, and it was found doping level is much more important than the identity of the dopant cation. It is also concluded that the proton conductivity of a BZY support promotes the rate of ammonia synthesis over ruthenium catalysts, via a reduction in hydrogen poisoning. This is possible due to the proposed spillover mechanism.

5. 9 Acknowledgements

Fitting of neutron diffraction data was carried out by Chris Foo. Neutron diffraction data was collected by Dr Pu Zhao. TEM images were collected by Dr Elizabeth Raine at the University of Oxford, and by Dr Weiran Zheng at The Hong Kong Polytechnic University. STEM-HAADF images were collected by Ping-Luen Ho. The collection of the NAP XPS data was assisted by Prof Georg Held, Alex Large, and Simson Wu.

5. 10 References

(1) Bécue, T.; Davis, R. J.; Garces, J. M. Effect of Cationic Promoters on the Kinetics of Ammonia Synthesis Catalyzed by Ruthenium Supported on Zeolite X. *J. Catal.* **1998**, *179* (1), 129–137. https://doi.org/10.1006/jcat.1998.2212.

(2) Kitano, M.; Inoue, Y.; Sasase, M.; Kishida, K.; Kobayashi, Y.; Nishiyama, K.; Tada, T.; Kawamura, S.; Yokoyama, T.; Hara, M.; Hosono, H. Self-Organized Ruthenium–Barium Core–Shell Nanoparticles on a Mesoporous Calcium Amide Matrix for Efficient Low-Temperature Ammonia Synthesis. *Angew. Chem.* **2018**, *130* (10), 2678–2682. https://doi.org/10.1002/ange.201712398.

(3) Kitano, M.; Inoue, Y.; Yamazaki, Y.; Hayashi, F.; Kanbara, S.; Matsuishi, S.; Yokoyama, T.; Kim, S.-W.; Hara, M.; Hosono, H. Ammonia Synthesis Using a Stable Electride as an Electron Donor and Reversible Hydrogen Store. *Nat. Chem.* **2012**, *4* (11), 934–940. https://doi.org/10.1038/nchem.1476.

(4) Kanbara, S.; Kitano, M.; Inoue, Y.; Yokoyama, T.; Hara, M.; Hosono, H. Mechanism Switching of Ammonia Synthesis Over Ru-Loaded Electride Catalyst at Metal–Insulator Transition. *J. Am. Chem. Soc.* **2015**, *137* (45), 14517–14524. https://doi.org/10.1021/jacs.5b10145.

(5) Murata, S.; Aika, K.-I. Preparation and Characterization of Chlorine-Free Ruthenium Catalysts and the Promoter Effect in Ammonia Synthesis: 1. An Alumina-Supported Ruthenium Catalyst. *J. Catal.* **1992**, *136* (1), 110–117. https://doi.org/10.1016/0021-9517(92)90110-4.

(6) Zhong, Z.; Aika, K. Effect of Ruthenium Precursor on Hydrogen-Treated Active Carbon Supported Ruthenium Catalysts for Ammonia Synthesis. *Inorganica Chim. Acta* **1998**, *280* (1), 183–188. https://doi.org/10.1016/S0020-1693(98)00202-3.

(7) Aika, K.; Takano, T.; Murata, S. Preparation and Characterization of Chlorine-Free Ruthenium Catalysts and the Promoter Effect in Ammonia Synthesis: 3. A Magnesia-Supported Ruthenium Catalyst. *J. Catal.* **1992**, *136* (1), 126–140. https://doi.org/10.1016/0021-9517(92)90112-U.

(8) Niwa, Y.; Aika, K. The Effect of Lanthanide Oxides as a Support for Ruthenium Catalysts in Ammonia Synthesis. *J. Catal.* **1996**, *162* (1), 138–142. https://doi.org/10.1006/jcat.1996.0268.

(9) Cisneros, M. D.; Lunsford, J. H. Characterization and Ammonia Synthesis Activity of Ruthenium Zeolite Catalysts. *J. Catal.* **1993**, *141* (1), 191–205. https://doi.org/10.1006/jcat.1993.1129.

(10) Fishel, C. T.; Davis, R. J.; Garces, J. M. Ammonia Synthesis Catalyzed by Ruthenium Supported on Basic Zeolites. *J. Catal.* **1996**, *163* (1), 148–157. https://doi.org/10.1006/jcat.1996.0314.

(11) Kitano, M.; Kanbara, S.; Inoue, Y.; Kuganathan, N.; Sushko, P. V.; Yokoyama, T.; Hara, M.; Hosono, H. Electride Support Boosts Nitrogen Dissociation over Ruthenium Catalyst and Shifts the Bottleneck in Ammonia Synthesis. *Nat. Commun.* **2015**, *6*, 6731. https://doi.org/10.1038/ncomms7731.

(12) Siporin, S. E.; Davis, R. J. Use of Kinetic Models to Explore the Role of Base Promoters on Ru/MgO Ammonia Synthesis Catalysts. *J. Catal.* **2004**, *225* (2), 359–368. https://doi.org/10.1016/j.jcat.2004.03.046.

(13) Zheng, J.; Liao, F.; Wu, S.; Jones, G.; Chen, T.-Y.; Fellowes, J.; Sudmeier, T.; McPherson, I. J.; Wilkinson, I.; Tsang, S. C. E. Efficient Non-Dissociative Activation of Dinitrogen to Ammonia over Lithium-Promoted Ruthenium Nanoparticles at Low Pressure. *Angew. Chem. Int. Ed.* **2019**, *58* (48), 17335–17341. https://doi.org/10.1002/anie.201907171.

(14) Wang, Z.; Liu, B.; Lin, J. Highly Effective Perovskite-Type BaZrO3 Supported Ru Catalyst for Ammonia Synthesis. *Appl. Catal. Gen.* **2013**, *458*, 130–136. https://doi.org/10.1016/j.apcata.2013.03.037.

(15) Raróg-Pilecka, W.; Miśkiewicz, E.; Jodzis, S.; Petryk, J.; Łomot, D.; Kaszkur, Z.; Karpiński, Z.; Kowalczyk, Z. Carbon-Supported Ruthenium Catalysts for NH3 Synthesis Doped with Caesium Nitrate: Activation Process, Working State of Cs–Ru/C. *J. Catal.* **2006**, *239* (2), 313–325. https://doi.org/10.1016/j.jcat.2006.01.035.

(16) Madhavaram, H.; Idriss, H.; Wendt, S.; Kim, Y. D.; Knapp, M.; Over, H.; Aßmann, J.; Löffler, E.; Muhler, M. Oxidation Reactions over RuO2: A Comparative Study of the Reactivity of the (110) Single Crystal and Polycrystalline Surfaces. *J. Catal.* **2001**, *202* (2), 296–307. https://doi.org/10.1006/jcat.2001.3281.

(17) Altamirano-Gutiérrez, A.; Jiménez-Sandoval, O.; Uribe-Godínez, J.; Castellanos, R. H.; Borja-Arco, E.; Olivares-Ramírez, J. M. Methanol Resistant Ruthenium Electrocatalysts for Oxygen Reduction Synthesized by Pyrolysis of Ru3(CO)12 in Different Atmospheres. *Int. J. Hydrog. Energy* **2009**, *34* (19), 7983–7994. https://doi.org/10.1016/j.ijhydene.2009.07.046.

(18) Narita, T.; Miura, H.; Sugiyama, K.; Matsuda, T.; Gonzalez, R. D. The Effect of Reduction Temperature on the Chemisorptive Properties of RuSiO2: Effect of Chlorine. *J. Catal.* **1987**, *103* (2), 492–495. https://doi.org/10.1016/0021-9517(87)90140-0.

(19) Li, Y.; Zhang, L. A.; Qin, Y.; Chu, F.; Kong, Y.; Tao, Y.; Li, Y.; Bu, Y.; Ding, D.; Liu, M. Crystallinity Dependence of Ruthenium Nanocatalyst toward Hydrogen Evolution Reaction. *ACS Catal.* **2018**, *8* (7), 5714–5720. https://doi.org/10.1021/acscatal.8b01609.

(20) Han, D.; Shinoda, K.; Sato, S.; Majima, M.; Uda, T. Correlation between Electroconductive and Structural Properties of Proton Conductive Acceptor-Doped Barium Zirconate. *J. Mater. Chem. A* **2014**, *3* (3), 1243–1250. https://doi.org/10.1039/C4TA05701E.

(21) Han, D.; Hatada, N.; Uda, T. Chemical Expansion of Yttrium-Doped Barium Zirconate and Correlation with Proton Concentration and Conductivity. *J. Am. Ceram. Soc.* **2016**, *99* (11), 3745–3753. https://doi.org/10.1111/jace.14377.

(22) Ricote, S.; Bonanos, N.; Manerbino, A.; Coors, W. G. Conductivity Study of Dense BaCexZr(0.9−x)Y0.1O(3−δ) Prepared by Solid State Reactive Sintering at 1500 °C. *Int. J. Hydrog. Energy* **2012**, *37* (9), 7954–7961. https://doi.org/10.1016/j.ijhydene.2011.08.118.

(23) Fabbri, E.; Pergolesi, D.; Licoccia, S.; Traversa, E. Does the Increase in Y-Dopant Concentration Improve the Proton Conductivity of BaZr1−xYxO3−δ Fuel Cell Electrolytes? *Solid State Ion.* **2010**, *181* (21), 1043–1051. https://doi.org/10.1016/j.ssi.2010.06.007.

(24) Iwahara, H.; Yajima, T.; Hibino, T.; Ozaki, K.; Suzuki, H. Protonic Conduction in Calcium, Strontium and Barium Zirconates. *Solid State Ion.* **1993**, *61* (1), 65–69. https://doi.org/10.1016/0167-2738(93)90335-Z.

(25) Sata, N.; Hiramoto, K.; Ishigame, M.; Hosoya, S.; Niimura, N.; Shin, S. Site Identification of Protons in ${\mathrm{SrTiO}}_{3}$: Mechanism for Large Protonic Conduction. *Phys. Rev. B* **1996**, *54* (22), 15795–15799. https://doi.org/10.1103/PhysRevB.54.15795.

(26) Ito, T.; Nagasaki, T.; Iwasaki, K.; Yoshino, M.; Matsui, T.; Igawa, N.; Ishii, Y. Location of Deuterium Atoms in BaSn0.5In0.5O2.75+α by Neutron Powder Diffraction at 10 K. *Solid State Ion.* **2007**, *178* (1), 13–17. https://doi.org/10.1016/j.ssi.2006.10.030.

(27) Yamazaki, Y.; Blanc, F.; Okuyama, Y.; Buannic, L.; Lucio-Vega, J. C.; Grey, C. P.; Haile, S. M. Proton Trapping in Yttrium-Doped Barium Zirconate. *Nat. Mater.* **2013**, *12* (7), 647–651. https://doi.org/10.1038/nmat3638.

(28) Kochetova, N.; Animitsa, I.; Medvedev, D.; Demin, A.; Tsiakaras, P. Recent Activity in the Development of Proton-Conducting Oxides for High-Temperature Applications. *RSC Adv.* **2016**, *6* (77), 73222–73268. https://doi.org/10.1039/C6RA13347A.

(29) Yang, B. X.; Kirz, J. Soft X-Ray Absorption Cross Section of Argon Determined by a Variable Absorber Technique. *Appl. Opt.* **1987**, *26* (18), 3823–3826. https://doi.org/10.1364/AO.26.003823.

(30) Wang, P.; Chang, F.; Gao, W.; Guo, J.; Wu, G.; He, T.; Chen, P. Breaking Scaling Relations to Achieve Low-Temperature Ammonia Synthesis through LiH-Mediated Nitrogen Transfer and Hydrogenation. *Nat. Chem.* **2017**, *9* (1), 64–70. https://doi.org/10.1038/nchem.2595.

(31) Ogura, Y.; Sato, K.; Miyahara, S.; Kawano, Y.; Toriyama, T.; Yamamoto, T.; Matsumura, S.; Hosokawa, S.; Nagaoka, K. Efficient Ammonia Synthesis over a Ru/La 0.5 Ce 0.5 O 1.75 Catalyst Pre-Reduced at High Temperature. *Chem. Sci.* **2018**, *9* (8), 2230–2237. https://doi.org/10.1039/C7SC05343F.

(32) Shimoda, N.; Kimura, Y.; Kobayashi, Y.; Kubota, J.; Satokawa, S. Ammonia Synthesis over Yttrium-Doped Barium Zirconate and Cerate-Based Perovskite-Type Oxide Supported Ruthenium Catalysts. *Int. J. Hydrog. Energy* **2017**, *42* (50), 29745–29755. https://doi.org/10.1016/j.ijhydene.2017.10.108.

(33) Sato, K.; Imamura, K.; Kawano, Y.; Miyahara, S.; Yamamoto, T.; Matsumura, S.; Nagaoka, K. A Low-Crystalline Ruthenium Nano-Layer Supported on Praseodymium Oxide as an Active Catalyst for Ammonia Synthesis. *Chem. Sci.* **2016**, *8* (1), 674–679. https://doi.org/10.1039/C6SC02382G.

(34) Wu, S.; Peng, Y.-K.; Chen, T.-Y.; Mo, J.; Large, A.; McPherson, I.; Chou, H.-L.; Wilkinson, I.; Venturini, F.; Grinter, D.; Ferrer Escorihuela, P.; Held, G.; Tsang, S. C. E. Removal of Hydrogen Poisoning by Electrostatically Polar MgO Support for Low-Pressure NH3 Synthesis at a High Rate over the Ru Catalyst. *ACS Catal.* **2020**, *10* (10), 5614–5622. https://doi.org/10.1021/acscatal.0c00954.

(35) Lin, B.; Liu, Y.; Heng, L.; Wang, X.; Ni, J.; Lin, J.; Jiang, L. Morphology Effect of Ceria on the Catalytic Performances of Ru/CeO2 Catalysts for Ammonia Synthesis. *Ind. Eng. Chem. Res.* **2018**, *57* (28), 9127–9135. https://doi.org/10.1021/acs.iecr.8b02126.

Chapter 6 Conclusions, Future Work, & Outlook

Given the need to develop carbon-free alternatives to the essential Haber-Bosch process, this thesis attempted to demonstrate electrochemical synthesis of ammonia in barium zirconate cells at low pressures. The original objectives were to develop the procedure and apply new electrode catalysts to improve upon electrochemical ammonia production rates already published literature. Cells prepared in-house from BZY20 ceramics showed poor performance compared to literature, and in cells prepared from commercial BCZY electrolytes it was not possible to conclusively show electrochemical ammonia synthesis.

An alternative route to carbon-free ammonia uses heterogeneous catalysis at low pressures combined with electrolytic hydrogen production, as discussed in chapter 1. This will require new catalysts, displaying high activity and conversions at low temperatures. Ruthenium catalysts are the most promising candidate for this process but are limited at low temperatures by hydrogen poisoning. In this thesis it was shown how proton conducting supports can be used to reduce this poisoning effect.

6. 1 Conclusions

Chapter 3 focussed on the preparation of electrochemical cells, particularly the preparation of barium zirconate (BZ) electrolytes. Proton conducting membranes require careful preparation to ensure they are will sintered and conductive.

Various aspects of this multi-step synthesis procedure were investigated for their outcome on pellet structure. A synthetic procedure was developed which involved: sol-gel procedure followed by calcination at 1300 ºC for 3 hours, milling the resulting powders, pressing, and sintering at 1500 ºC. Particles were characterised during processing using BET, LDS, XRD and the morphology of the sintered pellets was investigated using SEM. Development of this procedure yielded a BZY20 membrane in which proton conductivity could be measured.

The proton conductivity of the BZY20 membranes was investigated using DC voltammetry and AC impedance spectroscopy techniques. Using AC impedance spectroscopy, the bulk and grain boundary conductivities were determined, and found to be comparable to literature values for the material. Challenges encountered when sintering BZY20 powders to dense membranes ultimately led to in-house preparation of electrolytes being suspended in favour of commercial samples, but it was demonstrated that the conductivity of prepared membranes could be measured with AC impedance spectroscopy. Development of this measurement protocol was essential for the work in chapter 4.

Rates of electrochemical ammonia synthesis were measured in the prepared BZY20 cells. Electrochemical ammonia synthesis rates were successfully measured in these cells; however, these rate values were extremely low, comparable only with the lowest reports in literature, and barely exceeding

the open circuit rate. Due to the poor performance of these cells, in-house electrolyte preparation was suspended.

Chapter 4 focussed on the preparation of cells for electrochemical ammonia synthesis, using BCZY electrolytes (supported on a Ni/BCZY electrode), supplied by CoorsTek. Cells prepared in this manner showed significantly higher current densities than in-house prepared BZY20 cells. It was theorised that the high currents would lead to higher activity for electrochemical ammonia synthesis. Surprisingly, it was not possible to measure any electrochemical ammonia production using these cells.

A range of electrode catalysts were prepared, characterised, and tested. SEM was used extensively to examine cell morphologies both before and after testing. Electrochemical characterisation enabled determination of cell conductivities, and Arrhenius plots were constructed to determine the activation energies for the intra- and inter-grain proton transport processes. An interesting finding showed that addition of a platinum catalyst to a Ag electrode clearly enhanced the rate of hydrogen oxidation to protons, but that the kinetics of the hydrogen evolution reaction were unchanged by the presence of platinum. The possibility of a Ag HER catalyst is an intriguing prospect warranting further exploration.

Rates of electrochemical ammonia synthesis using a number of electrode catalyst configurations were reported. However, in all cases it proved impossible to separate the contribution of the electrochemical ammonia synthesis reaction from the thermal ammonia synthesis reaction. Electrochemical ammonia synthesis could not be demonstrated in any of the tested cells. It was proposed that conversion of nitrogen to ammonia was limited by thermal equilibrium in these cells, obscuring electrochemically produced ammonia.

Finally, a two-chamber reactor enabling separation of anode and cathode gas streams was manufactured. This was done with the intention that it would highlight electrochemical ammonia synthesis, as any ammonia produced must be electrochemical. However, engineering this reactor to a gas tight specification proved not possible, and this investigation route was suspended.

Chapter 5 explored how proton conducting barium zirconate materials could be used as oxide supports for metallic ruthenium catalysts. Catalytic activity was observed to be dependent on the doping level of the support. This was linked to the proton conductivity of the support, and a mechanism for spillover of protons from metallic ruthenium was proposed and investigated.

Synthesising a range of lanthanide-doped barium zirconate supports did not highlight any trend in activity with changing dopant cation, except that yttrium dopants performed significantly better than all others. Investigations on the effect of changing the doping level of yttrium-doped barium zirconate (BZY) showed an increasing activity with proton conductivity of the support.

Caesium promotion was found to be essential in order to obtain a stable catalyst and comparing a range of Cs-promoted catalysts showed that catalysts supported on 10 or 20% doped BZY performed significantly better than those on 0 or 30% doped BZY. The hydrogen order of reaction was determined

for BZY20 at low conversion values, and it was found that at higher temperatures, the reaction was no longer limited by hydrogen poisoning. It was theorised the reduction in hydrogen poisoning and high rates over BZY10- and 20-supported catalysts is due to the proton conducting support promoting spillover of protons from the ruthenium metal.

To support the theory of hydrogen spillover, evidence was sought using neutron diffraction and in-situ XPS studies. Neutron diffraction showed that the presence of ruthenium particles increased the deuteration of the support. In-situ XPS showed changes in ruthenium oxidation state which were attributed to the spillover of a proton from Ru to the support resulting in a 1 electron reduction of the Ru particle. From this it was concluded that the high proton conductivity of BZY10 and 20 supports increases the activity of ruthenium catalysts to ammonia synthesis, due to a reduction of hydrogen poisoning via spillover of protons from the Ru particles to the support.

The original aim of this thesis, to demonstrate electrochemical ammonia synthesis using novel electrode catalysts, could not be realised. The high proton currents and thermal rates of ammonia synthesis measured in Chapter 4 suggested these materials may also be appropriate for mitigating hydrogen poisoning of ruthenium particles. Testing of barium zirconate materials for application to the heterogeneous catalysis of ammonia revealed a highly active catalyst which is dependent on the proton conducting nature of the support.

6. 2 Future Work

The work of chapter 3 is considered complete and not in need of further experiments since all original objectives were met successfully. Measured ammonia production rates and conductivities of the prepared BZY20 membranes were low compared to literature. Improving the performance of the BZY20 membranes would require new equipment (such as an isostatic press and high-temperature furnace). Given the commercial availability of highly conductive proton conducting electrolytes, in-house preparation of membranes offers little benefit.

Surprisingly, the BCZY cells tested in chapter 4 did not show any ammonia synthesis, despite displaying high current densities, and precedent in literature. The next step should be a significant reactor redesign. In the current system where gas flow is not actively directed over the electrodes, but allowed to flow around them, localised pockets of low flow over the electrodes may result in produced electrochemical ammonia reaching thermal equilibrium conversion before leaving the reactor. The reactor should be redesigned to allow accurate calculation of conversion and GHSV values. It is suggested that some literature reports of electrochemical ammonia synthesis in single chamber reactors would also benefit from a redesign to ensure rates are not limited by equilibrium. A more straightforward solution would be to conduct the experiments in a double chamber reactor, where the gas flow over each electrode is separated, and flow rates could be increased or decreased independently to vary the GHSV over each electrode. A two-chamber reactor would also eliminate the possibility for production of thermal ammonia.

The work of chapter 5 showed two highly active catalysts for ammonia synthesis (Cs-Ru/BZY10 and Cs-Ru/BZY20). Comparing these catalysts to literature showed they underperformed on a per-mole of ruthenium basis. The ruthenium loading of the catalysts should be reduced to give smaller and more defined ruthenium particles. This will give a higher ratio of surface to bulk ruthenium atoms, allowing more efficient metal usage. To accompany these new catalysts, a complete morphological characterisation of each catalyst should be carried out. This should include for all samples, ICP-MS results, HR-TEM, and H_2 chemisorption studies (in addition to the CO chemisorption studies already carried out). With more accurate data on the size and surface area of ruthenium particles, and ruthenium weight percent loading, the ruthenium dispersion should be calculated for each catalyst. These new, low loading ruthenium catalysts should be re-tested and compared to literature for activity per mole of ruthenium.

The temperature dependant conversion studies should be extended to include all catalyst samples. In addition, for the BZY10 and BZY20 supported catalysts, more temperature points should be collected. The peak of conversion of both catalysts relative to temperature, particularly for the BZY10 sample, has not yet been determined. In addition to these conversion studies, the hydrogen reaction order should be calculated for all catalysts at temperatures below 20% conversion. If reduced hydrogen poisoning is observed for BZY10 supported catalysts, but not for the BZ or BZY30 ones, this would be a very interesting result indeed. Determination of the reaction order for nitrogen and ammonia should be carried out to give a more complete picture of how reaction kinetics are affected by support proton conductivity.

6. 3 Outlook

Significant barriers remain for the commercialisation of electrochemical ammonia synthesis. As discussed in chapter 1, all currently published works fail to meet the current density and efficiency targets for commercialisation set by a U.S. Department of Energy grant program. Currently the systems with the highest current density and efficiency values are molten salt reactors. The comparatively low temperatures (200-400 ºC) will allow higher conversions to be achieved than at the higher temperatures reported using solid ceramic electrolyte-based cells. Near-ambient conditions electrochemical ammonia synthesis has been widely reported using water-based electrolytes. However, the synthesis rates remain far below the level required for commercialisation. For all electrochemical ammonia synthesis systems, significant development of electrode catalysts will be required before current density and efficiency reach industrially relevant levels.

It remains to be seen if ruthenium catalysts can compete with iron-based ones for the industrial ammonia synthesis process. The metrics to consider when evaluating a ruthenium-based process are costs, both capital and operational, and ammonia mass produced per unit time. The capital costs, or expenditure (CAPEX), include the cost to purchase the equipment and the catalyst. Operational expenditure (OPEX) is primarily composed of the energy costs. The equipment is composed primarily

of a system to supply hydrogen and nitrogen (syn-gas), compressors, a reactor vessel, and a recycle loop. The recycle loop is used because the per-pass conversion of reactants is low. Therefore, to avoid wasting valuable reactants, ammonia product is condensed out, and unreacted nitrogen and hydrogen are fed back into the reactor. A brief discussion follows of the CAPEX and OPEX of the standard Haber-Bosch process using an iron catalyst, and a so-called islanded process. The use of a ruthenium catalyst in a standard Haber-Bosch process is not considered, as this has already been tested in an industrial setting using the Kellogg Advanced Ammonia Process discussed in Chapter 1.

The current industrial ammonia synthesis reaction is carried out in very large volumes, due to economies of scale. Modern plants are capable of producing more than 3000 metric tons of ammonia per day.[1] The reaction is carried out over an iron catalyst, at temperatures above 350 ^{0}C, and pressures above 150 bar. The large reactor vessel must be able to withstand these high pressures, and due to increasing vessel wall thickness, the CAPEX scales with the pressure used according to Palys et al.[2] The iron catalyst used is very cheap, around 13 USD kg^{-1}, contributing little to the overall CAPEX.[3]

Generation of the synthesis gas (syn-gas) is an energy intensive process. The most common process for nitrogen generation is cryogenic distillation of air.[4] Hydrogen is generated by steam reforming of methane.[4] Methane is first de-sulphurised, then reacted with water to generate carbon monoxide and hydrogen. CO is further reacted with water to generate additional hydrogen and carbon dioxide. Carbon oxides must be removed from the hydrogen stream, which is subsequently mixed with the nitrogen stream in a 3:1 ratio to generate the syn-gas. The syn-gas has a very high purity requirement, around 99.99% must be of the desired components.[3] The generation, pressurisation, and preheating of the syn-gas has a high associated OPEX.

According to I. Dybkjaer in 'Ammonia: Catalysis and Manufacture', the ammonia synthesis loop consists of the following components: a reactor system, units for cooling the outflow gas to recover heat and condense ammonia product, units for separation of ammonia product from unreacted syngas, units for preheating of the reactor feed (often integrated with the heat cooling and condensation systems).[4]

Per pass conversions are low in the industrial process; I. Dybkjaer in 'Ammonia: Catalysis and Manufacture' reports outlet concentrations of ammonia in plants using iron catalysts of 17.1 and 19.9 mol. % operating at 140 and 220 bars respectively, while Bañares-Alcantara et al. stated per-pass conversions of 15-25% for the industrial process over iron catalysts. Through the use of syn-gas recovery and recycle systems, overall conversion can approach 97%, according to Benner et al.[5] M. Appl in chapter 4, section 5 of 'Ammonia Principles and Industrial Practice' comments on several syn-gas recovery technologies.[6] In general, it is possible to recover a large quantity of hydrogen (>90%), but significantly less nitrogen (20-30%). The energy required to operate the gas recycle loop, along with the loss of syn-gas have high associated OPEX. Higher per-pass conversions which permit less gas recycling are desirable.

Large amounts of energy are required to produce ammonia, contributing significantly to the OPEX of the process. Estimates of the average consumption vary, but it can be seen how the estimates decrease over time as the process is further optimised. M. Appl showed how average energy use per ton has decreased from 39.5 to 28.0 GJ t^{-1}_{NH3} in 1966 and 1991 respectively.[6] A report by Benner et al., using data from 1999, stated the production of ammonia requires 22.1 GJ t^{-1}_{NH3} to produce the feedstock, and 7.2-9.0 GJ t^{-1}_{NH3} as fuel.[5] Schlögl reported in 2003 an energy consumption of 4.81 Gcal t^{-1}_{NH3} (20.1 GJ t^{-1}_{NH3}) for the production of liquid ammonia from liquid water, air, and natural gas.[7] Reducing the energy consumption greatly reduces the OPEX of running Haber-Bosch reactors.

As previously stated, ruthenium catalysts have been tested in large-scale synthesis plants in the development of the KAAP process. An alternative use of ruthenium catalysts is in so called 'islanded' Haber-Bosch reactors. These smaller scale plants have been proposed for several applications; providing ammonia fuel for remote islands,[8] and for energy storage applications.[3,9] Ruthenium catalysts may find an advantage over iron ones in this scenario, thanks to reduced CAPEX of equipment and OPEX.

Ruthenium catalysts show higher activity than iron-based ones. This means the reactor temperature can be reduced while maintaining similar or higher turnover numbers and per-pass conversion values (Chapter 1, Figure 1-2). At lower temperatures less energy is required to heat the reactor, reducing OPEX. Additionally, the equilibrium conversion is higher, so if a catalyst can reach higher conversion values, the per-pass conversion will be increased, allowing for less gas recycling and reduced OPEX associated with running the recycle loop. It may also be desirable to reduce the operating pressure. As the lower temperatures are less limited by the thermodynamic conversion, it is possible that pressure can be reduced without limiting the per-pass conversion. At lower pressures, the CAPEX associated with purchasing of compressors and a synthesis loop capable of operating at higher pressures will both be reduced, as will the OPEX associated with running the compressors.

Reactors using ruthenium catalysts do have economic disadvantages. Firstly, the scarcity and resultant high price of ruthenium metal means the catalyst represents a significant CAPEX. According to Bañares-Alcántara et al., iron-based catalysts have a cost of 13 USD kg^{-1}, compared to a ruthenium based catalyst costing 1930 USD kg^{-1}.[3] However, in the case of BZY-supported ruthenium catalysts, the cost of the support may increase this figure . This material is currently produced primarily for specialist solid-oxide fuel cell and gas separation membrane applications, meaning both demand and production are low. One laboratory supplier (fuelcellmaterials.com) lists the price for BZY20 as 2790 USD kg^{-1}.[10] While the cost of this material will be lower when purchasing at the scales required for use in industrial ammonia synthesis catalysts, it is not known how much this will reduce the price. The raw costs of the minerals required to produce BZY and carbon supports are summarised in Table 6-1. The high price of yttrium and zirconium could mean that the use of BZY supports will be more expensive than carbon ones.

Secondly, the syn-gas supplied to islanded reactors may be significantly more expensive than to conventional reactors, due to differences in supply technologies, and economies of scale. The

technologies capable of supplying nitrogen and hydrogen to islanded Haber-Bosch reactors were reviewed by Bañares-Alcántara et al.[3] Hydrogen would be supplied using water electrolysis, with several different systems available. The best electrolysis technology will be dependent on specific details of the synthesis loop such as expected hydrogen consumption, water purity requirements, and whether excess hydrogen could be stored on site during power generation surges. According to an analysis by Stoll and von Linde,[11] at higher hydrogen output levels steam-reforming methane is significantly cheaper than electrolysis in terms of both CAPEX and OPEX. At lower hydrogen output levels, the situation is less clear, but according to their analysis, electrolysis has lower CAPEX, but (depending on electricity prices) generally higher OPEX. Nitrogen is supplied to conventional Haber-Bosch via cryogenic air separation (CAS), but for smaller scale operations pressure swing adsorption (PSA) is a viable alternative.[3] PSA can have an advantage over CAS in cases where renewable energy is utilised and power generation fluctuates, as it can operate over a wider load range. PSA however requires more energy than CAS, with energy consumption values of 0.29 and 0.11 kWh kg^{-1}_{N2} respectively (Wiessner 1988, Morgan et al. 2014), making the OPEX higher.[8,12]

Table 6-1: Cost of raw minerals needed to produce BZY or carbon supports. All figures from the 2016 United States Geological Survey Minerals yearbook,[13] except (*) which is from a market report on lifegreencharcoal.com.[14]

Mineral	Cost (USD per metric ton)
Barite (total price of crushed or ground barite sold or used in the USA)	179
Yttrium (99.999% purity)	3000
Zircon (standard grade)	950-1,100
Coconut shell derived activated carbon (2018 price range)*	600-2500

Modelling of the costs of islanded Haber-Bosch reactors by Bañares-Alcántara et al. compared iron and ruthenium catalysts operating at 150 and 100 bars, respectively. The Ru process using lower pressure means CAPEX of compressors is notably lower than Fe process (480 vs 637 thousand USD). However, catalyst CAPEX is much higher for ruthenium than iron (537 vs 3.6 thousand USD). Other capital costs were very similar between the two processes. OPEX are determined (primarily) by energy consumption. The analysis showed electrolysis (H_2 generation) is by far the biggest consumer of energy (94-97%). Electrolysis for the Fe process consumes very slightly less energy than the Ru process (around 0.1%). Air separation (nitrogen generation) consumes the same amount of energy for the two processes, and accounts for only 1% of total power consumption. NH_3 synthesis accounts for between 2-5% of total power consumption, and the Fe process consumes notably more energy than the Ru process (6-28% more, depending on H_2 and N_2 supply technology). The catalyst which formed the basis of this model had a Ru loading of 4.5%. Developing active catalysts with lower Ru loadings is the simplest way to reduce the cost of the catalysts. Another option is to improve the activity of Ru-based catalysts. Improving the performance or reducing the cost of ruthenium-based catalysts is a necessity before they

can be considered for islanded Haber-Bosch systems. Addressing the hydrogen poisoning is key to improving their performance, and yttrium-doped barium zirconate supports show promise in this regard.

In summary, the adoption of a ruthenium catalyst for islanded Haber-Bosch synthesis holds promise thanks to the higher activity of Ru but is currently limited by the high cost of Ru metal. Ru catalysts have not seen widespread adoption in classical Haber-Bosch, according to Smith et al. they are currently used in less than 5% of worldwide ammonia production, and only in secondary reactors. Again, this is due to unfavourable economic conditions.

Proton conducting supports for heterogeneous catalysts is a relatively unexplored field. This support property has been seen in this thesis to influence catalyst activity. Specifically, that ytrrium-doped barium zirconate supports reduce hydrogen poisoning of ruthenium catalysts. The proposed spillover mechanism could find useful applications in other catalyst systems in which hydrogen transfer occurs. Additionally, characterisation of this spillover mechanism using in-situ XPS is found to be a useful technique.

6. 4 References

(1) Williams, G.; Pattabathula, V. One Hundred Years of Ammonia Production–A Recap of Significant Contributions to Feeding the World. In *58th Atmual Safety in Ammonia Plants and Related Facilities Symposium, AIChE (Aug. 25-29, 20 13). sure. Capacities increased from*; 2013; Vol. 100, pp 40–50.

(2) Palys, M. J.; McCormick, A.; Cussler, E. L.; Daoutidis, P. Modeling and Optimal Design of Absorbent Enhanced Ammonia Synthesis. **2018**, 17.

(3) Bañares-Alcántara, R.; Dericks III, G.; Grünewald, P.; Masa Lopez, J.; Tsang, E.; Yang, A.; Ye, L.; Zhao, S. *Analysis of Islanded Ammonia-Based Energy Storage Systems*; University of Oxford: Oxford, 2015.

(4) Dybkjaer, I. Ammonia Production Processes. In *Ammonia: Catalysis and Manufacture*; Nielsen, A., Ed.; Springer-Verlag: Berlin Heidelberg, 1995; pp 199–328.

(5) Benner, J.; Lieshout, M.; Croezen, H. *Identifying Breakthrough Technologies for the Production of Basic Chemicals: A Long Term View on the Sustainable Production of Ammonia, Olefins and Aromatics in the European Region*; CE Delft, 2012.

(6) Appl, M. *Ammonia: Principles and Industrial Practice*; Wiley-VCH: Weinheim ; New York, 1999.

(7) Schlögl, R. Catalytic Synthesis of Ammonia—A "Never-Ending Story"? *Angew. Chem. Int. Ed.* **2003**, *42* (18), 2004–2008. https://doi.org/10.1002/anie.200301553.

(8) Morgan, E.; Manwell, J.; McGowan, J. Wind-Powered Ammonia Fuel Production for Remote Islands: A Case Study. *Renew. Energy* **2014**, *72*, 51–61. https://doi.org/10.1016/j.renene.2014.06.034.

(9) Smith, C.; Hill, A. K.; Torrente-Murciano, L. Current and Future Role of Haber–Bosch Ammonia in a Carbon-Free Energy Landscape. *Energy Environ. Sci.* **2020**, *13* (2), 331–344. https://doi.org/10.1039/C9EE02873K.

(10) BZY20 Yttria doped Barium Zirconate https://fuelcellmaterials.com/products/powders/electrolyte-powders/proton-conducting/bzy20-yttria-doped-barium-zirconate/ (accessed Jan 11, 2021).

(11) Stoll, R.; Von Linde, F. Hydrogen-What Are the Costs. *Hydrocarb. Process* **2000**, *79* (12), 42–46.

(12) Wiessner, F. G. Basics and Industrial Applications of Pressure Swing Adsorption (PSA), the Modern Way to Separate Gas. *Gas Sep. Purif.* **1988**, *2* (3), 115–119. https://doi.org/10.1016/0950-4214(88)80026-4.

(13) USGS. *Minerals Yearbook: Volume I. Metals and Minerals*; 2016.

(14) Market Review of Coconut Shell Charcoal https://www.lifegreencharcoal.com/market-review-of-coconut-shell-charcoal/ (accessed Dec 8, 2020).

Chapter 7 Appendices

7. 1 List of Publications & Conference Presentations

List of publications:

1. McPherson IJ, Sudmeier T, Fellowes J, Tsang SCE. Materials for electrochemical ammonia synthesis. Dalton Trans. 2019 Jan 30;48(5):1562–8.

2. McPherson IJ, Sudmeier T, Fellowes JP, Wilkinson I, Hughes T, Tsang SCE. The Feasibility of Electrochemical Ammonia Synthesis in Molten LiCl–KCl Eutectics. Angew. Chem. Int. Ed. 2019 Nov 25;58(48):17433–41.

3. Zheng J, Liao F, Wu S, Jones G, Chen T-Y, Fellowes J, et al. Efficient Non-dissociative Activation of Dinitrogen to Ammonia over Lithium-Promoted Ruthenium Nanoparticles at Low Pressure. Angew Chem Int Ed. 2019 Nov 25;58(48):17335–41.

The author's (Joshua Fellowes) contributions to each publication are as follows:

1. Data review and manuscript preparation for the section on high-temperature proton conducting cells, and general manuscript and figure preparation.

2. Development, implementation, and validation of a procedure for measurement of dissolved ammonia. Additionally, general experimental help and assistance with data collection.

3. Discussions and development of theory, general experimental assistance.

List of conference presentations:

1. UK Catalysis Hub Conference (2016): Application of Barium Zirconate Materials to Ammonia Synthesis (oral presentation)

2. Materials Research Society Winter Meeting (2017): Electrochemical Ammonia Synthesis in Barium Zirconate Cells for Energy Storage (poster presentation)

7. 2 Python Code

All graphs were plotted in python using the matplotlib module. The code used for calculation of experimental quantities is listed below.

Linear line of best fit:

```
from statistics import mean

def best_fit_slope(xs,ys):

    m = (((mean(xs)*mean(ys)) - mean(xs*ys)) /

        ((mean(xs)*mean(xs)) - mean(xs*xs)))

    b = (mean(ys) - (m * mean(xs)))

    return m, b
```

Find peaks:

```
from scipy.signal import find_peaks

peaks, peak_props = scipy.signal.find_peaks(signal, height = 5)
```

Data smoothing:

```
y_signals.rolling(z).mean()
```

where z = no of points to use average

Generate histogram plot

```
# the histogram of the data

    n, bins, patches = plt.hist(data_set, number_bins, density=True)

# best fit of data

    (mu, sigma) = sciStat.norm.fit(allData[data].iloc[:,0])


    # add a 'best fit' line

    y = sciStat.norm.pdf( bins, mu, sigma)

    l = plt.plot(bins, y)
```

Peak area (by trapezoidal integration)

```
def trap(f, x):

    area = 0

    N = len(x)-1
```

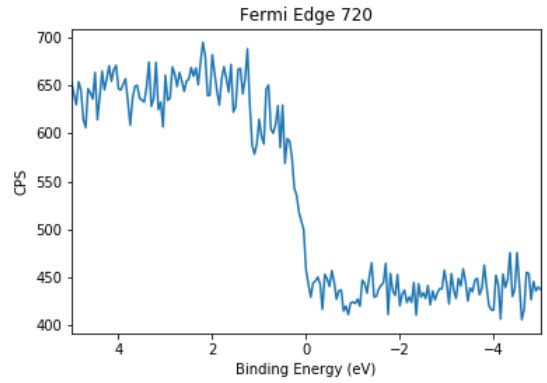
```
dx = x[1] - x[0]
for k in range(1, N):
    area += (f(x[k - 1]) + f(x[k])) * dx / 2
return area
```

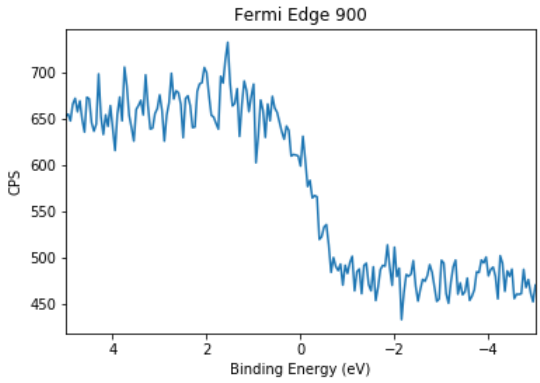
7. 3 XPS Calibration Spectra

Fermi-edge scans used for energy calibration of ruthenium (720) and oxygen (900) XPS data

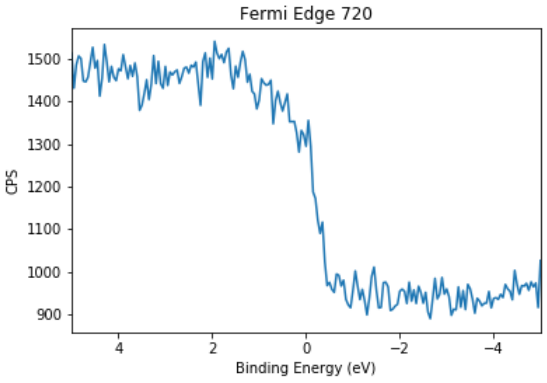
7. 3. 1. A Ru/BZ

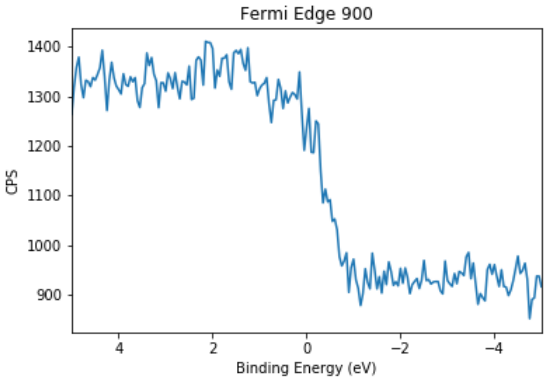
H_2 1st



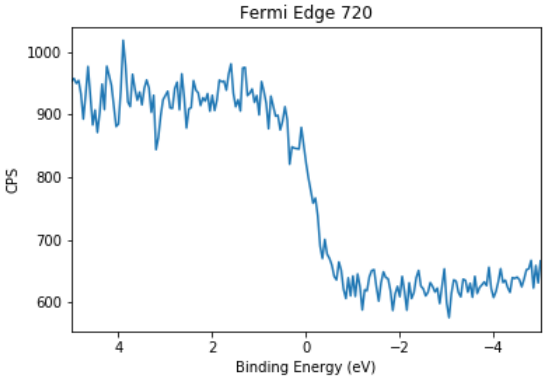


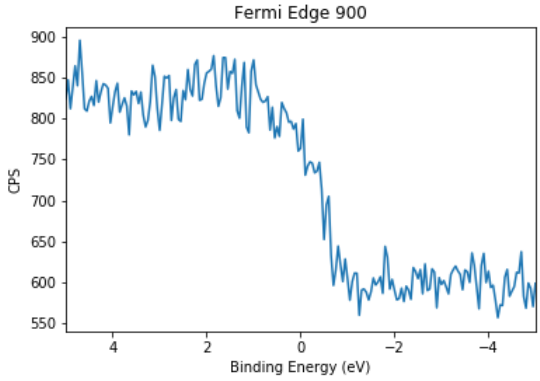
Ar





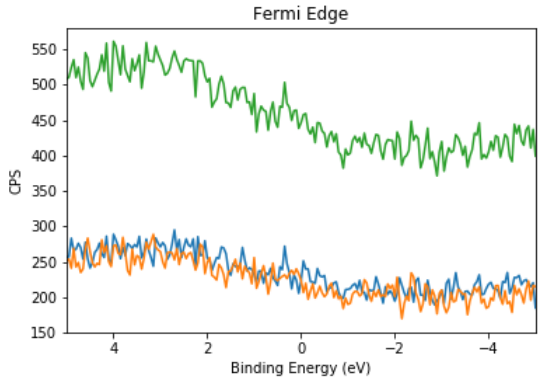
H_2 2nd

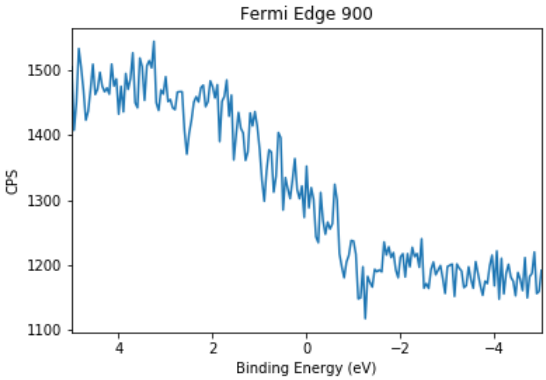




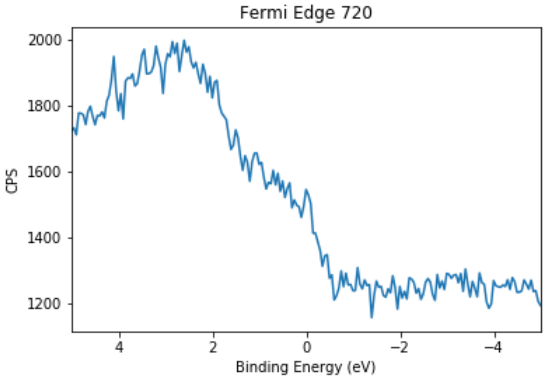
7. 3. 1. B Ru/BZY10

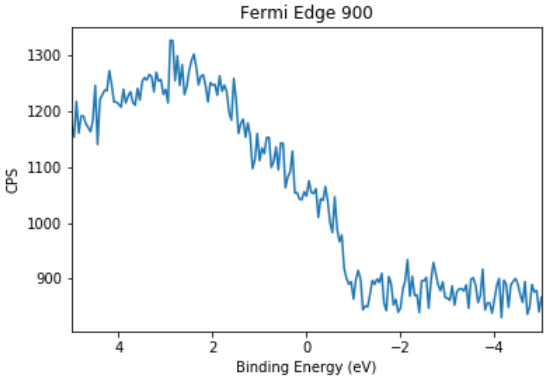
H_2 1st



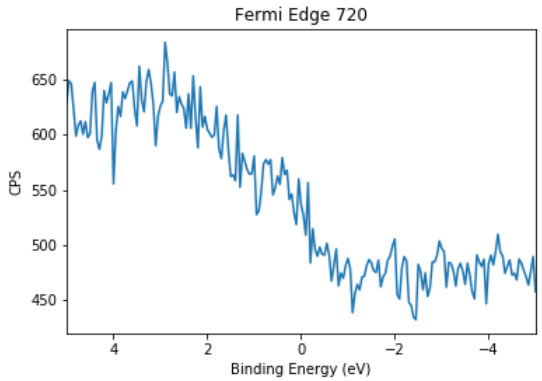


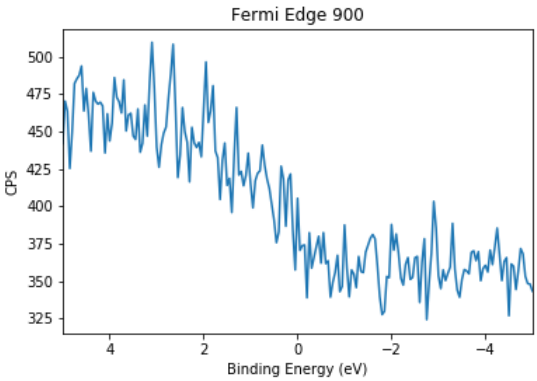
Ar





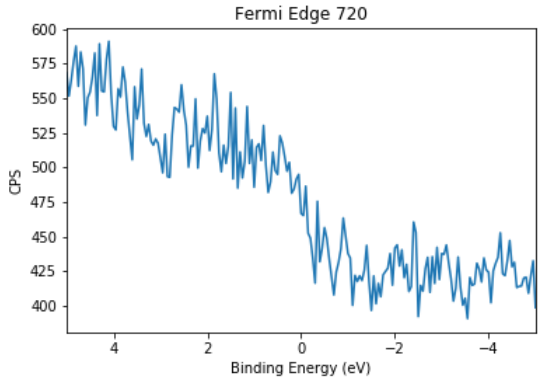
H_2 2nd

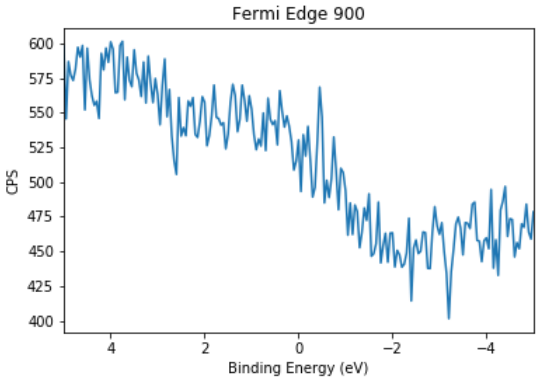




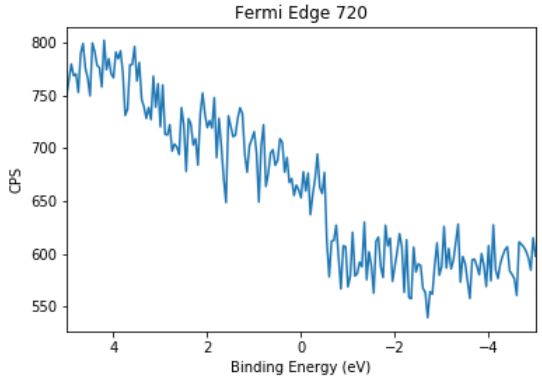
7. 3. 1. C Ru/BZY20

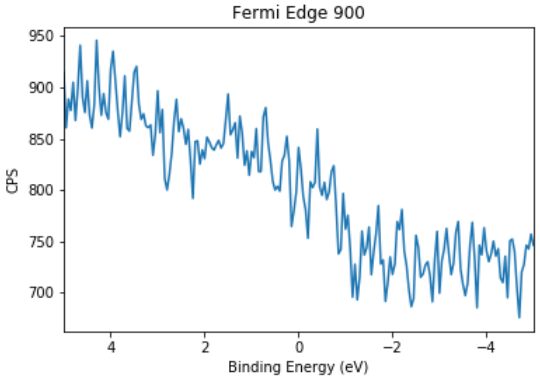
H_2 1st



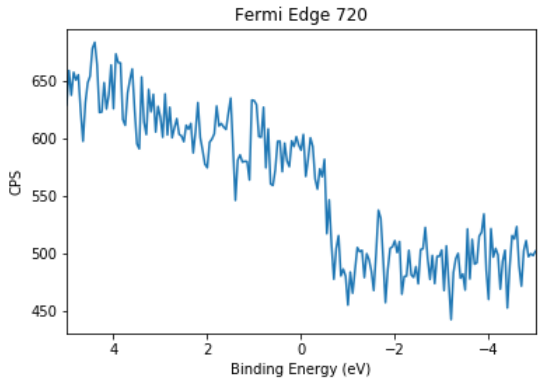


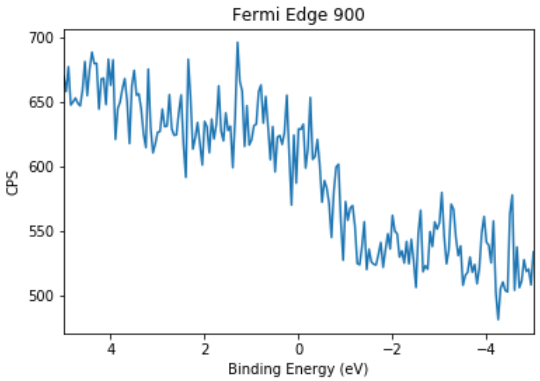
Ar





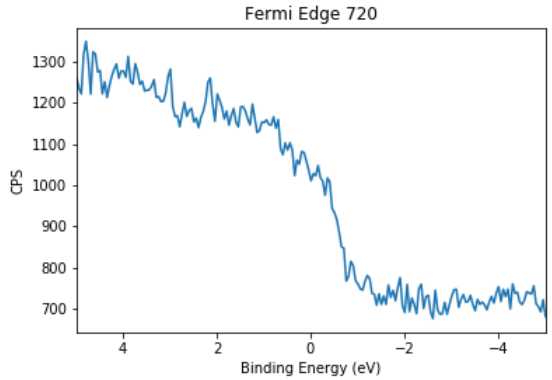
H_2 2nd

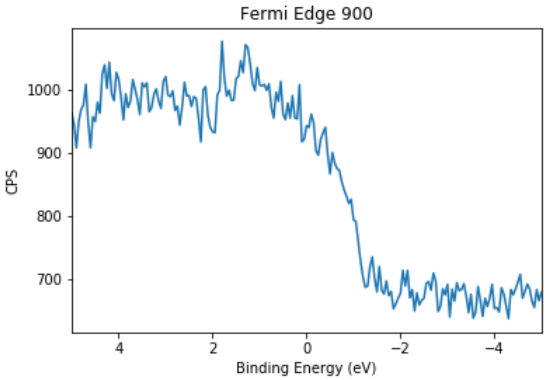




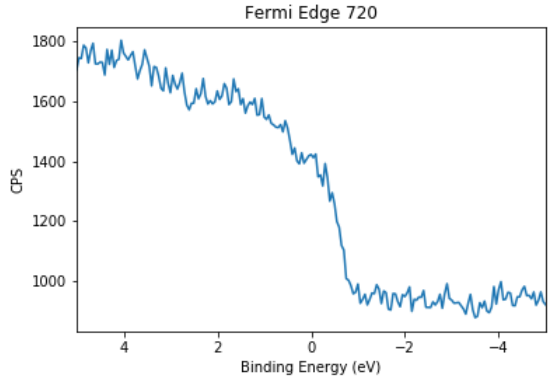
7. 3. 1. D Ru/BZY30

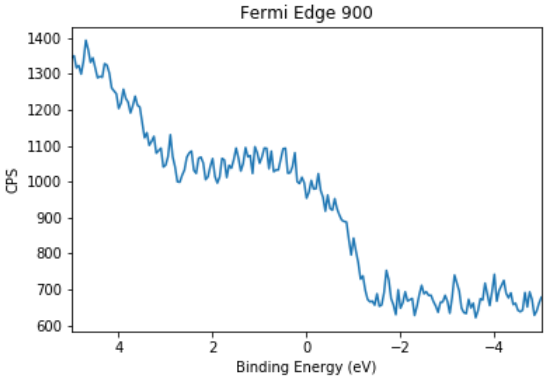
H_2 1st





Ar





H_2 2nd

